TM-87414

NASA-TM-87414 19860008651

SEPARATION OF AIRBORNE AND STRUCTUREBORNE NOISE RADIATED BY PLATES CONSTRUCTED OF CONVENTIONAL AND COMPOSITE MATERIALS WITH APPLICATIONS FOR PREDICTION OF INTERIOR NOISE PATHS IN PROPELLER DRIVEN AIRCRAFT

BY

MICHAEL C. McGARY

NF01541

3 1176 01321 6404

SEPARATION OF AIRBORNE AND STRUCTUREBORNE NOISE RADIATED BY PLATES CONSTRUCTED OF CONVENTIONAL AND COMPOSITE MATERIALS WITH APPLICATIONS FOR PREDICTION OF INTERIOR NOISE PATHS IN PROPELLER DRIVEN AIRCRAFT

A DISSERTATION

SUBMITTED TO THE DEPARTMENT OF AERONAUTICS AND ASTRONAUTICS

AND COMMITTEE ON GRADUATE STUDIES

OF STANFORD UNIVERSITY

IN PARTIAL FULFILLMENT OF THE REQUIREMENTS

FOR THE DEGREE OF

DOCTOR OF PHILOSOPHY

By

Michael C. McGary

January 1986

I certify that I have read this thesis and that in my opinion it is fully adequate, in scope and quality, as a dissertation for the degree of Doctor of Philosophy.

_____

(Principal Advisor)

I certify that I have read this thesis and that in my opinion it is fully adequate, in scope and quality, as a dissertation for the degree of Doctor of Philosophy.

_____

I certify that I have read this thesis and that in my opinion it is fully adequate, in scope and quality, as a dissertation for the degree of Doctor of Philosophy.

_____

I certify that I have read this thesis and that in my opinion it is fully adequate, in scope and quality, as a dissertation for the degree of Doctor of Philosophy.

_____

Approved for the University Committee on Graduate Studies:

_____

Dean of Graduate Studies and Research

ABSTRACT

The anticipated application of advanced turboprop propulsion systems and use of composite materials in primary structure is expected to increase the interior noise of future aircraft to unacceptably high levels. The absence of technically and economically feasible noise source-path diagnostic tools has been a prime obstacle in the development of efficient noise control treatments for propeller driven aircraft. A new diagnostic method which permits the separation and prediction of the fully coherent airborne and structureborne components of the sound radiated by plates or thin shells has been developed. Analytical and experimental studies of the proposed method were performed on plates constructed of both conventional and composite materials. The results of the study indicate that the proposed method can be applied to a variety of aircraft materials, could be used in flight, and has fewer encumbrances than the other diagnostic tools currently available. The study has also revealed that the noise radiation of vibrating plates in the low frequency regime due to combined airborne and structureborne inputs possesses a strong synergistic nature. The large influence of the interaction between the airborne and structureborne terms has been hitherto ignored by researchers of aircraft interior noise problems.

ACKNOWLEDGEMENTS

The author gratefully acknowleges the support of the National Aeronautics and Space Administration in this research. The work was sponsered by the Structural Acoustic Branch, Acoustics Division of the NASA Langley Research Center. I would like to thank the division chief, Homer G. Morgan, and branch chiefs Dave G. Stephens and C. A. Powell for their technical assistance and backing. I would also like to thank Frank Owens and George Allison of the Employee Development Branch for overseeing the financial arrangements of my graduate leave at Stanford. Special thanks goes to Bill Mayes, my immediate supervisor, who puts up with me. I would also like to express my eternal gratitude to Professor George Springer of Stanford who was willing to take a chance and serve as my advisor.

The entire effort was made possible by my loving wife, Charlotte, who unselfishly supported me through those difficult times at Stanford, also by my parents, Ivan and Vernett McGary, who taught me the value of self-discipline and hard work, and by the Grace of God.

TABLE OF CONTENTS

Chapter — Page

ABSTRACT.....iii

ACKNOWLEDGEMENTS.....iv

TABLE OF CONTENTS.....v

LIST OF FIGURES.....xii

LIST OF TABLES.....xvi

LIST OF SYMBOLS.....xvii
English letters.....xvii
Greek letters.....xxii
Superscripts.....xxv
Subscripts.....xxv
Special symbols.....xxvi
Abbreviations.....xxvi

I. INTRODUCTION.....1

A. INTERIOR NOISE IN PROPELLER DRIVEN AIRCRAFT..1

B. REDUCTION OF INTERIOR NOISE IN PROPELLER DRIVEN AIRCRAFT.....2

C. THE PURPOSE OF THIS RESEARCH.....3

II. PROBLEM APPROACH.....5

A. OVERVIEW OF THE DIAGNOSTIC APPROACH.....5

B. PROOF OF CONCEPT.....6

C. BASIS FOR THE ANALYTICAL AND EXPERIMENTAL STUDIES.....7

Chapter Page

III. ANALYSIS.....10

A. GOVERNING DIFFERENTIAL EQUATION OF THE PLATE DYNAMICS.....10

B. THE ADDITION OF DAMPING TO THE DYNAMIC MODEL.....14

C. DEFINITION OF THE FORCING FUNCTION FOR THE DYNAMIC MODEL.....17

D. SOLUTION TO THE FORCED RESPONSE DYNAMIC PROBLEM.....19

E. THEORY OF THE SOUND GENERATION OF PLATES.....22

F. THEORY OF THE ACOUSTIC RADIATION EFFICIENCY OF PLATES.....26

G. DIAGNOSTIC APPROACH AND ANALYSIS.....31

H. CONTRIBUTION OF THE CROSS TERM TO THE DIAGNOSTICS.....35

I. ERROR ANALYSIS OF THE PROPOSED DIAGNOSTIC METHOD.....37

J. IMPLEMENTATION OF THE ANALYTICAL MODEL.....37

K. SIMULATION OF THE PROPOSED DIAGNOSTIC METHOD.....38

IV. THEORY OF MEASUREMENT AND EXPERIMENTAL APPARATUS....43

A. THEORY OF MEASUREMENT.....43

B. MEASURMENT PROCEDURE.....48

C. PROPOSED DIAGNOSTIC PROCEDURE.....52

D. EXPERIMENTAL APPARATUS.....55

E. TEST PANELS.....58

Chapter Page

IV (cont'd)

F. INSTRUMENTATION AND DATA ACQUISITION.....58

G. DATA REDUCTION AND ANALYSIS.....61

H. VERIFICATION OF THE PROPOSED DIAGNOSTIC METHOD.....62

V. RESULTS AND DISCUSSION.....73

A. INTRODUCTION.....73

B. EFFECTS OF RELATIVE MAGNITUDE AND PHASE.....76

C. EFFECTS OF ALTERING THE INPUT PATHS (SHAKER LOCATION).....83

D. EFFECTS OF ADDED DAMPING.....86

E. EFFECTS OF COMPOSITE MATERIAL PLATE CONSTRUCTION.....89

F. RADIATION EFFICIENCIES OF COMPOSITE TAPE PLY PANELS.....92

G. DISCUSSION OF THE RESULTS.....95

H. OBSERVED DIFFERENCES BETWEEN THEORY AND EXPERIMENT.....100

VI. SUMMARY AND CONCLUSIONS.....123

A. REVIEW OF THE OBJECTIVE.....123

B. MAJOR FINDINGS OF THE STUDY.....123

C. APPLICABILITY OF THE DIAGNOSTIC METHOD TO AIRCRAFT.....125

D. AREAS FOR FUTURE RESEARCH.....126

REFERENCES.....128

Appendix Page

I. BACKGROUND INFORMATION AND DEFINITIONS.....134

A. FUTURE TRENDS IN AIRCRAFT DESIGN.....134

B. CHARACTERISTICS OF AIRBORNE PROPELLER NOISE.....136

C. CHARACTERISTICS OF STRUCTUREBORNE PROPELLER NOISE.....138

D. SEPARATION OF AIRBORNE AND STRUCTUREBORNE NOISE.....139

E. ACOUSTIC QUANTITIES.....141

F. FOURIER AND INVERSE FOURIER TRANSFORMS.....141

G. FINITE FOURIER TRANSFORMS.....141

H. RELATIONSHIP BETWEEN VELOCITY AND ACCELERATION.....142

I. AUTO CORRELATION FUNCTIONS.....142

J. CROSS CORRELATION FUNCTIONS.....143

K. SPECTRAL DENSITY FUNCTIONS.....144

L. ONE-SIDED AUTO SPECTRAL DENSITY FUNCTIONS.....145

M. ONE-SIDED CROSS SPECTRAL DENSITY FUNCTIONS.....146

N. EXPECTED VALUE OPERATOR.....148

O. ESTIMATION OF THE SPECTRAL DENSITY FUNCTIONS.....148

P. ACOUSTIC INTENSITY.....149

Q. SOUND POWER.....150

R. ACOUSTIC IMPEDANCE.....151

S. MEAN SQUARE SURFACE VELOCITY.....152

Appendix Page

I. (cont'd)

T. ACOUSTIC RADIATION EFFICIENCY.....152

U. CRITICAL FREQUENCY.....153

II. FREE VIBRATIONAL RESPONSE OF A SIMPLY SUPPORTED RECTANGULAR ORTHOTROPIC PLATE.....158

A. GOVERNING DIFFERENTIAL EQUATION.....158

B. FREE RESPONSE FOR THE UNDAMPED CASE.....159

C. FREE RESPONSE FOR THE DAMPED CASE.....163

III. FORCED VIBRATIONAL RESPONSE OF A SIMPLY SUPPORTED RECTANGULAR ORTHOTROPIC PLATE.....167

A. GOVERNING DIFFERENTIAL EQUATION.....167

B. DEFINITION OF THE FORCING FUNCTION.....167

C. STEADY STATE RESPONSE TO THE FORCING FUNCTION.....170

D. TRANSVERSE VIBRATIONAL VELOCITY OF THE PLATE.....172

IV. POWER FLOW FOR COMBINED AIRBORNE AND STRUCTUREBORNE INPUTS TO A SIMPLY SUPPORTED RECTANGULAR ORTHOTROPIC PLATE.....173

A. SPACE-TIME AVERAGED MEAN SQUARE SURFACE VELOCITY.....173

B. POWER INPUT.....177

C. POWER DISSIPATED.....181

V. SOUND RADIATION OF A POINT SOURCE.....184

A. MONOPOLE SOUND RADIATION.....184

B. MONOPOLE NEAR A REFLECTING SURFACE.....185

Appendix Page

VI. SOUND RADIATION FROM A SIMPLY SUPPORTED RECTANGULAR FLAT ORTHOTROPIC PLATE.....188

A. GEOMETRIC CONSIDERATIONS.....188

B. DERIVATION OF THE EQUATION FOR PRESSURE.....189

C. EVALUATION OF THE INTEGRALS.....194

D. CALCULATION OF THE SOUND POWER RADIATED.....199

E. SOUND POWER FOR THE SPECIAL CASE OF COMBINED INPUTS.....202

VII. CALCULATION OF THE BENDING RIGIDITY CONSTANTS FOR A SYMMETRIC LAMINATE WITH MULTIPLE GENERALLY ORTHOTROPIC LAYERS.....206

A. STRESS-STRAIN RELATIONS.....206

B. CALCULATION OF THE BENDING RIGIDITIES.....207

VIII. MEASUREMENT ERROR ANALYSIS.....209

A. DESCRIPTION OF THE ANALYSIS.....209

B. ERRORS IN THE STRUCTUREBORNE ESTIMATE.....210

C. ERRORS IN THE AIRBORNE ESTIMATE.....212

D. CONCLUSIONS.....214

IX. COMPUTER PROGRAMS.....222

A. PROGRAM MODAL.....222

B. PROGRAM SOUND.....224

C. PROGRAM PREDICT.....227

Appendix Page

X. VALIDATION OF THE COMPUTER PROGRAMS.....251

A. GRAPHICAL APPROACH.....251

B. VALIDATION OF PROGRAM MODAL.....251

C. VALIDATION OF PROGRAM SOUND.....252

XI. TWO MICROPHONE ACOUSTIC INTENSITY MEASUREMENT METHOD.....271

A. DERIVATION OF THE FUNDAMENTAL EQUATION FOR INTENSITY.....271

B. ERRORS ASSOCIATED WITH ACOUSTIC INTENSITY MEASUREMENTS.....276

XII. INSTRUMENT SPECIFICATIONS.....280

LIST OF FIGURES

Fig. No.		Page
III-1	Small and moderate damping coefficients for a plate constructed of AA 2024 aluminum.	40
III-2	Fraction of the cross term sound power attributed to the estimate of the structureborne sound power.	41
III-3	Fraction of the cross term sound power attributed to the estimate of the airborne sound power.	42
IV-1	Acoustic wedges covering the back wall and floor of the receiving room.	65
IV-2	Mounting brackets for the panels and array of six loudspeakers.	66
IV-3	Close-up cross sectional view of the mounting brackets for the panels.	67
IV-4	Acoustic intensity radiated by each of the six loudspeakers.	68
IV-5	Forcing function produced by the shaker -rod-panel system.	69
IV-6	Block diagram of the instrumentation used for the measurements.	70
IV-7	Two microphone acoustic intensity probe used for the measurements.	71
IV-8	Data aquisition, reduction, and analysis systems.	72
V-1	Analytical results for plate no. 1 with a dominant airborne source, the shaker located near the corner, and the small damping model.	104-105

LIST OF FIGURES (cont'd)

Fig. No.		Page
V-2	Analytical results for plate no. 1 with a dominant structureborne source, the shaker located near the corner, and the small damping model.	106-107
V-3	Experimental results for plate no. 1 with the shaker located near the corner.	108-109
V-4	Analytical results for plate no. 1 with a dominant airborne source, the shaker located at the center, and the small damping model.	110-111
V-5	Experimental results for plate no. 1 with the shaker located at the center.	112-113
V-6	Analytical results for plate no. 1 with a dominant airborne source, the shaker located near the corner, and the moderate damping model.	114-115
V-7	Experimental results for plate no. 1 with the shaker located near the corner and with damping tape added to the plate.	116-117
V-8	Analytical results for plate no. 2 with a dominant airborne source, the shaker located near the corner, and the small damping model.	118-119
V-9	Experimental results for plate no. 2 with the shaker located near the corner.	120
V-10	Analytical airborne and structureborne radiation efficiency curves for the symmetric angle ply composite panels (plates 3-6).	121
V-11	Measured airborne and structureborne radiation efficiency curves for the symmetric angle ply composite panels (plates 3-6).	122

LIST OF FIGURES (cont'd)

Fig. No.		Page
AI-1	Model of an advanced turboprop propulsion system (from reference 3).	154
AI-2	Noise signature of an advanced turboprop in a quiet wind tunnel (from reference 15).	155
AI-3	Spatial sound field distribution for an advanced turboprop (from reference 16).	156
AI-4	Sound field directivity and angle of incidence for an advanced turboprop (from reference 17).	157
AV-1	Monopole near a infinite reflecting surface.	185
AVI-1	Geometry of the simply supported plate.	188
AVIII-1	Error in the structureborne sound power estimate due to measurement errors in σ_s.	216
AVIII-2	Error in the structureborne sound power estimate due to measurement errors in σ_a.	217
AVIII-3	Error in the structureborne sound power estimate due to measurement errors in σ.	218
AVIII-4	Error in the airborne sound power estimate due to measurement errors in σ_s.	219
AVIII-5	Error in the airborne sound power estimate due to measurement errors in σ_a.	220
AVIII-6	Error in the airborne sound power estimate due to measurement errors in σ.	221

LIST OF FIGURES (cont'd)

Fig. No.		Page
AX-1	Natural frequencies versus mode number m for different values of mode number n for plate no. 1.	262
AX-2	Plate no. 1 directivity plots at 20 m distance for a 1 Pa peak, normally incident, spatially uniform acoustic input with a forcing frequency of 500 Hz.	263
AX-3	Plate no. 1 directivity plots at 20 m distance for a 1 Pa peak, normally incident, spatially uniform acoustic input with a forcing frequency of 1000 Hz.	264
AX-4	Plate no. 1 directivity plots at 20 m distance for a .01 N peak, point vibrational input at the center of the plate with a forcing frequency of 500 Hz.	265
AX-5	Plate no. 1 directivity plots at 20 m distance for a .01 N peak, point vibrational input at the center of the plate with a forcing frequency of 1000 Hz.	266
AX-6	Plate no. 1 directivity plots at 20 m distance for a .01 N peak, point vibrational input near the corner of the plate with a forcing frequency of 500 Hz.	267
AX-7	Plate no. 1 directivity plots at 20 m distance for a .01 N peak, point vibrational input near the corner of the plate with a forcing frequency of 1000 Hz.	268
AX-8	Airborne and structureborne radiation efficiencies of an extremely stiff plate constructed of an imaginary material.	269
AX-9	Airborne and structureborne sound powers radiated by an extremely stiff plate constructed of an imaginary material.	270

LIST OF TABLES

Table No.		Page
II-1	Description of the plate construction.	63
II-2	Material properties of the plate plies.	63
II-3	Calculated bending rigidities of the plates.	64

LIST OF SYMBOLS

a	fluid particle acceleration - also used as an arbitrary constant in Appendix VI
$\vec{a}$	fluid particle acceleration vector
a_{kl}	influence coefficient of the klth structural mode due to an acoustic (airborne) input
a_{mn}	influence coefficient of the mnth structural mode due to an acoustic (airborne) input
A	Fourier transform of the magnitude of the fluid particle acceleration vector
b	used as an arbitrary constant in Appendix VI
c_o	speed of sound in air at ambient atmospheric conditions
c_1	shaker location in the α_1 coordinate direction
c_2	shaker location in the α_2 coordinate direction
C_{pa}	real part of the one sided cross spectral density between acoustic pressure and acoustic fluid particle acceleration
C_{pv}	real part of the one sided cross spectral density between acoustic pressure and acoustic fluid particle velocity
$\cos()$	denotes the cosine of the angle inside the parenthesis
d_1	plate dimension in the α_1 coordinate direction
d_2	plate dimension in the α_2 coordinate direction
D_{ij}	flexural rigidity which relates bending moments to the curvature of the plate (i,j=1,2,6)

LIST OF SYMBOLS (cont'd)

D/Dt	denotes the substantial or total derivative with respect to time
e	the base of the natural logrithms
$\vec{e}_r$, $\vec{e}_{r'}$	radially outward unit vectors
E_1	modulus of elasticity (Young's modulus) in the α_1 coordinate direction
E_2	modulus of elasticity (Young's modulus) in the α_2 coordinate direction
$E\{\ \}$	expected value operator
f	frequency, Hertz
f_a	airborne forcing function (acoustic input)
f_s	structureborne forcing function (vibrational input)
$\vec{F}$	input force or resistive force on the plate
F_v	component of the resistive force in the direction of the surface velocity
$F\{\ \}$	Fourier transform operator
$\vec{g}$	acceleration due to gravity
G	shear modulus of elasticity (modulus of rigidity)
G_{aa}	one sided auto spectral density of the acoustic fluid particle acceleration
G_{pa}	one sided cross spectral density between acoustic pressure and fluid particle acceleration
G_{pp}	one sided auto spectral density of the acoustic pressure
G_{pv}	one sided cross spectral density between acoustic pressure and fluid particle velocity
G_{xx}	one sided auto spectral density of signal x

LIST OF SYMBOLS (cont'd)

G_{xy}	one sided cross spectral density between signals x and y
h	thickness of the plate - also used as the distance between a monopole and a nearby reflecting surface
I	magnitude of the acoustic intensity vector
$\vec{I}$	acoustic intensity vector
Im{ }	imaginary part of the quantity inside brackets
j	square root of -1 (imaginary number)
k	alternate mode number for the α_1 coordinate
l	alternate mode number for the α_2 coordinate
L_i	linear stiffness operator for the ith equation
L_3	linear stiffness operator for the partial differential equation governing the transverse deflection of the plate $u_3 = u$
m	mode number for the α_1 coordinate
n	mode number for the α_2 coordinate
$\vec{n}$	unit vector normal to the surface
p	acoustic pressure
P	Fourier transform of the pressure signal
q	forcing function applied to the plate
Q_{ij}	reduced stiffness relating stress and strain
$\bar{Q}_{ij}$	transformed reduced stiffness
Q_{pa}	minus the imaginary part of the one sided cross spectral density between acoustic pressure and acoustic fluid particle acceleration

Q_{pv}	minus the imaginary part of the one sided cross spectral density between acoustic pressure and acoustic fluid particle velocity
r	distance between the origin of the coordinate system and the point of observation
$\vec{r}$	position vector of the point of observation
r'	distance between an arbitrary point on the plate and the point of observation - also used as the distance between an acoustic monopole radiator and the point of observation in Appendix V
$\vec{r}'$	vector joining an acoustic monopole radiator and the point of observation
r_1, r_2, r_3	coordinates of the point of observation
R_{pv}	cross correlation between acoustic pressure and acoustic fluid particle acceleration
R_{xx}	auto correlation of signal x
R_{xy}	cross correlation of signals x and y
Re{ }	real part of the quantity inside brackets
S	surface area of the plate (one side)
S_{pv}	cross spectral density between acoustic pressure and fluid particle velocity
S_{xx}	auto spectral density of signal x
S_{xy}	cross spectral density between signals x and y
s_{kl}	influence coefficient of the klth structural mode of the plate due to a vibrational (structureborne) input
s_{mn}	influence coefficient of the mnth structural mode of the plate due to a vibrational (structureborne) input

LIST OF SYMBOLS (cont'd)

sgn()	has value +1 if the quantity inside the parenthesis is positive, -1 if the quantity inside the parenthesis is negative
sin()	denotes the sine of the angle inside the parenthesis
t	time
T	time interval of observation or data collection
u	transverse displacement of the plate (= u_3)
u_i	displacement of the plate in the ith direction
u_1, u_2, u_3	displacement of the plate in the α_1, α_2, α_3 coordinate directions respectively
$\dot{u}$	transverse velocity of the plate
U_{kl}	structural mode shape associated with the klth mode
U_{mn}	structural mode shape associated with the mnth mode
v	magnitude of the acoustic fluid particle velocity vector - often used interchangeably with the transverse velocity of the plate since the two quantities are equal at the surface of the plate
v_a	surface velocity of the plate due solely to the airborne input
v_s	surface velocity of the plate due solely to the structureborne input
v_{sxa}	surface velocity of the plate due to cross terms between inputs
$\vec{v}$	acoustic fluid particle velocity vector
V	Fourier transform of the magnitude of the acoustic fluid particle velocity vector signal
$\dot{W}$	power input to the plate by the forcing function

x	dummy variable x
X	Fourier transform of x - also used as the imaginary part of the specific acoustic impedance
y	dummy variable y
Y	Fourier transform of dummy variable y
Z	specific acoustic impedance
Z_k	complex number associated with the kth mode (see Appendix VI)
Z_l	complex number associated with the lth mode (see Appendix VI)
Z_m	complex number associated with the mth mode (see Appendix VI)
Z_n	complex number associated with the nth mode (see Appendix VI)

Greek

$\alpha_1, \alpha_2, \alpha_3$	cartesian coordinate system with the origin at the corner of the plate
$\beta_1, \beta_2, \beta_3$	cartesian coordinate system with the origin at the center of the plate
γ	dummy complex argument
γ_{kl}	phase angle associated with the klth mode due to the damping coefficient ξ_{kl}
γ_{mn}	phase angle associated with the mnth mode due to the damping coefficient ξ_{mn}
γ_{12}	shear strain
∂	used to denote partial derivatives
$\delta()$	Dirac delta function
Δf	frequency resolution (bandwidth)

Greek (cont'd)

Δx	spacing between microphones for the acoustic intensity probe
ε_i	extensional strain in the ith direction
η_i	modal participation factor for the ith mode
η_{kl}	influence coefficient of the klth mode
η_{mn}	influence coefficient of the mnth mode
θ	polar angle in a spherical coordinate system
θ_{kl}	phase angle associated with the klth mode
θ_{mn}	phase angle associated with the mnth mode
θ_1	relative phase of microphone 1
θ_2	relative phase of microphone 2
λ	equivalent viscous damping coefficient - also used as the wavelength of an acoustic disturbance in Appendix VII
μ	Poisson's ratio for an isotropic material
μ_1	Poisson's ratio in the α_1 coordinate direction
μ_2	Poisson's ratio in the α_2 coordinate direction
ξ_{mn}	equivalent viscous critical damping coefficient associated with the mnth mode
π	ratio of the circumference to the diameter of a circle
Π	sound power radiated by the plate
Π_a	sound power radiated by the plate due solely to the airborne input

Greek (cont'd)

Π_s	sound power radiated by the plate due solely to the structureborne input
Π_{sxa}	cross term sound power radiated by the plate
ρ	mass per unit area of the plate
ρ_o	density of the acoustic fluid medium (air)
σ	acoustic radiation efficiency
σ_i	extensional stress (i=1,2)
σ_a	radiation efficiency of the airborne component of the sound power
σ_f	fractional radiation efficiency
σ_{fx}	fractional efficiency of the cross terms
σ_s	radiation efficiency of the structureborne component of the sound power
σ_{sxa}	radiation efficiency of the cross terms
τ	time delay
τ_{12}	shear stress
$\vec{\vec{\tau}}$	viscous stress tensor (rank 2)
ϕ	azimuthal angle in spherical coordinates
ϕ_a	relative phase of the airborne input
ϕ_s	relative phase of the structureborne input
$\underline{\underline{\Phi}}$	potential function for a simple acoustic source
ω	radian driving frequency
ω_{mn}	radian natural frequency of the mnth mode
Ω_{mn}	damped radian modal natural frequency

Superscripts

'	associated with a newly defined quantity
*	denotes the complex conjugate
~	denotes an estimated value
$\vec{}$	denotes a vector
$\vec{\vec{}}$	denotes a tensor of rank 2

Subscripts

a	airborne component - also acoustic fluid particle acceleration
i	denotes the ith mode
k	denotes the kth mode in the α_1 direction
l	denotes the lth mode in the α_2 direction
m	denotes the mth mode in the α_1 direction
n	denotes the nth mode in the α_2 direction
o	denotes the ambient conditions
p	acoustic pressure
r	space
r,t	space-time
s	structureborne component
sxa	denotes the cross term component
t	time
v	acoustic fluid particle velocity
x	dummy variable x
y	dummy varible y

Special symbols

$\lim_{T\to\infty}$	denotes the limit as time T approaches infinity
∞	infinity
$\sum_{=1}^{\infty}$	denotes summation from 1 to infinity
$\sum_{=1}^{N}$	denotes summation from 1 to N
$< >_t$	denotes a time average
$< >_{r,t}$	denotes a space-time average
$\| \|$	denotes the magnitude of the quantity inside
∇	denotes the gradient operator
$\nabla\cdot$	denotes the divergence operator

Abbreviations

A.B.	denotes the results for the airborne component
S.B.	denotes the results for the structureborne component
0 deg	denotes the results when the inputs are combined at 0 degrees (in phase)
90 deg	denotes the results when the inputs are combined at 90 degrees (uncorrelated)
180 deg	denotes the results when the inputs are combined at 180 degrees (out of phase)
SUM	denotes the results when the structureborne and airborne components are summed

Abbreviations (cont'd)

COMBINED (+)	denotes the results when the inputs are combined with positive polarity on the shaker
COMBINED (-)	denotes the results when the inputs are combined with negative polarity on the shaker
A.B. EST.	denotes the airborne component estimated by the proposed diagnostic method
S.B. EST.	denotes the structureborne component estimated by the proposed diagnostic method

Chapter I

INTRODUCTION

A. INTERIOR NOISE IN PROPELLER DRIVEN AIRCRAFT

Interior noise levels of propeller driven aircraft have been measured between 84 and 104 dB on the A-weighted scale. (See references 1 and 2.) Limited exposure to these noise levels can cause a temporary shift in the hearing threshold of the passengers. Prolonged exposure can result in permanent hearing damage. (Pilot and crew are at risk.) The noise can also interfere with the operational safety of the aircraft and the efficiency of the pilot and crew. For these reasons, high interior noise levels in propeller driven aircraft have historically been a cause for concern in both the commercial and the military sectors of the aircraft industry.

Problems with interior noise levels in future aircraft are expected to intensify due to the advanced turboprop propulsion systems now being incorporated into the design of transport aircraft and because of the anticipated widespread use of composite materials in the primary structure of aircraft. (See Appendix I for a discussion of how the future trends in aircraft design are expected to effect interior noise levels in aircraft.) (Also see references 1-27 for background information relating to interior noise in propeller driven aircraft.)

The noise entering the cabin of a propeller driven aircraft is generally divided into two major categories, viz. airborne noise and structureborne noise. Airborne noise is generated aerodynamically by the propellers and propagates along an acoustic path (the fluid medium being air in this case). This noise then strikes the sidewalls of the aircraft and is transmitted into the interior of the aircraft. Structureborne noise has its source in the vibration of the wings or other structural members of the aircraft. This vibrational energy propagates along structural paths into the cabin of the aircraft where it causes vibration of the sidewalls and other surfaces inside the aircraft. This structural vibration then radiates noise inside the aircraft cabin.

B. REDUCTION OF INTERIOR NOISE IN PROPELLER DRIVEN AIRCRAFT

The distinction between airborne noise and structureborne noise is important because the methods typically used in reducing airborne and structureborne noise are quite different. For example, if the predominant source of the noise in the aircraft is structureborne, then the problem might be solved through the use of vibration isolators, or by the application of damping materials. If the predominant source of noise is airborne, then the problem might be solved by aft mounting the propellers or by adding massive materials to the sidewalls.

Since much of the success or failure of a particular aircraft design depends on the performance of the aircraft in terms of the payload capacity, range, and other weight sensitive parameters, an aircraft designer/manufacturer can add mass to an aircraft for noise control purposes only on the areas of the fuselage where it is absolutely necessary. Thus, to optimize the noise control design and treatment of an aircraft from a cost/performance standpoint, a confident knowledge of the relative importance of the airborne and structureborne noise transmission is essential. This knowledge can be obtained only if the aircraft designer and manufacturer has reliable and effective noise source/path diagnostic tools. Unfortunately, the diagnostic measurement and prediction methods currently available to the aircraft industry for determining the relative contributions of airborne and structureborne noise have proven themselves either inadequate or technically and/or economically unfeasible. (See Appendix I for a brief review of the most recent diagnostic methods applied to aircraft.) (Also see references 1-27 for background information.)

C. THE PURPOSE OF THIS RESEARCH

Recently, several new noise source/path identification tools have come into widespread use. Among the most promising of these new tools are several methods for measuring the acoustic intensity vector. (See references 28-34.) In the

past 5 years, researchers have begun apply these methods to noise transmission problems in aircraft. (See references 35-41.) The purpose of this research is to develop a new measurement method, based on the two microphone cross spectral acoustic intensity measurement method, for separating and predicting the airborne and structureborne components of the noise radiated by aircraft-type panels.

Chapter II

PROBLEM APPROACH

A. OVERVIEW OF THE DIAGNOSTIC APPROACH

The measurement method proposed in this study utilizes a two microphone acoustic intensity probe to measure the time averaged sound power radiated, $\langle \Pi \rangle_t$, and an array of miniature accelerometers to measure the space-time averaged mean square surface velocity, $\langle v^2 \rangle_{r,t}$, of a thin shell structure. The method employs these two types of measurements (exclusively) along with several equations developed by the author (based on theoretical considerations) to separate and predict the relative amounts of the total (combined) sound power that can be attributed to the airborne and structureborne components (respectively) due to some unknown combination of acoustic and vibrational inputs.

The scheme of the proposed diagnostic method is to:
(1) determine the radiation efficiency of the structure when it is radiating purely airborne noise (σ_a),
(2) determine the radiation efficiency of the structure when it is radiating purely structureborne noise (σ_s),
(3) use the information obtained in steps (1) and (2) along with measurements of $\langle \Pi \rangle_t$ and $\langle v^2 \rangle_{r,t}$ (while the structure is being driven by the combined noise sources of interest) to predict the airborne and structureborne components of the combined sound power.

B. PROOF OF CONCEPT

In order to validate the proposed diagnostic method it was decided that both analytical and experimental studies should be performed. The purpose of the analytical study was to develop a theoretical foundation for the proposed diagnostic method (based on the theory of sound radiation of thin shell structures) and to simulate the performance of the diagnostic method under various operating conditions. The purpose of the experimental study was then to verify the expected behavior of the diagnostic method by showing that the trends predicted by the analytical simulations are the same trends that are observed under actual measurement conditions.

It was decided that simple rectangular plates would serve as the test vehicle for both analytical simulations and experimental verification of the proposed diagnostic method. Plates were chosen because they possess most of the vibrational and sound radiative properties that are exhibited by actual aircraft sidewalls (due to their thin shell construction). Since the accuracy of the proposed measurement method does not depend on the complexity of structures used, if the method works well on simple flat plates, it should also work on more complicated structures. Futhermore, the theory of vibration and sound radiation of plates is well developed enough so that the author could extend it

to include the case of combined airborne and structureborne inputs. Last, but not least, the plates could easily be constructed and mounted with the experimental facilities that were available.

The physical dimensions of the plates were chosen to be .4064 m x .2413 m (16 in x 9.5 in) since an extensive study of the transmission loss properties of plates of this size had already been completed by NASA researchers. Both conventional aluminum and composite materials were included in the study since it is expected that composites will be used in the primary structure of aircraft built in the 1990's and beyond.

C. BASIS FOR THE ANALYTICAL AND EXPERIMENTAL STUDIES

An analytical model of the vibration and sound radiation of plates of symmetric angle-ply laminate construction due to combined airborne and structureborne inputs was developed. Chapter III, which follows, will outline the development of the analytical model and present the theoretical basis for the proposed diagnostic method. (See Appendices II-VI for mathematical details of the theory used in developing the analytical model.)

The analytical model assumes that the plates are rectangular and simply supported in an infinite, rigid baffle. The plates are assumed to be symmetric laminates with multiple generally orthotropic layers (e.g. graphite, fiberglass,

or Kevlar regular symmetric angle-ply tape panels) or constructed of simple orthotropic materials (e.g. isotropic AA 2024 aluminum panels). The sound radiated by the plates is assumed to be generated by the flexural (bending) vibrational response of the plate and is radiated to a free-field acoustic space (anechoic). Futhermore, the dynamic response of the plate (which generates the sound) is assumed to be dependent only on the incident airborne and structureborne forcing functions on the plate and independent of (uncoupled from) the sound pressure radiated by the plate. (This last assumption is sometimes referred to as the blocked pressure assumption in acoustic transmission theory.)

A normally incident, spatially uniform pressure field was used to model the airborne input. A point load was used to model the structureborne input. The analysis was confined to the 0-1000 Hz frequency range since this range encompasses the most troublesome noise region for propeller driven aircraft.

The experimental study of the proposed diagnostic method was performed using the NASA Langley Research Center's acoustic transmission loss apparatus. Using this facility, the test panels could be subjected to the desired acoustic and vibrational inputs in the source room while the surface velocity and sound power radiated by the panels could be measured in the receiving room. Every effort was

made to emulate the simplifying assumptions used in the analytical modeling. Chapter IV, which follows, describes the special equipment that was constructed for mounting and driving the plates and the modifications that were made to the transmission loss apparatus.

The results of the analytical simulations of the application of the proposed diagnostic method under various operating conditions and the experimental verification of the predicted trends are presented and discussed in chapter V. The variation of several parameters and their effects on the proposed diagnostic method are presented for both the analytical and experimental investigations. Parameters studied include the effects on the diagnostic method due to changes in the relative magnitude and phase of the airborne and structureborne inputs, changes in the level of structural damping, changes in the location of the structureborne input, and changes in the thickness, density, and fiber orientation for the composites.

Chapter III

ANALYSIS

A. GOVERNING DIFFERENTIAL EQUATION OF THE PLATE DYNAMICS

The governing equation for the transverse undamped free vibration of a flat rectangular orthotropic plate is given by

$$D_{11}\partial^4 u/\partial\alpha_1^4 + 2(D_{12}+2D_{66})\partial^4 u/\partial\alpha_1^2\partial\alpha_2^2 + D_{22}\partial^4 u/\partial\alpha_2^4 + \rho h\ddot{u} = 0 , \qquad (3.1)$$

where α_1 and α_2 are the in-plane coordinates, u is the transverse displacement of the plate and the D_{ij} are the plate bending rigidity constants. (See Appendix II for a more complete discussion of the parameters in this equation.) This equation can be solved exactly for the case of simply supported boundary conditions by using the method of separation of variables. From Appendix II, the solution is given by

$$u(\alpha_1,\alpha_2,t) = \sum_{m=1}^{\infty}\sum_{n=1}^{\infty} \eta_{mn}\sin(m\pi\alpha_1/d_1)\sin(n\pi\alpha_2/d_2)e^{j(\omega_{mn}t+\theta_{mn})} \qquad (3.2)$$

where the ω_{mn} are the radian natural frequencies of the plate given by

$$\omega_{mn}^2 = \pi^4/\rho h \cdot \left[D_{11}(m/d_1)^4 \right.$$

$$\left. + 2(D_{12}+2D_{66})(m/d_1)^2(n/d_2)^2 + D_{22}(n/d_2)^4 \right] . \qquad (3.3)$$

The governing equation for the transverse undamped free vibration of a flat rectangular plate of symmetric angle-ply laminate construction contains two additional terms due to the coupling between shear stress and extensional deformation and coupling between normal stresses and shear deformation and is given by (see reference 42, pg. 273)

$$D_{11}\partial^4 u/\partial\alpha_1^4 + 4D_{16}\partial^4 u/\partial\alpha_1^3\partial\alpha_2 + 2(D_{12}+2D_{66})\partial^4 u/\partial\alpha_1^2\partial\alpha_2^2$$

$$+ 4D_{26}\partial^4 u/\partial\alpha_1\partial\alpha_2^3 + D_{22}\partial^4 u/\partial\alpha_2^4 + \rho h\ddot{u} = 0. \qquad (3.4)$$

(See Appendix VII for a complete discussion on the calculation of the bending rigidity constants D_{ij} for symmetric laminates with multiple generally orthotropic layers.)

Equation (3.4) can not be solved exactly using the method of separation of variables because of the additional fourth order differentials. In fact, no exact solution of any kind has been found for equation (3.4). It can be shown by dimensional analysis (see reference 43), however, that an

equation analogous to the equation (3.3) for the radian natural frequencies of the plate is given by

$$\omega_{mn}^2 = \pi^4/\rho h \cdot \Big[D_{11}(m/d_1)^4 - C(D_{16})(m/d_1)^3(n/d_2) + 2(D_{12}+2D_{66})(m/d_1)^2(n/d_2)^2 - C(D_{26})(m/d_1)(n/d_2)^3 + D_{22}(n/d_2)^4 \Big] \qquad (3.5)$$

where C is some unknown constant. Bert (reference 43) utilized results obtained from the Raleigh-Ritz analysis performed by Ashton and Waddoups (reference 44) and results obtained from Green's classical Fourier analysis performed by Whitney (reference 45) to estimate an upper and lower bound on the value of the constant C. With these two analyses it was estimated that a value of C=2 was a good approximation for the unknown constant of equation (3.5). From this analysis performed by Bert (reference 43), it was decided that an estimate of the natural frequencies for a regular symmetric angle-ply laminate is given by

$$\omega_{mn}^2 = \pi^4/\rho h \cdot \Big[D_{11}(m/d_1)^4 - 2(D_{16})(m/d_1)^3(n/d_2) + 2(D_{12}+2D_{66})(m/d_1)^2(n/d_2)^2 - 2(D_{26})(m/d_1)(n/d_2)^3 + D_{22}(n/d_2)^4 \Big] . \qquad (3.6)$$

Thus, the solution of the transverse undamped free-vibration problem governed by equation (3.4) is approximated by equation (3.2) with the natural frequencies, ω_{mn}, calculated from equation (3.6). Hence, the analytical model chosen for this work treats the regular symmetric angle-ply laminates in exactly the same fashion as the simpler orthotropic plate with the only difference being that the natural frequencies of the laminates are calculated using equation (3.6). It should be noted that this model approximates both the eigenvalues and the eigenfunctions of equation (3.4) since the sine waves of equation (3.2) satisfy the geometric boundary conditions but do not satisfy the natural boundary conditions or the differential equation. These two approximations will cause no error in the analysis of the noise radiation of symmetric laminates with multiple specially orthotropic layers (e.g. a 0/90 lay-up) since, for that case, D_{16} and D_{26} are zero and the problem reduces to the orthotropic case. Since it is known that the true eigenfunctions are not exactly sine waves for a symmetric laminate with multiple generally orthotropic layers (e.g. a +45/-45 lay-up), the use of equation (3.2) can be expected to cause some inaccuracies in the calculated dynamic response, and subsequently the noise radiation in those cases (see reference 46, pp. 101-110). Inasmuch as the behavior of the symmetric angle-ply plates converges to the

orthotropic solution as the number of plies become large, the sine wave approximation is considered acceptable for plates with 8 or 16 plies.

B. THE ADDITION OF DAMPING TO THE DYNAMIC MODEL

The governing equation for the transverse damped free vibration of a flat, rectangular orthotropic plate is given by (see Appendix II)

$$D_{11}\partial^4 u/\partial\alpha_1^4 + 2(D_{12}+2D_{66})\partial^4 u/\partial\alpha_1^2\partial\alpha_2^2 + D_{22}\partial^4 u/\partial\alpha_2^4 + \lambda\dot{u} + \rho h\ddot{u} = 0 \qquad (3.7)$$

where λ is an equivalent viscous damping coefficient.

We now make the assumption that the vibrational modes of the plate are uncoupled. Technically, the flexural modeshapes of a rectangular plate are uncoupled only when the damping is related to the mass and stiffness properties of the plate in a special fashion (see reference 47, pp. 390-394). Thus, by making this assumption, our mathematical relations for the orthotropic plate become approximations. The assumption that the modes are uncoupled can be used without serious error when the damping is a second order effect. Furthermore, the assumption is aided by the fact that the modal density for flexural modes of a rectangular plate is nearly constant at low frequency. This means that there are no frequency regions of high modal density and

therefore little opportunity for the exchange of energy among modes. With this assumption it is shown in Appendix II that the solution to equation (3.7) is given by

$$u(\alpha_1,\alpha_2,t) =$$

$$\sum_{m=1}^{\infty}\sum_{n=1}^{\infty} \eta_{mn}\sin(m\pi\alpha_1/d_1)\sin(n\pi\alpha_2/d_2)$$

$$\cdot\ e^{-\xi_{mn}\omega_{mn}t}\ e^{j(\Omega_{mn}t+\theta_{mn})} \quad . \tag{3.8}$$

And the damped radian natural frequencies Ω_{mn} are given by

$$\Omega_{mn} = \omega_{mn}\left[\ 1-\xi_{mn}^2\ \right]^{1/2} \quad , \tag{3.9}$$

where the modal damping coefficient ξ_{mn} is defined by

$$\xi_{mn} = \lambda/(2\rho h\omega_{mn}) \quad . \tag{3.10}$$

Once it is assumed that the modal damping coefficients are independent of one another, a value must be chosen for each. Reasonable damping coefficients for 2024 aluminum are in the range of $\xi = 0.01$. A more moderately damped structure might have damping coefficients in the range $\xi = 0.04$. Because of the large energy loss due to sound radiation at low frequency, however, experimentally determined damping coefficients for the first few resonance frequencies will appear to be much, much larger than this. (On the

order of $\xi = 0.1$.) These inflated damping coefficients are a direct result of the blocked pressure assumption discussed earlier. Thus, the large damping coefficients at low resonance frequencies do not owe their existence to any erroneous assumptions about the nature of the damping in the structure, but rather are the result of neglecting the significant fluid loading effect in the model of the forcing function. For these reasons, two different damping models were investigated in this study given by the equations

$$\xi_{mn} = .09(\omega_{11}/\omega_{mn}) + .01 \ , \tag{3.11}$$

$$\xi_{mn} = .06(\omega_{11}/\omega_{mn}) + .04 \ , \tag{3.12}$$

where the hyberbolic term in each equation corrects for the fluid loading effect at the first few resonance frequencies and the constant term in each equation represents the inherent damping of the structure. Equation (3.11) shall be subsequently referred to as the small damping model while equation (3.12) shall be referred to as the moderate damping model. A plot of these two damping models for a plate constructed of AA 2024 aluminum is shown in figure (III-1).

C. DEFINITION OF THE FORCING FUNCTION FOR THE DYNAMIC MODEL

The governing differential equation for the forced dynamic response of a simply supported, rectangular orthotropic plate (from Appendix III) is given by

$$D_{11}\partial^4 u/\partial\alpha_1^4 + 2(D_{12} + 2D_{66})\partial^4 u/\partial\alpha_1^2\partial\alpha_2^2 + D_{22}\partial^4 u/\partial\alpha_2^4 + \lambda\dot{u} + \rho h\ddot{u} = q(\alpha_1,\alpha_2,t) \ , \qquad (3.13)$$

where, for the purposes of this study, the forcing function $q(\alpha_1,\alpha_2,t)$ will be defined by the equation

$$q(\alpha_1,\alpha_2,t) = \left[f_s\, e^{-j\phi_s}\, \delta(\alpha_1-c_1)\delta(\alpha_2-c_2) + f_a\, e^{-j\phi_a} \right] e^{j\omega t} \ . \qquad (3.14)$$

(See Appendix III for the definitions of the various terms in this equation.) Thus, the acoustic (airborne) input is chosen to be a normally incident, spatially uniform, simple harmonic forcing function and the vibrational (structure-borne) input is chosen to be a simple harmonic, point vibrational load.

The reasons for choosing a normally incident airborne input are threefold. As discussed in Appendix I, the propeller noise which impinges on the sidewall of an aircraft is an oblique incidence problem with a slowly varying

spatial pressure distribution caused by the extremely long wavelengths of the low frequency sound. Secondly, the case of normal incidence produces an airborne radiation efficiency that is numerically smaller than the corresponding oblique or random incidence cases. (This can be verified theoretically and will be recognized immediately if the reader is familiar with acoustic transmission loss theory.) Thus, the normal incidence case produces a worst case scenerio in which the airborne radiation efficiency is as small as possible. (The reasons why this is desirable will become evident later.) Thirdly, it is comparatively much easier to construct an experimental apparatus that approximates the normal incidence condition.

The point vibrational input was chosen to model the structureborne input primarily because it is easily mimicked experimentally using a shaker. It might be argued that a line load is a more realistic structureborne model since aircraft panels have ring frames and stringers attached to them. Because of the wide variation in design of composite airframes and in wing attachment, however, it is not clear that a line load model would be any more realistic. Furthermore, for the purposes of verifying the measurement method proposed in Chapter II, the point load model will, in principle, work just as well as a more complicated model.

D. SOLUTION TO THE FORCED RESPONSE DYNAMIC PROBLEM

From Appendix III, the steady state solution for the dynamic response of an orthotropic plate due to combined simple harmonic airborne and structureborne inputs (the solution to equation (3.13)) is given by

$$u(\alpha_1,\alpha_2,t) = \sum_{m=1}^{\infty}\sum_{n=1}^{\infty}\left[s_{mn}\, e^{-j\phi_s} + a_{mn}\, e^{-j\phi_a} \right]$$

$$\cdot \sin(m\pi\alpha_1/d_1)\sin(n\pi\alpha_2/d_2)\, e^{j(\omega t-\gamma_{mn})}\,, \qquad (3.15)$$

where s_{mn} and a_{mn} are the structureborne and airborne influence coefficents, respectively, of the vibrational modes of the structure and are defined by the equations

$$s_{mn} = 4f_s/(d_1 d_2 \rho h \omega_{mn})\, \sin(m\pi c_1/d_1)\sin(n\pi c_2/d_2)$$

$$/\left[(1-\omega^2/\omega_{mn}^2)^2 + (2\xi_{mn}\omega/\omega_{mn})^2 \right]^{1/2}\,, \qquad (3.16)$$

and

$$a_{mn} = 4f_a/(mn\pi^2\rho h\omega_{mn}) \left[(1-\cos(m\pi))(1-\cos(n\pi)) \right]$$

$$/\left[(1-\omega^2/\omega_{mn}^2)^2 + (2\xi_{mn}\omega/\omega_{mn})^2 \right]^{1/2}\,. \qquad (3.17)$$

(See Appendix III for details.)

Simple differentiation with respect to time of the equation for displacement yields the equation for the surface velocity of the structure (see Appendix III):

$$v(\alpha_1,\alpha_2,t) =$$

$$\sum_{m=1}^{\infty}\sum_{n=1}^{\infty}\left[j\omega \left[s_{mn}\, e^{-j\phi_s} + a_{mn}\, e^{-j\phi_a} \right]\right.$$

$$\left.\cdot \sin(m\pi\alpha_1/d_1)\sin(n\pi\alpha_2/d_2)\; e^{j(\omega t-\gamma_{mn})} \right] . \qquad (3.18)$$

Equation (3.18) can then be used to calculate the space-time averaged mean square surface velocity $\langle v^2\rangle_{r,t}$. From the results of the calculations given in Appendix IV:

$$\langle v^2\rangle_{r,t} = \omega^2/8 \cdot$$

$$\sum_{m=1}^{\infty}\sum_{n=1}^{\infty}\left[s_{mn}^2 + a_{mn}^2 + 2s_{mn}a_{mn}\cos(\phi_s-\phi_a) \right] . \qquad (3.19)$$

Redefining the terms in equation (3.19) as discussed in Appendix IV, the equation becomes

$$\langle v^2\rangle_{r,t} = \langle v_s^2\rangle_{r,t} + \langle v_a^2\rangle_{r,t} + \langle v_{sxa}^2\rangle_{r,t} , \qquad (3.20)$$

where

$\langle v^2 \rangle_{r,t}$ = the space-time averaged mean square surface velocity,

$\langle v_s^2 \rangle_{r,t}$ = the structureborne component of the space-time averaged mean square surface velocity,

$\langle v_a^2 \rangle_{r,t}$ = the airborne component of the space-time averaged mean square surface velocity,

$\langle v_{sxa}^2 \rangle_{r,t}$ = the cross term component of the space-time averaged mean square surface velocity.

See Appendices III and IV for the derivations of the components of equation (3.20) in terms of series expansions in the modal influence coefficients of the structure. The last term in equation (3.20) accounts for the interaction between the structureborne and airborne inputs in terms of the panel dynamics. Thus, equation (3.20) shows that the dynamic response of the panel to the combined airborne and structureborne inputs is, in general, not equal to the sum of the responses to the airborne and structureborne inputs individually. Similar cross term components arise in the derivations of the power input to the plate and the power dissipated by the plate. (See Appendix IV.) One of the important features of equation (3.20) is that although it contains cross terms due to the combined inputs, it contains no cross terms between different modes of the structure. (See Appendix IV for more details.) (This absence of cross

terms between modes is a direct consequence of the orthogonality principle between modes of the structure.) Equation (A4.12) indicates that when the structureborne and the airborne inputs are precisely 90 degrees out of phase, the inputs are uncorrelated and the cross term is zero. Thus, when the two inputs are uncorrelated, the space-time averaged mean square surface velocity of the panel due to the combined inputs is exactly equal to the sum of the space-time averaged mean square surface velocities due to the structureborne and airborne inputs acting individually.

E. THEORY OF THE SOUND GENERATION OF PLATES

Once the surface velocity distribution of the plate has been found (equation (3.18)), the sound generated by the plate can be calculated. The classical approach for calculating the sound radiation from a vibrating plate, which utilizes Huygens principle of superposition of simple sources, was used in this study to calculate the sound power radiated by the plate. This theory models each incremental area of the vibrating plate as a point monopole source near an infinitely rigid reflecting surface. (A review of the theory of point monopole sound radiation is presented in Appendix V.) The mathematical details of this classical theory were derived for the particular case of combined structureborne and airborne inputs. The results of the derivations are presented in Appendix VI. The scheme of the

derivation is as follows: An equation is derived for the incremental acoustic pressure at a point in space due to the surface velocity of an incremental area of the plate. (See Appendix VI, eqn. (A6.3).) This equation is then simplified using a far-field approximation which assumes that the point of observation is at a distance from the plate which is much, much greater than the largest of the two plate dimensions. (See Appendix VI eqn. (A6.12).) This equation for the incremental pressure, as a function of the surface velocity of an incremental area on the plate, is then integrated over the entire surface of the plate. (See Appendix VI, eqn. (A6.13).) The expression for the surface velocity (equation (A3.16)) is then substituted into this equation and, after several complicated integrals are evaluated, an equation for the pressure at a point in the far acoustic field, as a function of polar and azimuthal angles, is obtained. (See Appendix VI eqn. (A6.36).) Since pressure and particle velocity are in phase in the far acoustic field, this equation for acoustic pressure can be used to calculate the time averaged acoustic intensity. (See Appendix VI, eqn. (A6.40).) The sound power radiated by the plate can then be calculated by integrating the equation for intensity over the polar and azimuthal angles. (See Appendix VI, eqn. (A6.43).) The final step in the analysis is to evaluate the expression for the special case of combined airborne and

structureborne inputs to the plate. (See Appendix VI, eqn. (A6.47).) This results in the equation on the following page for the time averaged sound power radiated by the plate:

$$
\begin{aligned}
&\langle \Pi(t) \rangle_t = \\
&\int_0^{2\pi} \int_0^{\pi/2} (\rho_o \omega^2/(2\pi))^2 \sin(\theta)/(2\rho_o c_o) \cdot \Bigg[\\
&\sum_{k=1}^{\infty} \sum_{l=1}^{\infty} \Bigg[s_{kl}^2 \, |Z_k|^2 \, |Z_l|^2 \\
&+ \mathrm{Re}\Big\{ \sum_{m=1}^{\infty} \sum_{\substack{n=1 \\ (kl \neq mn)}}^{\infty} s_{kl} \, s_{mn} \, e^{j(\gamma_{kl}-\gamma_{mn})} \, Z_k^* \, Z_l^* \, Z_m \, Z_n \Big\} \Bigg] \\
&+ \sum_{k=1}^{\infty} \sum_{l=1}^{\infty} \Bigg[a_{kl}^2 \, |Z_k|^2 \, |Z_l|^2 \\
&+ \mathrm{Re}\Big\{ \sum_{m=1}^{\infty} \sum_{\substack{n=1 \\ (kl \neq mn)}}^{\infty} a_{kl} \, a_{mn} \, e^{j(\gamma_{kl}-\gamma_{mn})} \, Z_k^* \, Z_l^* \, Z_m \, Z_n \Big\} \Bigg] \\
&+ \sum_{k=1}^{\infty} \sum_{l=1}^{\infty} 2 \Bigg[s_{kl} \, a_{kl} \cos(\phi_s - \phi_a) \, |Z_k|^2 \, |Z_l|^2 \\
&+ \mathrm{Re}\Big\{ \sum_{m=1}^{\infty} \sum_{\substack{n=1 \\ (kl \neq mn)}}^{\infty} s_{kl} \, a_{mn} \, e^{j(\phi_s-\phi_a)} \, e^{j(\gamma_{kl}-\gamma_{mn})} \\
&\cdot Z_k^* \, Z_l^* \, Z_m \, Z_n \Big\} \Bigg] \Bigg] \, d\theta d\phi \, . \qquad (3.21)
\end{aligned}
$$

(See Appendix VI for more information on the various terms in this equation.) Redefining the various terms in equation (3.21) as outlined in Appendix VI, the equation becomes

$$\langle \Pi \rangle_t = \langle \Pi_s \rangle_t + \langle \Pi_a \rangle_t + \langle \Pi_{sxa} \rangle_t \ , \qquad (3.22)$$

where

$\langle \Pi \rangle_t$ = the total time averaged sound power radiated,

$\langle \Pi_a \rangle_t$ = the time averaged sound power radiated due solely to the airborne input,

$\langle \Pi_s \rangle_t$ = the time averaged sound power radiated due solely to the structureborne input,

$\langle \Pi_{sxa} \rangle_t$ = the time averaged sound power radiated due to cross terms between the inputs.

See Appendices V and VI for the derivations of the components of equation (3.22) in terms of series expansions in the modal influence coefficients of the structure. The last term in equation (3.22) accounts for the interaction between the structureborne and airborne inputs in terms of the sound power radiated. Thus, equation (3.22) similarly shows that the sound power generated by the panel due to the combined airborne and structureborne inputs is, in general, not equal to the sum of the individual sound powers radiated by the panel due to the airborne and structureborne inputs acting individually. Unlike equation (3.20) for the panel dynamics, however, equation (3.22) contains cross terms between

the different modes of the structure. (See Appendix VI for more details.) The additional cross terms between different flexural modeshapes arise because the spatial average of the acoustic intensity used in calculating the sound power takes place over a hemi-spherical surface in the far acoustic field, and not over the surface of the plate (the area of spatial averaging for the analysis of the dynamic response of the plate). Thus, the orthogonality principle does not apply when calculating the sound power radiated by the plate. Furthermore, equation (A6.51) indicates that even when the structureborne and airborne inputs are precisely 90 degrees out of phase (uncorrelated), there are still many non-zero cross term components between the two inputs which contribute to the total sound power radiated due to the existence of the cross terms between different flexural modes of the structure. Therefore, in general, the total sound power radiated due to the simultaneously combined structureborne and airborne inputs is never exactly equal to the sum of the sound powers radiated due to the structure-borne and airborne inputs acting individually.

F. THEORY OF THE ACOUSTIC RADIATION EFFICIENCY OF PLATES

The acoustic radiation efficiency, σ, of a vibrating thin shell structure is defined as (see reference 48)

$$\sigma = \langle \Pi \rangle_t / (\rho_o c_o \langle v^2 \rangle_{r,t} S) , \qquad (3.23)$$

where

$\langle \Pi \rangle_t$ = the time averaged sound power radiated by the structure,

$\rho_o c_o$ = the characteristic acoustic impedance of the fluid medium,

$\langle v^2 \rangle_{r,t}$ = the space-time averaged mean square surface velocity of the structure,

S = the surface area of the structure.

(See Appendix I, sections P - T for more information.)

The equations for the acoustic radiation efficiencies for airborne and structureborne inputs to simple thin shell structures can be found in the literature. (See references 48 and 49.) Theoretical discussions in the text of reference 48 point out that in the frequency region below the critical frequency of a flat plate, the radiation efficiencies of airborne noise and structureborne noise are different. (See reference 48 or Appendix I, section U for the definition of the critical frequency.) Recently, Forssen and Crocker (reference 41) and McGary (references 39 and 40) have experimentally demonstrated this difference in the airborne and structureborne radiation efficiencies on panels in the frequency range below the critical frequency using a two microphone cross spectral acoustic intensity probe.

A rigorous explanation of the difference in the airborne and structureborne radiation efficiencies for thin

shell structures can be made in terms of the vibrational modes of the structure. It is well known in classical vibration theory that the vibrational response of a thin shell structure to any type of input (airborne or structure-borne) can always be found from the superposition of the individual reponses of the flexural mode shapes of the structure. Mathematically, the vibrational response is expressed as a series expansion in the mode shapes of the structure, with each mode in the series being multiplied by a modal participation factor that is uniquely associated with that particular mode. The modal participation factors consist of both the magnitude of the response, called the influence coefficient, and the relative phase of the response for each of the individual modes. The influence coefficients determine the relative amount of control or influence that each individual mode retains over the total response of the structure. (See Appendix II for the eigenvalue analysis and free vibrational response of a simply supported, rectangular orthotropic plate in terms of its natural modes. See Appendix III for the complete mathematical derivation of the forced vibrational response of a simply supported, rectangular orthotropic plate to simultaneously combined airborne and structureborne inputs in terms of its natural modes.)

If the total vibrational response is controlled primarily by modes whose resonance frequencies are within the frequency band of excitation, the vibrational response is said to be resonance controlled. If the total vibrational response is controlled by modes whose resonance frequencies are below the frequency band of excitation, the vibrational response is said to be mass controlled. In the frequency bands at and above the fundamental resonance frequency of the structure, the vibrational response of the structure to most types of structureborne inputs (e.g. a point or line load) is primarily resonance controlled, and the vibrational response of the structure to acoustic inputs (which are for the most part distributed loads) can be either resonance or mass controlled. Below the critical frequency of a flat plate, a resonance controlled panel response is a very inefficient noise generator (sometimes called acoustically slow), whereas a non-resonant or mass controlled panel response is a very efficient noise generator (sometimes called acoustically fast).

The difference in acoustic radiation efficiencies (in the frequency range below the critical frequency) for the resonance and non-resonant controlled cases stems from the difference in the effective flexural wave speeds for the two cases. For the case of a resonance controlled response, the product of the characteristic length (the wavelengths of the

resonant modes) and the forcing frequency is equal to the free vibrational or traveling flexural wavespeed in the structure. Below the critical frequency of the structure this free vibrational wavespeed is subsonic. Hence the resonance controlled response is an inefficient noise generating mechanism (acoustically slow). For the case of a non-resonant or mass controlled response, the product of the characteristic length scale (the wavelengths of the non-resonant modes) and the forcing frequency are much larger than the free vibrational or traveling flexural wavespeed in the structure and can exceed the speed of sound in air (supersonic). Hence the non-resonant or mass controlled response can be a very efficient noise generating mechanism.

At and above the critical frequency of the structure, both the non-resonant and resonant responses are efficient noise generators (acoustically fast). This is because structures are dispersive mediums for free vibrational (traveling) flexural waves. (The flexural wavespeed is proportional to the 1/2 power of the forcing frequency.) Thus, at and above the critical frequency, the free vibrational wavespeed is equal to or exceeds the speed of sound. Hence, there is very little difference in the acoustic radiation efficiencies for structureborne and airborne inputs at these high frequencies.

G. DIAGNOSTIC APPROACH AND ANALYSIS

In Section D, it was shown that the total space-time averaged mean square surface velocity of a simply supported, rectangular, orthotropic plate due to simultaneously combined airborne and structureborne inputs is given by (see Appendix IV, equation (A4.13))

$$\langle v^2 \rangle_{r,t} = \langle v_s^2 \rangle_{r,t} + \langle v_a^2 \rangle_{r,t} + \langle v_{sxa}^2 \rangle_{r,t} \ . \qquad (3.20)$$

Similarly, in Section E, it was shown that the total time averaged sound power radiated by a simply supported, rectangular, orthotropic plate due to simultaneously combined structureborne and airborne inputs is given by (see Appendix VI, equation (A6.52))

$$\langle \Pi \rangle_t = \langle \Pi_s \rangle_t + \langle \Pi_a \rangle_t + \langle \Pi_{sxa} \rangle_t \ . \qquad (3.22)$$

Multiplying equation (3.20) by the constant $\rho_o c_o$ S, and rearranging it algebraically one obtains the relation

$$\rho_o c_o \langle v^2 \rangle_{r,t} S - \rho_o c_o \langle v_{sxa}^2 \rangle_{r,t} S$$

$$= \rho_o c_o \langle v_s^2 \rangle_{r,t} S + \rho_o c_o \langle v_a^2 \rangle_{r,t} S \ . \qquad (3.24)$$

Utilizing the definition of radiation efficiency (equation (3.23)), and substituting into equation (3.24) the result is

$$\langle \Pi \rangle_t/\sigma - \langle \Pi_{sxa} \rangle_t/\sigma_{sxa} = \langle \Pi_s \rangle_t/\sigma_s + \langle \Pi_a \rangle_t/\sigma_a \ , \qquad (3.25)$$

where

σ = the radiation efficiency for the simultaneously combined inputs,

σ_{sxa} = the radiation efficiency of the cross terms between the two inputs,

σ_s = the radiation efficiency of the structureborne component,

σ_a = the radiation efficiency of the airborne component.

Now rearranging equations (3.22) algebraically, the following system of equations is obtained:

$$\langle \Pi \rangle_t/\sigma - \langle \Pi_{sxa} \rangle_t/\sigma_{sxa} = \langle \Pi_s \rangle_t/\sigma_s + \langle \Pi_a \rangle_t/\sigma_a \ , \qquad (3.25)$$

$$\langle \Pi \rangle_t - \langle \Pi_{sxa} \rangle_t = \langle \Pi_s \rangle_t + \langle \Pi_a \rangle_t \ . \qquad (3.26)$$

Solving this system of two equations and two unknowns for structureborne and airborne components of the sound power, one obtains

$$\langle \Pi_a \rangle_t = \langle \Pi \rangle_t \ (\sigma_a/\sigma) \ (\sigma - \sigma_s)/(\sigma_a - \sigma_s)$$

$$- \langle \Pi_{sxa} \rangle_t \ (\sigma_a/\sigma_{sxa}) \ (\sigma_{sxa} - \sigma_s)/(\sigma_a - \sigma_s) \ , \qquad (3.27)$$

$$\langle \Pi_s \rangle_t = \langle \Pi \rangle_t \, (\sigma_s/\sigma) \, (\sigma_a - \sigma)/(\sigma_a - \sigma_s)$$

$$- \langle \Pi_{sxa} \rangle_t \, (\sigma_s/\sigma_{sxa}) \, (\sigma_a - \sigma_{sxa})/(\sigma_a - \sigma_s) \, . \qquad (3.28)$$

Equations (3.27) and (3.28) are exact expressions which give the airborne and structureborne sound power components respectively in terms of the acoustic radiation efficiencies, the total sound power, and the cross term sound power. As discussed earlier, the cross term sound power depends on the relative phase between the two inputs. This dependence on phase makes the cross term sound power, and cross term radiation efficiency difficult to measure in practice. In contrast to the cross terms, the structureborne and airborne radiation efficiencies do not depend on the magnitudes or the relative phase of the inputs, and (as will be discussed in a later section) can easily be measured. Similarly, the total sound power and radiation efficiency for the combined inputs can be measured with relative ease. For these reasons, the following definitions of estimates of the structureborne and airborne components of the sound power are made:

An estimate of the airborne sound power is

$$\langle \tilde{\Pi}_a \rangle_t = \langle \Pi \rangle_t \, (\sigma_a/\sigma) \, (\sigma - \sigma_s)/(\sigma_a - \sigma_s) \, , \qquad (3.29)$$

so that

$$\langle \tilde{\Pi}_a \rangle = \langle \Pi_a \rangle_t$$

$$+ \langle \Pi_{sxa} \rangle_t \, (\sigma_a/\sigma_{sxa}) \, (\sigma_{sxa} - \sigma_s)/(\sigma_a - \sigma_s) \, . \qquad (3.30)$$

An estimate of the structureborne sound power is

$$\langle \tilde{\Pi}_s \rangle_t = \langle \Pi \rangle_t \, (\sigma_s/\sigma) \, (\sigma_a - \sigma)/(\sigma_a - \sigma_s) \, , \qquad (3.31)$$

so that

$$\langle \tilde{\Pi}_s \rangle_t = \langle \Pi_s \rangle_t$$

$$+ \langle \Pi_{sxa} \rangle_t \, (\sigma_s/\sigma_{sxa}) \, (\sigma_a - \sigma_{sxa})/(\sigma_a - \sigma_s) \, . \qquad (3.32)$$

Note that these estimates of the structureborne and airborne components of the sound power involve only the airborne and structureborne radiation efficiencies, and the total sound power and radiation efficiency due to the combined inputs. Another important feature of these estimates is that their sum is power preserving, i.e.

$$\langle \Pi \rangle_t = \langle \tilde{\Pi}_s \rangle_t + \langle \tilde{\Pi}_a \rangle_t \, . \qquad (3.33)$$

Furthermore, equations (3.29) and (3.31) suggest that measurable differences in radiation efficiencies for airborne and structureborne noise permits the separation, and prediction of an estimate of the airborne and structureborne components of the total sound power radiated by some unknown combination of structureborne and airborne inputs to a panel.

H. CONTRIBUTION OF THE CROSS TERM TO THE DIAGNOSTICS

Recall equations (3.30) and (3.32) from the previous section of this chapter:

$$\langle \tilde{\Pi}_a \rangle = \langle \Pi_a \rangle_t + \langle \Pi_{sxa} \rangle_t \, (\sigma_a/\sigma_{sxa}) \, (\sigma_{sxa} - \sigma_s)/(\sigma_a - \sigma_s) \, . \qquad (3.30)$$

$$\langle \tilde{\Pi}_s \rangle_t = \langle \Pi_s \rangle_t + \langle \Pi_{sxa} \rangle_t \, (\sigma_s/\sigma_{sxa}) \, (\sigma_a - \sigma_{sxa})/(\sigma_a - \sigma_s) \, . \qquad (3.32)$$

An analysis was performed on these two equations to determine how much of the cross term sound power, $\langle \Pi_{sxa} \rangle_t$, is attributed to the estimated airborne and structureborne sound power components. The results of the analysis is given in figures (III-2) and (III-3). Figure (III-2) shows the fractional amount of the cross term sound power (0 to 1) which is attributed to the estimate of the structureborne component plotted against the fractional radiation efficiency of the cross term. Figure (III-3) shows the fractional amount of the cross term sound power (0 to 1) which is attributed to the estimate of the airborne component plotted against the fractional radiation efficiency of the cross term. The fractional radiation efficiency of the cross term is defined by

$$\sigma_{fx} = (\sigma_{sxa} - \sigma_s)/(\sigma_a - \sigma_s) \, . \qquad (3.34)$$

Thus, σ_{fx} is equal to 0 when the cross term radiation efficiency, σ_{sxa}, is equal to the structureborne radiation efficiency, σ_s, and is equal to 1 when the cross term radiation efficiency, σ_{sxa}, is equal to the airborne radiation efficiency, σ_a. The various curves in figures (III-2) and (III-3) show how the results of the analysis depend on the difference between the structureborne and airborne radiation efficiencies. If the difference between the airborne and structureborne efficiencies, $\sigma_a - \sigma_s$, is small (e.g. 5 dB or less), the relationship between the fraction of the cross term attributed to the estimates and the fractional cross term radiation efficiency is nearly linear. If the difference between the structureborne and airborne efficiencies, $\sigma_a - \sigma_s$, is large (e.g. 20 or 25 dB) the relationship between the fraction of the cross term attributed to the estimates and the fractional cross term efficiency is seen to be hyperbolic with most of the cross term sound power being attributed to the estimate of the airborne component irregardless of the radiation efficiency of the cross term. Thus, if the measurements show a large difference in the radiation efficiencies of the individual components, one can be reasonably certain that the effects of the cross terms will manifest themselves primarily in the estimates of the airborne component of the total sound power.

I. ERROR ANALYSIS OF THE PROPOSED DIAGNOSTIC METHOD

Recall equations (3.29) and (3.31):

$$\langle \tilde{\Pi}_a \rangle_t = \langle \Pi \rangle_t \, (\sigma_a/\sigma) \, (\sigma - \sigma_s)/(\sigma_a - \sigma_s) \, , \qquad (3.29)$$

$$\langle \tilde{\Pi}_s \rangle_t = \langle \Pi \rangle_t \, (\sigma_s/\sigma) \, (\sigma_a - \sigma)/(\sigma_a - \sigma_s) \, . \qquad (3.31)$$

An error analysis was performed to determine the severity of the errors in these two estimates due to errors in the measurements. The results of this error analysis are given in Appendix VIII. The analysis includes the effects on the estimates due to measurement errors in the structure-borne radiation efficiency, σ_s, the airborne radiation efficiency, σ_a, and the radiation efficiency of the combined noise, σ. The severity of error is found to be sensitive to the actual values of σ and $(\sigma_a - \sigma_s)$ in some cases. The main conclusion of the study is that measurement errors are much more likely to cause inaccuracies in $\langle \tilde{\Pi}_s \rangle_t$ than $\langle \tilde{\Pi}_a \rangle_t$.

J. IMPLEMENTATION OF THE ANALYTICAL MODEL

Two computer programs were written in ANSI Standard FORTRAN 77 to implement the analysis outlined in the previous sections. The first program, entitled MODAL, calculates the natural frequencies of the plate under investigation. The second program, entitled SOUND, uses the

output of the first program and calculates the dynamic response, sound power radiated, and radiation efficiency as a function of forcing frequency for a specified combination of the airborne and structureborne inputs discussed earlier. Source code listings of these two programs along with detailed discussions of their calculation schemes are given in Appendix IX.

Compilation and execution of these two programs were performed on the Analysis and Computation Division's Cyber 175 computers (built by Control Data Corporation) under the Network Operating System (NOS). The ASCII data files containing the results of these computations (entitled DATA files) were then down loaded to a Tandy 2000 personal computer using a public domain terminal emulation program (COMSH), loaded into a spreadsheet-graphics program (LOTUS 1-2-3), and plotted on peripheral devices such as a Radio Shack CGP-220 color ink jet printer or a Hewlett-Packard 7470A pen plotter.

Several preliminary runs of programs MODAL and SOUND were performed in order to ensure that the computations were free from serious error. The results of several simple tests designed to validate the computer codes are presented in Appendix X.

K. SIMULATION OF THE PROPOSED DIAGNOSTIC METHOD

A third computer program, entitled PREDICT, was developed on the Tandy 2000 system to be used in conjunction with three of the output data files (DATA) generated by the program SOUND. The purpose of program PREDICT is to simulate the proposed diagnostic method. PREDICT uses the radiation efficiencies calculated by program SOUND for the cases of purely airborne and purely structureborne inputs (contained in two different DATA files) to separate and predict the airborne and structureborne sound power components of some combined inputs case of interest (contained in a third DATA file). Thus, program PREDICT is the implementation of equations (3.29) and (3.31). A listing of program PREDICT is given in Appendix IX.

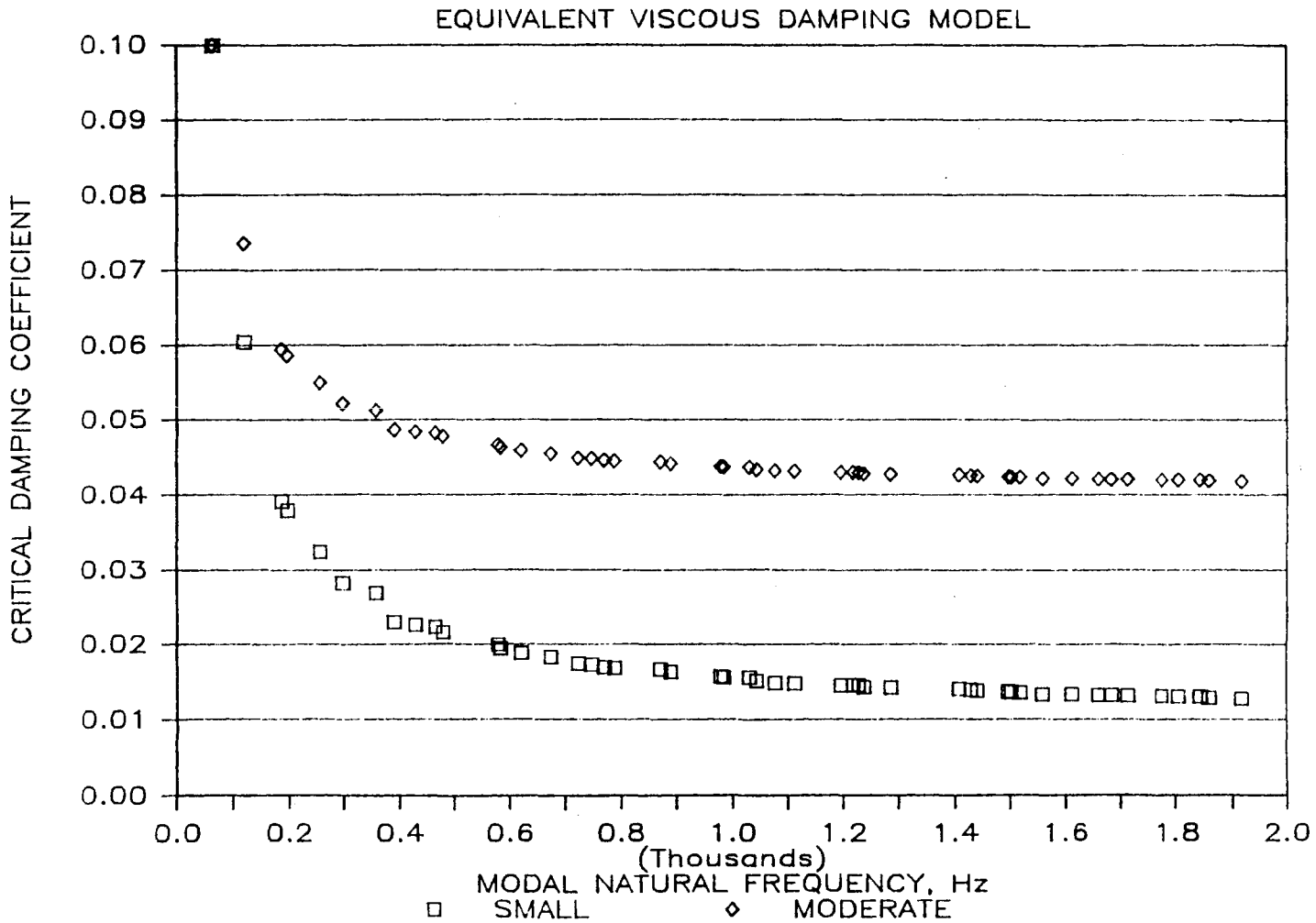

Figure (III-1) -- Small and moderate damping coefficients for a plate constructed of AA 2024 aluminum.

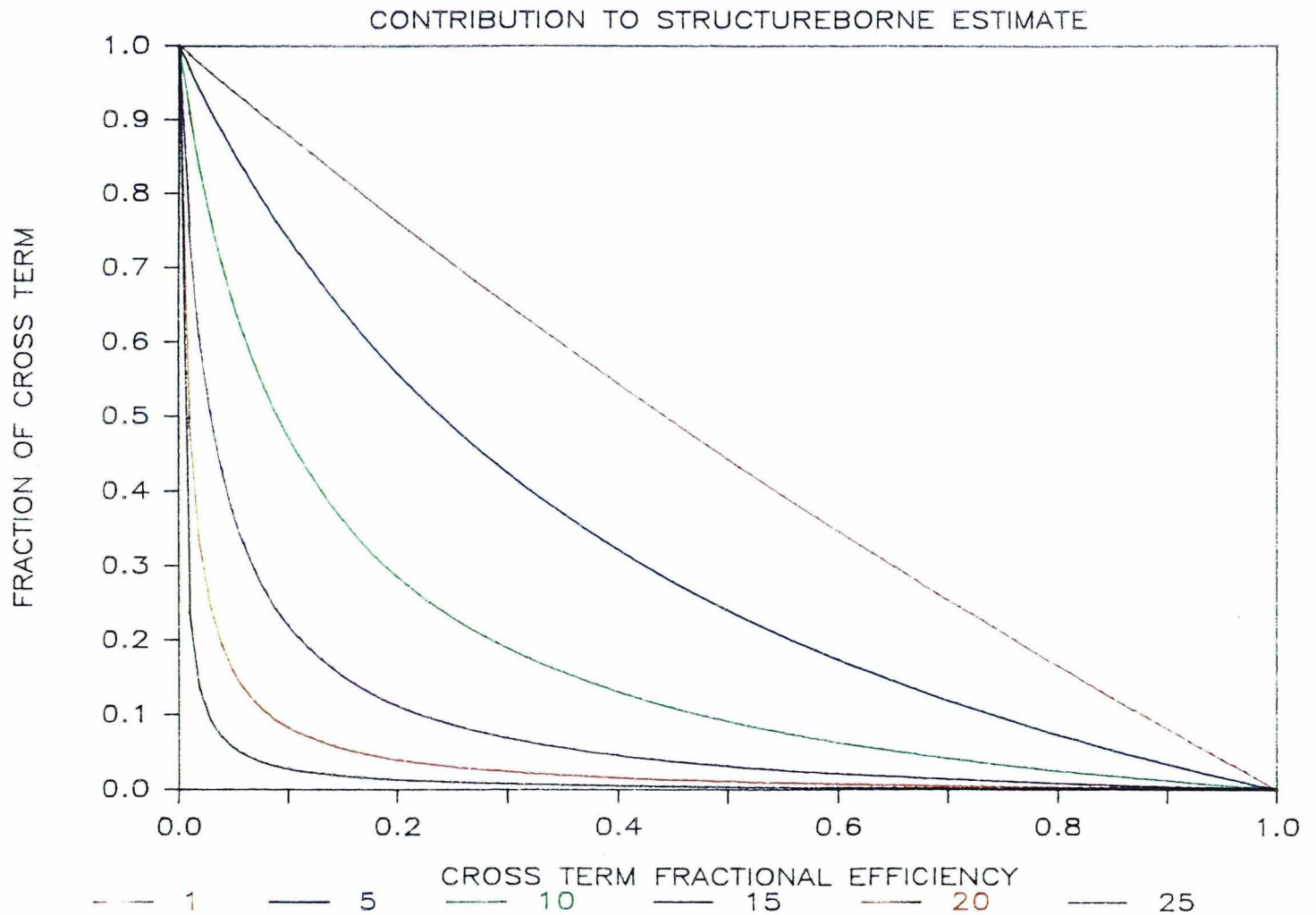

Figure (III-2) -- Fraction of the cross term sound power attributed to the estimate of the structureborne sound power.

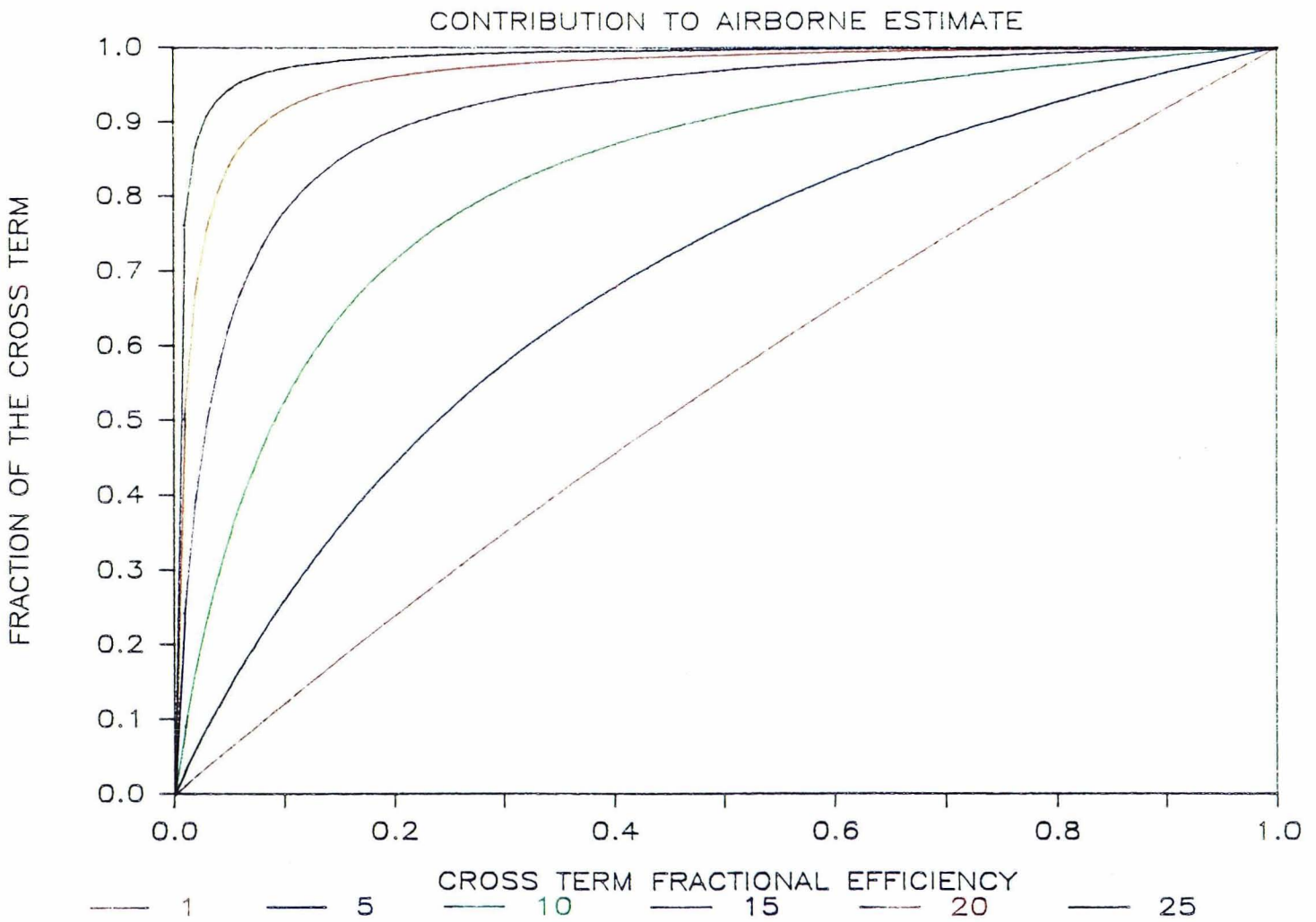

Figure (III-3) -- Fraction of the cross term sound power attributed to the estimate of the airborne sound power.

Chapter IV

THEORY OF MEASUREMENT AND EXPERIMENTAL APPARATUS

A. THEORY OF MEASUREMENT

In chapter III a diagnostic analysis was suggested whereby the structureborne and airborne components of the total sound power radiated by a plate or thin shell structure could be predicted. To implement this diagnostic analysis, the airborne and structureborne radiation efficiencies must be known and the sound power and radiation efficiency of the structure for the combined inputs case of interest must be measured. The present section deals with how the sound power and radiation efficiency of a structure can be measured in theory.

Recall that the time averaged sound power radiated by the surface of a structure is given by the equation (see Appendix I, equations (A1.50) and (A1.55))

$$\langle \Pi \rangle_t = \iint \langle \vec{I} \cdot \vec{n} \rangle_t \, dS = \langle \vec{I} \cdot \vec{n} \rangle_{r,t} \, S \quad , \tag{4.1}$$

where $\vec{I}$ is the acoustic intensity vector measured at the surface, $\vec{n}$ is the unit normal vector to the surface, and S is the surface area. The acoustic intensity vector normal to the surface can be measured using a two microphone, cross spectral, acoustic intensity probe. The theoretical basis for this type of probe is summarized in Appendix XI. The

acoustic intensity is calculated from the imaginary part of the one-sided cross spectral density between the two signals produced by two closely spaced microphones. The equation for the time averaged acoustic intensity is given by (see Appendix XI, equation (A11.22))

$$\langle I \rangle_t = -Q_{12}\Delta f/(\rho_o \omega \Delta x) \ , \qquad (4.2)$$

where

Q_{12} = minus the imaginary part of the one-sided cross spectral density between the two microphone signals,

Δf = the frequency resolution (bandwidth) in Hertz,

ρ_o = the density of the acoustic fluid medium,

ω = the radian frequency of the acoustic disturbance,

Δx = the spacing between the two microphones.

The quadrature spectral density, Q_{12}, can be easily measured with a dual channel or a multichannel Fast Fourier Transform (FFT) analyzer. The remaining terms in equation (4.2) are either constant or are parameters (such as bandwidth) which are set by the FFT analyzer. The space-time averaged acoustic intensity, $\langle I \rangle_{r,t}$, is found in practice by slowly sweeping the two microphone acoustic intensity probe near the surface of the intended measurement area as the FFT analyzer calculates the time averaged cross spectral density between the microphone signals. Thus, the space averaging and the time averaging of the cross spectral

density is performed simultaneously. (The consequences of the use of this method of space-time average for obtaining the space-time averaged acoustic intensity is discussed briefly in Appendix XI.) Once the space-time averaged cross spectral density between microphone signals is measured, the space-time averaged acoustic intensity is calculated as a function of frequency using equation (4.2) by computer, or by the FFT analyzer (depending on the analyzer's level of sophistication). The total sound power radiated is then calculated by multiplying the space-time averaged intensity by the measurement area. (See equation (4.1).) The measurement area may be the surface area of the structure, providing that the intensity probe is swept close enough to the surface, and if there are no stiffeners, etc.. attached to the intended measurement surface.

Recall from Appendix I, equation (A1.53) that the space-time averaged mean square surface velocity of a vibrating surface is given by the relation

$$\langle v^2 \rangle_{r,t} = 1/S \iint R_{vv}(0)\, dS = \langle \int_0^\infty G_{vv}(f)\, df \rangle_r , \qquad (4.3)$$

where G_{vv} is the one-sided auto spectral density of the surface velocity. Substituting an estimate of the auto spectral density from the equations given in Appendix I (see equation (A1.38))

$$\langle v^2 \rangle_{r,t} = \left\langle \int_0^\infty 2/T \; V^*(f)V(f) \; df \right\rangle_r . \qquad (4.4)$$

Substituting from the relationships between velocity and acceleration given in Appendix I (see equation (A1.9))

$$\langle v^2 \rangle_{r,t} = \left\langle \int_0^\infty 2/T \; A^*(f)A(f)/\omega^2 \; df \right\rangle_r . \qquad (4.5)$$

And from the definition of the estimated value of the one-sided auto spectral density of acceleration (see equation (A1.38))

$$\langle v^2 \rangle_{r,t} = \left\langle \int_0^\infty G_{aa}(f)/\omega^2 \; df \right\rangle_r , \qquad (4.6)$$

where G_{aa} is the one-sided auto spectral density of the surface acceleration.

The auto spectral density of the surface acceleration can be easily measured using an accelerometer together with an FFT analyzer. The time averaged mean square surface velocity can then be calculated from equation (4.6) by using a computer, or by integrating directly on the FFT analyzer (if that function is available on the analyzer). The space-time averaged mean square surface velocity is obtained in practice by measuring and calculating the time averaged mean square surface velocity from each of several accelerometers

which are attached to the measurement surface, and then simply averaging the results together as follows:

$$\langle v^2 \rangle_{r,t} = 1/N \sum_{k=1}^{N} (\langle v^2 \rangle_t)_k \ . \qquad (4.7)$$

This space averaged estimate will be normally distributed about its true value as the number of samples (accelerometers), N, increases to infinity, irregardless of the particular spatial distribution of the surface velocity. (This is a direct consequence of the central limit theorem.) One must be careful, however, not to place so many accelerometers on the surface that the added mass produces a large bias error in the measurements. Furthermore, the accelerometers should be placed on the surface in a random pattern (irregular as opposed to a regular pattern) so that the space average is not biased toward any particular mode shape of the structure.

Once the time averaged sound power and the space-time averaged mean square surface velocity are calculated, the acoustic radiation efficiency of the structure may be calculated using equation (3.23):

$$\sigma = \langle \Pi \rangle_t / (\rho_o c_o \langle v^2 \rangle_{r,t} S) \ . \qquad (3.23)$$

B. MEASUREMENT PROCEDURE

In the last section, the measurement theory used in determining the sound power and radiation efficiency of a structure was discussed. The present section outlines the implementation of this measurement theory in terms of a procedure for the measurement of sound power and radiation efficiency.

The following procedure is proposed for the measurement of the sound power and radiation efficiency of an exposed surface in the interior of a propeller driven aircraft:

Collect the Necessary Equipment - The following items are necessary for the measurements:

1. A two microphone acoustic intensity probe. Homemade probes will do just as well as the commercially available varieties. For measurements over the 0-1000 Hz frequency range, it is recommended that the probe consist of two 1/2 inch high gain microphones (to lower the noise floor and increase the signal level).
2. A minimum of two miniature (2 gram) piezoelectric accelerometers with the appropriate charge amplifiers (if charge amplifiers are necessary).
3. A dual channel or multichannel FFT analyzer with its own storage medium. The analyzer must be capable of being interfaced with a minicomputer or microcomputer via IEEE-488, RS-232C, or some other interface communication system.

4. Acoustic absorptive material to place in the enclosed space in which the measurements are to take place. Polyurethane foam or fiberglass wedges are recommended.

5. A barometer and thermometer.

6. A pistonphone and vibration calibration device.

Calibrate the Equipment - The following steps should be performed in calibrating the equipment:

1. The microphones used for the acoustic intensity probe should be calibrated with the pistonphone to obtain the appropriate gain factors. If the acoustic intensity probe is home made, it may also be necessary to phase calibrate the microphones. The need for phase calibration is dependent on the frequency range over which the measurements are intended. (See Appendix XI for a discussion of the possible measurement errors associated with the two microphone method of acoustic intensity measurement.)

2. Select the microphone spacing for the acoustic intensity probe. The exact spacing is a function of the frequency range of interest of the intended measurement. (See Appendix XI for a brief discussion of the selection of an appropriate microphone spacing.)

3. Calibrate the accelerometers for the appropriate gain factors using the vibration calibration device.

4. Record all of the gain factors, the ambient temperature, and the barometric pressure for later computer analysis and data reduction. (The computer software uses the atmospheric conditions to calculate the characteristic acoustic impedance of the fluid medium, $\rho_o c_o$, which is used in the acoustic intensity calculations.)

Prepare the Structure for the Measurements - Select the sidewall area for the intended measurements as follows:

1. The area selected may be any area of the structure which is basically of a thin plate or shell type construction. The boundary conditions on the measurement area are unimportant. Any type of boundary condition is acceptable. The chosen area may include stiffeners (e.g. ring frames or stringers), however it is best to choose the area small enough so that the majority of the stiffeners are along the boundaries. It is important that the trim material is removed from the measurement area before the measurements are performed.

2. Place the acoustic absorptive material inside the receiving space so as to minimize reflected sound. It may also be necessary to erect an acoustic barrier in the receiving space to prevent errors in the measurements due to flanking if there is a strong noise source near the selected measurement area.

Procedure - Use the following procedure:

1. Attach the array of accelerometers to the measurement surface in a random pattern. (A regular pattern may bias the measurements toward one particular mode shape or a family of mode shapes.)
2. Turn on the noise sources of interest and adjust the gain factors so that the resulting vibrational and acoustic signal levels are above the instrumentation thresholds over the frequency range of interest.
3. Measure the time averaged auto spectral density of acceleration of the measurement surface using the array accelerometers and the multichannel FFT analyzer. Store this information on the analyzer.
4. Use the two microphone acoustic intensity probe along with the FFT analyzer to measure the space-time averaged cross spectral density between the microphones by slowly sweeping the handheld probe over the surface. Store this information on the analyzer.
5. Turn off the noise sources of interest.
6. Use the information gathered in steps 3 and 4 to calculate the acoustic radiation efficiency of the measurement surface as outlined in section A.

C. PROPOSED DIAGNOSTIC PROCEDURE

The following diagnostic procedure is proposed for the separation and prediction of the structureborne and airborne components of the total sound power radiated by an exposed surface in the interior of a propeller driven aircraft:

Collect the Necessary Equipment - In addition to the equipment discussed in section B, the following additional items are necessary for the measurements:

1. A mechanical shaker with its associated power amplifier.
2. A loud speaker with its associated power amplifier.
3. A white noise (broad band frequency) signal generator.

Determine the Structureborne Radiation Efficiency -

1. Attach the mechanical shaker to the same attachment point as the source of the structureborne noise. (In the case of an aircraft, this would be the points at which the engines or wings attach to the aircraft.) If the structureborne noise source has more than one attachment point, then attach the shaker in line with the center of mass of the source. Keep in mind that it is not important that the shaker reproduce the level or the character of the actual structureborne noise source, but only that the vibrational energy takes the same path as the vibrational energy produced by the actual structureborne noise source.
2. Connect the white noise generator to the mechanical shaker's power amplifier.

3. Turn on the noise generator and adjust the level so that the resulting vibrational and acoustic signal levels are above the instrumentation thresholds over the frequency range of interest.

4. Perform the measurment procedure outlined in section B.

5. Turn off the noise generator, and disconnect the mechanical shaker. Leave the acoustic absorptive material in place.

6. Use the information gathered in step 4 to calculate the acoustic radiation efficiency of the measurement surface for the case of a purely structureborne input.

Determine the Airborne Radiation Efficiency -

1. Position the loud speaker so that it is approximately the same distance from the measurement area as the source of the airborne noise. (In the case of an aircraft, this may be in or aft of the propeller tip path plane.) Orient the loud speaker so that it has approximately the same directivity with respect to the measurement area as the actual airborne noise source. Keep in mind that it is not important that the loudspeaker reproduce the level or character of the actual airborne noise source, but only that the path of the acoustic propagation is the same.

2. Connect the white noise generator to the loudspeaker to the loudspeaker's amplifier.

3. Turn on the noise generator and adjust the level so that the resulting vibrational and acoustic signal levels are above the instrumentation thresholds over the frequency range of interest.

4. Perform the measurment procedure outlined in section B.

5. Turn off the noise generator, and remove the loudspeaker. Leave the acoustic absorptive material in place.

6. Use the information gathered in step 4 to calculate the acoustic radiation efficiency of the measurement surface for the case of a purely airborne input.

Measurements on the Noise Sources of Interest -

1. Turn on the actual noise source of interest. (In the case of an aircraft, bring the engines to the desired power setting and feather the propellers to the desired thrust setting. Altitude and airspeed may also be variables of interest.)

2. Perform the measurment procedure outlined in section B.

3. Use the information gathered in step 2 to calculate the sound power and the acoustic radiation efficiency of the measurement surface for the combined inputs case of interest.

Calculations - Now use equations (3.29) and (3.31) to separate and predict the structureborne and airborne components of the total sound power radiated by the measurement surface for the combined inputs case of interest.

D. EXPERIMENTAL APPARATUS

An experimental study of the proposed diagnostic method was performed using the NASA Langley Research Center's acoustic transmission loss apparatus. This facility is a hard walled, two room facility designed for acoustic transmission loss measurements using the classical room acoustics method. The two rooms have an adjoining wall which is designed so that simple or built-up aircraft panels can be mounted between the two rooms. With this arrangement, test panels could be subjected to the desired acoustic and vibrational inputs in the source room while the surface velocity and sound power radiated by the panels could be measured in the receiving room. Since the analytical model discussed in chapter III assumes that the test panels radiate sound to an acoustic free field condition, and since the accuracy of intensity measurements are in question under reverberent conditions, the receiving room of the transmission loss apparatus was modified to semi-anechoic conditions. This was accomplished by covering the back wall of the receiving room with .91 m deep acoustic wedges and covering the floor of the room with .46 m deep acoustic wedges. The acoustic wedges, constructed of polyurethane foam, are shown in the photograph of figure (IV-1). No further modifications of the transmission loss apparatus were required to perform the measurements. (Additional information regarding the

acoustic properties of the NASA acoustic transmission loss apparatus is available in references 50 and 51.)

A special apparatus for mounting the test panels was constructed so that the experimental conditions would emulate the conditions assumed for the analytical modeling. The apparatus consisted of a speaker box which completely enclosed the incident side of the test panels. Two small holes were drilled through the enclosure so that a steel rod and shaker could be attached to the test panels in one of two locations. The test panels were then clamped in the mounting brackets seen in figure (IV-2) in front of six 4 inch diameter loudspeakers . The mounting brackets, shown in close-up in figure (IV-3), were constructed with a rubber O-ring type material so that the test panels would have some rotational degree of freedom, thus approximating the simply supported conditions assumed in the analytical modeling.

The array of six loudspeakers shown in figure (IV-2) were used to produce a normally incident, spatially uniform acoustic (airborne) input to the test panels. The loudspeakers were positioned 5.7 cm from the surface of the test panels, thus insuring that the acoustic resonances in the cavity between the panels and the speakers have natural frequencies much greater than 1000 Hz. The elimination of any significant influence due to the cavity modes helped to produce an acoustic input that was nearly uniform over the

0-1000 Hz frequency range. The small distance between the speakers and the panels also insured that the direct sound field from the speakers would overwhelm the effects of any cross modes in the cavity, thereby approximating the spatially uniform conditions. A preliminary set of measurements were performed on the loudspeakers to insure that they were in phase and produced the same level of sound over the 0-1000 Hz range. A plot of the measured space-time averaged acoustic intensity radiated by each of the six loudspeakers to the free field over the 0-1000 Hz frequency range is given in figure (IV-4).

A 44.5 N (force) vibration shaker was used in conjunction with a .635 cm diameter steel rod to simulate the point vibrational (structureborne) input. The shaker was mounted outside of the speaker box by suspending it freely with bungee cord that was attached to a scaffold-type apparatus. This arrangement ensured that the shaker-rod-panel system had a low natural frequency and reduced any d.c. component of the point forcing function to a minimum. The threaded rod was attached to the panel, in each case, by drilling a hole in the panel, slipping the rod through the hole, and tightening a hex nut down on each side of the panel.

A typical example of the forcing function produced by this apparatus over the 0-1000 Hz frequency range is given in the plot of figure (IV-5).

E. TEST PANELS

The test structures chosen for use in this study consisted of rectangular, simply supported plates constructed of isotropic or composite materials. Six different types of test panels were chosen for study by the author. The NASA Langley Research Center's Materials Division then fabricated the test panels to the desired specifications. A summary of the physical characteristics and stiffness properties of the plates chosen for study are given in Tables IV-1, IV-2, and IV-3.

F. INSTRUMENTATION AND DATA ACQUISITION

A block diagram of the instrumentation used for the measurements is shown in figure (IV-6). The specifications for the instruments are given in Appendix XII.

The white noise generator, shown in the figure, provided a broadband random signal (0-5000 Hz) that was used to simultaneously drive both the loudspeakers and the shaker system. This single source ensured that the airborne and structureborne inputs were fully coherent. The signal was filtered using both a high pass and a low pass filter so that the sound radiated by the panels would be concentrated in the 100-1000 Hz frequency range. A signal attenuator was used to adjust the level of the airborne input so that the relative amounts of airborne and structureborne noise radiated by the panels were roughly equal.

An array of four miniature (2 gram) piezoelectric accelerometers were used to measure the space-time averaged surface acceleration of the panels. The accelerometers were attached to the surface of the panels using double sticky back tape in a random pattern. Each accelerometer was used in four different locations for a given measurement of the surface acceleration. Thus, a total of sixteen different accelerometer locations were used to obtain the space average for each measurement of the surface acceleration. A total of 100 ensemble averages at each accelerometer location (obtained by the FFT analyzer) were used to obtain the time average in each case.

The two microphone acoustic intensity probe, used to measure the sound power radiated by the panels, is shown in figure (IV-7). The probe consisted of two 1.27 cm diameter high gain microphones in a face-to-face configuration. The solid nylon cylindrical spacer between the microphones provided a constant separation distance of 50 mm. This separation distance between microphones ensures that the sound power measurements are accurate over the 100-1000 Hz frequency range. Below 100 Hz the sound power measurements are suspect due to phase mismatch errors. Above 1000 Hz the sound power measurements are inaccurate due to finite difference error. (See Appendix XI for details.) Since the microphone interchange technique was used for the

measurements, the intensity probe was used twice for any given measurement of space-time averaged acoustic intensity. (This method reduces the phase mismatch error. See Appendix XI for details.) The FFT analyzer obtained 200 ensemble averages for each of the two passes of the intensity probe. Thus, a total of 400 ensemble averages were used to obtain the time averaged intensity. The space average was obtained by slowly sweeping the intensity probe near the surface of the panel (as outlined in section A).

Calibration of the accelerometers and the microphones were performed using a GENRAD 1557A vibration exciter and a GENRAD 1986 sound level calibrator respectively. The transducers were calibrated prior to the measurement on each day that a measurement was to take place. The voltages produced by the transducers due to a known input were read on the digital voltmeter shown in figure (IV-6). Calibration was then implemented by adjusting the gain on the accelerometer signal conditioners and the microphone amplifiers so that the gain factors were always .01 volt/(m/sec^2) for the accelerometers and .1 volts/Pascal for the microphones. The oscilloscope shown in figure (IV-6) was used to insure that the signals received during calibration were free of distortion, thus making certain that the transducers were in acceptable operating condition. The scanner shown in figure (IV-6) was utilized during both calibration and measurement

so that any of the 8 data channels could be monitored without disconnecting or reconnecting any wire leads.

The data acquisition was performed by the GENRAD 2515 8-channel FFT analyzer. This data acquisition system is particularly well suited for work on aircraft because of its small size and portability. Two of the 2515's 8 channels were used for the microphones, while four of the channels were used for the accelerometers. The two remaining channels were used to monitor the white noise input signal and the signal provided by the force gauge (see figure (IV-6). In addition to the data obtained by the analyzer, the atmospheric conditions including temperature and barometric pressure were recorded each day and entered into the data files. The atmospheric data were used later in the computations to calculate the density, ρ_o, and characteristic acoustic impedance, $\rho_o c_o$, of the fluid medium. (These quantities are used in calculating the sound power radiated by the plate.)

G. DATA REDUCTION AND ANALYSIS

Once the data were obtained, they were uploaded to the Acoustics Division's VAX 11/780 via the KERMIT file transfer protocol. A computer program, written in FORTRAN 77, was then used to reduce the acquired data and calculate the sound power radiated and radiation efficiency of the panels as a function of frequency. The program was written so that

the ASCII data files produced by the experiments had precisely the same file format as the DATA files produced by the analytical program SOUND. These data files produced by the experiments were then down loaded to a Tandy 2000 personal computer via the KERMIT file transfer protocol. The data files were then loaded into a spreadsheet-graphics program (LOTUS 1-2-3) and plotted on either a Radio Shack CGP-220 ink jet printer or a Hewlett-Packard pen plotter. A block diagram of the equipment used in this research for data acquisition, reduction, and analysis is shown in figure (IV-8).

H. VERIFICATION OF THE PROPOSED DIAGNOSTIC METHOD

Program PREDICT, discussed in section K of chapter III, was used in conjunction with the data files produced by the experiments to test the diagnostic method proposed in chapter III. PREDICT uses the measured radiation efficiencies for the cases of a purely airborne and a purely structureborne inputs (contained in two different data files) to separate and predict the airborne and structureborne sound power components of some combined inputs case of interest (contained in a third data file).

Table II-1 -- Description of the plate construction.

Plate No.	Material	Number of plies	Fiber lay-up	Density (kg/m^2)	Thickness (mm)
1	Aluminum	1	isotropic	2.22	0.79
2	*Graphite	8	0/90 /0/90	1.59	1.02
3	*Graphite	8	+45/-45 /+45/-45	1.59	1.02
4	*Graphite	16	+45/-45 /+45/-45 /+45/-45 /+45/-45	3.05	1.85
5	*Kevlar	8	+45/-45 /+45/-45	1.37	1.02
6	*Fiberglass	8	+45/-45 /+45/-45	2.21	1.02

Table II-2 -- Material properties of the plate plies.

Plate No.	Material	E_{11} (Pa)	E_{22} (Pa)	G (Pa)	μ_{12}
1	Aluminum	.731e11	.731e11	.276e11	.330
2-4	*Graphite	.137e12	.965e10	.480e10	.300
5	*Kevlar	.760e11	.550e10	.210e10	.340
6	*Fiberglass	.390e11	.900e10	.240e10	.300

*See note on page 64.

Table II-3 -- Calculated bending rigidities of the plates.

Plate	D_{11} (N*m)	D_{22} (N*m)	D_{12} (N*m)	D_{66} (N*m)	D_{16} (N*m)	D_{26} (N*m)
1	3.42	3.42	1.13	1.15	0.00	0.00
2	8.65	4.40	0.26	0.42	0.00	0.00
3	3.82	3.82	2.97	3.13	1.06	1.06
4	22.77	22.77	17.70	18.70	3.17	3.17
5	2.09	2.09	1.72	1.73	0.59	0.59
6	1.42	1.42	0.99	0.96	0.25	0.25

*NOTE - All materials used for construction of the composite panels were procured as pre-preg tape from:

FIBERITE corporation
General Headquarters
501 West Third Street
Winona, Minnesota 55987

The material designations were as follows:

Graphite tape - Celion 6000/Epoxy resin 934

Fiberglass tape - E glass/Epoxy resin 934

Kevlar tape - Kevlar 49/Epoxy resin 934

The panels were layed-up and cured by NASA Langley's Materials Division.

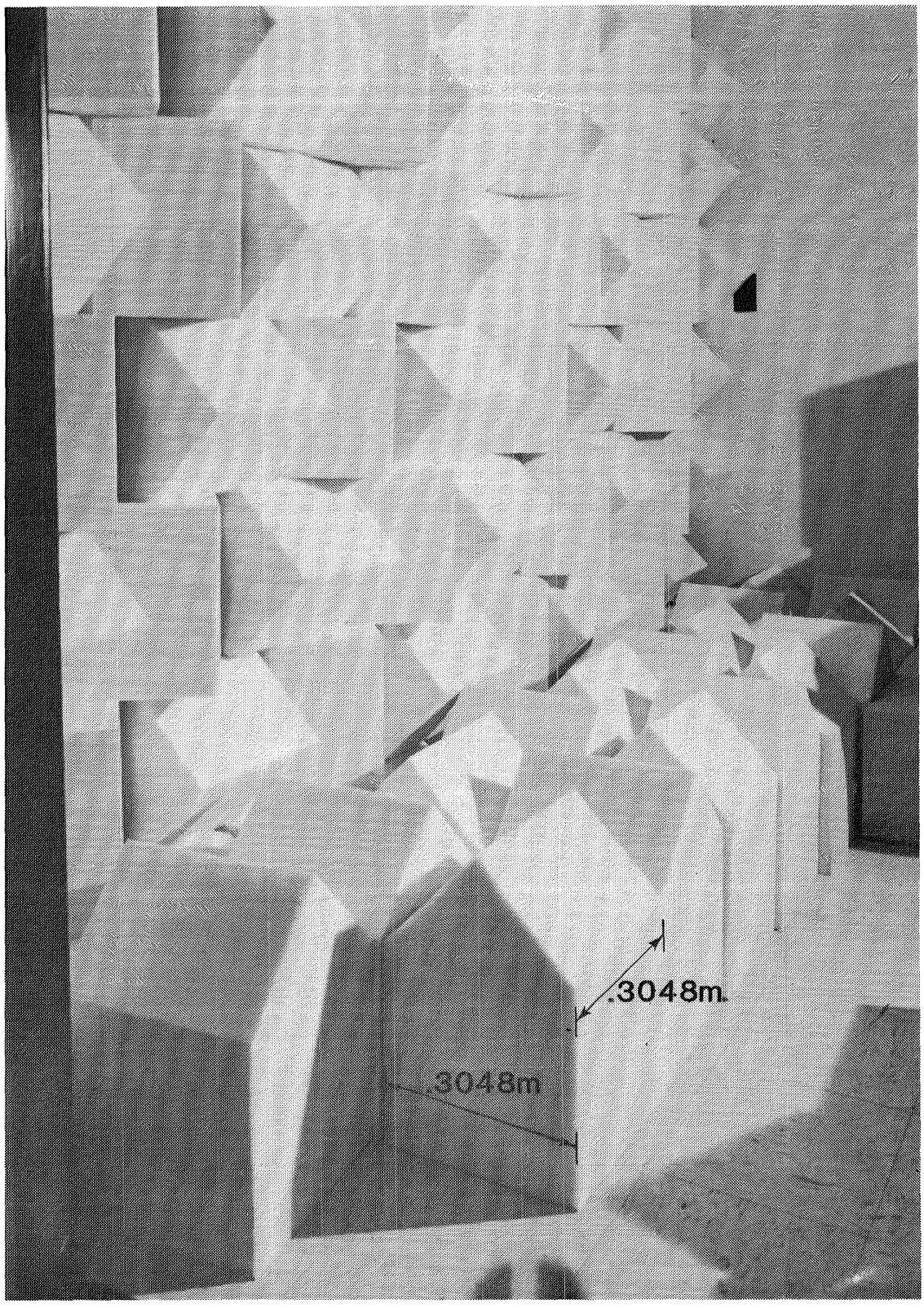

Figure (IV-1) -- Acoustic wedges covering the back wall and floor of the receiving room.

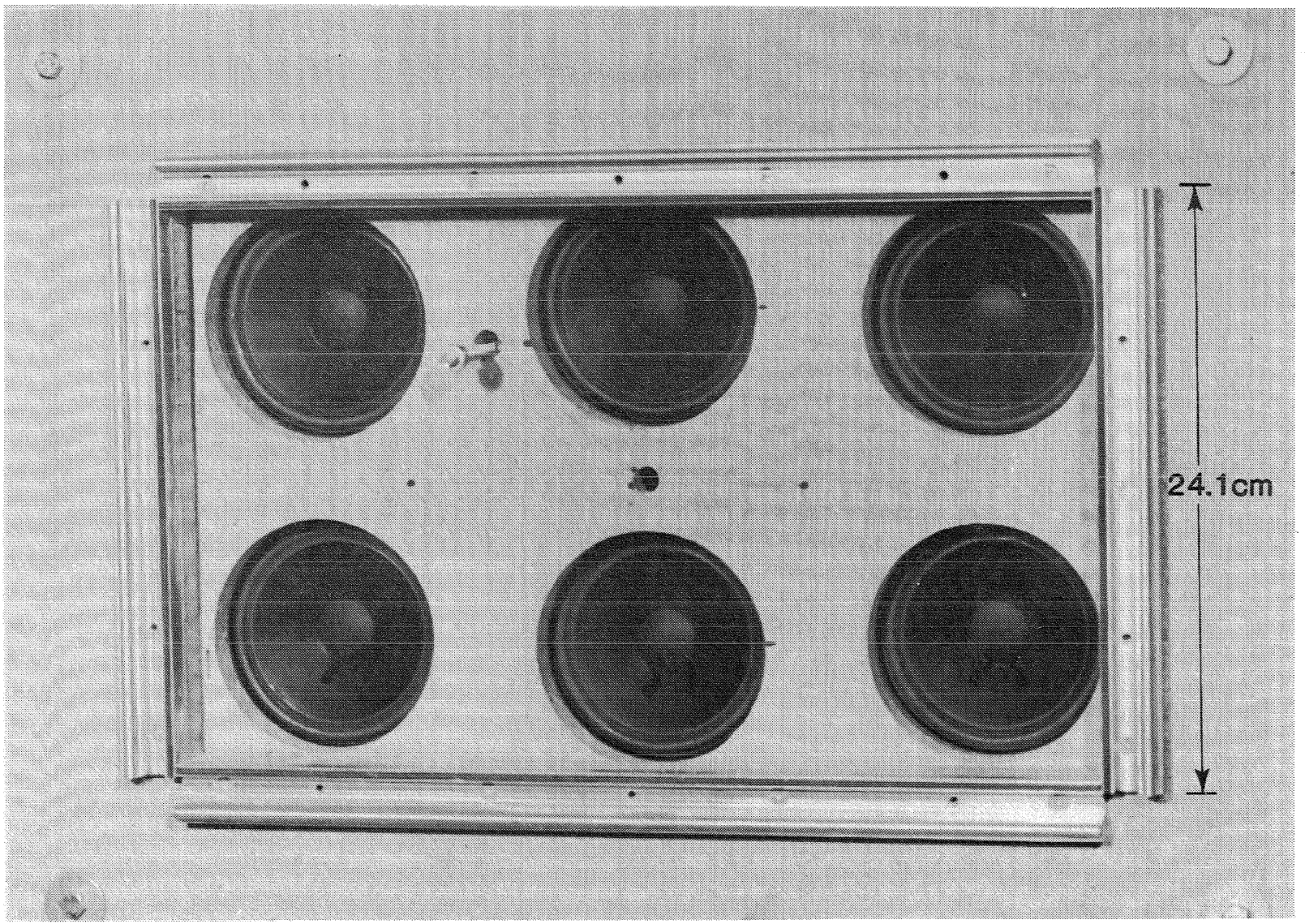

Figure (IV-2) -- Mounting brackets for the panels and array of six loudspeakers.

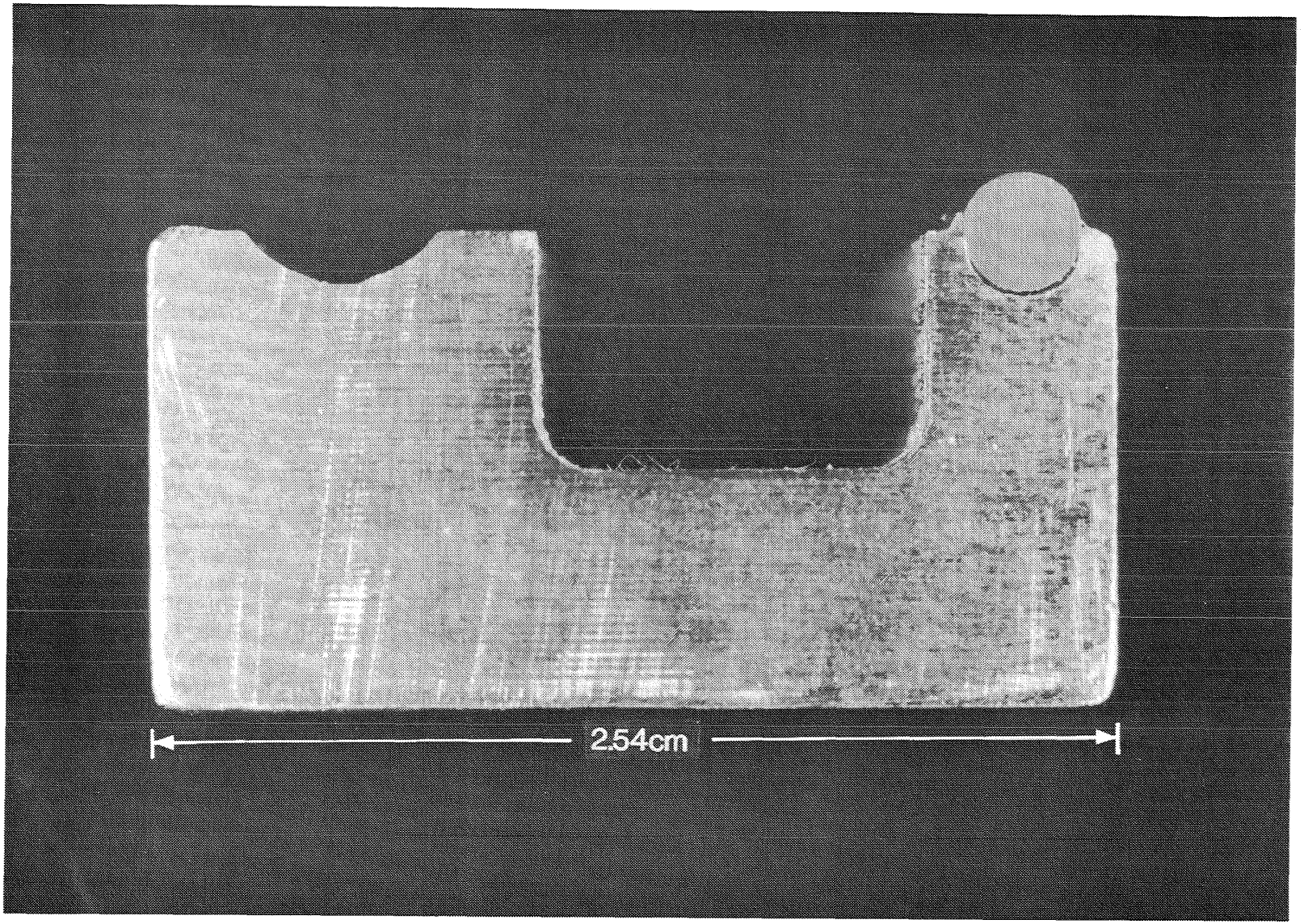

Figure (IV-3) -- Close-up cross sectional view of the mounting brackets for the panels.

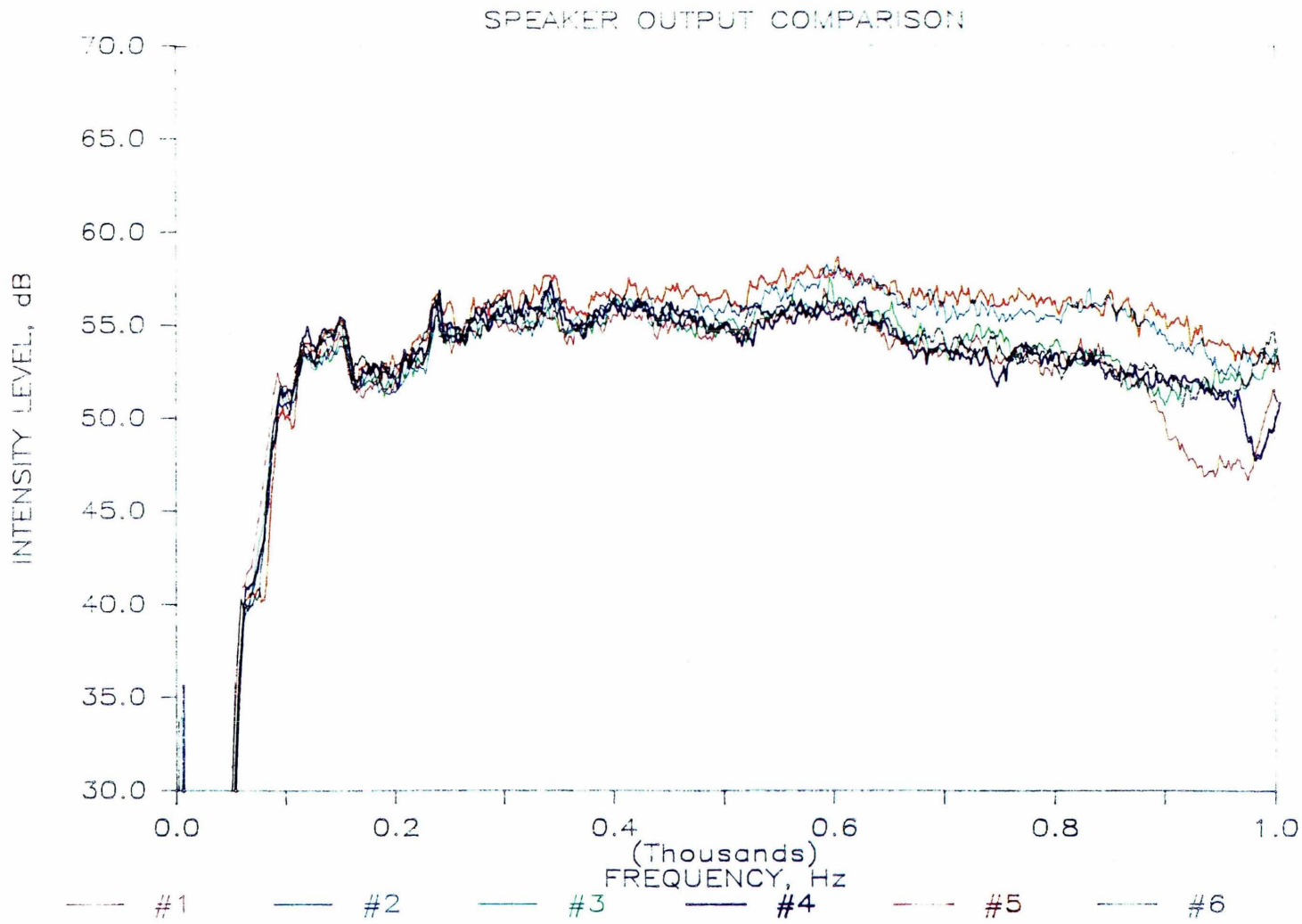

Figure (IV-4) -- Acoustic intensity radiated by each of the six loudspeakers.

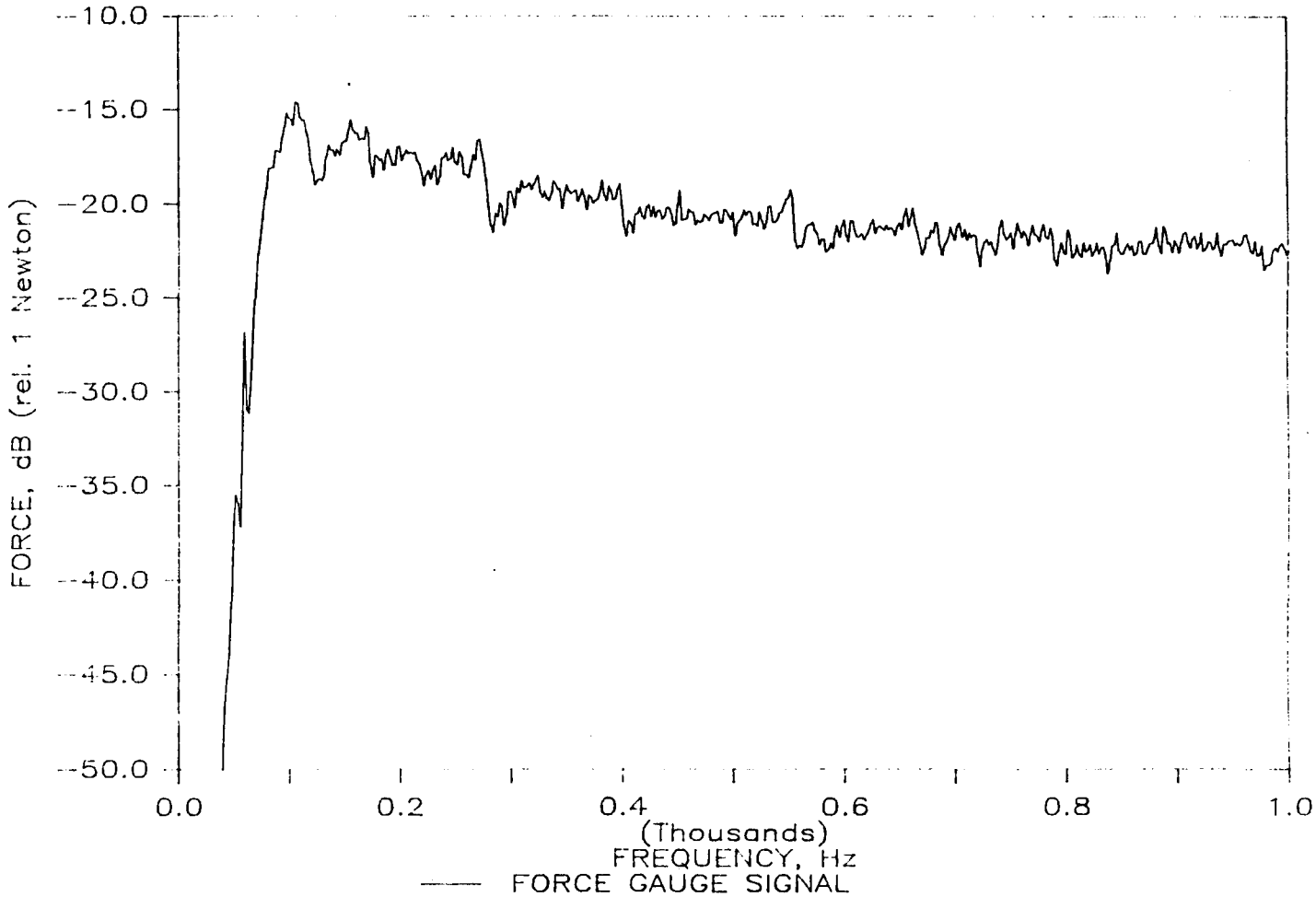

Figure (IV-5) -- Forcing function produced by the shaker-rod-panel system.

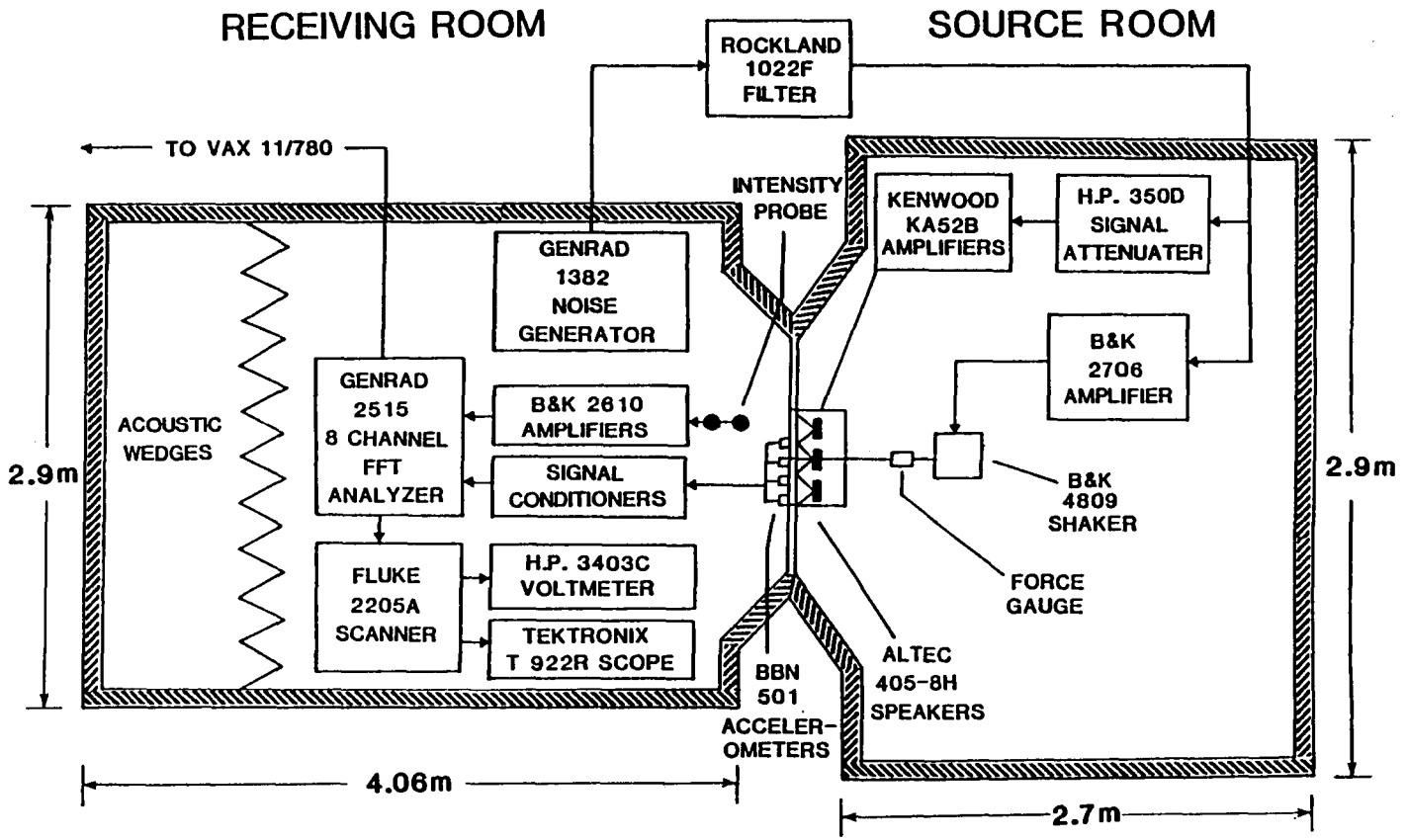

Figure (IV-6) -- Block diagram of the instrumentation used for the measurements.

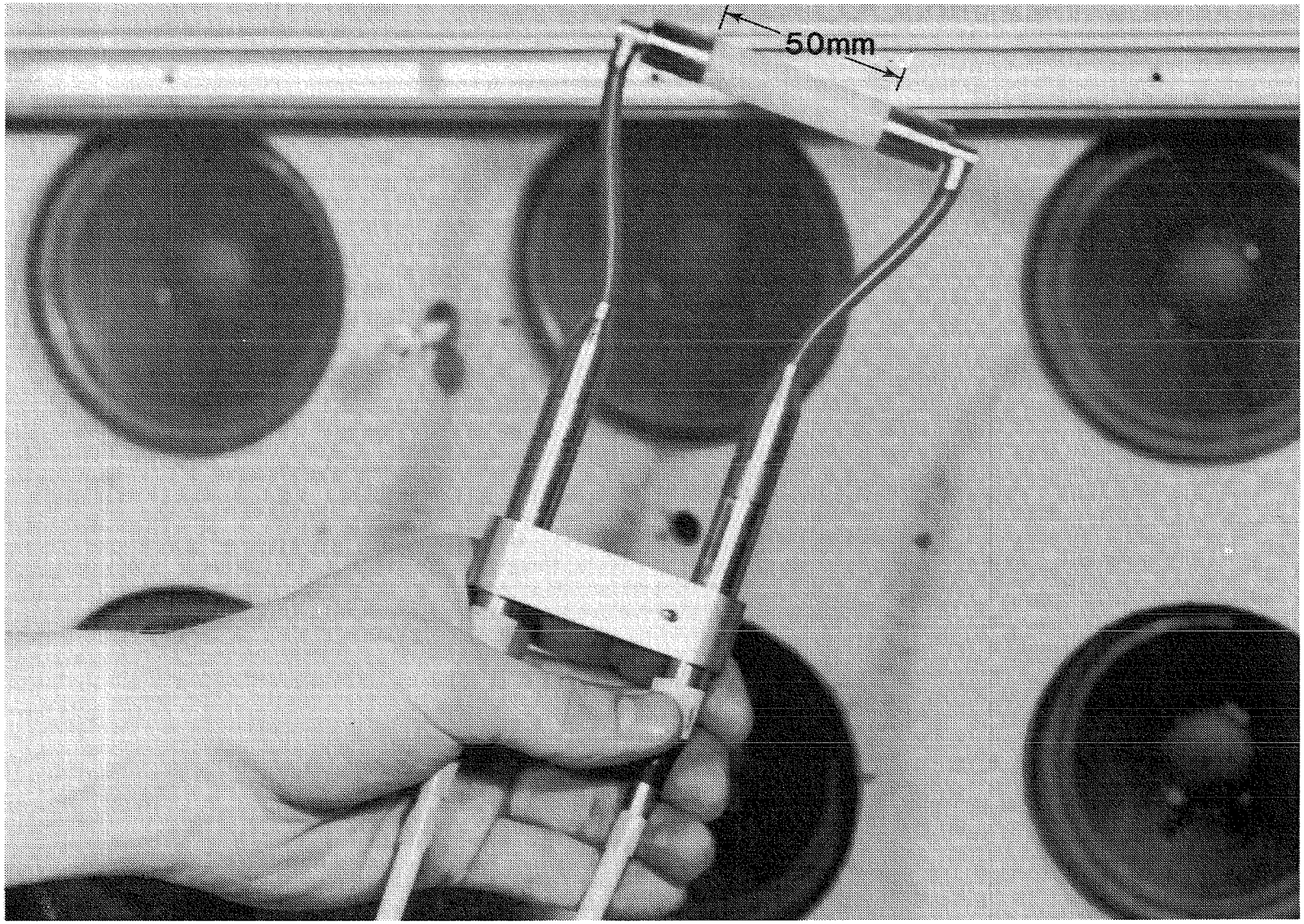

Figure (IV-7) -- Two microphone acoustic intensity probe used for the measurements.

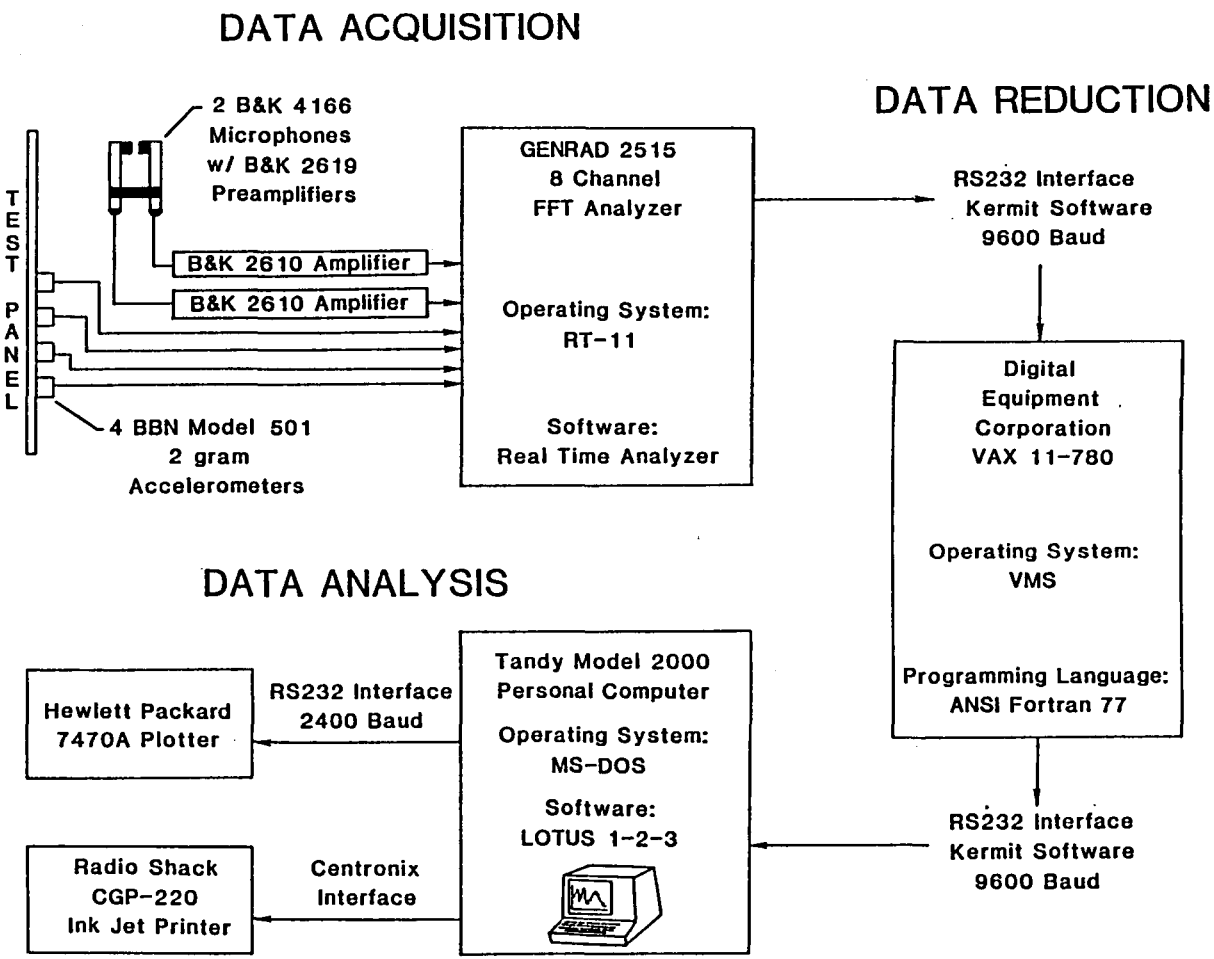

Figure (IV-8) -- Data acquisition, reduction, and analysis systems.

Chapter V

RESULTS AND DISCUSSION

A. INTRODUCTION

This chapter contains selected results of the studies. The analytical results shown here are intended to simulate the performance of the proposed diagnostic method under various operating conditions. The experimental results are then presented alongside the analytical results and are intended to verify the predicted trends. Since the electronic equipment necessary for controlling the relative magnitude and phase of the inputs as a function of frequency was unavailable, the corresponding analytical and experimental cases presented are not exactly the same. Therefore, the direct comparison of the analytical and experimental results (overlaying the plots) would be ludicrous. The reader should keep in mind that the purpose of the analytical and experimental comparisons is not to compare quantative results, but rather is intended to show that predicted and observed trends are similar in a qualitative sense. (The electronic boards necessary for controlling the phase and amplitudes of the inputs as a function of frequency are being constructed at this writing. Future tests are planned for an aircraft fuselage using these gain/phase boards.)

The analytical results presented in this chapter were produced using the theoretical developments and computer

programs (SOUND and PREDICT) discussed in chapter III. Unless explicitly stated otherwise, the results are for the case of a normally incident, spatially uniform, 1 Pa peak acoustic load and a .01 N peak point vibrational load located at the coordinates of α_1=.06033 m and α_2= .13547 m, and are for the case of the small damping model represented by equation (3.11). In all cases the forcing functions were applied uniformly over the frequency range at 2 Hz intervals.

The experimental results presented in this chapter were obtained using the apparatus and computer programs discussed in chapter IV. The results that demonstrate the effects produced by changes in the relative phase of the inputs were obtained by reversing the polarity of the shaker system. This was accomplished simply by switching the wire leads connecting the shaker to the input signal. This reversal of the polarity of the shaker is tantamount to changing the relative phase between the acoustic and vibrational inputs by 180 degrees from the existing phase difference at all frequencies.

Several conditions were consistently maintained for all of the experimental results shown. The same input signal was applied to both the array of speakers and the shaker so that the two inputs were fully coherent. The input signal was filtered so that the input was approximately uniform

over the 0-1000 Hz frequency range. The overall gain factors of the acoustic and vibrational inputs were adjusted so that the airborne sound power component would be dominant in some frequency ranges while the structureborne sound power component was dominant in other ranges. Also, in order to match the resolution of the analytical results, the FFT analyzer was set with a constant bandwidth of 2 Hz. Finally, unless explicitly stated otherwise, the experimental results presented here were measured data on an aluminum plate (plate no. 1) for the case of an approximately uniform normal acoustic load and a point vibrational load located at the coordinates of α_1= .06033 m and α_2=.13547 m.

The results that follow are divided into five sections which examine the effects of several parameters on (1) the airborne and structureborne noise radiative characteristics of plates and (2) the proposed diagnostic method. In the first section (section B), the effects of the relative magnitudes and phase of the inputs is examined for the baseline case of an aluminum plate. In section C, the effects produced by changing the shaker location (altering the path of the structureborne input) are examined. Section D examines the effects of adding damping treatment to the aluminum plate. Finally, sections E and F examine the effects produced by altering the plate material to various types of composite materials.

B. EFFECTS OF RELATIVE MAGNITUDE AND PHASE

Analytical Results for a Dominant Airborne Source

Figures (V-1a) and (V-1b) show the radiation efficiencies and sound power levels obtained from the analytical program SOUND for the aluminum plate (plate no. 1) produced by individual airborne and structureborne inputs. Figure (V-1a) clearly demonstrates that the airborne noise is much more efficient than the structureborne noise as expected. Figure (V-1b) shows that, in this case, the airborne source is dominant.

The radiation efficiencies and sound powers of plate no. 1 produced by combining the airborne and structureborne inputs at 0 degrees in phase, 180 degrees out of phase, and 90 degrees are shown in figures (V-1c) and (V-1d) respectively. These plots show that the sum of the results of the individual inputs is roughly equivalent to results obtained by combining the inputs at 90 degrees over most of the frequency range. The plots show that large deviations occur, however, when the inputs are combined at 0 or 180 degrees. This result underscores the importance of the cross term $\langle \Pi_{sxa} \rangle_t$ contained in equation (3.22) by showing that its contribution to the overall sound power radiated can be as large as the dominant term. Furthermore, since the sign of $\langle \Pi_{sxa} \rangle_t$ can be positive or negative, the overall noise

generated can vary over a tremendous range depending on the relative phase of the inputs.

Figures (V-1e), (V-1f), and (V-1g) shows the results of applying program PREDICT (the proposed noise path separation method) to the cases of combined inputs at 90, 0, and 180 degrees respectively. PREDICT uses σ_a and σ_s shown in figure (V-1a) along with equations (3.29) and (3.31) to estimate the airborne and structureborne components of the total sound power in figure (V-1d). In each of figures (V-1e) through (V-1g) the actual airborne and structureborne components are plotted against the components estimated by the proposed diagnostic method. In all cases the proposed separation method correctly identifies the airborne input as the dominant noise source over most of the frequency range.

Figure (V-1e) (uncorrelated inputs) shows good agreement between the curves over nearly the entire 0-1000 Hz frequency range. Discrepancies are seen to occur in this figure only in those ranges where $\sigma_a - \sigma_s$ is very small. Good agreement is expected in this case since the cross terms are smallest when the inputs are uncorrelated.

Figure (V-1f) indicates that some anomalies occur in the estimated components when the inputs are in phase. The larger differences in the curves are caused by the strong influence of $\langle \Pi_{sxa} \rangle_t$. For example, in figure (V-1f) $\langle \tilde{\Pi}_a \rangle_t$ exceeds the combined noise in the 800-900 Hz

frequency range. Since it is known that the estimates are power preserving, this indicates that the $\langle \tilde{\Pi}_s \rangle_t$ has a negative value in this range. From equation (3.32) it is known that $\langle \tilde{\Pi}_s \rangle_t$ can have negative values only if $\langle \Pi_{sxa} \rangle_t$ is negative or if σ_{sxa} is greater than σ_a. From the figure (V-1d), it can be inferred that $\langle \Pi_{sxa} \rangle_t$ is negative in this case and larger than $\langle \Pi_s \rangle_t$.

Figure (V-1g) shows a similar irregularity in the 800-900 Hz frequency range except that in this case $\langle \tilde{\Pi}_a \rangle_t$ is negative. Since figure (V-1d) indicates that $\langle \Pi_{sxa} \rangle_t$ is positive, it can be inferred from equation (3.30) that σ_{sxa} is less than σ in this case. This implies that over 100 percent of $\langle \Pi_{sxa} \rangle_t$ is attributed to $\langle \tilde{\Pi}_s \rangle_t$.

In spite of the anomalies seen in figures (V-1f) and (V-1g), the proposed prediction method correctly identifies the dominant input over most of the frequency range and provides valuable information about the interaction between inputs in those ranges where the cross terms are significant. It is worth noting that the 800-900 Hz frequency range where the cross term has such a significant effect is a region where there is strong cross coupling between different modes, $\sigma_a - \sigma_s$ is small, and $\langle \Pi_a \rangle_t$ is nearly equal to $\langle \Pi_s \rangle_t$. (See figures (V-1a) through (V-1d).)

Analytical Results for a Dominant Structureborne Source

Figures (V-2a) and (V-2b) show the computed radiation efficiencies and sound power levels, respectively, produced by plate no. 1 due to a .2 Pa peak acoustic load and an independent .05 N peak vibrational load. Figure (V-2b) shows that, in this case, the structureborne source is dominant. Comparing figure (V-1a) and figure (V-2a) it is clearly seen that the radiation efficiencies are independent of the magnitude of the inputs.

The radiation efficiencies and sound powers of plate no. 1 produced by combining these two inputs at 0 degrees in phase, 180 degrees out of phase, and 90 degrees are shown in figures (V-2c) and (V-2d) respectively. These figures again show that large deviations occur when the inputs are combined at 0 or 180 degrees. Particularly good agreement between the sum of the individual inputs and the case of uncorrelated, combined inputs is seen to occur in these figures.

Figures (V-2e), (V-2f), and (V-2g) show the results of applying program PREDICT to the cases of combined inputs at 90, 0, and 180 degrees respectively. In all three cases the proposed separation method correctly identifies the structureborne input as the dominant noise source over the entire frequency range. Figure (V-2e) (uncorrelated inputs) shows good agreement between the component curves and the diagnostic curves except in those ranges where $\sigma_a - \sigma_s$

is small. Figure (V-2f) (inputs in phase) and figure (V-2g) (inputs out of phase) show much larger differences in the curves due to the extreme influence of $\langle \Pi_{sxa} \rangle_t$. Note that $\langle \tilde{\Pi}_a \rangle_t$ has a negative value over almost the entire frequency range when the inputs are combined out of phase (see figure (V-2g)). The much more radical influence of $\langle \Pi_{sxa} \rangle_t$ in figures (V-2f) and (V-2g) (compared to figures (V-1f) and (V-1g)) can be explained by the analysis in section H of chapter III where it was shown that the effects of $\langle \Pi_{sxa} \rangle_t$ are more likely to manifest themselves in $\langle \tilde{\Pi}_a \rangle_t$ than in $\langle \tilde{\Pi}_s \rangle_t$. In spite of these large differences, the prediction method correctly identifies the dominant input over the entire frequency range and once again provides valuable information about the interaction between inputs in those ranges where the cross terms dominate.

Experimental Verification of the Results

Figures (V-3a) and (V-3b) show the measured radiation efficiencies and sound power levels, respectively, produced by plate no. 1 due to the acoustic and vibrational inputs acting independently (alone). Figure (V-3a) shows that the airborne sound power generation is more efficient than the structureborne sound power generation as predicted by the analytical study. Figure (V-3b) shows that, in this case, the structureborne component of the sound power is dominant

in several small discrete frequency regions while the airborne component is dominant over most of the frequency range. Note that the radiation efficiency and sound power curves appear to be somewhat more jagged than the smooth curves obtained in the analytical study. This change in the quality of the smoothness of the curves is quite understandable in light of the many approximations employed by the analytical model and particularly since the inputs to the plate are only approximately uniform over the 0-1000 Hz frequency range.

The radiation efficiencies and sound powers of plate no. 1 produced by combining the airborne and structureborne components are shown in figures (V-3c) and (V-3d) respectively. In each of these two figures, the three curves show the results of (1) summing the individual airborne and structureborne components, (2) combining the airborne and structureborne inputs with positive polarity on the shaker, and (3) combining the inputs with negative polarity on the shaker. These figures show that the sum of the results of the individual inputs is roughly equivalent to the results obtained by combining the inputs over much of the frequency range. Large differences in the curves are seen to occur, however, predominantly in frequency regions where the radiation efficiency curve reaches a local peak. These differences are most certainly a reflection of the large infuence

of the cross term $\langle \Pi_{sxa} \rangle_t$ in those localized frequency ranges.

Figures (V-3e) and (V-3f) show the results of applying program PREDICT (the proposed noise path separation method) to the two cases of combined inputs shown in figure (V-3d). PREDICT uses σ_a and σ_s shown in figure (V-3a) along with equations (3.29) and (3.31) to predict the airborne and structureborne components of the total sound power in figure (V-3d). Figures (V-3e) and (V-3f) show that the proposed separation method correctly identifies the dominant noise source over most of the frequency range. It is evident, however, that because of the close proximity of σ_a and σ_s, the separation method was unable to make a reliable prediction in a number of ranges. Close comparison of the curves in figures (V-3e) and (V-3f) suggests that the cross term $\langle \Pi_{sxa} \rangle_t$ manifests itself primarily in the airborne estimate $\langle \tilde{\Pi}_a \rangle_t$ as predicted by the analytical study. As expected, figure (V-3e) indicates that $\langle \tilde{\Pi}_a \rangle_t$ overestimates the airborne component when $\langle \Pi_{sxa} \rangle_t$ is large and positive while figure (V-3f) indicates that $\langle \tilde{\Pi}_a \rangle_t$ underestimates the airborne component when $\langle \Pi_{sxa} \rangle_t$ is large and negative. Note that the structureborne estimate, $\langle \tilde{\Pi}_s \rangle_t$, is quite accurate in both figures (V-3e) and (V-3f).

C. EFFECTS OF ALTERING THE INPUT PATHS (SHAKER LOCATION)

Analytical Results

Figures (V-4a) through (V-4d) show the results that were obtained from program SOUND for the case of a normally incident uniform acoustic load and a point vibrational load located at the new coordinates of α_1=.12065 m and α_2=.20320 m. These coordinates place the vibrational point load at the center of the plate, thus driving exactly the same modes as the acoustic input (i.e. the odd modes of the plate). The small damping model, represented by equation (3.11), was used again for this simulation.

Figures (V-4a) and (V-4b) show the radiation efficiencies and sound power levels, respectively, produced by plate no. 1 due to a 1 Pa peak acoustic load and an independent .01 N peak vibrational load. Figure (V-4a) shows once again that the airborne noise is more efficient than the structureborne noise over most of the frequency range. The regions where $\sigma_a - \sigma_s$ is small or where the two curves intersect are seen to cover a larger portion of the curves than for previous analytical cases, however. Figure (V-4b) shows that the airborne source is dominant or at least of equal influence over the entire frequency range for these inputs.

The radiation efficiencies and sound powers produced by combining these two inputs are shown in figures (V-4c) and

(V-4d). The figures show that the overall noise radiation due to combined inputs is extremely sensitive to changes in the relative phases between the inputs. This result indicates that the cross term $\langle \Pi_{sxa} \rangle_t$ has an even larger influence on the overall noise radiation if and when the airborne and structureborne inputs drive the same modes of the structure.

Figures (V-4e) through (V-4g) show the results of applying program PREDICT to the three cases of combined inputs at 90 degrees, 0 degrees, and 180 degrees respectively. In all three cases the proposed separation method correctly identifies the dominant noise source except in those ranges where $\sigma_a - \sigma_s$ is small or zero. Note that figures (V-4f) and (V-4g) show very large differences between the estimated components and actual airborne and structureborne components. The differences in the curves are not so large, however, that the information contained in the estimates is deemed unusable.

Experimental Verification of the Results

Figures (V-5a) through (V-5d) show the measured data that were obtained from plate no. 1 for the case of an approximately uniform acoustic load and a point vibrational load located at the new coordinates of α_1=.12065 m and α_2=.20320 m. These coordinates place the vibrational

point load at the center of the plate, thus driving exactly the same modes as the acoustic input.

Figures (V-5a) and (V-5b) show the radiation efficiencies and sound power levels, respectively, produced by plate no. 1 due to independent acoustic and vibrational loads. Figure (V-5a) shows once again that the airborne noise is more efficient than the structureborne noise over most of the frequency range. Figure (V-5b) shows that the structureborne component of the sound power is dominant in several small discrete frequency regions while the airborne component is dominant over most of the frequency range. Smoother structureborne curves are expected in this case, since the shaker drives only the odd modes of the panel. Note that the structureborne radiation efficiency and sound power curves are indeed smoother than the curves obtained when the panel was driven near the corner.

The measured radiation efficiencies and sound powers of plate no. 1 produced by combining these two inputs are shown in figures (V-5c) and (V-5d) respectively. These figures again show that the sum of the results of the individual inputs is roughly equivalent to the results obtained by combining the inputs. Significant differences in the curves are seen to occur, however, in many frequency regions. These differences can again be explained by the influence of the cross term $\langle \Pi_{sxa} \rangle_t$.

Figures (V-5e) and (V-5f) show the results of applying program PREDICT to the combined inputs cases of figure (V-5d). These figures show that the proposed separation method correctly identifies the dominant noise source over nearly the entire frequency range. The separation method was again unable to make a reliable prediction in some ranges due to the small value of $\sigma_a - \sigma_s$. The comparisons are seen to be quite good with significant discrepancies occuring only in regions where $\sigma_a - \sigma_s$ is small.

D. EFFECTS OF ADDED DAMPING

Analytical Results

Figures (V-6a) through (V-6d) show the results that were obtained from program SOUND for baseline conditions (shaker located at $\alpha_1 = .06033$ m and $\alpha_2 = .13547$ m) on the aluminum plate with the moderate damping model represented by equation (3.12).

Figures (V-6a) and (V-6b) show the radiation efficiencies and sound power levels, respectively, produced by plate no. 1 due to a 1 Pa peak acoustic load and an independent .01 N peak vibrational load. Figure (V-6a) shows a marked increase in the airborne radiation efficiency and considerable smoothing of the structureborne radiation efficiency curve. The regions where $\sigma_a - \sigma_s$ is small are seen to cover a much smaller band of frequencies than for

previous cases. Figure (V-6b) shows that the airborne source is highly dominant over the entire frequency range.

The radiation efficiencies and sound powers produced by combining these two inputs are shown in figures (V-6c) and (V-6d). The figures show that overall noise radiation due to combined inputs is still sensitive to changes in the relative phases between the inputs.

Figures (V-6e) through (V-6g) show the results of applying program PREDICT to the cases of combined inputs. In all three cases the proposed separation method correctly identifies the dominant noise source except in one small range in figure (V-6g). Figure (V-6e) (uncorrelated inputs) shows extremely good agreement between the curves over nearly the entire frequency range. Figure (V-6f) (inputs in phase) and figure (V-6g) (inputs out of phase) show moderate differences in the curves with the largest deviations occuring when the inputs are in phase.

Experimental Verification of the Results

Figures (V-7a) through (V-7d) show the measured results that were obtained from plate no. 1 with damping tape added to the plate. The self-adhesive damping tape added to the panel consisted of single layer of polystyrene type foam material with an outer layer of aluminum foil. The tape added approximately 1.44 kg/m^2 to the surface density of the panel. This type of damping tape is commercially available

from several manufacturers and is routinely used to dampen vibration of the sidewalls of general aviation aircraft.

Figures (V-7a) and (V-7b) show the radiation efficiencies and sound power levels, respectively, produced by the damped plate due to independent acoustic and vibrational loads. Figure (V-7a) shows a marked increase in the airborne radiation efficiency and a drastic smoothing of the structureborne radiation efficiency curve. The regions where $\sigma_a - \sigma_s$ is small are seen to be confined to frequencies below 200 Hz with crossovers confined to the region below 100 Hz. Figure (V-7b) shows that the airborne source is dominant over nearly the entire frequency range.

The radiation efficiencies and sound powers produced by combining these two inputs are shown in figures (V-7c) and (V-7d). Figure (V-7c) shows that the radiation efficiency of the combined noise can vary over an extremely large range of values depending on the phase relationship between the inputs. Likewise, figure (V-7d) shows that the combined sound power is largely influenced by the cross term $<\Pi_{sxa}>_t$.

Figures (V-7e) and (V-7f) show the results of applying program PREDICT to the two cases of combined inputs. In figure (V-7e) the proposed diagnostic method correctly identifies the airborne component as the dominant noise source. In figure (V-7f), however, the airborne prediction

is seen to be overwhelmed by the large negative cross term $\langle \Pi_{sxa} \rangle_t$. The structureborne estimate $\langle \tilde{\Pi}_s \rangle_t$ is seen to exhibit close agreement with the independent structureborne sound power $\langle \Pi_s \rangle_t$ in both cases, however.

E. EFFECTS OF COMPOSITE MATERIAL PLATE CONSTRUCTION

Analytical Results

Figures (V-8a) through (V-8d) show the results that were obtained from program SOUND for baseline conditions (shaker located at α_1= .06033 m and α_2=.13547 m with the small damping model) for the case of a symmetric tape ply graphite epoxy plate with a 0/90 lay-up (plate no. 2). (See Tables IV-1 through IV-3 for additional information on the characteristics of this plate.)

Figures (V-8a) and (V-8b) show the radiation efficiencies and sound power levels, respectively, produced by plate no. 2 due to a 1 Pa peak acoustic load and an independent .01 N peak vibrational load. Figure (V-8a) shows considerable smoothing of the radiation efficiency curves when compared with the baseline aluminum case. The explanation for this phenomenon can be found in the eigenvalue analysis which indicates that plate no. 2 has fewer modes with natural frequencies in the 0-2000 Hz range. Thus, the curves are smoother for the composite plate simply because there are fewer modes to cause the peaks and valleys. The regions where $\sigma_a - \sigma_s$ is small or zero are seen to

cover a larger band of frequencies than for the aluminum plate, however. Figure (V-8b) shows that, in this case, the airborne source is highly dominant over the entire frequency range.

The radiation efficiencies and sound powers produced by combining these two inputs are shown in figures (V-8c) and (V-8d). The figures show that overall noise radiation due to combined inputs is still sensitive to changes in the relative phases between the inputs.

Figures (V-8e) through (V-8g) show the results of applying program PREDICT to the cases of combined inputs. In all three cases the proposed separation method correctly identifies the dominant noise source except in those ranges where $\sigma_a - \sigma_s$ is small. Figure (V-8e) (uncorrelated inputs) shows good agreement between the curves over nearly the entire frequency range. Figure (V-8f) (inputs in phase) and figure (V-8g) (inputs out of phase) tend to indicate much larger differences in the curves with the largest deviations occuring when the inputs are out of phase. The differences in these figures between the estimated components and the actual components are not so large as to render the diagnostic information unusable however.

Experimental Verification of the Results

Figures (V-9a) through (V-9d) show the measured results that were obtained from plate no. 2.

Figures (V-9a) and (V-9b) show the radiation efficiencies and sound power levels, respectively, produced by plate no. 2 due to independent acoustic and vibrational loads. Figure (V-9a) shows radiation efficiencies that are qualitatively similar to the efficiencies of figure (V-3a) (plate no. 1). Futher scrutiny of figure (V-9a) tends to confirm that the composite plate possesses fewer resonance frequencies in the 0-2000 Hz range than the aluminum plate. The regions of figure (V-9a) where $\sigma_a - \sigma_s$ is small or zero are seen to occur quite frequently. Figure (V-9b) shows that, for this case, the structureborne source is dominant in many discrete frequency regions.

The sound power produced by combining the inputs with positive polarity on the shaker is shown in figure (V-9c). This figure shows that the cross term $\langle \Pi_{sxa} \rangle_t$ can have a large influence on the combined sound power.

Figure (V-9d) shows the results of applying program PREDICT to the combined inputs case shown in figure (V-9c). Figure (V-9d) shows that the proposed diagnostic method correctly identifies the dominant noise source except in those frequency regions where $\sigma_a - \sigma_s$ is small or zero.

F. RADIATION EFFICIENCIES OF COMPOSITE TAPE PLY PANELS

Analytical Results

The results of an analytical study of the radiative characteristics of several symmetric angle-ply composite tape panels (plates 3-6) are given in figure (V-10). (See Tables IV-1 through IV-3 for additional information on the physical characteristics of these plates.) The data shown were predicted by program SOUND for the case of the baseline conditions outlined in section A.

Figure (V-10a) shows the calculated radiation efficiencies of a symmetric 8 ply graphite tape panels with a +45/-45 lay-up. The radiation efficiency curves are seen to be similar in character to the curves in figure (V-8a) for the 0/90 lay-up. The curves in both figures are somewhat smoother than the radiation efficiency curves for the aluminum panel. This is a strong indication that the graphite panels are stiffer than the baseline aluminum panel. The eigenvalue analysis performed indicates that both of these panels have 48 modes with natural frequencies in the 0-2000 Hz frequency range whereas the aluminum panel has 68 modes with natural frequencies in this range.

Figure (V-10b) shows the calculated radiation efficiencies of a 16 ply graphite tape panel with a +45/-45 lay-up. The radiation efficiencies curves in this case are smoother and show a smaller difference in the airborne and

structureborne curves. This is a direct consequence of the increased stiffness of the panel caused by the larger number of plies. The eigenvalue analysis performed indicated that this panel has only 26 modes with natural frequencies in the 0-2000 Hz frequency range.

Figure (V-10c) shows the calculated radiation efficiencies of an 8 ply Kevlar tape panel with a +45/-45 lay-up. The radiation efficiencies curves are seen to be remarkably similar to the curves obtained in figure (V-10a) for the 8 ply graphite tape panel with the +45/-45 lay-up. Close comparison of these two figures indicates that the Kevlar panel has lower resonance frequencies than the graphite panel. The greater compliance of the Kevlar panel was confirmed by the eigenvalue analysis which predicted 63 modes with natural frequencies in the 0-2000 Hz frequency range compared to 48 for the graphite panel.

Figure (V-10d) shows the calculated radiation efficiencies of an 8 ply fiberglass tape panel with a +45/-45 lay-up. The 2.21 kg/m^2 surface density of the fiberglass panel is very close to that of the baseline aluminum panel and therefore invites comparison. The extreme dissimilarity of figures (V-1a) and (V-10d) indicates that the fiberglass panel has many more resonance frequencies in the 0-2000 Hz range than the aluminum panel. The greater stiffness of the aluminum panel was confirmed by the eigenvalue analysis

which predicted 103 modes with natural frequencies in the 0-2000 Hz frequency range for the fiberglass panel compared to 68 for the aluminum panel.

Experimental Verification of the Results

The measured radiation efficiencies of several symmetric angle-ply composite tape panels (plates 3-6) are given in figure (V-11). First the results for the 8 ply graphite panel with a +45/-45 lay-up (plate no. 3) are shown in figure (V-11a). Secondly, the results for the 16 ply graphite panel with a +45/-45 lay-up (plate no. 4) are shown in figure (V-11b). Next, the results for the 8 ply Kevlar panel with a +45/-45 lay-up (plate no. 5) are shown in figure (V-11c). Finally, the results for the 8 ply fiberglass panel with a +45/-45 lay-up (plate no. 6) are shown in figure (V-11d).

These measurements produced results that were qualitatively similar to the results obtained in the analytical study. For example, figure (V-11b) indicates that the 16 ply graphite panel was again the stiffest panel showing the fewest natural frequencies in the 0-1000 Hz range. Figure (V-11d) indicates that the 8 ply fiberglass panel was again the most compliant panel showing the greatest number of natural frequencies in the 0-1000 Hz range. All five composite panels exhibited marked differences in their respective airborne and structureborne radiation efficiencies as

predicted by the analytical model with plate no. 4 showing the smallest difference (as predicted). Thus, both the analytical and experimental studies of the composite panels suggest that the coincidence phenomenon, which would result in little or no difference in σ_a and σ_s, occurs at some frequency outside the 0-1000 Hz range. Therefore, the application of the proposed noise path separation method would not differ significantly if used on an aircraft fuselage constructed of composite materials.

G. DISCUSSION OF THE RESULTS

To the author's knowledge, this is the first comprehensive study of the problem of the sound radiation of aircraft type materials due to fully coherent combined airborne and structureborne inputs in the low frequency regime. The single most significant finding in the results of this study was the discovery of the relative importance of the cross term sound power component $\langle \Pi_{sxa} \rangle_t$. The importance of this finding can not be over emphasized in light of the fact that all of the previous analytical and experimental studies performed in the last 7 or 8 years have neglected the interaction between the airborne and structureborne inputs in the low frequency regime. By NASA's count (see reference 3), some 93 publications appeared in the open literature between 1978 and 1984 which devoted their attention strictly to the airborne noise transmission through the sidewalls of

aircraft. A smaller number of studies (see references 18-22), addressing the problem of structureborne noise paths in aircraft, similarly restricted the scope of their analysis. The conclusions of some of these studies now seem dubious at best.

Evidence to support this claim can be found in the results such as those found in figures (V-6) and (V-7). Computations on the analytical results in these figures (for the damped aluminum panel) show that while $\langle \Pi_a \rangle_t$ = 82 dB overall and $\langle \Pi_s \rangle_t$ = 68.6 dB overall, the levels for the combined sound power ranged anywhere from 80.7 dB to 83.3 dB overall. Thus, the overall level of the combined sound power varied over a 2.6 dB range depending on the phase relationship between the airborne and structureborne inputs. Simple calculations show that the sum of individual components is 82.2 dB or, in other words, one would expect a 0.2 dB increase in the overall sound power level due to the addition of the structureborne noise to the dominant airborne noise <u>if the sound powers were additive</u>. The implication here is that the structureborne component does not have to radiate a significant amount of noise on its own in order to significantly change the level of the combined sound. In fact, the structureborne component needs only to change the <u>dynamics</u> of the problem in order to also significantly influence the overall noise radiation.

The most significant finding with respect to the proposed noise path separation method was the extremely large influence of the cross term $\langle \Pi_{sxa} \rangle_t$ on the airborne estimate $\langle \tilde{\Pi}_a \rangle_t$. This effect was observed in earlier experimental studies performed by the author on panels and on an aircraft fuselage (see references 39 and 40) but, at that time, was not fully understood. The analysis performed in section H of chapter III has shown that the effects of the cross terms are most likely to manifest themselves in the airborne estimate. The results of both the analytical study and experimental study clearly exhibit this behavioral aspect of equations (3.29) and (3.31). The results obtained from the measurements on the damped aluminum panel (see figures V-6 and V-7) illustrate the effect in a particularly dramatic fashion by showing that the cross term $\langle \Pi_{sxa} \rangle_t$ can be larger than the airborne component $\langle \Pi_a \rangle_t$ even when it is the dominant component of the noise. This result should serve as a warning to a potential user of this separation method that one must be especially cautious in interpreting the airborne estimate $\langle \tilde{\Pi}_a \rangle_t$. The fact that the airborne estimate $\langle \tilde{\Pi}_a \rangle_t$ is often negative when the inputs are out of phase should not be seen as a weakness in the diagnostic approach, however. By indicating a negative value, the estimates tell the measurer that a decrease in one component of the sound power might actually

increase the total or combined sound power radiated. This is obviously a very useful piece of information to have when modifying the structure for noise control purposes.

The results also indicate that the proposed separation method produces meaningful results irregardless of which source (airborne or structureborne) is dominant. Admittedly, however, the results may be more difficult to interpret when the structureborne noise is dominant since, when the inputs are correlated, the cross term tends to overwhelm the airborne estimate $\langle \tilde{\Pi}_a \rangle_t$.

The results obtained when the structureborne and airborne inputs drove the same modes (shaker at the center of the plate) indicate that there will be less difference in the airborne and structureborne noise radiative characteristics for this case and more frequency regions where $\sigma_a - \sigma_s$ is small. This causes added difficultly in the implementation of the proposed separation method. It also appears that the effects of the cross terms are more severe in this case. These difficulties are primarily of academic interest, however, since the actual physical occurence of this case is unlikely. The most important aspect of these results is that they demonstrate the sensitivity of the structureborne radiation efficiency to changes in the point of application of the load. Comparison of figures (V-1) and (V-4) and comparison of figures (V-3) and (V-5) suggest that

σ_s is very path dependent. Thus, if the proposed separation method is to be successful, the measurer must be certain that path of the structureborne inputs during calibration and measurement are the same.

The results obtained on the damped aluminum panel (figures (V-6) and (V-7)) show that the principle effects of the added damping are to smooth the σ_s curve, reduce the $\langle \Pi_s \rangle_t$ component, and to dramatically increase the airborne radiation efficiency σ_a. The results also suggest that the cross term $\langle \Pi_{sxa} \rangle_t$ has a large influence in the damped case as well as the undamped case. The increase in σ_a due to damping is caused by the reduction of the resonance controlled component of the vibration (which is very inefficient). The importance of this result lies in its potential to aid the measurer in cases where the difference $\sigma_a - \sigma_s$ is too small to utilize the proposed separation method. Comparison of figures (V-1a) and (V-6a) demonstrates the large change in radiation efficiencies that can be realized through small changes in the damping of the structure.

Finally, the analytical and experimental results obtained on the composite panels indicate that the noise radiative properties of these materials do not differ radically from those of aluminum in the 0-1000 Hz range. The results do suggest, however, that significant tayloring

of the noise radiative properties in isolated frequency regions can be achieved by adjusting parameters such as panel lay-up and the number of plies. This fact might be used to the noise control engineer's advantage if the interior noise of the aircraft in question has a discrete frequency character (such as in propeller driven aircraft). History has shown, however, that structural modifications such as this are more attuned to aircraft performance and load bearing considerations than to secondary considerations such as noise control.

H. OBSERVED DIFFERENCES BETWEEN THEORY AND EXPERIMENT

Analytical and experimental results for corresponding cases show considerable differences in the smoothness, location of resonances, and other characteristics of the radiation efficiency curves, etc... In this section, several possible sources of error in the analytical assumptions and in experimental data taking are discussed.

Possible sources of error in the analytical modeling include (1) the eigenvalue and eigenfunction analysis, (2) the assumed boundary conditions, (3) the damping model, (4) the forcing function, and (5) the radiation conditions.

The simple eigenvalue analysis used in this study is considered exact for the cases involving the aluminum plate and the symmetric ply laminates with specially orthotropic layers. No measure of the accuracy of equation (3.6) for

the eigenvalue analysis of the angle-ply laminates is available. The author concedes that eigenvalues obtained using this equation are not as accurate as those which could be obtained by a finite element model or even a Rayleigh-Ritz analysis. The necessity for using an approximative equation such as (3.6) arises, however, as the number of natural frequencies which contribute to the noise generation in the 0-1000 Hz range becomes large. And as seen from the results, some of the plates have as many as 100 natural frequencies in the 0-2000 Hz range. This large number of natural frequencies makes a numerical analysis such as the finite element method impracticable. The use of the sine-wave eigenfunctions could also cause some errors in the angle-ply laminate cases. These errors should be small, however, as long as the number of plies is large.

The analytical model also assumes simply supported boundary conditions. This assumption is likely to cause prediction errors in the first few natural frequencies of the plates. Because the actual boundary conditions are somewhere in between clamped and simply supported, the true natural frequencies of the plates are expected to be higher than those predicted. The severity of this error decreases with increasing mode numbers.

Errors introduced by the damping model are expected to have their largest impact on the airborne radiation

efficiency curves since it was shown that σ_a is very sensitive to damping. The damping model may also introduce some spurious cross coupling between modes which does not exist in the actual case under study.

Differences in the actual and analytically modeled forcing functions could be the source of discrepencies in the results. During the experimental phase of the study, the shaker-rod-panel system was attached throughout the measurement process. This means that the actual forcing functions experience an additional impedance due to the attached mass of the shaker at the rod attachment point. The analytical model tends to overestimate natural frequencies and overestimate the forced response because of this added driving impedance. A second source of error is the crude approximation of the spatial distribution of the forcing function. Small differences in the placement of the shaker, and differences in the approximately uniform airborne input are apt to cause large differences in the modal response of the structure. Finally, the fluid loading effects at the first few natural frequencies of the plate have been neglected in the forcing function. An effort was made to correct for this error through the damping model, however.

A final source of error in the analytical model is the assumption of free-field acoustic radiation conditions. Efforts were made to approximate these conditions in the

experimental portion of the study by the addition of the acoustic wedges to the receiving room of the TL apparatus. Realistically, however, the free-field conditions were probably achieved only above 200 Hz.

Sources of error in the data taking include (1) the acoustic intensity measurement method, and (2) random and bias errors in the space averaging and time averaging.

The most worrisome source of error (in this study) due to the acoustic intensity measurement method was near field effects. This type of error is most severe when the measurements are performed in a highly reactive acoustic field. This is precisely the type of noise field that is produced by a structureborne noise source. The existence of large time-averaged pressure gradients in these fields can cause large errors in the intensity measurements. A brief discussion this and several other types of error associated with the acoustic intensity method is given in Appendix XI.

Random errors in the the space and time averaging can be controlled by an appropriate choice of the number of accelerometer locations and the size of the area chosen for analysis. The measurer should also be aware of certain types of bias error that enter into the data taking due to effects such as leakage and aliasing which are inherent in the discrete Fourier tranform process. Appropriate measures can also be taken to control the influence of these errors.

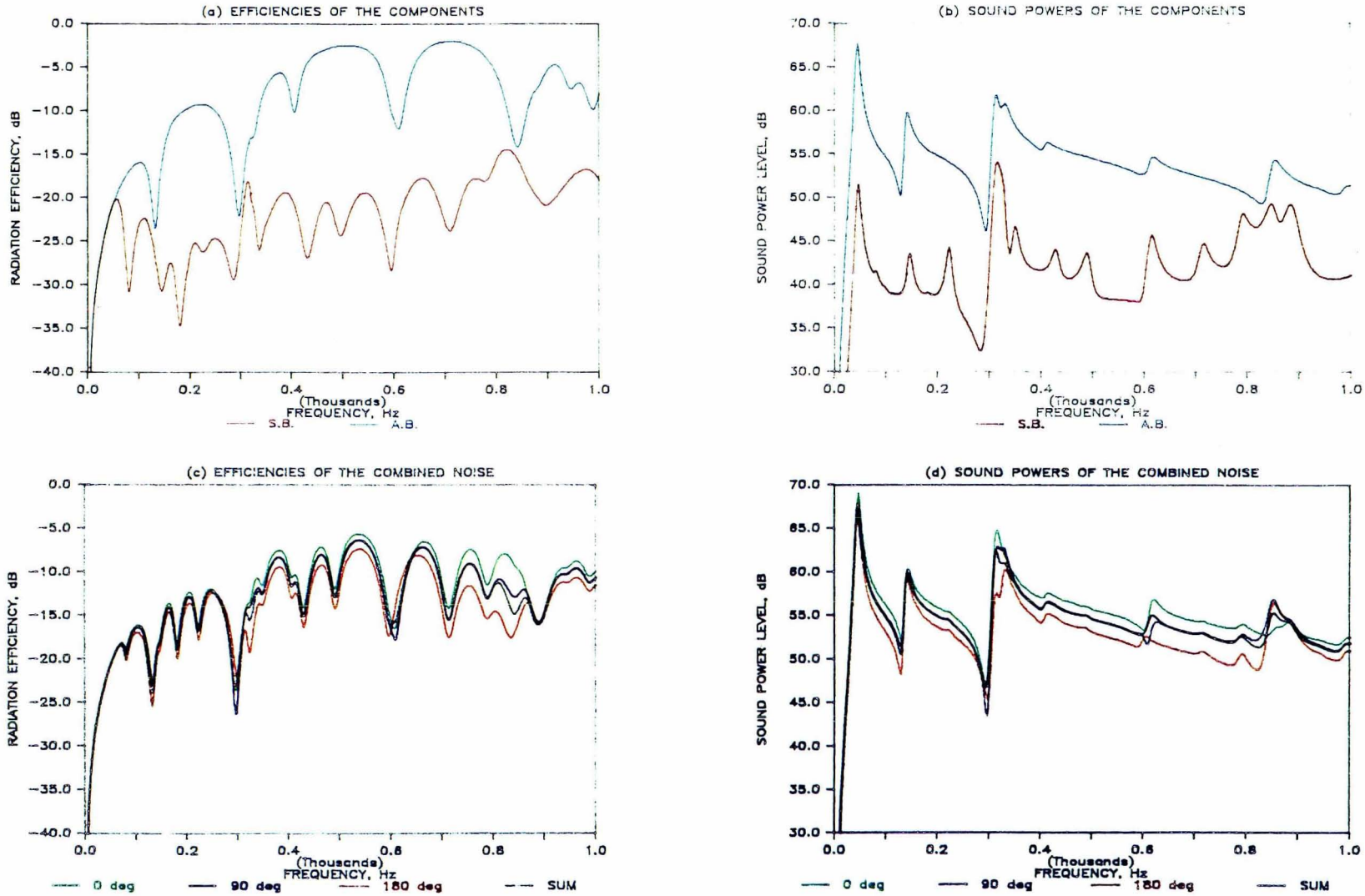

Figure (V-1) -- Analytical results for plate no. 1 with a dominant airborne source, the shaker located near the corner, and the small damping model.

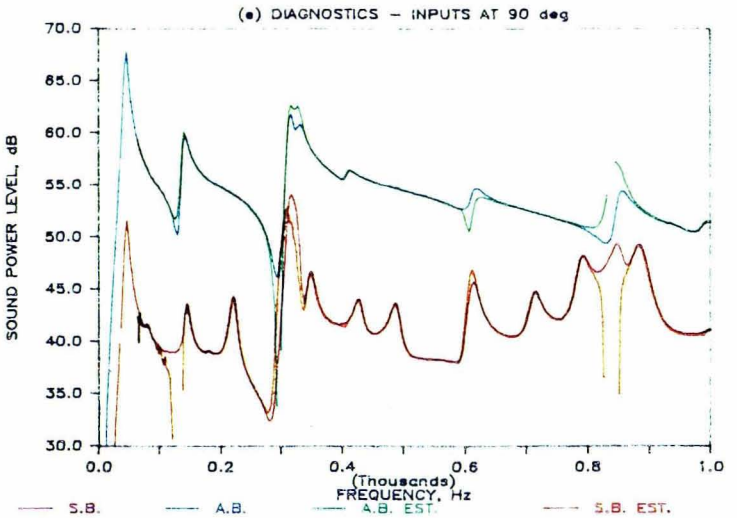

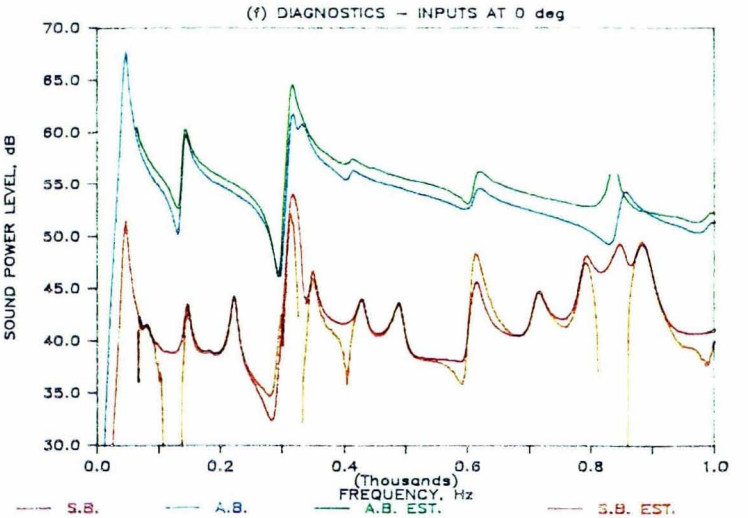

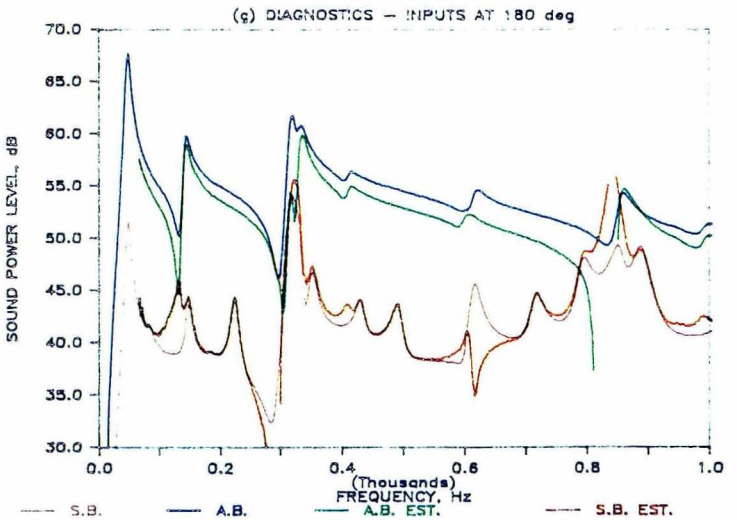

Figure (V-1) -- Analytical results for plate no. 1 with a dominant airborne source, the shaker located near the corner, and the small damping model (cont'd).

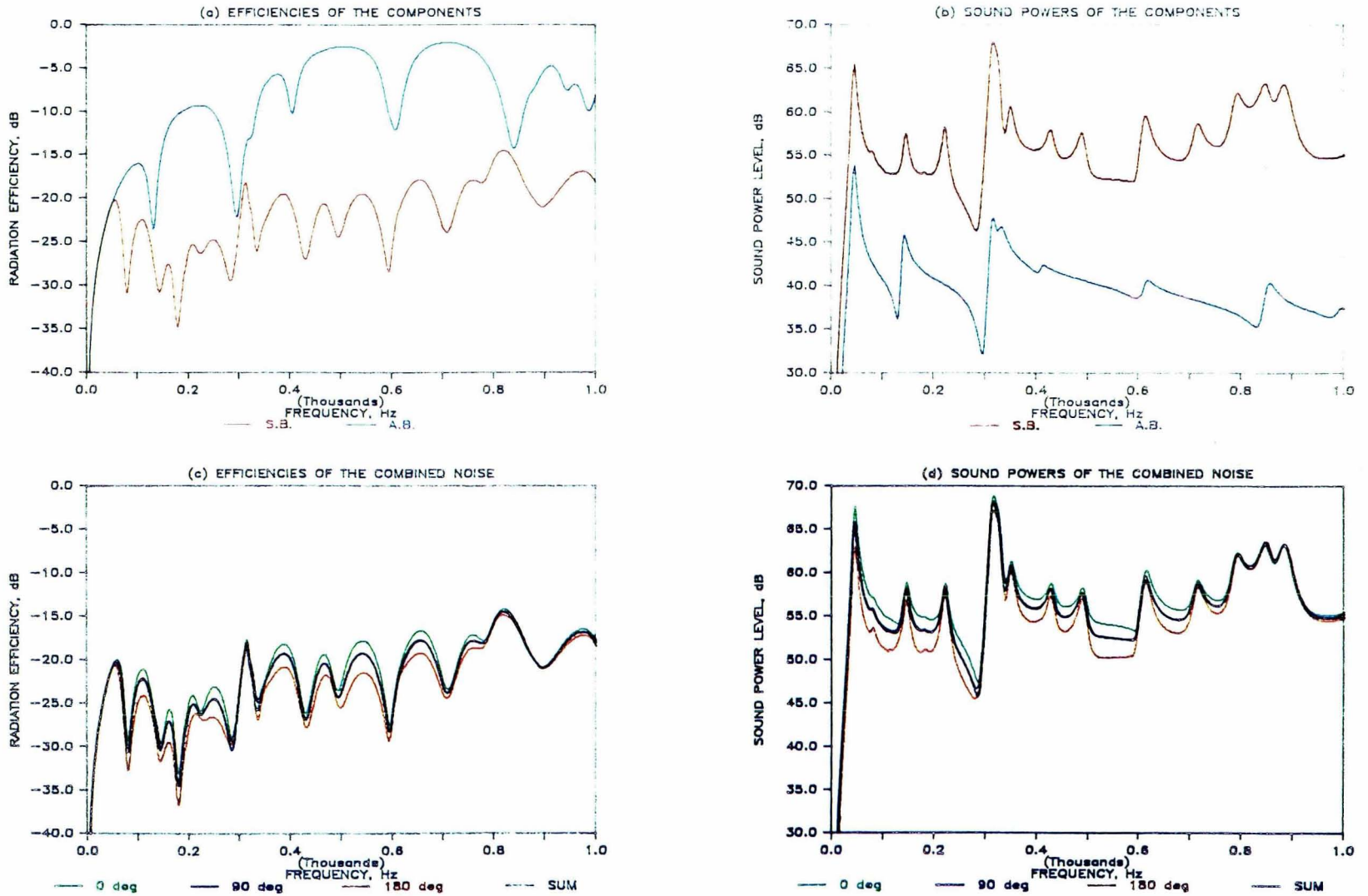

Figure (V-2) -- Analytical results for plate no. 1 with a dominant structureborne source, the shaker located near the corner, and the small damping model.

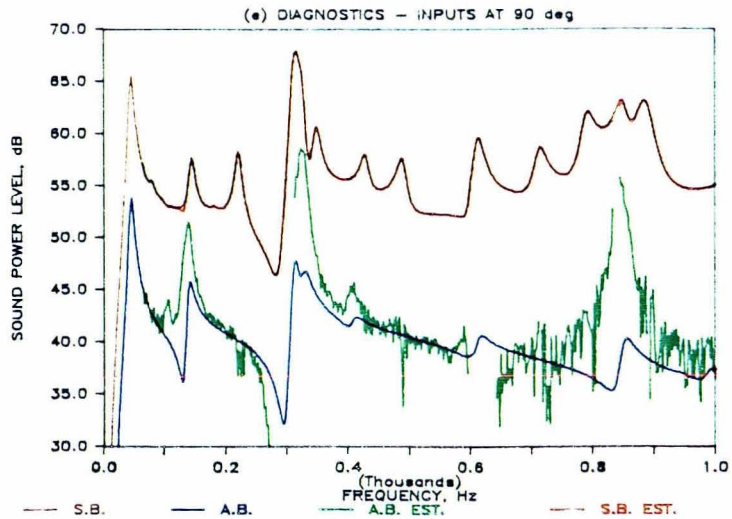

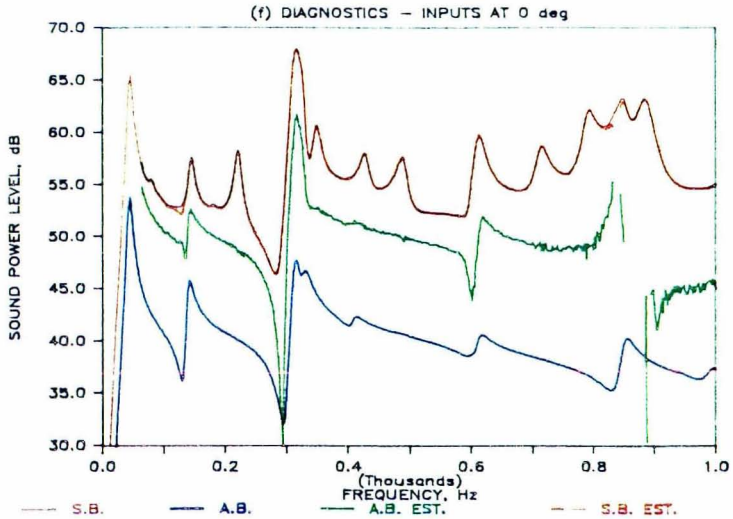

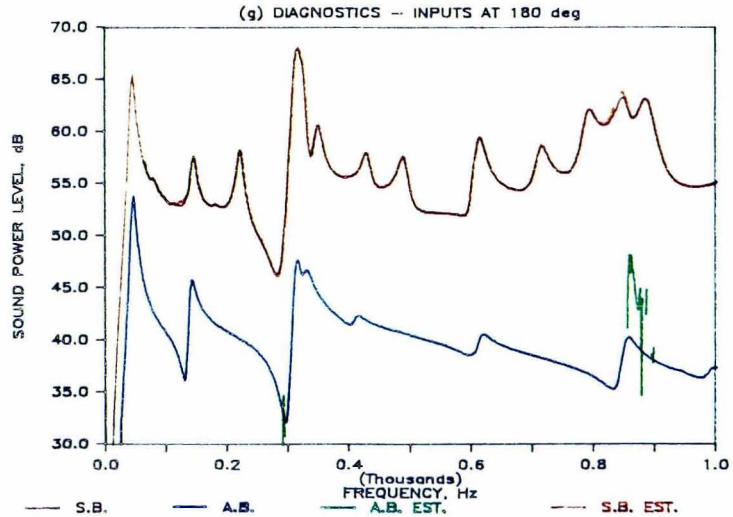

Figure (V-2) -- Analytical results for plate no. 1 with a dominant structureborne source, the shaker located near the corner, and the small damping model (cont'd).

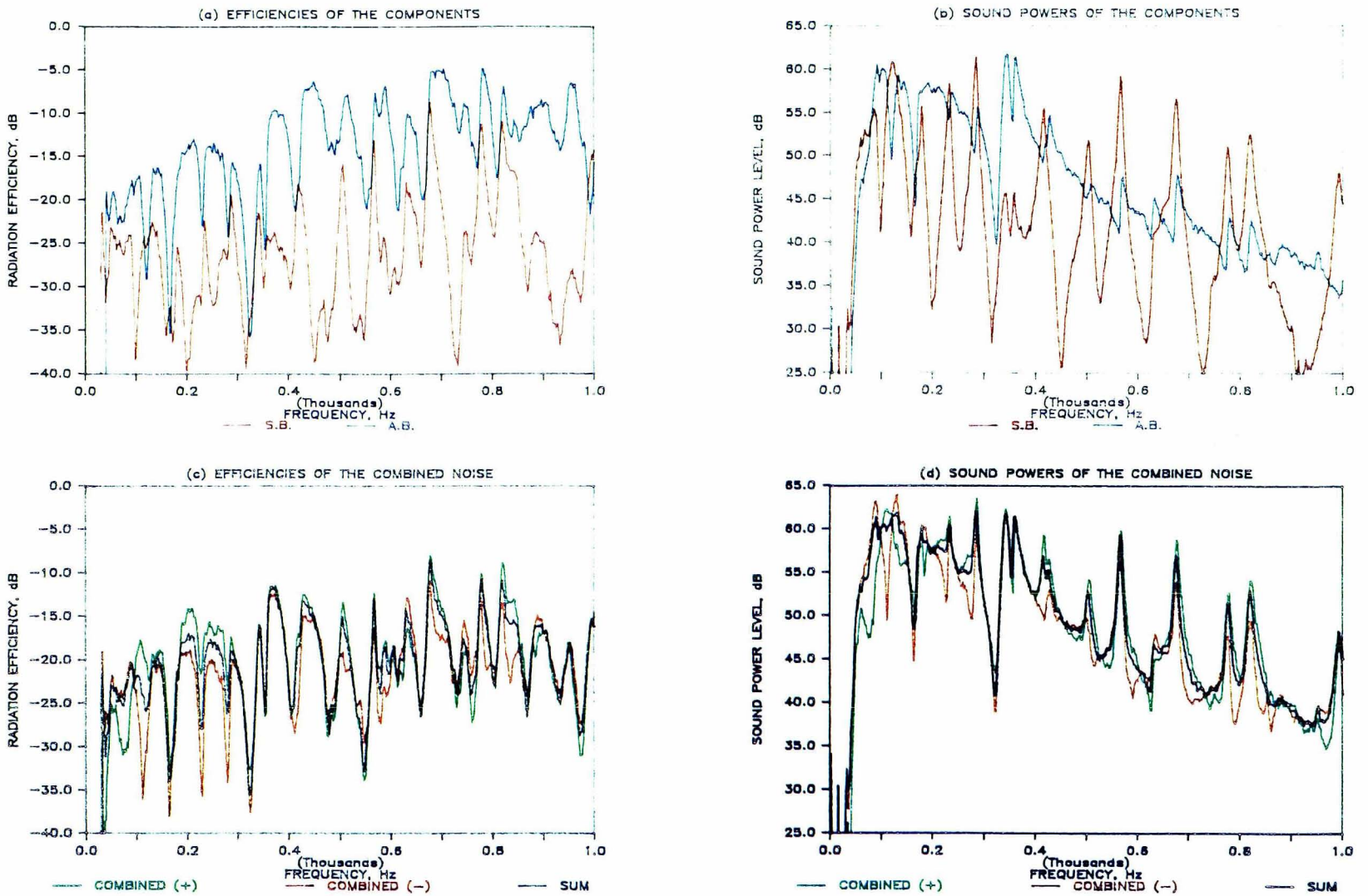

Figure (V-3) -- Experimental results for plate no. 1 with the shaker located near the corner.

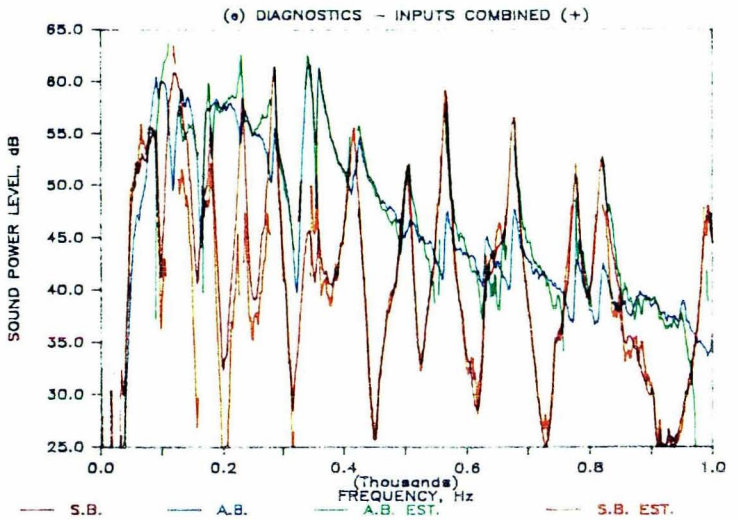

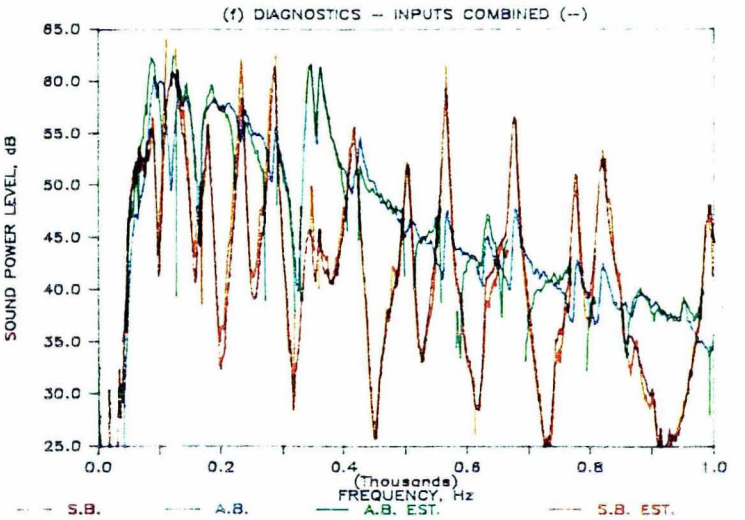

Figure (V-3) -- Experimental results for plate no. 1 with the shaker located near the corner (cont'd).

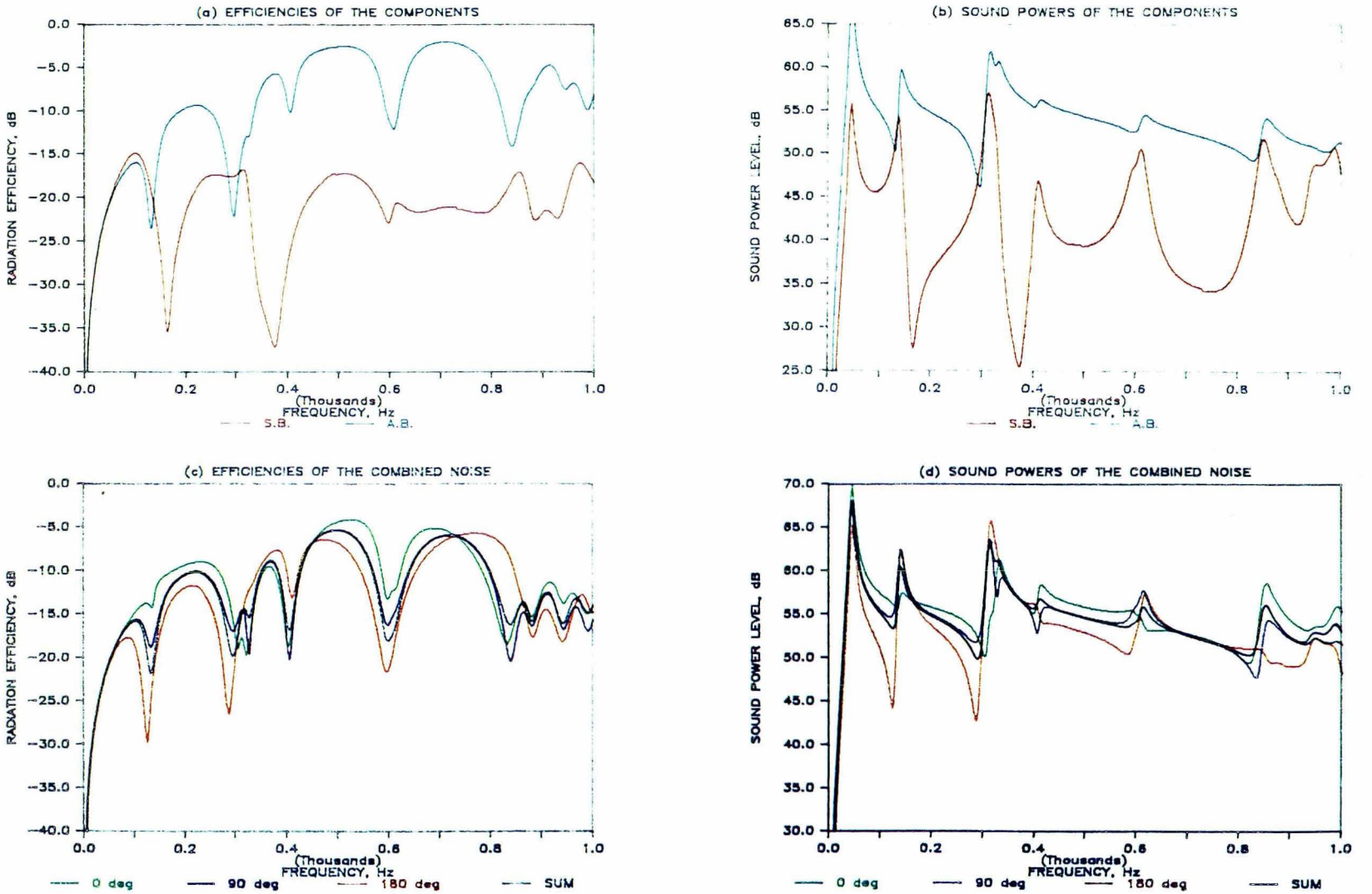

Figure (V-4) -- Analytical results for plate no. 1 with a dominant airborne source, the shaker located at the center, and the small damping model.

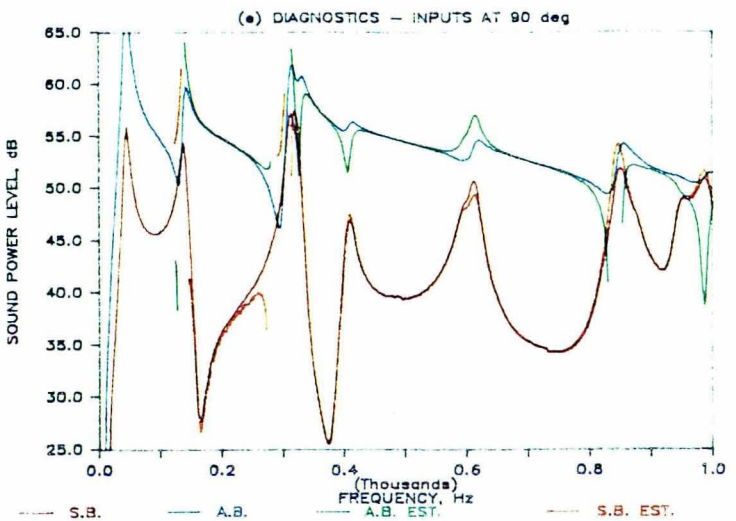

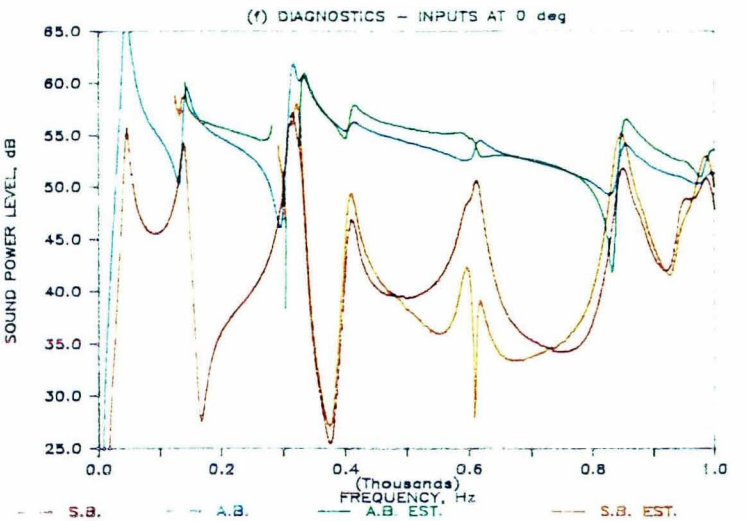

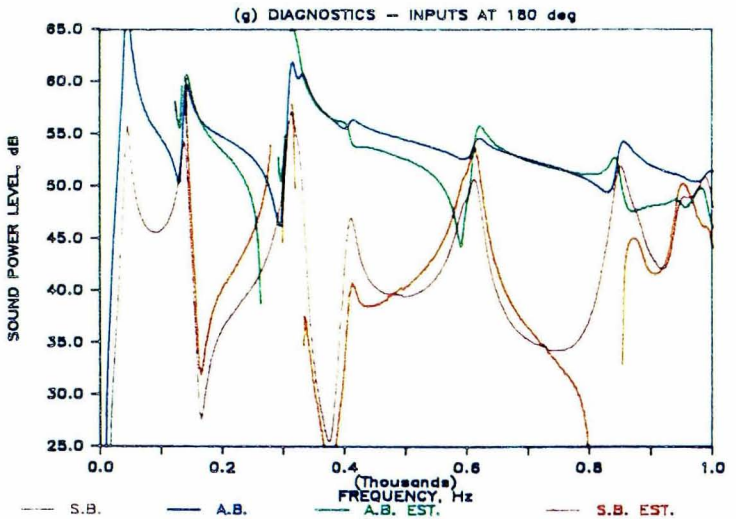

Figure (V-4) -- Analytical results for plate no. 1 with a dominant airborne source, the shaker located at the center, and the small damping model (cont'd).

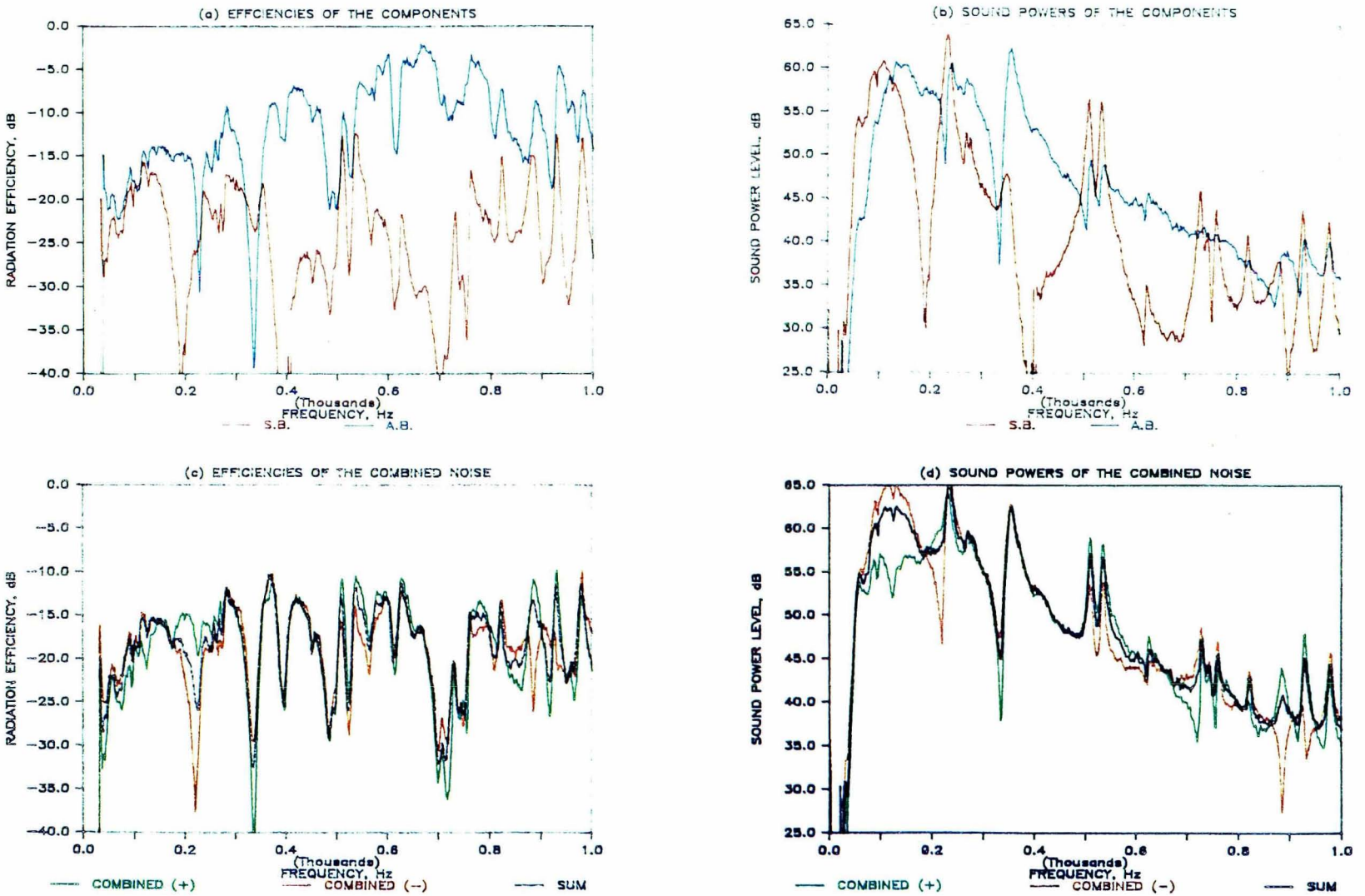

Figure (V-5) -- Experimental results for plate no. 1 with the shaker located at the center.

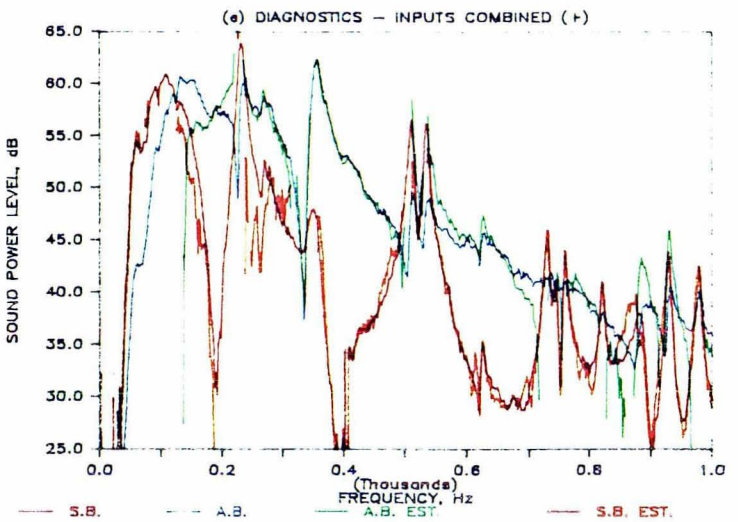

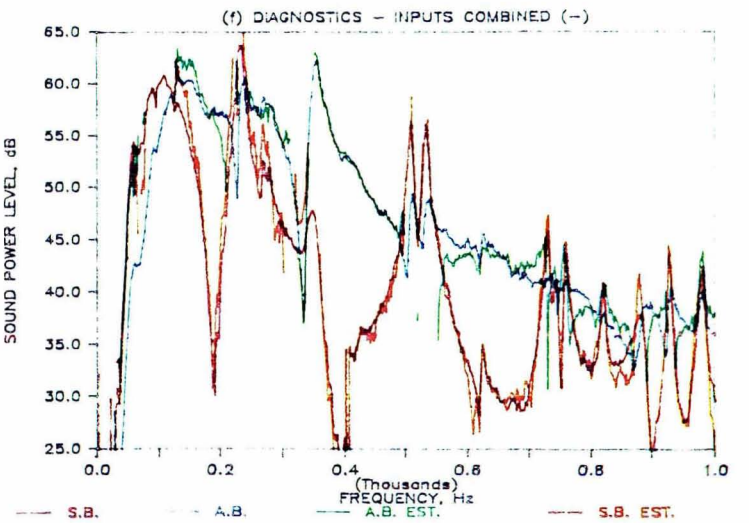

Figure (V-5) -- Experimental results for plate no. 1 with the shaker located at the center (cont'd).

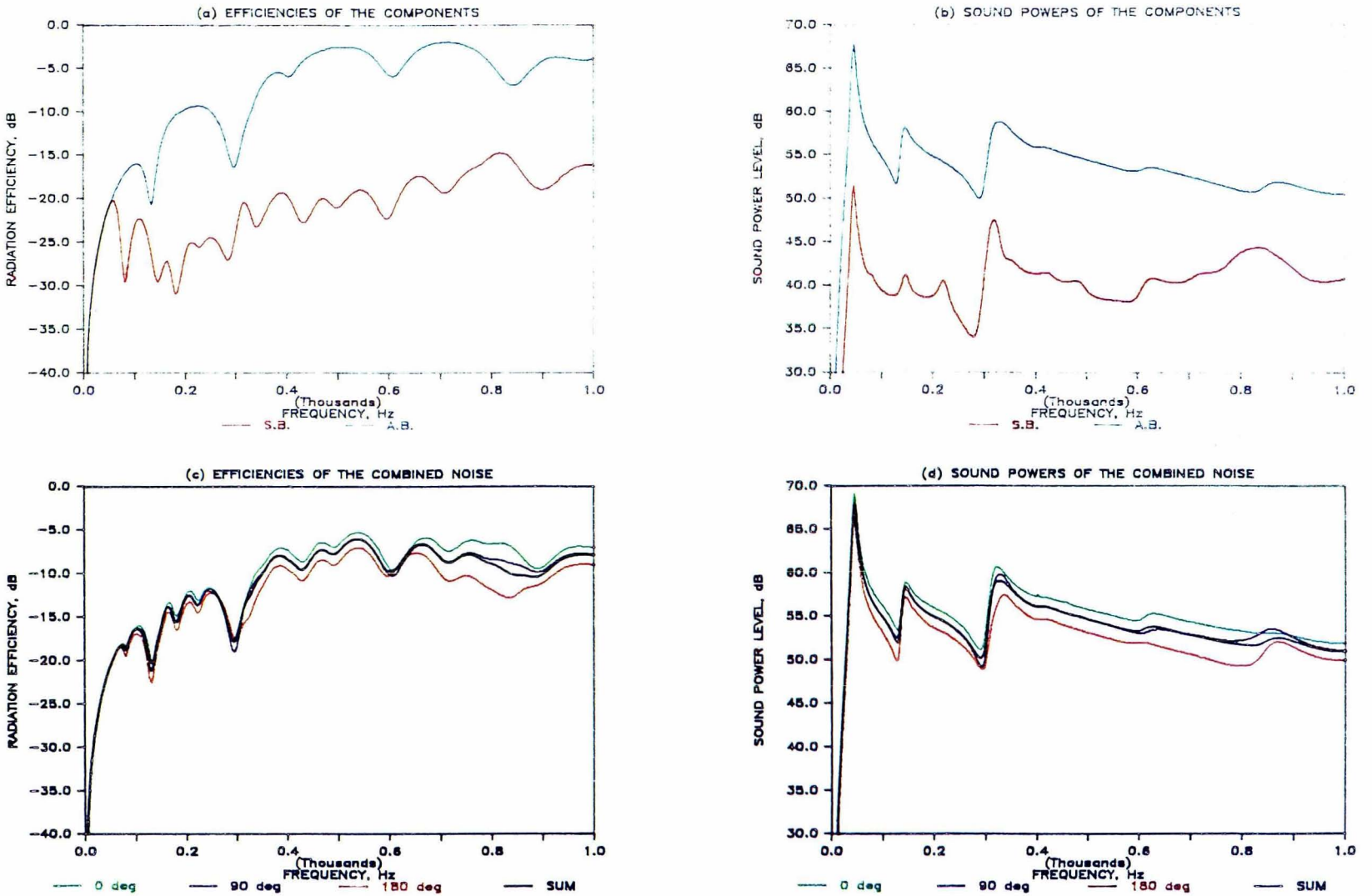

Figure (V-6) -- Analytical results for plate no. 1 with a dominant airborne source, the shaker located near the corner, and the moderate damping model.

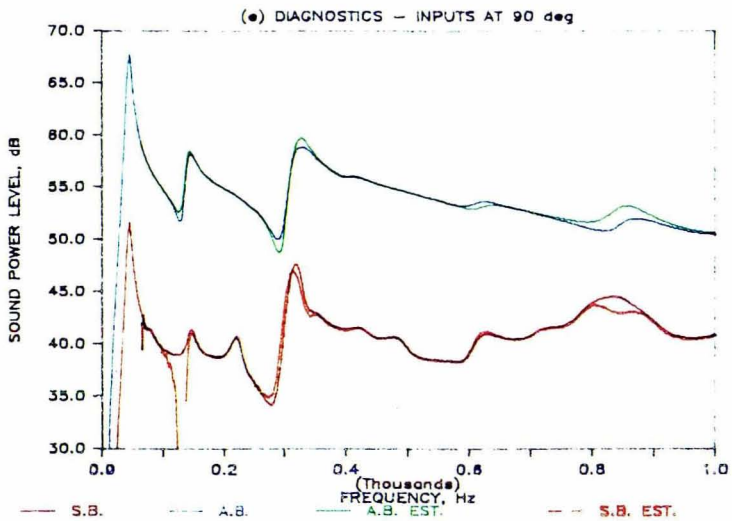

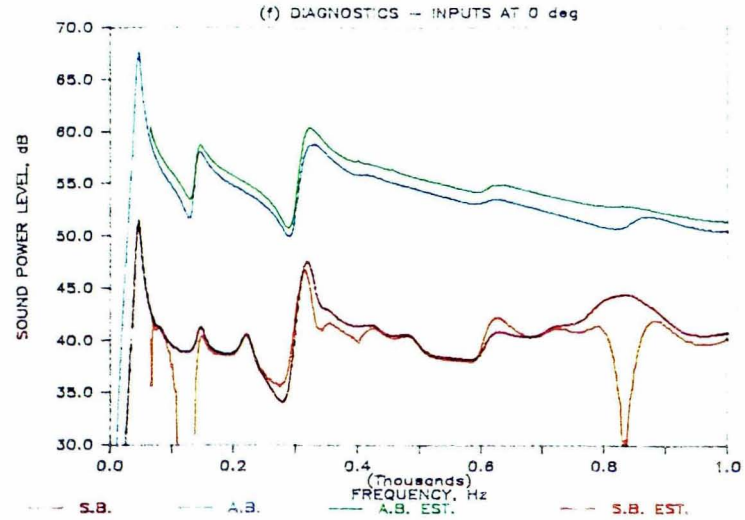

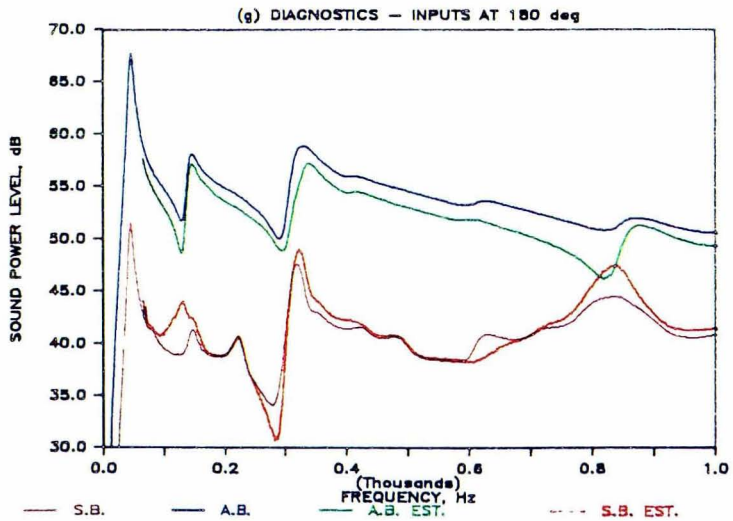

Figure (V-6) -- Analytical results for plate no. 1 with a dominant airborne source, the shaker located near the corner, and the moderate damping model (cont'd).

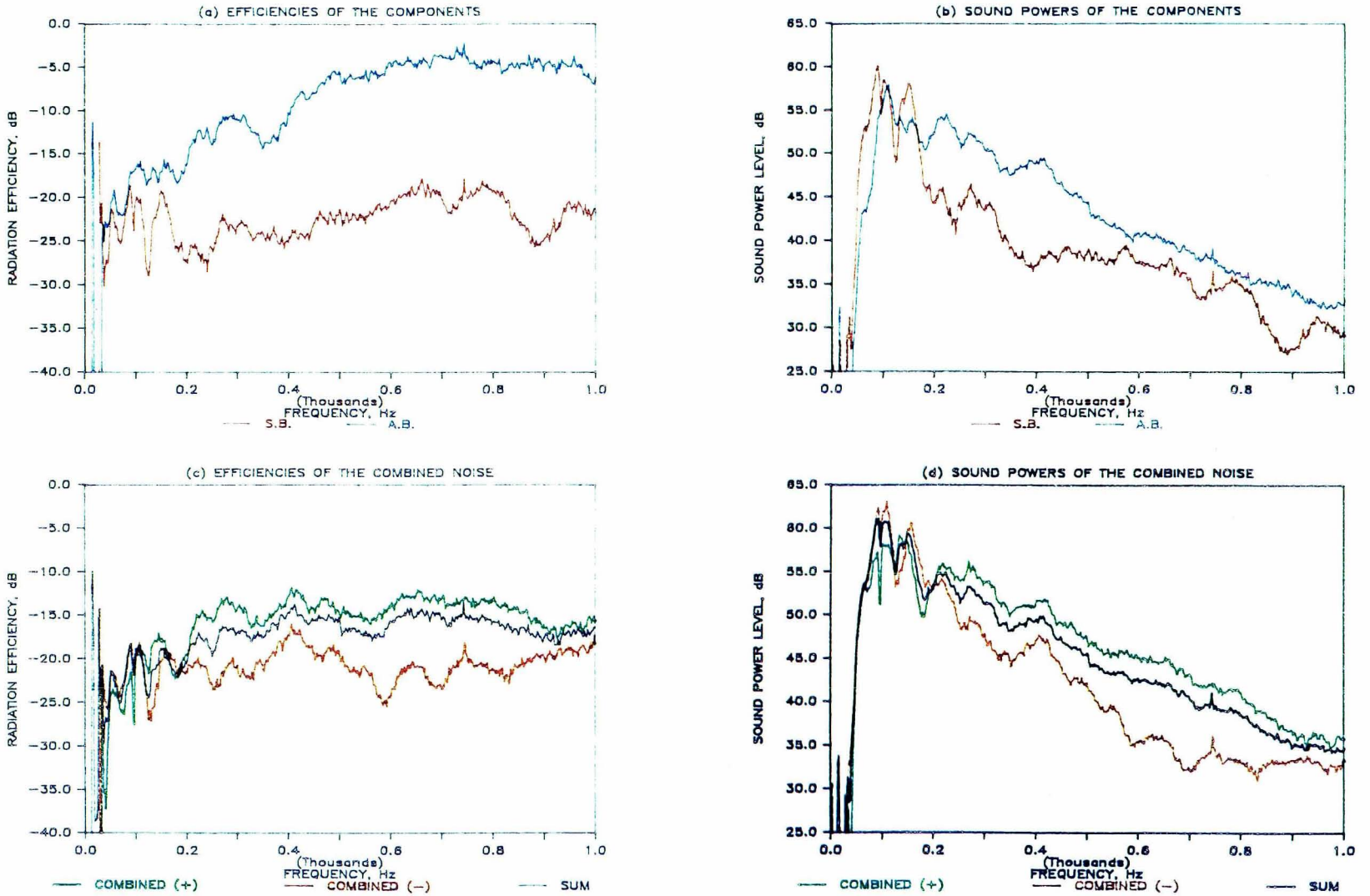

Figure (V-7) -- Experimental results for plate no. 1 with the shaker located near the corner and with damping tape added to the plate.

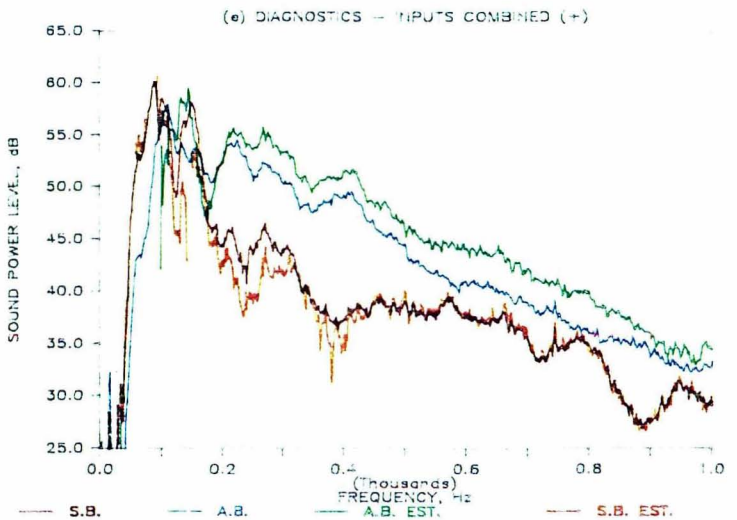

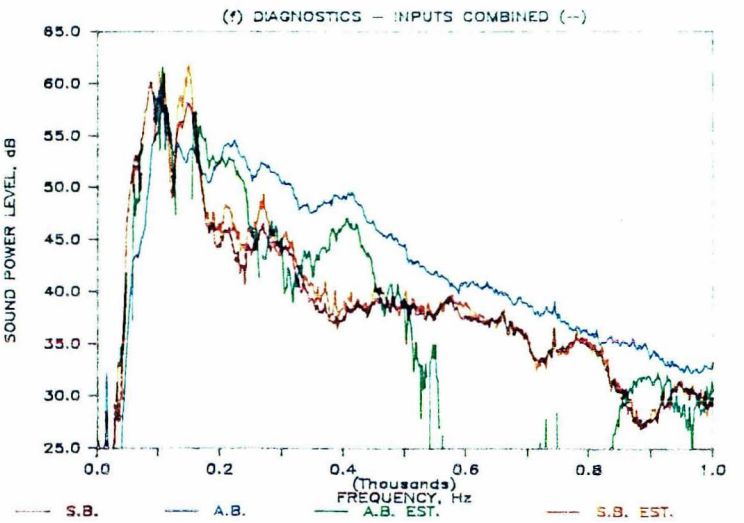

Figure (V-7) -- Experimental results for plate no. 1 with the shaker located near the corner and with damping tape added to the plate (cont'd).

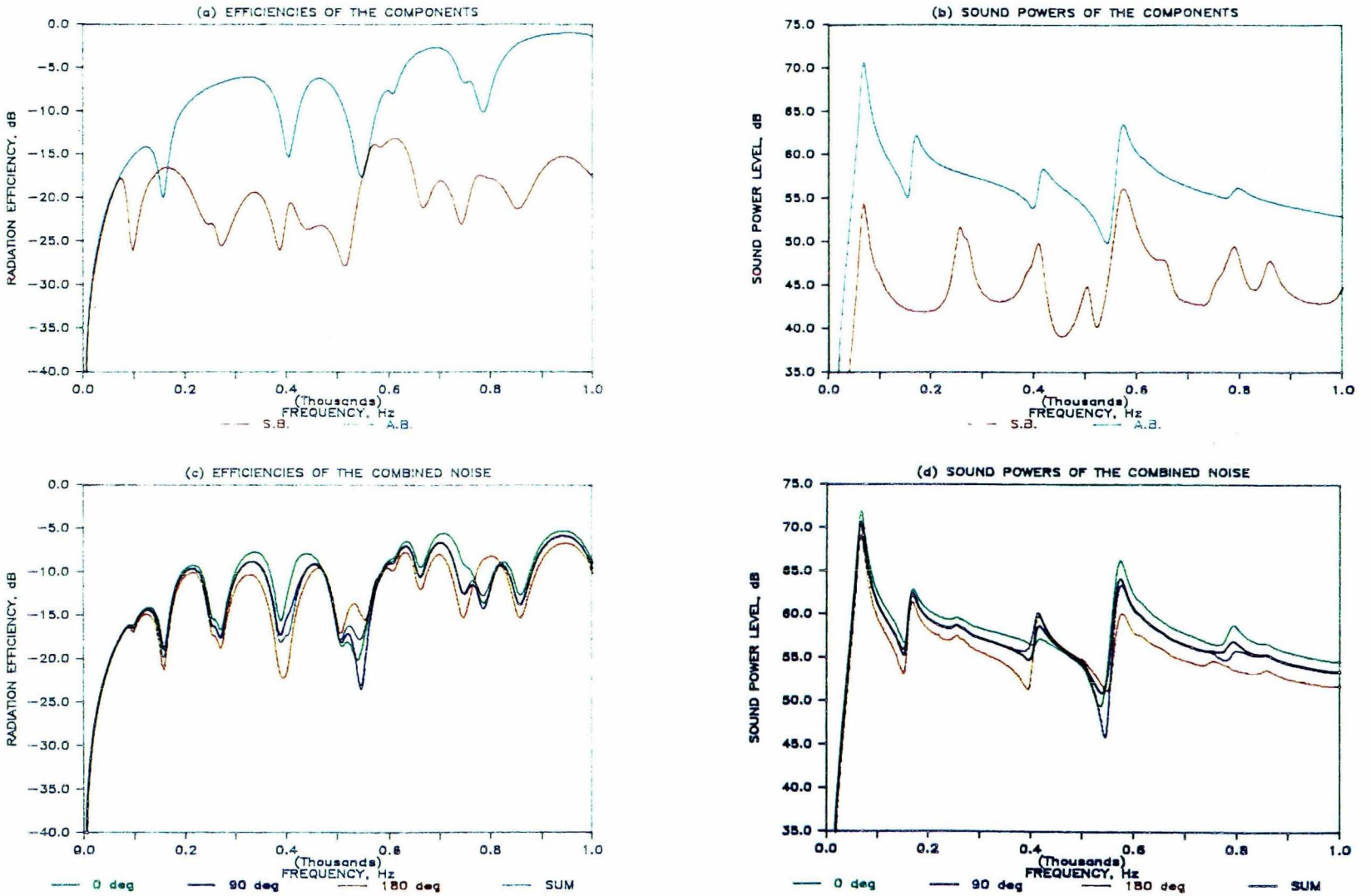

Figure (V-8) -- Analytical results for plate no. 2 with a dominant airborne source, the shaker located near the corner, and the small damping model.

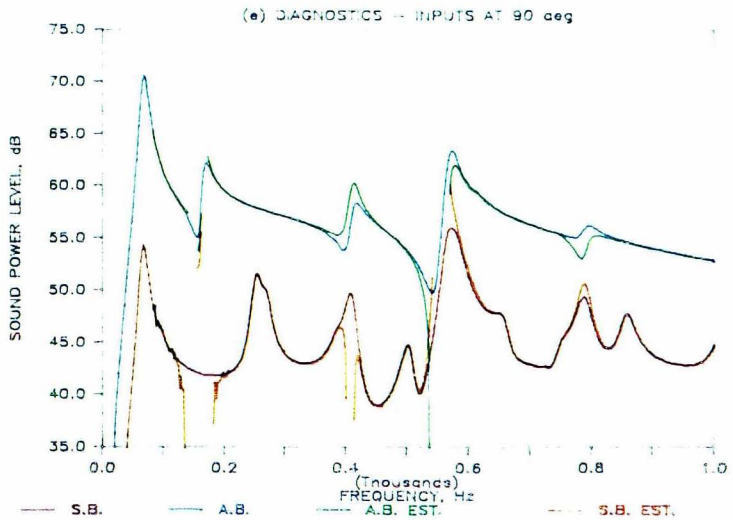

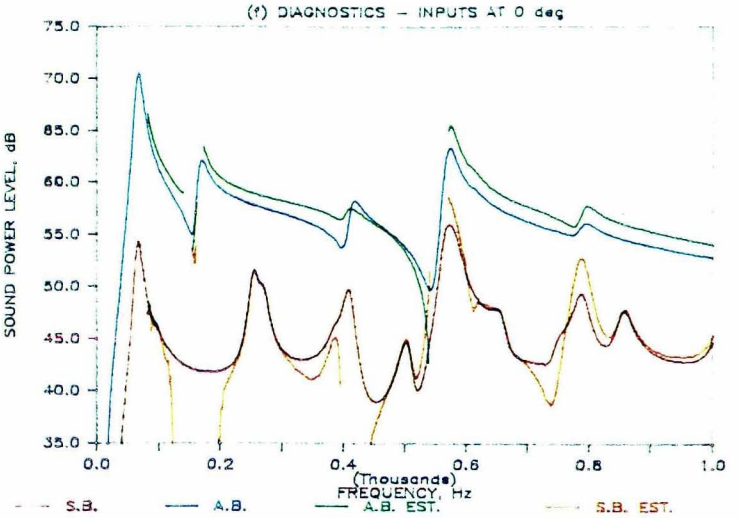

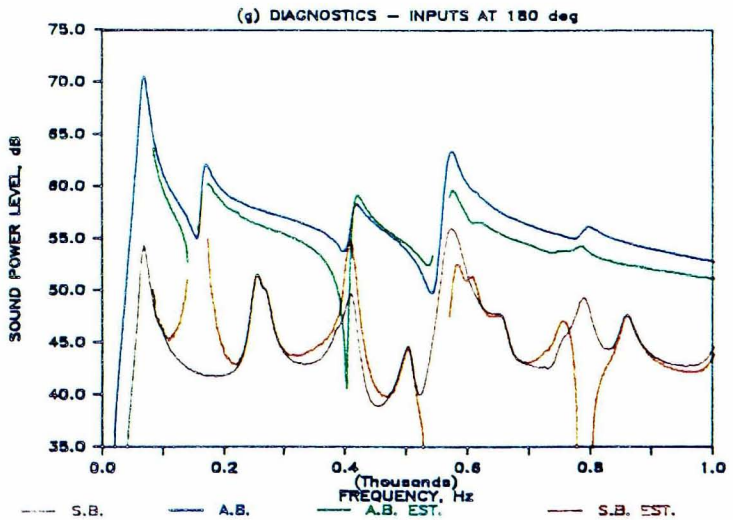

Figure (V-8) -- Analytical results for plate no. 2 with a dominant airborne source, the shaker located near the corner, and the small damping model (cont'd).

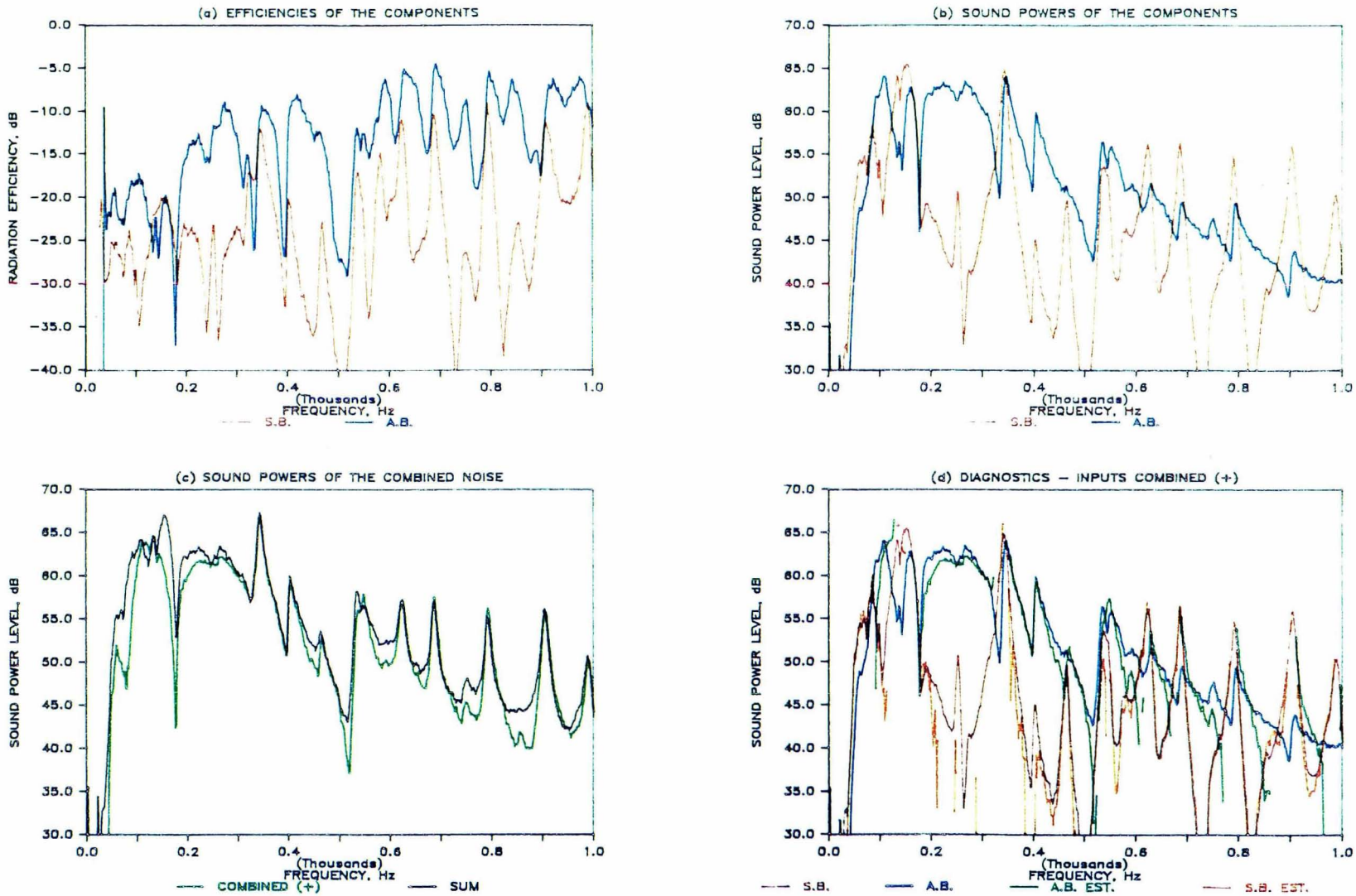

Figure (V-9) -- Experimental results for plate no. 2 with the shaker located near the corner.

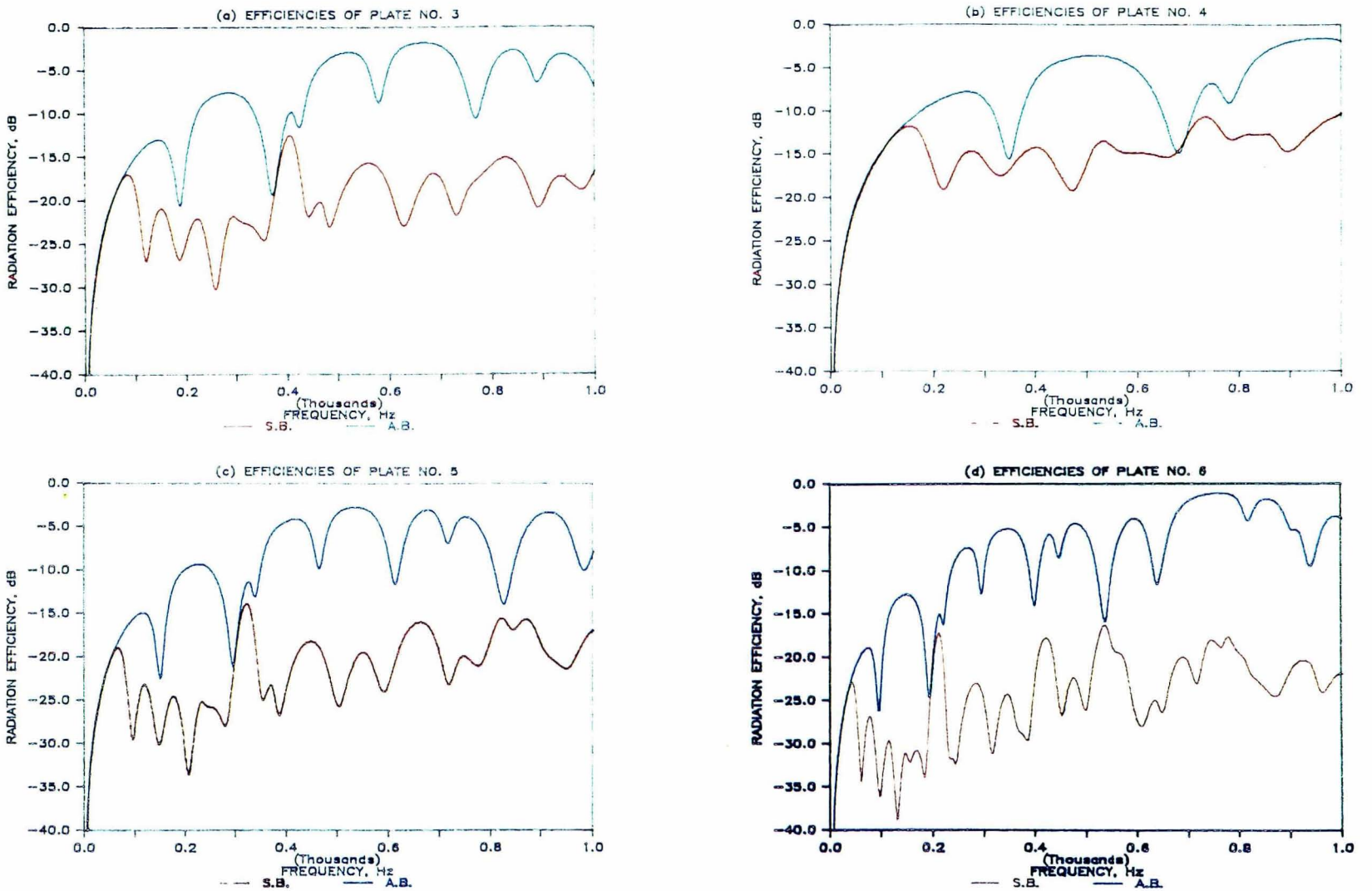

Figure (V-10) -- Analytical airborne and structureborne radiation efficiency curves for the symmetric angle ply composite panels (plates 3-6).

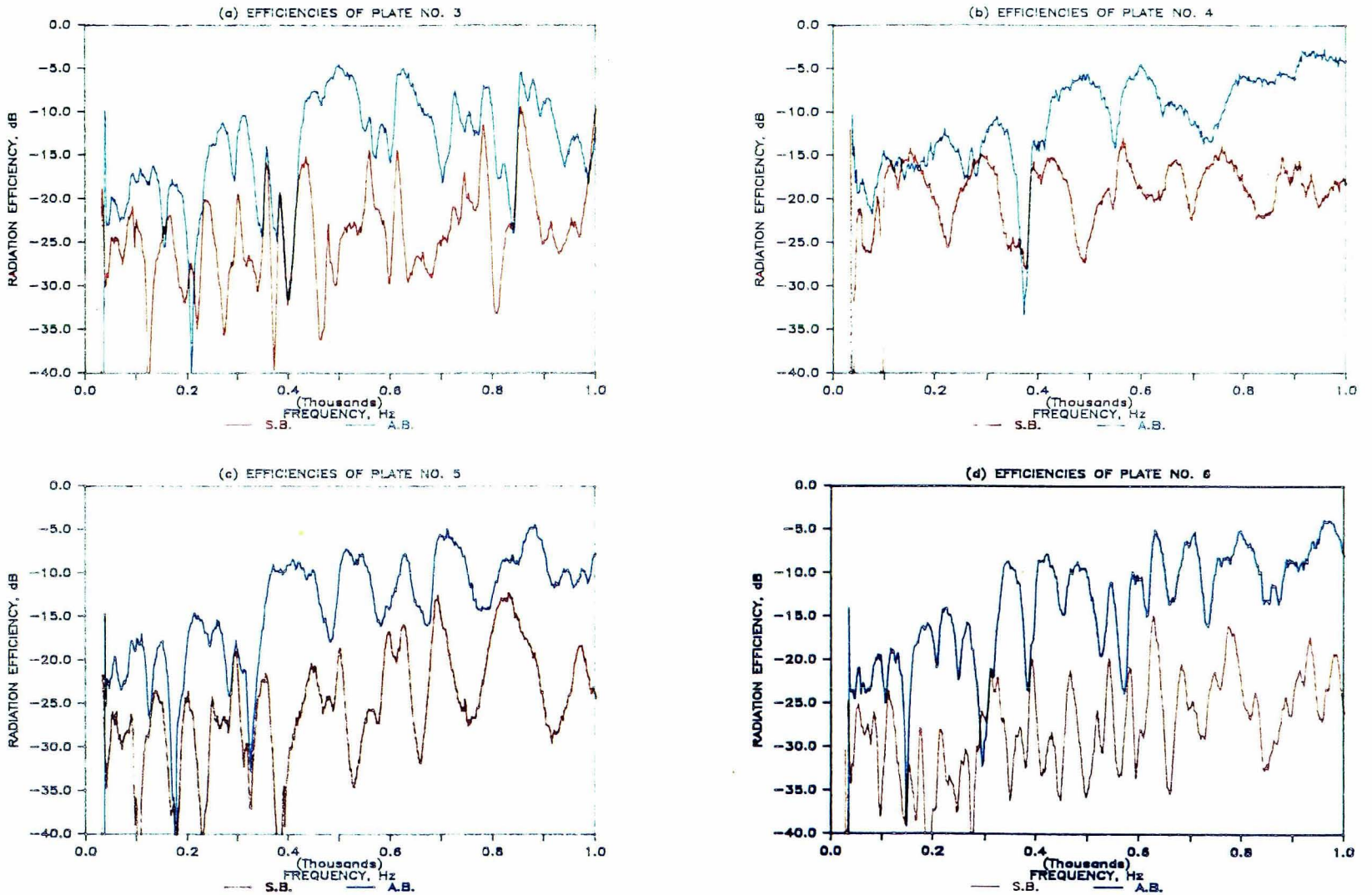

Figure (V-11) -- Measured airborne and structureborne radiation efficiency curves for the symmetric angle ply composite panels (plates 3-6).

Chapter VI

SUMMARY AND CONCLUSIONS

A. REVIEW OF THE OBJECTIVE

The purpose of this study was to develop a new diagnostic measurement method, based on the acoustic intensity measurement method and on several equations developed by the author, for separating and predicting the airborne and structureborne components of the sound power radiated by aircraft-type panels due to some unknown combination of acoustic and vibrational inputs. In order to validate the proposed method, both analytical and experimental studies were undertaken. The purpose of the analytical study was to provide the theoretical basis for the method and simulate its behavior under various operating conditions. The purpose of the experimental study was then to verify the expected behavior of the proposed diagnostic method.

B. MAJOR FINDINGS OF THE STUDY

The most significant finding of this study was the extremely large influence that the relative phase between the inputs has on the combined noise radiation of the plates. It has been shown that phase dependent effects manifest themselves as cross terms in both the dynamic and acoustic portions of the analysis. Both the analytical and experimental studies show that these cross terms can

radically alter both the combined sound power and combined radiation efficiencies of plates constructed of aircraft-type materials.

The diagnostic method proposed in this study has been used successfully to predict the relative contributions of the airborne and structureborne sound power components of fully coherent combinations of simultaneous acoustic and vibrational inputs to simple panels. The use of radiation efficiency measurements for separating the airborne and structureborne components of the total sound power radiated in aircraft appears to be a viable option to the other diagnostic tools currently available. The results of the study indicate that the method accurately predicts the dominant noise source, alerts the measurer to any strong interactive components, and can be applied to plate or thin shell structures constructed of a variety of materials.

Finally, both analytical and experimental studies on the composite panels show that, although the noise radiative characteristics of these materials are not radically different from those of the aluminum panel, the character of the radiation efficiency curves can be surprisingly sensitive to panel lay-up. This is an important finding since it suggests that the designer might be able to selectively modify the noise transmissive properties of the sidewalls of an aircraft with little or no weight penalty.

C. APPLICABILITY OF THE DIAGNOSTIC METHOD TO AIRCRAFT

Although the proposed noise path separation method was not applied to an actual aircraft structure in this study, a preliminary study of the feasibility of measuring radiation efficiencies in aircraft was performed by the author in an earlier experimental study. (See reference 40.) This earlier study demonstrated that the method has considerable promise for application in actual aircraft structures. The results of that earlier study coupled with the rigorous analysis performed in this study warrant the further investigation of this method as a noise source-path identification tool in aircraft.

The major advantage of the proposed method over the other diagnostic approaches currently available is that this new method does not necessarily require any modifications to the aircraft and could be used during flight. Also, the method can be used for fully coherent acoustic and vibrational inputs, whereas the partial/multiple coherence function methods can not, and the method works best in the low frequency regime where lead-wrapping fails because of the low transmission loss of lead.

Limitations of the proposed method include its low frequency restriction and its inapplicability when $\sigma_a - \sigma_s$ is small. The method can only be used at frequencies below the critical frequency of a thin shell structure. At

frequencies above the critical frequency, there will be little or no difference in σ_a and σ_s. Below the critical frequency, the difficulties of a small value of $\sigma_a - \sigma_s$ can be easily overcome, however, with the application of additional damping to the structure.

D. AREAS FOR FUTURE RESEARCH

Future research on the proposed diagnostic method and its applicability to aircraft should be directed at the study of the certainty of radiation efficiency measurements in aircraft. Studies should be performed to determine the sensitivity of radiation efficiency measurements to such factors as (1) changes in the acoustic source directivity, (2) changes in the path of the vibrational energy flow, and (3) changes in the number of acoustic and vibrational inputs.

The applicability of the proposed separation method to aircraft will remain in question until these problems are addressed. For example, a complex structure such as an aircraft may have several important structural transmission paths. By measuring σ_s for each structural transmission path, equations (3.29) and (3.31) become a system of two equations with many more than two unknowns. Thus, measuring structureborne radiation efficiencies for many structural transmission paths would not necessarily solve the problem since the relative importance of the different structural

paths may be unknown. As another example, suppose a loudspeaker is used as an acoustic source to determine the airborne radiation efficiency of some small area on a propeller driven aircraft fuselage. The acoustic directivity of the loudspeaker may be dissimilar to the directivity of the actual acoustic sources on the aircraft (that is the propellers). This approximation of σ_a could introduce considerable error into the structureborne sound power prediction $\langle \Pi_s \rangle_t$ (as indicated by the error analysis in Appendix VIII). Hypothetical situations such as these encourage the investigator to perform some preliminary measurement and analysis on the particular problem of interest before attempting to use the proposed separation method.

REFERENCES

1. Hayden, R.E.; Murray B.S.; Theobald M.A.: "A Study of Interior Noise Levels, Noise Sources, and Transmission Paths in Light Aircraft," NASA Contract Report 172152, July, 1983.

2. Catherines, J.J.; Jha, S.K.: "Sources and Characteristics of Interior Noise in General Aviation Aircraft," NASA Technical Memorandum X-72839, 1976.

3. Mixson, J.S.; Powell, C.A.: "Review of Recent Research on Interior Noise of Propeller Aircraft," AIAA/NASA 9th Aeroacoustics Conference, Williamsburg, Virginia, October, 1984.

4. "Study of the Cost/Benefit Tradeoffs for Reducing the Energy Consumption of the Commercial Air Transportation System," NASA Contract Report 137926, Lockheed California Company, August, 1976.

5. "Energy Consumption Characteristics of Transports Using the Prop-Fan Concept," NASA Contract Report 137927, Boeing Commercial Airplane Company, October, 1976.

6. Quinlivan, J.: "Advanced Composites on Boeing Commercial Airplanes," NASA Contract Report 172358, ACEE Composite Structures Technology Conference, August, 1984.

7. Watts, D.J.: "Joints and Cutouts in Fuselage Structure," NASA Contract Report 172359, ACEE Composite Structures Technology Conference, August, 1984.

8. Jackson, A.C.: "Impact Dynamics and Acoustic Transmission in Fuselage Structures," NASA Contract Report 172360, ACEE Composite Structures Technology Conference, August, 1984.

9. Ganesan, N.: "Composites for Noise Control," SAE paper 730339, April, 1973.

10. Getline, G.L.: "Low-Frequency Noise Reduction of Lightweight Airframe Structures," NASA Contract Report 145104, August, 1976.

11. Koval, L.R.: "Sound Transmission into a Laminated Composite Cylindrical Shell," Journal of Sound and Vibration, Vol. 71, No. 4, 1980, pp. 523-530.

12. Koval, L.R.: "Field-Incidence Transmission of Treated Orthotropic and Laminated Composite Panels," NASA Technical Memorandum 85680, August, 1983.

13. Roussos, L.A.; et. al.: "Noise Transmission Characteristics of Advanced Composite Structural Materials," AIAA paper 83-0694, April, 1983.

14. Roussos, L.A.; McGary, M.C.; Powell, C.A.: "Studies of Noise Transmission Characteristics of Advanced Composite Material Structures," NASA Conference Publication 2321, ACEE Composite Structures Technology Conference, August, 1984.

15. Mixson, J.S.; Farassat, F.; et. al.: "Interior Noise Considerations for Advanced High-Speed Turboprop Aircraft," Journal of Aircraft, Vol.20, No. 9, 1983, pp. 791-797.

16. Zorumski, W.E.: "Propeller Noise Prediction," NASA Technical Memorandum 85636, May, 1983.

17. Metzger, F.B.: "Prop-Fan Source Noise Measurements for Cabin Noise Research," The Second Aircraft Interior Noise Meeting, Co-sponsered by S.A.E. and NASA, October, 1984.

18. Metcalf, V.L.; Mayes, W.H.: "Structureborne Contribution to Interior Noise of Propeller Aircraft," S.A.E. Technical Paper 830735, 1983.

19. Unruh, J.F.; Scheidt, D.C.: "Engine Induced Structure-Borne Noise in a General Aviation Aircraft," S.A.E. Technical Paper Series 790626, April 1979.

20. Unruh, J.F.; Scheidt, D.C.: Pomerening, D.J.: "Engine Induced Structural-Borne Noise in a General Aviation Aircraft," NASA Contract Report 159099, 1979.

21. Unruh, J.F.: "Structural-Borne Noise Prediction for a Single Engine General Aviation Aircraft," A.I.A.A. paper 80-1037, June 1980.

22. Junger, M.C.; et. al.: "Analytical Model of the Structureborne Interior Noise Induced by a Propeller Wake," NASA Contract Report 172381, May, 1984.

23. Jha, S.K.; Catherines, J.J.: "Interior Noise Studies for General Aviation Types of Aircraft Part I: Field Studies," Journal of Sound and Vibration, Vol. 58, No. 3, June 1978, pp. 375-390.

24. Jha, S.K.; Catherines, J.J.: "Interior Noise Studies for General Aviation Types of Aircraft Part II: Laboratory Studies," Journal of Sound And Vibration, Vol. 58, No.3, June 1978, pp. 391-406.

25. Bendat, J.S.; Piersol, A.G.: Engineering Applications of Correlation and Spectral Analysis, John Wiley and Sons Inc., New York, 1980.

26. Keefe, L.: "Interior Noise Path Identification in Light Aircraft Using Multivariate Spectral Analysis," A.I.A.A. paper 79-0644, March 1979.

27. Howlett, J.T.: "A Study of Partial Coherence for Identifying Interior Noise Sources and Paths on General Aviation Aircraft," NASA Technical Memorandum 80197, 1979.

28. Fahy, F.J.: "Measurement of Acoustic Intensity Using the Cross Spectral Density of Two Microphone Signals," Journal of the Acoustic Society of America, Vol. 62, No. 4, October 1977, pp. 1057-1059.

29. Lambrich, H.P.; Stahel, W.A.: "A Sound Intensity Meter and Its Applications in Car Acoustics," Proceedings of INTER-NOISE 77, 1977, pp. B142-B147.

30. Chung, J.Y.: "Fundamental Aspects of the Cross Spectral Method of Measuring Acoustic Intensity," Recent Developments in Acoustic Intensity Measurement, Cent. Tech. Ind. Mech., 1981, pp. 1-10.

31. Hodgson, T.H.: "Investigation of the Surface Acoustical Intensity Method for Determining the Noise Sound Power of a Large Machine In Situ," Journal of the Acoustic Society of America, Vol. 61, No. 2, February 1977, pp. 487-493.

32. Brito, J.D.: Sound Intensity Patterns for Vibrating Surfaces, Ph.D. Thesis, M.I.T., 1977.

33. McGary, M.C.: Noise Source Identification of Diesel Engines Using Surface Intensity Measurements, M.S. Thesis, Purdue, 1980.

34. Boone, D.E.; Hodgson T.H.: "Surface Intensity Measurements using a Fiber Optic-Pressure Probe," Recent Developments in Acoustic Intensity Measurements, Cent. Tech. Ind. Mech., 1981, pp. 89-94.

35. Forssen, B.; et. al.: "A Study of Methods of Prediction and Measurement of the Transmission of Sound Through the Walls of Light Aircraft," Herrick Laboratories Report 81-19, Purdue University, August, 1981.

36. McGary, M.C.: "Interior Noise Source/Path Identification of Propeller Driven Aircraft using Acoustic Intensity Methods," Proceedings of NOISE CON 81, 1981, pp. 261-264.

37. Crocker, M.J.; Raju, P.K.; Forssen, B.: "Measurement of Transmission Loss of Panels by the Direct Determination of Transmitted Acoustic Intensity," Noise Control Engineering, Vol. 17, No. 1, July-August 1981, pp. 6-11.

38. McGary, M.C.: "Noise Transmission Loss of Aircraft Panels Using Acoustic Intensity Methods," NASA Technical Paper 2046, August 1982.

39. McGary, M.C.: "A New Measurement Method for Separating Airborne and Structureborne Aircraft Interior Noise Radiated by Aircraft-Type Panels,", NASA Technical Publication 2079, September 1982.

40. McGary, M.C.; Mayes, W.H.: "A New Measurement Method for Separating Airborne and Structureborne Aircraft Interior Noise," Noise Control Engineering, Vol. 20, No. 1, January-February 1983.

41. Forssen,B.; Crocker, M.J.: "Estimation of Surface Velocity by Use of the Two-Microphone Technique," Proceedings of INTER-NOISE 82, 1982.

42. Jones, R.M.: Mechanics of Composite Materials, McGraw-Hill Book Company, 1975.

43. Bert, C.W.: "Optimal Design of a Composite Material Plate to Maximize its Fundamental Frequency," Journal of Sound and Vibration, Vol. 50, No. 2, 1977, pp. 229-237.

44. Ashton, J.E.; Waddoups, M.E.: "Analysis of Anisotropic Plates," Journal of Composite Materials, No. 3, 1969, pp. 148-165.

45. Whitney, J.M.: "Free Vibration of Anistropic Rectangular Plates," Journal of the Acoustical Society of America, Vol. 52, 1972, pp. 448-449.

46. Ashton, J.E.; Whitney, J.M.: Theory of Laminated Plates, Technomic, Stamford, CT, 1970.

47. Meirovitch, L.: Analytical Methods in Vibrations, The MacMillan Company, New York, 1967.

48. Ver, I.L.; Holmer, C.I.: "Interaction of Soundwaves with Solid Structures," Noise and Vibration Control, ed. Beranek, McGraw-Hill, pp. 270-361, 1971.

49. Manning, J.; Maidanik, G.: "Radiation Properties of Cylindrical Shells," Journal of the Acoustic Society of America, Vol. 36, No. 9, 1964, pp. 1691-1698.

50. McGary, M.C.: "Sound Field Diffusivity in NASA Langley Research Center Hardwalled Acoustic Facilities," NASA Technical Memorandum 83275, March 1982.

51. Grosveld, F.W.: "Characteristics of the Transmission Loss Apparatus at NASA Langley Research Center," NASA Contractor Report 172153.

52. Bracewell,R.N.: The Fourier Transform and its Applications, McGraw-Hill Book Co., New York, 1978.

53. Hoel, P.G.: Introduction to Mathematical Statistics, John Wiley and Sons Inc., New York, 1947.

54. Papoulis, A.: Probability, Random Variables and Stochastic Processes, McGraw-Hill, New York, 1965.

55 Bendat, J.S.; Piersol, A.G.: Random Data: Analysis and Measurement Procedures, John Wiley and Sons Inc., New York, 1971.

56. Soedel, W.: Vibrations of Shells and Plates, Marcel Dekker Inc., New York, 1981.

57. Smith, P.W.; Lyon, R.H.:"Sound and Structural Vibration," NASA Contract Report 160, March, 1965.

58. Ugural, A.C.: Stresses in Plates and Shells, McGraw-Hill Book Co., New York, 1981.

59. Pierce, A. D.: Acoustics: An Introduction to Its Physical Principles and Applications, McGraw-Hill Book Co., New York, 1981.

60. Kinsler, L.E.; Frey, A.R.: Fundamentals of Acoustics, John Wiley and Sons Inc., New York, 1962.

61. Richards, E.J.; Mead D.J.: Noise and Acoustic Fatigue in Aeronautics, John Wiley and Sons Ltd., London, 1968.

62. Standard Mathematical Tables, 21st edition, The Chemical and Rubber Co., 1973.

63. Thompson, J.K.; Tree, D.R.: "Finite Difference Errors in Acoustic Intensity Measurements," Journal of Sound and Vibration, Vol. 75, No. 2, March, 1981, pp. 229-238.

64. Seybert, A. F.: "Statistical Errors in Acoustic Intensity Measurements," Journal of Sound and Vibration, Vol. 75, No. 4, April 1981, pp. 519-526.

65. Bockhoff, M.: "Some Remarks on the Continuous Sweeping Method in Sound Power Determination," Proceedings of INTER-NOISE 84, December, 1984, pp. 1173-1176.

Appendix I

BACKGROUND INFORMATION AND DEFINITIONS

A. FUTURE TRENDS IN AIRCRAFT DESIGN

Recent research on fuel efficient aircraft designs has focused on the new advanced turboprop (ATP) propulsion systems (sometimes called propfans) which have been proposed for future use in both the commercial and military fleets in the 1990's and beyond. A model of one of these advanced turboprop propulsion systems is shown in figure (AI-1). (See reference 3.) These propulsion systems were first proposed for use in high speed aircraft in 1974, and are characterized by their unusual number of blades (8 or more), their use of advanced airfoil design, and their use of highly swept blades (which reduce the blade tip Mach No. of the blades thereby increasing the propulsive efficiency of the design). They have since been the subject of numerous aircraft studies as a part of the NASA Aircraft Energy Efficiency Program. The results of these studies suggest that, through the use of these advanced turboprops, it may be possible to reduce the average fuel consumption of an 0.8 Mach No. advanced aircraft by 20 to 40 percent, when compared to aircraft equipped with high bypass turbofan engines of equivalent technology (see references 4 and 5). At the same time, one of the potentially severe problem areas that was identified in these studies was the probable high interior

noise levels that could be expected in an aircraft with this type of turboprop propulsion system.

Another technological development which is expected to have a dramatic impact on the future design of aircraft is the emergence of composites materials. Current composite applications to large transport aircraft include secondary structure such as the wings and empennage as well as fairings and nacelle components (see reference 6). Future aircraft can be expected to utilize significant quantities of composites in the primary structures as well. A recent study on an all composite fuselage which meets all the design requirements for a 1990's large transport aircraft estimated a 32 percent weight savings for the fuselage when compared to a baseline aluminum shell. (See reference 7.) Roughly 1/2 of this weight savings was in the design of skin panels alone.

The trends toward all composite fuselage structures is considerable cause for concern for the noise control engineer since relatively few studies have been performed to quantify the noise radiative properties of these materials (see references 8-14), and because the results of preliminary studies suggest that composites (because they are lighter) transmit airborne noise more readily than their metal counterparts. (See references 13-14). Preliminary studies also indicate that the noise transmissive properties

of composite panels are surprisingly sensitive to parameters such as panel lay-up or fiber orientation. (See reference 14.)

B. CHARACTERISTICS OF AIRBORNE PROPELLER NOISE

The sound pressure field produced by a propeller is characterized by its complex periodic nature. The pressure pulses produced by the propeller repeat themselves (with some unsteadiness) with each rotation of the propeller shaft. This periodic nature of the signal produces a sound pressure spectrum which consists of discrete tones, beginning with the fundamental blade passage frequency (propeller shaft rpm times the number of blades) which is lowest in frequency, followed by tones which have frequencies that are integer multiples of the fundmental (referred to as the propeller harmonics). An example of both the time history and the spectrum of the pressure signal which is produced by a ATP propulsion system is shown in figure (AI-2). (See reference 15.) The predicted and measured data in figure (AI-2) are for a two foot diameter model of an ATP tested at 0.8 Mach No. cruise speed. The propeller was mounted on top of an aircraft fuselage and microphones were flush mounted in the fuselage. As suggested by the data, the fundamental blade passage frequency (BPF) and the first few harmonics are the most significant of the tones. Aircraft interior noise studies have indicated that the higher harmonics

(tones with frequencies above the fifth harmonic of the BPF) are overwhelmed by other sources of noise in the cabin such as the turbulent boundary layer noise (see references 1-2). Thus, the crux of the propeller noise problems lies in the low frequency regime. And for nearly all propeller aircraft configurations presently under consideration, the fundamental and first few harmonics of the propeller BPF fall in the 0 - 1000 Hz frequency range.

Another important aspect of the sound pressure field produced by a propeller is its highly directional character. The spatial characteristics of the sound field show a strong preference for sound radiation in the plane of the propeller blades. Figure (AI-3) shows the spatial sound field distribution for a high speed propeller (ATP) in flight. (See reference 16.) Theoretical predictions and measurements such as these indicate that the vast majority of the sound which impinges on the fuselage of an aircraft is essentially confined to an area within one propeller diameter on either side of the plane of the propeller. Figure (AI-4) (from reference 17) shows that the preferred direction of radiation of a typical ATP is at an angle of roughly 45 degrees in the static configuration. The figure shows that the effect of forward flight is to move the region of peak radiation to a position in space that is close to the plane of the propeller. The effect of the boundary layer on the

fuselage wall is to further bend the apparent angle of incidence of the incoming sound waves. Thus, the apparent angle of incidence of the noise impinging on the fuselage is generally oblique. The wavelengths of the incoming sound waves are typically very long (1 to 3 meters) due to the low frequency character of the propeller noise. Thus, despite the fact that the angle of incidence of the waves is oblique, the distribution of pressure over the surface of the fuselage (with respect to phase) is slowly varying.

C. CHARACTERISTICS OF STRUCTUREBORNE PROPELLER NOISE

Since very few studies have been funded in the area of structureborne noise in propeller driven aircraft, the characteristics of structureborne noise are not as well understood and therefore are more difficult to generalize. Two separate studies recently completed by NASA and its contractors (references 18 and 19-21) and a third on-going study (reference 22), however, have identified two major contributors to the structureborne noise in propeller driven aircraft. Studies completed by Southwest Research Corporation (references 19-21) indicated that, at least on some single engine propeller aircraft, roughly 1/2 of the noise enters the aircraft cabin via vibrational energy that begins as engine vibration and propagates along the engine mounting system and into the aircraft cabin where it is ultimately radiated as noise. A second study performed in house at

NASA Langley Research Center (reference 18) indicated that on some wing mounted propeller airplanes, the propeller downwash effects on the wing can be a significant source of interior noise. The study suggests that the trailing vortices shed from the propeller tips collide with the wing on each rotation of the propeller shaft. This sets up vibration in the wings which propagates along a structural path into the aircraft cabin.

The frequency character of the structureborne noise is generally the same as the airborne noise. Both sources of noise manifest discrete frequency tones at the BPF and its harmonics. Past research on aircraft with reciprocating engines (see references 1-2) has shown that quite often, even the piston firing harmonics of the engine coincide in frequency with the propeller harmonics.

D. SEPARATION OF AIRBORNE AND STRUCTUREBORNE NOISE

Three measurement methods which have most recently been proposed for separation of airborne and structureborne noise in aircraft have included:

1) Measuring noise levels in the cabin with the engines running normally and with the engines detached. (See references 19-21.)

2) The conventional lead wrapping technique. (See references 18 and 23-24.)

3) The partial coherence function method. (See references 25-27.)

The obvious limitation of the first method is that the tests cannot be performed in flight. Detaching the engines may also prove to be a prohibitively expensive method for determining the relative contributions of the airborne and structureborne noises for a diverse fleet of aircraft.

Attempts to identify noise paths in aircraft using the second method (the lead wrapping technique) have been largely unsuccessful because of the poor transmission loss of lead at low frequencies. As discussed earlier, the distinguishing characteristic of the noise generated by a propeller is its low frequency tonal nature.

The use of partial and multiple coherence function methods to determine the principle noise paths in aircraft proves inadequate if the various noise generating mechanisms of the aircraft are fully coherent. Unfortunately, for many of the aircraft in question, the airborne and structureborne components are fully coherent since they both ultimately have the same source, viz. the propellers. Thus, because of the fully coherent nature of the noise propagated along these two paths, the problem of separating and predicting the relative contributions of the airborne and structureborne noises in propeller driven aircraft has remained largely unsolved.

E. ACOUSTIC QUANTITIES

$p(\vec{r},t)$ = instantaneous acoustic pressure as a function of position in space.

$\vec{v}(\vec{r},t)$ = instantaneous acoustic fluid particle velocity vector as a function of position.

$\vec{a}(\vec{r},t)$ = instantaneous acoustic fluid particle acceleration vector as a function of position.

F. FOURIER AND INVERSE FOURIER TRANSFORMS

The Fourier and inverse Fourier transforms shall be defined as

$$X(f) = F\{x(t)\} = \int_{-\infty}^{\infty} x(t)\, e^{-j2\pi ft}\, dt\ , \qquad \text{(A1.1)}$$

$$x(t) = F^{-1}\{X(f)\} = \int_{-\infty}^{\infty} X(f)\, e^{j2\pi ft}\, df\ . \qquad \text{(A1.2)}$$

G. FINITE FOURIER TRANSFORMS

In general

$$X(f) = F\{x(t)\} = \int_{0}^{T} x(t)\, e^{-j2\pi ft}\, dt\ . \qquad \text{(A1.3)}$$

The finite Fourier transform of the acoustic pressure is

given by

$$P(\vec{r},f) = F\{p(\vec{r},t)\} = \int_0^T p(\vec{r},t)\, e^{-j2\pi ft}\, dt \ . \qquad (A1.4)$$

The finite Fourier transform of the acoustic fluid particle velocity is given by

$$V(\vec{r},f) = F\{v(\vec{r},t)\} = \int_0^T v(\vec{r},t)\, e^{-j2\pi ft}\, dt \ . \qquad (A1.5)$$

The finite Fourier transform of the acoustic fluid particle acceleration is given by

$$A(\vec{r},t) = F\{a(\vec{r},t)\} = \int_0^T a(\vec{r},t)\, e^{-j2\pi ft}\, dt \ . \qquad (A1.6)$$

H. RELATIONSHIP BETWEEN VELOCITY AND ACCELERATION

$$\vec{a}(t) = d/dt\{\vec{v}(t)\} \ . \qquad (A1.7)$$

$$\vec{A}(f) = -j2\pi f\vec{V}(f) = j\omega\vec{V}(f) \ . \qquad (A1.8)$$

$$\vec{V}(f) = -j/(2\pi f)\ \vec{A}(f) = -j/\omega\ \vec{A}(f) \ . \qquad (A1.9)$$

I. AUTO CORRELATION FUNCTIONS

In general

$$R_{xx}(\tau) = \lim_{T\to\infty} 1/T \int_0^T x(t)x(t+\tau)\, dt \ . \qquad (A1.10)$$

An estimate of $R_{xx}(\tau)$ with finite data is

$$\tilde{R}_{xx}(\tau) = 1/(T-\tau) \int_0^{T-\tau} x(t)x(t+\tau)\, dt \ . \qquad \text{(A1.11)}$$

Important properties:

If the variable x(t) is real, then $R_{xx}(\tau)$ is a real, even function of τ.

J. CROSS CORRELATION FUNCTIONS

In general

$$R_{xy}(\tau) = \lim_{T\to\infty} \int_0^{T} x(t)y(t+\tau)\ dt \ . \qquad \text{(A1.12)}$$

An estimate of $R_{xy}(\tau)$ with finite data is

$$\tilde{R}_{xy}(\tau) = 1/(T-\tau) \int_0^{T-\tau} x(t)y(t+\tau)\, dt \ . \qquad \text{(A1.13)}$$

The cross correlation between acoustic pressure and fluid particle velocity is given by

$$R_{pv}(\tau) = \lim_{T\to\infty} 1/T \int_0^{T} p(t)v(t+\tau)\, dt \ . \qquad \text{(A1.14)}$$

Evaluating the preceding equation at $\tau=0$, one obtains

$$R_{pv}(0) = \lim_{T\to\infty} 1/T \int_0^{T} p(t)v(t)\ dt \ . \qquad \text{(A1.15)}$$

Important properties:

If variables x(t) and y(t) are real, $R_{xy}(\tau)$ is also real. $R_{xy}(\tau)$, in general, is neither an even nor an odd function of τ.

K. SPECTRAL DENSITY FUNCTIONS

The auto spectral density function is defined by

$$S_{xx}(f) = \int_{-\infty}^{\infty} R_{xx}(\tau)\, e^{-j2\pi f\tau}\, d\tau \ . \qquad \text{(A1.16)}$$

From the theory of Fourier transforms (see reference 52),

$$R_{xx}(\tau) = \int_{-\infty}^{\infty} S_{xx}(\tau)\, e^{j2\pi f\tau}\, df \ . \qquad \text{(A1.17)}$$

The cross spectral density function is defined by

$$S_{xy}(f) = \int_{-\infty}^{\infty} R_{xy}(\tau)\, e^{-j2\pi f\tau}\, d\tau \ . \qquad \text{(A1.18)}$$

From the theory of Fourier transforms (see reference 52),

$$R_{xy}(\tau) = \int_{-\infty}^{\infty} S_{xy}(f)\, e^{j2\pi f\tau}\, df \ . \qquad \text{(A1.19)}$$

Important properties:

Given that $R_{xx}(\tau)$ is a real function, $S_{xx}(f)$ is a real, even function of f. Given that $R_{xy}(\tau)$ is real, $S_{xy}(f)$ will, in general, be complex with its real part

being a even function of f and its imaginary part being an odd function of f. Note that $S_{xy}(f)$ is defined for both positive and negative frequencies. For practical problems of interest, negative frequencies have no physical interpretation.

L. ONE-SIDED AUTO SPECTRAL DENSITY FUNCTIONS

Recall that by definition

$$R_{xx}(\tau) = \int_{-\infty}^{\infty} S_{xx}(f)\, e^{j2\pi f\tau}\, df \ . \qquad \text{(A1.20)}$$

Given that $R_{xx}(\tau)$ and $S_{xx}(f)$ are both real, even functions

$$R_{xx}(\tau) = \int_{-\infty}^{\infty} S_{xx}(f)\, \cos(2\pi f\tau)\, df \ . \qquad \text{(A1.21)}$$

Since the integrand in (A1.21) is even,

$$R_{xx}(\tau) = 2 \int_{0}^{\infty} S_{xx}(f)\, \cos(2\pi f\tau)\, df$$

$$= \int_{0}^{\infty} 2S_{xx}(f)\, e^{j2\pi f\tau}\, df \ . \qquad \text{(A1.22)}$$

Thus it is convenient to define the one-sided auto spectral density as

$$G_{xx}(f) = 2S_{xx}(f) \qquad (0<f<\infty) \ . \tag{A1.23}$$

Thus,

$$R_{xx}(\tau) = \int_0^\infty G_{xx}(f)\, e^{j2\pi f\tau}\, df \ . \tag{A1.24}$$

And by a similar analysis,

$$G_{xx}(f) = 2 \int_{-\infty}^{\infty} R_{xx}(\tau)\, e^{-j2\pi f\tau}\, d\tau \ . \tag{A1.25}$$

M. ONE-SIDED CROSS SPECTRAL DENSITY FUNCTIONS

Recall that by definition

$$R_{xy}(\tau) = \int_{-\infty}^{\infty} S_{xy}(f)\, e^{j2\pi f\tau}\, df \ . \tag{A1.26}$$

Given that $R_{xy}(\tau)$ is real, it follows that

$$R_{xy}(\tau) = \int_{-\infty}^{\infty} \left[\mathrm{Re}\{S_{xy}\}\cos(2\pi f\tau) - \mathrm{Im}\{S_{xy}\}\sin(2\pi f\tau) \right] df$$

$$= \int_{-\infty}^{\infty} \mathrm{Re}\{S_{xy}(f)\}\cos(2\pi f\tau)\, df$$

$$- \int_{-\infty}^{\infty} \mathrm{Im}\{S_{xy}(f)\}\sin(2\pi f\tau)\, df \ . \tag{A1.27}$$

Now since $Re\{S_{xy}\}$ is even and $Im\{S_{xy}\}$ is odd,

$$R_{xy}(\tau) = \int_0^\infty 2Re\{S_{xy}(f)\}\cos(2\pi f\tau)\, df$$

$$- \int_0^\infty 2Im\{S_{xy}(f)\}\sin(2\pi f\tau)\, df \ . \qquad (A1.28)$$

Therefore,

$$R_{xy}(\tau) = \int_0^\infty 2S_{xy}(f)\, e^{j2\pi f\tau}\, df \ . \qquad (A1.29)$$

Thus, the one-sided cross spectral density is defined as

$$G_{xy}(f) = 2S_{xy}(f) \qquad (0<f<\infty) \ . \qquad (A1.30)$$

Therefore,

$$R_{xy}(\tau) = \int_0^\infty G_{xy}(f)\, e^{j2\pi f\tau}\, df \ . \qquad (A1.31)$$

And by a similar analysis

$$G_{xy}(f) = 2\int_{-\infty}^\infty R_{xy}(\tau)\, e^{-j2\pi f\tau}\, d\tau \ . \qquad (A1.32)$$

Furthermore, the co-spectral density $C_{xy}(f)$ and the quad-spectral density $Q_{xy}(f)$ are defined as

$$G_{xy}(f) = C_{xy}(f) - jQ_{xy}(f) \ , \qquad \text{(A1.33)}$$

where C_{xy} and Q_{xy} are both real so that

$$R_{xy}(\tau) =$$

$$\int_0^\infty \left[C_{xy}(f)\cos(2\pi f\tau) + Q_{xy}(f)\sin(2\pi f\tau) \right] df \ . \qquad \text{(A1.34)}$$

N. EXPECTED VALUE OPERATOR

The expected value of any real single valued continuous function g of the random variable x is defined as

$$E\{g(x)\} = \int_{-\infty}^{\infty} g(x)p(x)\, dx \ , \qquad \text{(A1.35)}$$

where p(x) is the probability density function of the random variable x. (See reference 53, pp. 28-34 or reference 54, pp. 83-97 and pp. 165-173 for a discussion of the probability density function of a random variable.)

O. ESTIMATION OF THE SPECTRAL DENSITY FUNCTIONS

The one-sided spectral density functions can be defined in terms of the Fourier transform as (see reference 55)

$$G_{xx}(f) = \lim_{T\to\infty} 2/T \ E\{X^*(f)X(f)\}, \qquad \text{(A1.36)}$$

and

$$G_{xy}(f) = \lim_{T\to\infty} 2/T \ E\{X^*(f)Y(f)\} \ . \qquad \text{(A1.37)}$$

Estimates of the spectral density functions are given by

$$\tilde{G}_{xx}(f) = 2/T \; |X(f)|^2 \; , \tag{A1.38}$$

and

$$\tilde{G}_{xy}(f) = 2/T \; \left[X^*(f)Y(f)\right] \; , \tag{A1.39}$$

where X(f) and Y(f) are Finite Fourier transforms.

P. ACOUSTIC INTENSITY

The instantaneous acoustic intensity vector at a point in space is defined by

$$\vec{I}(\vec{r},t) = p(\vec{r},t)\vec{v}(\vec{r},t) \; . \tag{A1.40}$$

The time averaged acoustic intensity vector is given by

$$\langle \vec{I}(\vec{r}) \rangle_t = \lim_{T\to\infty} 1/T \int_0^T p(\vec{r},t)\vec{v}(\vec{r},t) \; dt \; . \tag{A1.41}$$

Hence

$$\langle \vec{I}(\vec{r}) \rangle = \langle p(\vec{r})\vec{v}(\vec{r}) \rangle_t \; . \tag{A1.42}$$

Letting the spatial dependence be implicit and confining the analysis to the magnitudes of the vectors,

$$\langle I \rangle_t = \lim_{T\to\infty} 1/T \int_0^T p(t)v(t) \; dt \; . \tag{A1.43}$$

Recalling the definition of the cross correlation function

$$R_{pv}(\tau) = \lim_{T\to\infty} 1/T \int_0^T p(t)v(t+\tau)\, dt \ , \qquad \text{(A1.44)}$$

and substituting,

$$\langle I \rangle_t = R_{pv}(0) \ . \qquad \text{(A1.45)}$$

Recalling the definitions of the co-spectral and the quad-spectral density functions and their relation to the cross correlation function (equation (A1.34)),

$$R_{pv}(\tau) =$$

$$\int_0^\infty \left[C_{pv}(f)\cos(2\pi f\tau) + Q_{pv}(f)\sin(2\pi f\tau) \right] df \ , \qquad \text{(A1.46)}$$

and substituting $\tau=0$ into the last equation,

$$\langle I \rangle_t = R_{pv}(0) = \int_0^\infty C_{pv}(f)\, df = Re\{ \int_0^\infty G_{pv}(f)\ \ df\} \ . \qquad \text{(A1.47)}$$

Thus, the magnitude of the time averaged acoustic intensity vector is the real part of the cross spectrum between pressure and particle velocity summed over all frequencies.

Q. SOUND POWER

The instantaneous sound power, Π, radiated by a sound source is defined as

$$\Pi(t) = \iint \vec{I}(\vec{r},t)\cdot\vec{n}\ dS\ , \qquad (A1.48)$$

where $\vec{I}$ is the instantaneous acoustic intensity vector, $\vec{n}$ is a unit vector normal, and the integral is over a control surface enclosing the sound source. The time averaged sound power is given by

$$\langle\Pi\rangle_t = \lim_{T\to\infty} 1/T \int_0^T \Pi(t)\ dt$$

$$= \lim_{T\to\infty} 1/T \int_0^T \left[\iint \vec{I}\cdot\vec{n}\ dS \right] dt\ . \qquad (A1.49)$$

Interchanging the order of integration,

$$\langle\Pi\rangle_t = \iint \langle\vec{I}\cdot\vec{n}\rangle_t\ dS\ . \qquad (A1.50)$$

R. ACOUSTIC IMPEDANCE

The specific acoustic impedance, Z, is defined by

$$Z(\vec{r},f) = P(\vec{r},f)/V(\vec{r},f)\ . \qquad (A1.51)$$

Important properties:

In general, Z is complex and is a function of both frequency and position in space. At a great distance from the source of an acoustic disturbance, acoustic pressure and fluid particle velocity are in phase and $Z = \rho_o c_o$.

S. MEAN SQUARE SURFACE VELOCITY

The space-time averaged mean square surface velocity of a vibrating surface is given by

$$\langle v^2 \rangle_{r,t} = 1/S \iint \left[\lim_{T\to\infty} 1/T \int_0^T v^2(\vec{r},t)\, dt \right] dS \ , \qquad \text{(A1.52)}$$

where S is the surface area of the structure. Recalling the definition of the correlation function and substituting, the result is

$$\langle v^2 \rangle_{r,t} = 1/S \iint R_{vv}(0)\, dS = \left\langle \int_0^\infty G_{vv}(f)\ df \right\rangle_r \ . \qquad \text{(A1.53)}$$

T. ACOUSTIC RADIATION EFFICIENCY

The acoustic radiation efficiency of a vibrating surface, σ, is defined as

$$\sigma = \langle \Pi \rangle_t / (\rho_o c_o \langle v^2 \rangle_{r,t} S) \ . \qquad \text{(A1.54)}$$

Recall from section M. that $\langle \Pi \rangle_t$ is given by

$$\langle \Pi \rangle_t = \iint \langle \vec{I} \cdot \vec{n} \rangle_t \, dS = \langle \vec{I} \cdot \vec{n} \rangle_{r,t} S \ , \qquad \text{(A1.55)}$$

where the chosen control surface is the surface of the structure, and the intensity vector is measured at this surface. Substituting the previous result into the first equation of this section the result is

$$\sigma = \langle I_n \rangle_{r,t} / (\rho_o c_o \langle v^2 \rangle_{r,t}) \ , \qquad \text{(A1.56)}$$

where it should be understood that I_n represents the magnitude of the acoustic intensity vector measured normal to the vibrating surface of the structure.

U. CRITICAL FREQUENCY

The coincidence frequency is that frequency of vibration at which flexural waves in the plate travel (in a given direction) at the same speed as acoustic (compressional) waves in air. The critical frequency is that special case of the coincidence frequencies for which the wavelength of the flexural waves in the plate are also equal to the wavelength of the acoustic waves (which is the case of grazing incidence of the acoustic wave). The critical frequency is important because it is lowest in frequency of all the coincidence frequencies. The critical frequency for an infinite flat isotropic plate is given by the equation

$$f_c = c_o^2/(2\pi) \left[\rho h \, 12(1-\mu^2)/Eh^3 \right]^{1/2} , \qquad \text{(A1.57)}$$

where

c_o = the speed of sound in the acoustic medium,

ρ = the density of the plate material,

h = the plate thickness,

E = the modulus of elasticity (Young's modulus),

μ = Poisson's ratio for the plate material.

For an orthotropic or an anisotropic plate, the critical frequency depends on the direction of travel of the wave.

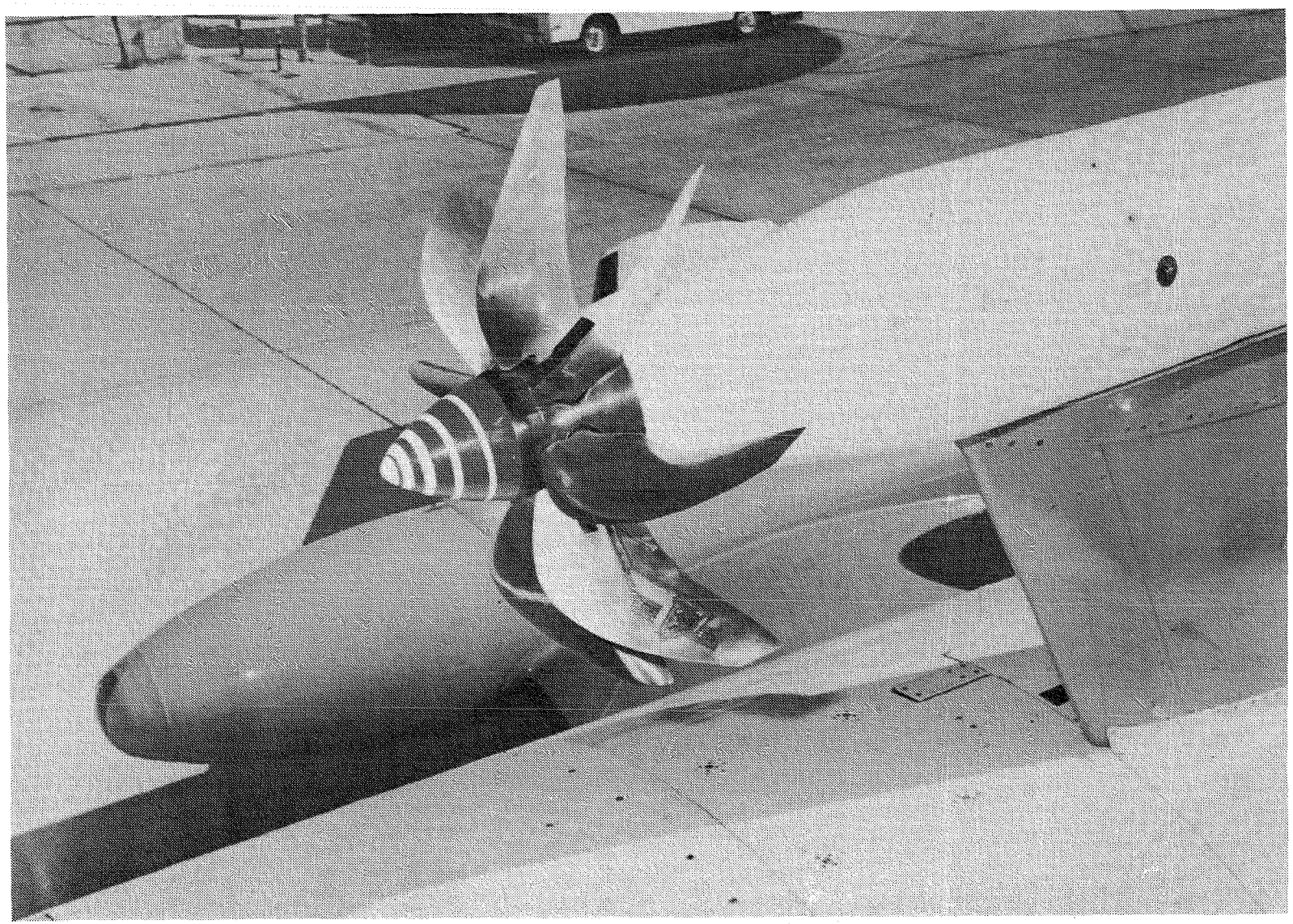

Figure (AI-1) -- Model of an advanced turboprop propulsion system (from reference 3).

ACOUSTIC SIGNATURE AND SPECTRUM OF AN ADVANCED PROPELLER

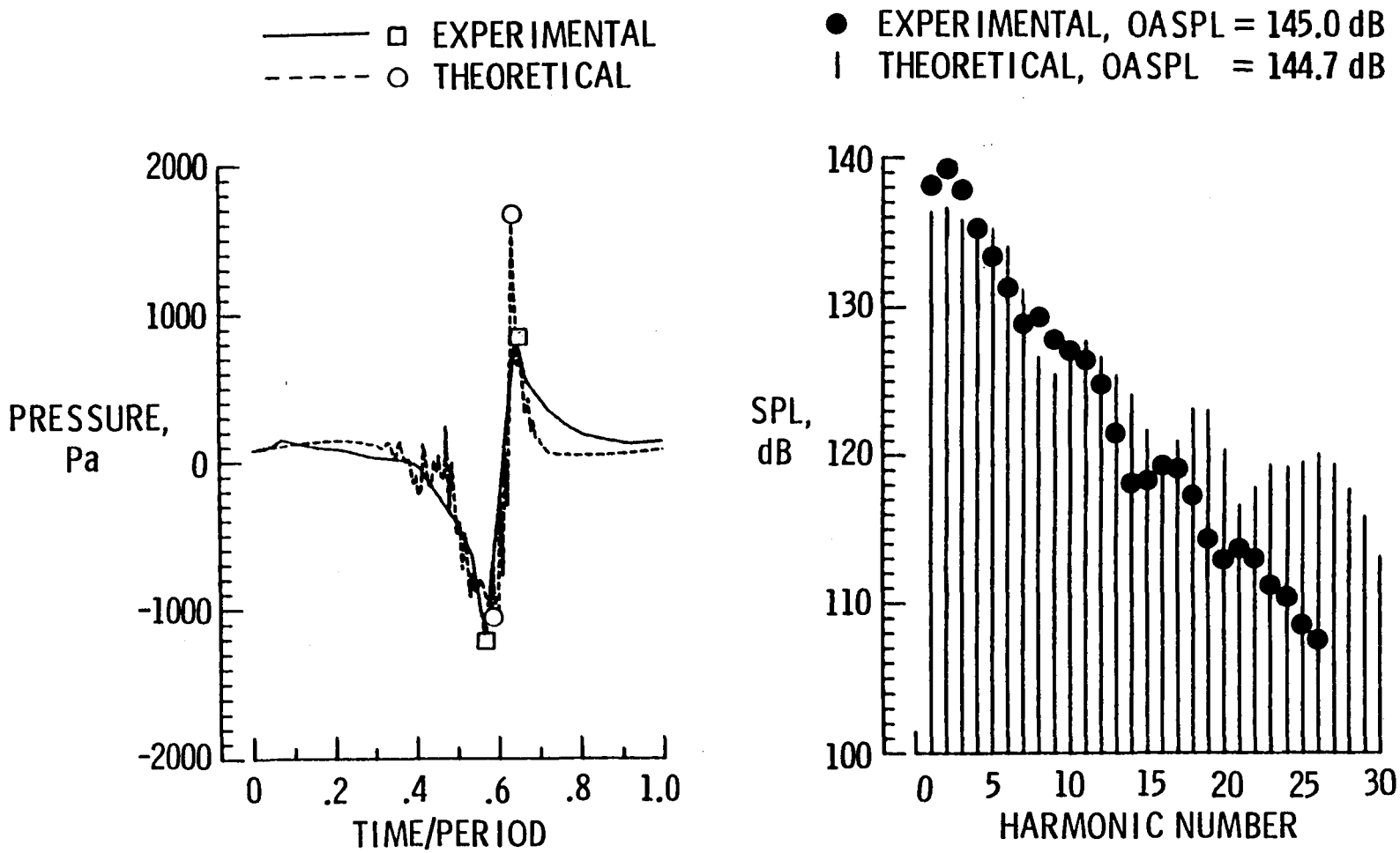

Figure (AI-2) -- Noise signature of an advanced turboprop in a quiet wind tunnel (from reference 15).

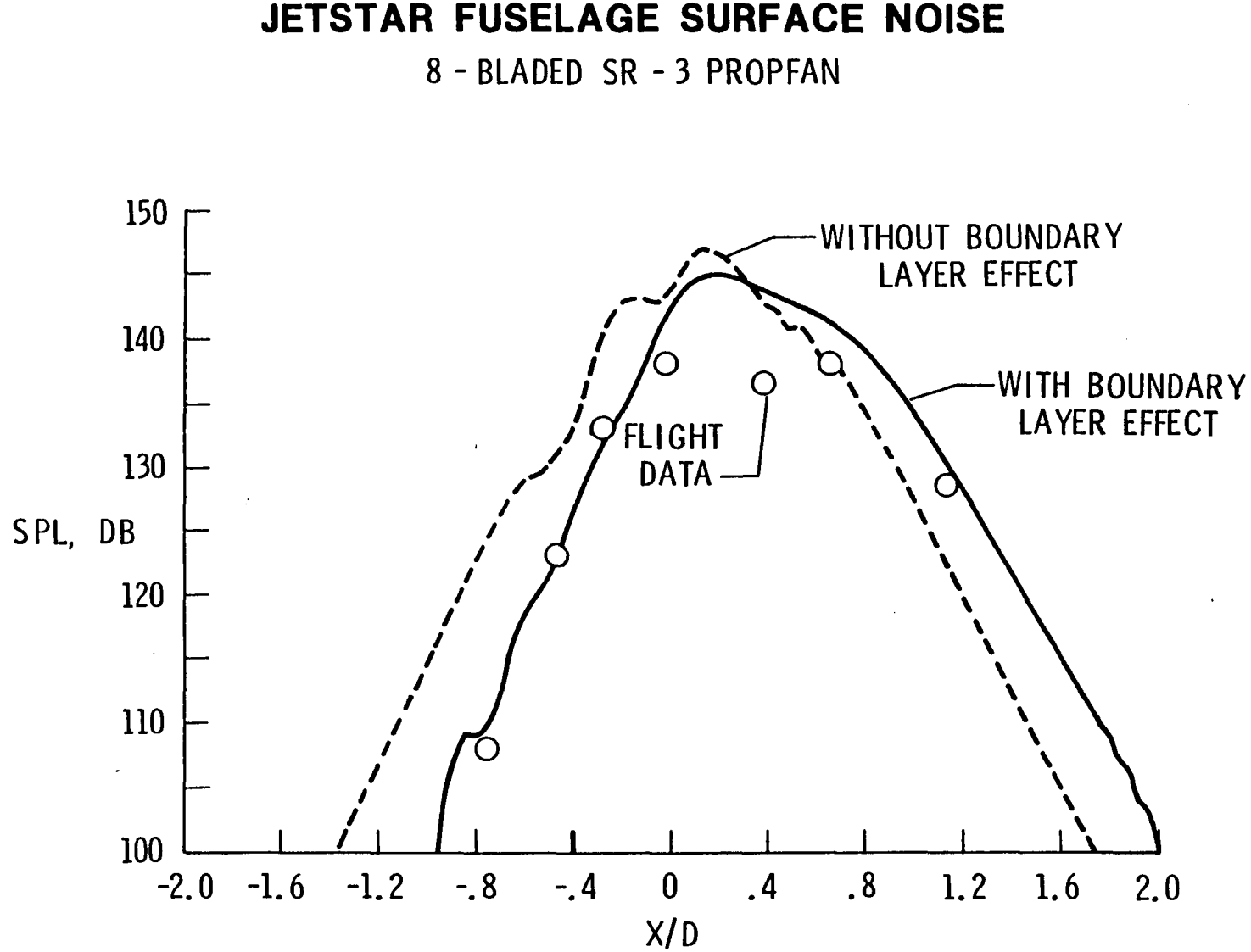

Figure (AI-3) -- Spatial sound field distribution for an advanced turboprop (from reference 16).

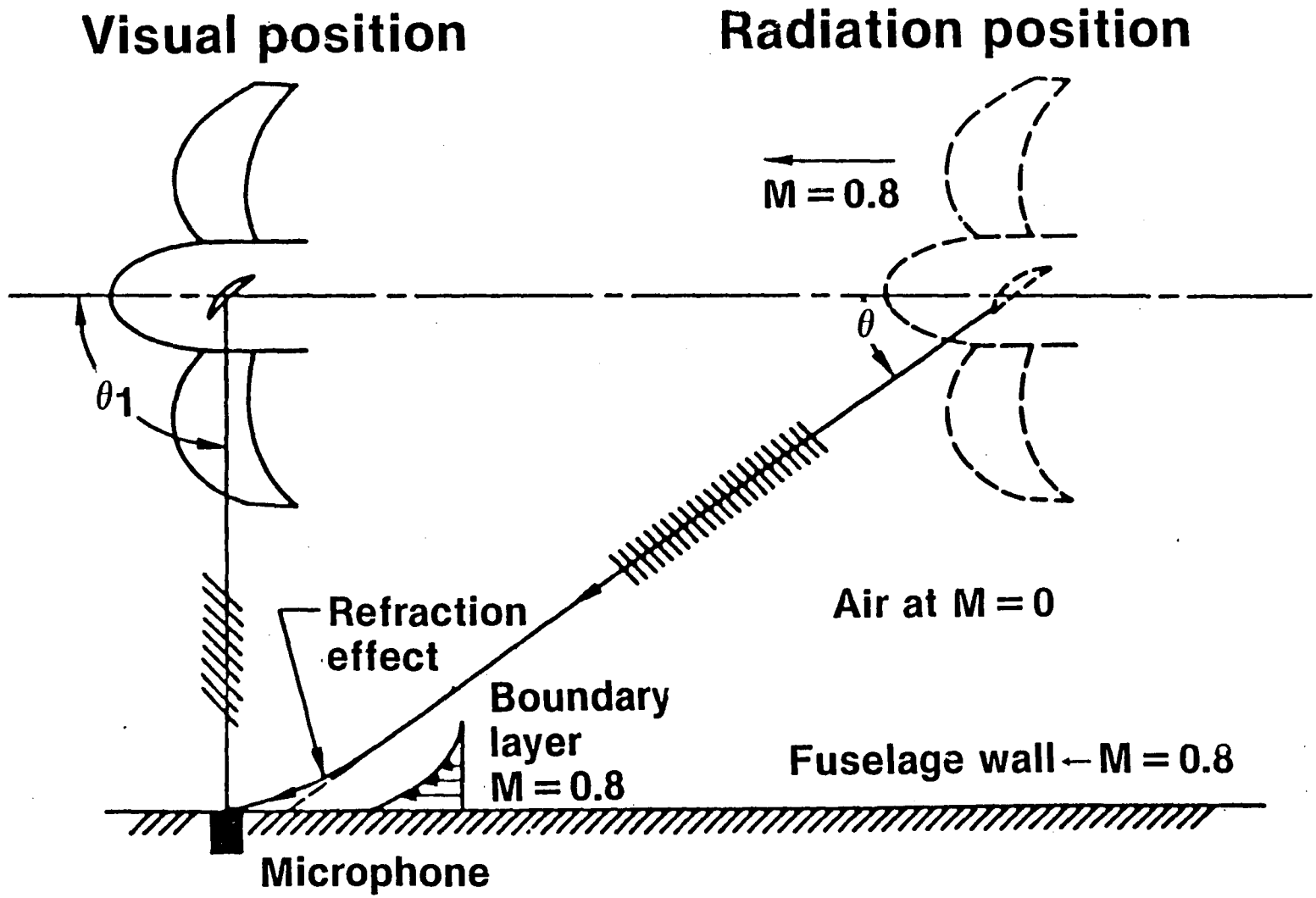

Figure (AI-4) -- Sound field directivity and angle of incidence for an advanced turboprop (from reference 17).

Appendix II

FREE VIBRATIONAL RESPONSE OF A SIMPLY SUPPORTED RECTANGULAR ORTHOTROPIC PLATE

A. GOVERNING DIFFERENTIAL EQUATION

The general free vibrational response of a thin shell structure is governed by the system of equations (see reference 56, eqn. 8.1.2)

$$-L_i(u_1,u_2,u_3) + \lambda_i \dot{u}_i + \rho h \ddot{u}_i = 0 \quad (i = 1,2,3) , \qquad (A2.1)$$

where $u_i = u_i(\alpha_1,\alpha_2,t)$.

L_i = linear stiffness operator for the ith equation.

α_i = coordinates in 3-D space for the shell or plate. $\alpha_1,\alpha_2,\alpha_3$ form an orthogonal curvilinear coordinate system with α_1 and α_2 being the surface coordinates located on the neutral surface and everywhere tangent to the midsurface of the shell. α_3 is everywhere outwardly normal to the shell.

u_i = displacement of the structure in the α_i direction.

ρ = mass per unit area of the shell.

h = thickness of the shell.

λ_i = equivalent viscous damping factor in the ith direction.

It is well known in the theory of vibration that the natural frequencies associated with the transverse (bending) vibrational mode shapes occur at much lower frequencies than their corresponding in plane (compressional) vibrational counterparts. (See reference 56, pg.97). It is also well known in the theory of sound radiation from structures that the transverse (bending) vibrational modes of the structure couple much more strongly to the sound field than their in plane (compressional) vibrational counterparts. (See reference 57, pg. 116). For these reasons we devote our attention solely to the transverse or flexural (bending) vibrational response of the structure. The system of equations then simplifies to a single equation, viz.,

$$-L_3(u_3) + \lambda\dot{u}_3 + \rho h\ddot{u}_3 = 0 \ . \qquad \text{(A2.2)}$$

B. FREE RESPONSE FOR THE UNDAMPED CASE

Consider a rectangular, orthotropic flat plate of dimensions d_1 and d_2 in the cartesian coordinate system $\alpha_1, \alpha_2, \alpha_3$. The stiffness operator L_3 (for flexure) in this case is given by (see reference 56, pp. 341-354, or reference 58, pp. 140-146)

$$-L_3 =$$

$$D_{11}\partial^4/\partial\alpha_1^4 + 2(D_{12}+2D_{66})\partial^4/\partial\alpha_1^2\partial\alpha_2^2 + D_{22}\partial^4/\partial\alpha_2^4 \ , \qquad \text{(A2.3)}$$

where the D_{ij} are the plate rigidity constants that relate the internal bending and twisting moments of the plate to the twists and curvatures they induce. For the flat orthotropic plate

$$D_{11} = h^3/12\ E_1/(1-\mu_1\mu_2)\ , \tag{A2.4}$$

$$D_{22} = h^3/12\ E_2/(1-\mu_1\mu_2)\ , \tag{A2.5}$$

$$D_{12} = h^3/12\ E_1\mu_2/(1-\mu_1\mu_2) = h^3/12\ E_2\mu_1/(1-\mu_1\mu_2)\ , \tag{A2.6}$$

$$D_{66} = h^3/12\ G\ , \tag{A2.7}$$

where

E_i = the effective modulus of elasticity (Young's modulus) in the ith direction,

μ_i = the effective Poisson's ratio in the ith direction,

G = the shear modulus of elasticity (modulus of rigidity),

h = is the thickness of the plate.

Thus the governing equation for the transverse vibration of a flat orthotropic plate is given by

$$D_{11}\partial^4u/\partial\alpha_1^4 + 2(D_{12}+2D_{66})\partial^4u/\partial\alpha_1^2\partial\alpha_2^2 + D_{22}\partial^4u/\partial\alpha_2^4$$

$$+\lambda\dot{u} + \rho h\ddot{u} = 0\ , \tag{A2.8}$$

where it should be understood that $u=u_3$. And if the damping term is temporarily neglected, the equation is

$$D_{11}\partial^4 u/\partial\alpha_1^4 + 2(D_{12}+2D_{66})\partial^4 u/\partial\alpha_1^2\partial\alpha_2^2 + D_{22}\partial^4 u/\partial\alpha_2^4 + \rho h\ddot{u} = 0 \ . \qquad \text{(A2.9)}$$

If the plate is simply supported on all four edges, the boundary conditions are zero displacement and zero bending moment along the edges. It can be shown that these two boundary conditions can be expressed as (see reference 56)

$$\text{at } \alpha_1 = 0, d_1 \qquad u = 0 \ , \qquad \text{(A2.10)}$$

$$\text{and} \qquad D_{11}\partial^2 u/\partial\alpha_1^2 + D_{12}\partial^2 u/\partial\alpha_2^2 = 0 \ , \qquad \text{(A2.11)}$$

$$\text{and at } \alpha_2 = 0, d_2 \qquad u = 0 \ , \qquad \text{(A2.12)}$$

$$\text{and} \qquad D_{12}\partial^2 u/\partial\alpha_1^2 + D_{22}\partial^2 u/\partial\alpha_2^2 = 0 \ . \qquad \text{(A2.13)}$$

It is well known in the theory of vibration that the general solution of the homogeneous partial differential equation is given by a series expansion in the natural modes of the structure, i.e.

$$u(\alpha_1,\alpha_2,t) = \sum_{i=1}^{\infty} \eta_i(t)\, U_i(\alpha_1,\alpha_2) \ , \qquad \text{(A2.14)}$$

where $\eta_i(t)$ are the modal participation factors, and

$U_i(\alpha_1,\alpha_2)$ are the eigenfunctions or modeshapes. In the case of the rectangular, simply supported, orthotropic flat plate, the eigenfunctions are given by

$$U_i(\alpha_1,\alpha_2) = U_{mn} = \sin(m\pi\alpha_1/d_1)\sin(n\pi\alpha_2/d_2) ,$$

$$m,n = 1,2,3,\ldots\infty , \qquad \text{(A2.15)}$$

and the modal participation factors are of the form

$$\eta_i(t) = \eta_{mn}\, e^{j(\omega_{mn}t+\theta_{mn})} , \qquad \text{(A2.16)}$$

where η_{mn} are the influence coefficients of the modes in units of displacement (determined by the initial conditions), ω_{mn} are the radian natural frequencies of the modes, and θ_{mn} are the phase angles associated with the modes (determined by the initial conditions). Thus, the general solution to the homogeneous partial differential equation is given by

$$u(\alpha_1,\alpha_2,t) =$$

$$\sum_{m=1}^{\infty}\sum_{n=1}^{\infty} \eta_{mn}\sin(m\pi\alpha_1/d_1)\sin(n\pi\alpha_2/d_2)e^{j(\omega_{mn}t+\theta_{mn})} . \qquad \text{(A2.17)}$$

And it is easily shown that this solution satisfies all of the simple support boundary conditions. Substituting this

solution into the governing partial differential equation of motion, one obtains

$$\sum_{m=1}^{\infty}\sum_{n=1}^{\infty}\Big[\, D_{11}(m\pi/d_1)^4 + 2(D_{12}+2D_{66})(m\pi/d_1)^2(n\pi/d_2)^2 + D_{22}(n\pi/d_2)^4 - \omega_{mn}^2\rho h \,\Big]\, \eta_{mn}\sin(m\pi\alpha_1/d_1)\sin(n\pi\alpha_2/d_2) \cdot e^{j(\omega_{mn}t+\theta_{mn})} = 0 \,. \qquad \text{(A2.18)}$$

If the series is zero for arbitrary values of η_{mn} and θ_{mn}, then each coefficient in the series must be identically zero. Thus

$$D_{11}(m\pi/d_1)^4 + 2(D_{12}+2D_{66})(m\pi/d_1)^2(n\pi/d_2)^2 + D_{22}(n\pi/d_2)^4 - \omega_{mn}^2\rho h = 0 \,. \qquad \text{(A2.19)}$$

Rearranging this last equation algebraically,

$$\omega_{mn}^2 = \pi^4/\rho h \cdot \Big[\, D_{11}(m/d_1)^4 + 2(D_{12}+2D_{66})(m/d_1)^2(n/d_2)^2 + D_{22}(n/d_2)^4 \,\Big] \,, \qquad \text{(A2.20)}$$

where the ω_{mn} are the radian natural frequencies of the plate.

C. FREE RESPONSE FOR THE DAMPED CASE

Now returning to the governing equation and reinstating the damping term,

$$D_{11}\partial^4 u/\partial\alpha_1^4 + 2(D_{12}+2D_{66})\partial^4 u/\partial\alpha_1^2\partial\alpha_2^2 + D_{22}\partial^4 u/\partial\alpha_2^4$$

$$+\lambda\dot{u} + \rho h\ddot{u} = 0 \ . \qquad \text{(A2.21)}$$

Now define the modal damping coefficient as

$$\xi_{mn} = \lambda/(2\rho h\omega_{mn}) \ . \qquad \text{(A2.22)}$$

Substituting into the governing equation, one obtains

$$D_{11}\partial^4 u/\partial\alpha_1^4 + 2(D_{12}+2D_{66})\partial^4 u/\partial\alpha_1^2\partial\alpha_2^2 + D_{22}\partial^4 u/\partial\alpha_2^4$$

$$+\rho h 2\xi_{mn}\omega_{mn}\dot{u} + \rho h\ddot{u} = 0 \ . \qquad \text{(A2.23)}$$

We now assume a solution of the form

$$u(\alpha_1,\alpha_2,t) =$$

$$\sum_{m=1}^{\infty}\sum_{n=1}^{\infty} \eta_{mn}\sin(m\pi\alpha_1/d_1)\sin(n\pi\alpha_2/d_2)\, e^{\gamma t + j\theta_{mn}} \ , \qquad \text{(A2.24)}$$

where γ may be complex. Substituting into the governing equation,

$$\sum_{m=1}^{\infty}\sum_{n=1}^{\infty} \Big[D_{11}(m\pi/d_1)^4 + 2(D_{12}+2D_{66})(m\pi/d_1)^2(n\pi/d_2)^2$$

$$+ D_{22}(n\pi/d_2)^4 + \rho h 2\xi_{mn}\omega_{mn}\gamma + \rho h\gamma^2 \Big]$$

$$\cdot \eta_{mn}\sin(m\pi/d_1)\sin(n\pi/d_2) = 0 \ . \qquad \text{(A2.25)}$$

Now recall from section B that

$$\rho h\omega_{mn}^2 = D_{11}(m\pi/d_1)^4$$

$$+ 2(D_{12}+2D_{66})(m\pi/d_1)^2(n\pi/d_2)^2 + D_{22}(n\pi/d_2)^4 \ . \qquad \text{(A2.26)}$$

Substituting, the result is

$$\sum_{m=1}^{\infty} \sum_{n=1}^{\infty} \left[\rho h\omega_{mn}^2 + \rho h 2\xi_{mn}\omega_{mn}\gamma + \rho h\gamma^2 \right]$$

$$\cdot \eta_{mn}\sin(m\pi\alpha_1/d_1)\sin(n\pi\alpha_2/d_2) = 0 \ . \qquad \text{(A2.27)}$$

Therefore, for arbitrary influence coefficients η_{mn}, it must be that

$$\rho h\omega_{mn}^2 + \rho h 2\xi_{mn}\omega_{mn}\gamma + \rho h\gamma^2 = 0 \ , \qquad \text{(A2.28)}$$

or

$$\gamma^2 + 2\xi_{mn}\omega_{mn}\gamma + \omega_{mn}^2 = 0 \ . \qquad \text{(A2.29)}$$

Solving this quadratic,

$$\gamma = -\xi_{mn}\omega_{mn} \pm \left[\xi_{mn}^2\omega_{mn}^2 - \omega_{mn}^2 \right]^{1/2} \ , \qquad \text{(A2.30)}$$

or

$$\gamma = -\xi_{mn}\omega_{mn} \pm j\omega_{mn} \left[1-\xi_{mn}^2 \right]^{1/2} \ . \qquad \text{(A2.31)}$$

Now define the damped radian natural frequencies as

$$\Omega_{mn} = \omega_{mn} \left[1-\xi_{mn}^2 \right]^{1/2} . \qquad \text{(A2.32)}$$

The general solution to the damped free vibration problem will then be

$$u(\alpha_1,\alpha_2,t) =$$

$$\sum_{m=1}^{\infty}\sum_{n=1}^{\infty} \eta_{mn}\sin(m\pi\alpha_1/d_1)\sin(n\pi\alpha_2/d_2)$$

$$\cdot\, e^{-\xi_{mn}\omega_{mn}t}\, e^{j(\Omega_{mn}t+\theta_{mn})} . \qquad \text{(A2.33)}$$

Appendix III

FORCED VIBRATIONAL RESPONSE OF A SIMPLY SUPPORTED RECTANGULAR ORTHOTROPIC PLATE

A. GOVERNING DIFFERENTIAL EQUATION

The general forced vibrational response of a simply supported, rectangular orthotropic plate is governed by the non-homogeneous partial differential equation

$$D_{11}\partial^4 u/\partial\alpha_1^4 + 2(D_{12} + 2D_{66})\partial^4 u/\partial\alpha_1^2\partial\alpha_2^2 + D_{22}\partial^4 u/\partial\alpha_2^4 + \lambda\dot{u} + \rho h\ddot{u} = q(\alpha_1,\alpha_2,t) \ . \qquad \text{(A3.1)}$$

B. DEFINITION OF THE FORCING FUNCTION

For the purposes of this study, the forcing function shall be defined as a normally incident (90° angle of incidence) acoustic plane wave impinging on the surface of the plate (refered to as the airborne component) combined simultaneously with a point vibrational input (referred to as the structureborne component). For this special case, the acoustic (airborne) input will be modeled as a simple harmonic forcing function, uniformly distributed over the surface of the plate and the vibrational (structureborne) input will be modeled as a simple harmonic forcing function, located at a discrete point on the plate. Thus, the right side of the governing equation is

$$q(\alpha_1,\alpha_2,t) =$$

$$\left[f_s\, e^{-j\phi_s}\, \delta(\alpha_1-c_1)\delta(\alpha_2-c_2) + f_a\, e^{-j\phi_a} \right] e^{j\omega t} \quad . \qquad \text{(A3.2)}$$

where

f_s = the magnitude of the structureborne input (units of force),

ϕ_s = the relative phase of the structureborne input,

f_a = the magnitude of the airborne input (units of force per area),

ϕ_a = the relative phase of the airborne input,

c_1 = the location of the point vibrational input in the α_1 coordinate direction,

c_2 = the location of the point vibrational input in the α_1 coordinate direction,

ω = the radian frequency of the simple harmonic forcing function,

and the symbol δ denotes the dirac delta function. Expanding this forcing function into a series representation,

$$\left[f_s\, e^{-j\phi_s}\, \delta(\alpha_1-c_1)\delta(\alpha_2-c_2) + f_a\, e^{-j\phi_a} \right] =$$

$$\sum_{k=1}^{\infty} \sum_{l=1}^{\infty} q_{kl} \sin(k\pi\alpha_1/d_1)\sin(l\pi\alpha_2/d_2) \quad . \qquad \text{(A3.3)}$$

Multiplying the equation by $\sin(m\pi\alpha_1/d_1)$

$\cdot \sin(n\pi\alpha_2/d_2)$ and integrating over the plate area

$$\int_0^{d_1}\int_0^{d_2}\left[f_s\, e^{-j\phi_s}\, \delta(\alpha_1 - c_1)\delta(\alpha_2 - c_2) + f_a\, e^{-j\phi_a} \right]$$

$$\cdot \sin(m\pi\alpha_1/d_1)\sin(n\pi\alpha_2/d_2)\, d\alpha_1 d\alpha_2 =$$

$$\sum_{k=1}^{\infty}\sum_{l=1}^{\infty} q_{kl} \int_0^{d_1}\int_0^{d_2} \sin(k\pi\alpha_1/d_1)\sin(l\pi\alpha_2/d_2)$$

$$\cdot \sin(m\pi\alpha_1/d_1)\sin(n\pi\alpha_2/d_2)\, d\alpha_1 d\alpha_2 \,. \qquad \text{(A3.4)}$$

Integrating the left side of the equation and using the orthogonality principle on the right side of the equation,

$$q_{mn} = 4f_s\, e^{-j\phi_s}/(d_1 d_2)\, \sin(m\pi c_1/d_1)\sin(n\pi c_2/d_2)$$

$$+ 4f_a\, e^{-j\phi_a}/(mn\pi^2)\, (1-\cos(m\pi))(1-\cos(n\pi)) \,. \qquad \text{(A3.5)}$$

Thus, the forcing function becomes

$$q(\alpha_1,\alpha_2,t) =$$

$$\sum_{m=1}^{\infty}\sum_{n=1}^{\infty}\left[\left[4f_s\, e^{-j\phi_s}/(d_1 d_2)\, \sin(m\pi c_1/d_1)\sin(n\pi c_2/d_2) \right.\right.$$

$$\left.\left. + 4f_a\, e^{-j\phi_a}/(mn\pi^2)\, (1-\cos(m\pi))(1-\cos(n\pi)) \right]\right.$$

$$\left.\cdot \sin(m\pi\alpha_1/d_1)\sin(n\pi\alpha_2/d_2) \right] e^{j\omega t} \,. \qquad \text{(A3.6)}$$

C. STEADY STATE RESPONSE TO THE FORCING FUNCTION

Now assume a solution of the form

$$u(\alpha_1,\alpha_2,t) =$$

$$\sum_{m=1}^{\infty}\sum_{n=1}^{\infty} \eta_{mn}\sin(m\pi\alpha_1/d_1)\sin(n\pi\alpha_2/d_2)\, e^{j(\omega t-\theta_{mn})} \qquad (A3.7)$$

where the transient (complementary) solution has been neglected, since it exponentially damps out to zero, and only the steady state (particular) solution is considered. Substituting this solution into the governing equation and equating the coefficients of the resultant series,

$$(\rho h\omega_{mn}+\rho h2\xi_{mn}\omega_{mn}(j\omega)-\rho h\omega^2)\ \eta_{mn}\ e^{-j\theta_{mn}} =$$

$$4f_s\ e^{-j\phi_s}/(d_1d_2)\ \sin(m\pi c_1/d_1)\sin(n\pi c_2/d_2)$$

$$+\ 4f_a\ e^{-j\phi_a}/(mn\pi^2)\ (1-\cos(m\pi))(1-\cos(n\pi))\ . \qquad (A3.8)$$

Now utilizing the theory of complex variables, redefine the first term in brackets in the previous equation as

$$(\rho h\omega_{mn}+\rho h2\xi_{mn}(j\omega)-\rho h\omega^2) =$$

$$\rho h\omega_{mn}\left[\ (1-\omega^2/\omega_{mn}^2)^2 + (2\xi_{mn}\omega/\omega_{mn})^2\ \right]^{1/2} e^{j\gamma_{mn}}\ , \qquad (A3.9)$$

where the phase angle γ_{mn} is defined to be

$$\gamma_{mn} = \tan^{-1}\left[(2\xi_{mn}\omega/\omega_{mn})/(1-\omega^2/\omega_{mn}^2) \right] . \qquad (A3.10)$$

Dividing through by this term, the equation for the modal influence coefficients is seen to be

$$\eta_{mn}\, e^{-j\theta_{mn}} = \left[s_{mn}\, e^{-j\phi_s} + a_{mn}\, e^{-j\phi_a} \right] e^{-j\gamma_{mn}} \qquad (A3.11)$$

where

$$s_{mn} = 4f_s/(d_1 d_2 \rho h \omega_{mn}) \sin(m\pi c_1/d_1)\sin(n\pi c_2/d_2)$$

$$/ \left[(1-\omega^2/\omega_{mn}^2)^2 + (2\xi_{mn}\omega/\omega_{mn})^2 \right]^{1/2} , \qquad (A3.12)$$

and

$$a_{mn} = 4f_a/(mn\pi^2 \rho h \omega_{mn}) \left[(1-\cos(m\pi))(1-\cos(n\pi)) \right]$$

$$/ \left[(1-\omega^2/\omega_{mn}^2)^2 + (2\xi_{mn}\omega/\omega_{mn})^2 \right]^{1/2} . \qquad (A3.13)$$

Thus, the steady state solution of the problem is

$$u(\alpha_1,\alpha_2,t) = \sum_{m=1}^{\infty} \sum_{n=1}^{\infty} \left[s_{mn}\, e^{-j\phi_s} + a_{mn}\, e^{-j\phi_a} \right]$$

$$\cdot \sin(m\pi\alpha_1/d_1)\sin(n\pi\alpha_2/d_2)\, e^{j(\omega t-\gamma_{mn})} . \qquad (A3.14)$$

D. TRANSVERSE VIBRATIONAL VELOCITY OF THE PLATE

The transverse vibrational velocity of the plate is defined by the relation

$$v(\alpha_1,\alpha_2,t) = d/dt\{u(\alpha_1,\alpha,t)\}, \tag{A3.15}$$

thus

$$v(\alpha_1,\alpha_2,t) =$$

$$\sum_{m=1}^{\infty}\sum_{n=1}^{\infty}\left[j\omega \left[s_{mn}\, e^{-j\phi_s} + a_{mn}\, e^{-j\phi_a} \right] \right.$$

$$\left. \cdot \sin(m\pi\alpha_1/d_1)\sin(n\pi\alpha_2/d_2)\, e^{j(\omega t-\gamma_{mn})} \right]. \tag{A3.16}$$

Rearranging this last equation, and recalling that

$$U_{mn} = \sin(m\pi\alpha_1/d_1)\sin(n\pi\alpha_2/d_2), \tag{A3.17}$$

the equation for the velocity becomes

$$v(\alpha_1,\alpha_2,t) =$$

$$\sum_{m=1}^{\infty}\sum_{n=1}^{\infty} \omega\left[s_{mn}e^{-j\phi_s} + a_{mn}e^{-j\phi_a} \right] U_{mn}e^{j(\omega t-\gamma_{mn}+\pi/2)}$$

$$= \sum_{m=1}^{\infty}\sum_{n=1}^{\infty} \omega\, \eta_{mn}e^{-j\theta_{mn}}\, U_{mn}\, e^{j(\omega t+\pi/2)}. \tag{A3.18}$$

Appendix IV

POWER FLOW FOR COMBINED AIRBORNE AND STRUCTUREBORNE INPUTS TO A SIMPLY SUPPORTED RECTANGULAR ORTHOTROPIC PLATE

A. SPACE-TIME AVERAGED MEAN SQUARE SURFACE VELOCITY

In Appendix III, it was found that the velocity of the plate is given by

$$v(\alpha_1,\alpha_2,t) =$$

$$\sum_{m=1}^{\infty}\sum_{n=1}^{\infty} \omega\eta_{mn}\, e^{-j\theta_{mn}}\, U_{mn}\, e^{j(\omega t+\pi/2)} \quad . \tag{A4.1}$$

Now from the theory of complex variables, the time averaged mean square value of the surface velocity, (which is simple harmonic in character) is given by

$$\langle v^2(\alpha_1,\alpha_2)\rangle_t = 1/2\ \mathrm{Re}\{v^*(\alpha_1,\alpha_2,t)\cdot v(\alpha_1,\alpha_2,t)\}$$

$$= 1/2 \left[\sum_{k=1}^{\infty}\sum_{l=1}^{\infty} \omega\eta_{kl}\, e^{+j\theta_{kl}}\, U_{kl}(\alpha_1,\alpha_2) \right] e^{-j(\omega t+\pi/2)}$$

$$\cdot \left[\sum_{m=1}^{\infty}\sum_{n=1}^{\infty} \omega\eta_{mn}\, e^{-j\theta_{mn}}\, U_{mn}(\alpha_1,\alpha_2) \right] e^{+j(\omega t+\pi/2)}$$

$$= 1/2 \left[\sum_{k=1}^{\infty}\sum_{l=1}^{\infty} \omega\eta_{kl}\, e^{+j\theta_{kl}}\, U_{kl}(\alpha_1,\alpha_2) \right]$$

$$\cdot \left[\sum_{m=1}^{\infty}\sum_{n=1}^{\infty} \omega\eta_{mn}\, e^{-j\theta_{mn}}\, U_{mn}(\alpha_1,\alpha_2) \right] . \tag{A4.2}$$

$$\langle v^2(\alpha_1,\alpha_2)\rangle_t = \omega^2/2 \sum_{k=1}^{\infty} \sum_{l=1}^{\infty} \sum_{m=1}^{\infty} \sum_{n=1}^{\infty}$$

$$\left[\eta_{kl}\, e^{+j\theta_{kl}}\, \eta_{mn}\, e^{-j\theta_{mn}}\, U_{kl}(\alpha_1,\alpha_2)\cdot U_{mn}(\alpha_1,\alpha_2) \right] . \qquad \text{(A4.3)}$$

Now finding the space averaged mean square surface velocity

$$\langle v^2(\alpha_1,\alpha_2,t)\rangle_{r,t} = 1/S \int_0^{d_2}\int_0^{d_1} \langle v^2(\alpha_1,\alpha_2,t)\rangle_t \, d\alpha_1 d\alpha_2$$

$$= \omega/2 \sum_{k=1}^{\infty} \sum_{l=1}^{\infty} \sum_{m=1}^{\infty} \sum_{n=1}^{\infty} \left[\eta_{kl}\, e^{+j\theta_{kl}}\, \eta_{mn}\, e^{-j\theta_{mn}} \right.$$

$$\left. \cdot\ 1/S \int_0^{d_2}\int_0^{d_1} U_{kl}(\alpha_1,\alpha_2)\cdot U_{mn}(\alpha_1,\alpha_2)\ d\alpha_1 d\alpha_2 \right] . \qquad \text{(A4.4)}$$

Now recalling the definitions of U_{kl} and U_{mn},

$$\int_0^{d_2}\int_0^{d_1} U_{kl}(\alpha_1,\alpha_2)\ U_{mn}(\alpha_1,\alpha_2)\ d\alpha_1 d\alpha_2$$

$$= \int_0^{d_1} \sin(k\pi\alpha_1/d_1)\sin(m\pi\alpha_1/d_1)\ d\alpha_1$$

$$\cdot \int_0^{d_2} \sin(l\pi\alpha_2/d_2)\sin(n\pi\alpha_2/d_2)\ d\alpha_2 . \qquad \text{(A4.5)}$$

Utilizing the principle of orthogonality, it can be seen that the integral over the eigenfunctions is identically zero in all cases except the single case where k=m and l=n. Therefore, all of the terms in the series expansion are zero except those terms where k=m and l=n. Thus, the series over k, l, m, and n, is simplified to a double series summing over m and n as follows:

$$\langle v^2(\alpha_1,\alpha_2,t)\rangle_{r,t} =$$

$$\omega^2/2 \sum_{m=1}^{\infty} \sum_{n=1}^{\infty} \left[\eta_{mn}\, e^{+j\theta_{mn}}\, \eta_{mn}\, e^{-j\theta_{mn}} \cdot 1/S \right.$$

$$\left. \cdot \int_0^{d_1} \sin^2(m\pi\alpha_1/d_1)\, d\alpha_1 \int_0^{d_2} \sin^2(n\pi\alpha_2/d_2)\, d\alpha_2 \right] . \qquad \text{(A4.6)}$$

Evaluating the integrals and noting that $S = d_1 d_2$,

$$\langle v^2(\alpha_1,\alpha_1,t)\rangle_{r,t} =$$

$$\omega^2/8 \sum_{m=1}^{\infty} \sum_{n=1}^{\infty} \eta_{mn}\, e^{+j\theta_{mn}}\, \eta_{mn}\, e^{-j\theta_{mn}} . \qquad \text{(A4.7)}$$

Now substituting from Appendix III for the values of the influence coefficients for the case of combined airborne and structureborne inputs,

$$\langle v^2 \rangle_{r,t} =$$

$$\omega^2/8 \sum_{m=1}^{\infty} \sum_{n=1}^{\infty} \left[s_{mn}\, e^{+j\phi_s} + a_{mn}\, e^{+j\phi_a} \right] e^{+j\gamma_{mn}}$$

$$\cdot \left[s_{mn}\, e^{-j\phi_s} + a_{mn}\, e^{-j\phi_a} \right] e^{-j\gamma_{mn}}. \qquad \text{(A4.8)}$$

Multiplying out terms and simplifying,

$$\langle v^2 \rangle_{r,t} = \omega^2/8 \cdot$$

$$\sum_{m=1}^{\infty} \sum_{n=1}^{\infty} \left[s_{mn}^2 + a_{mn}^2 + 2 s_{mn} a_{mn} \cos(\phi_s - \phi_a) \right] . \qquad \text{(A4.9)}$$

Now define the following terms

$$\langle v_s^2 \rangle_{r,t} = \omega^2/8 \sum_{m=1}^{\infty} \sum_{n=1}^{\infty} s_{mn}^2 . \qquad \text{(A4.10)}$$

$$\langle v_a^2 \rangle_{r,t} = \omega^2/8 \sum_{m=1}^{\infty} \sum_{n=1}^{\infty} a_{mn}^2 . \qquad \text{(A4.11)}$$

$$\langle v_{sxa}^2 \rangle_{r,t} = \omega^2/8 \sum_{m=1}^{\infty} \sum_{n=1}^{\infty} 2 s_{mn} a_{mn} \cos(\phi_s - \phi_a) . \qquad \text{(A4.12)}$$

Thus, it can be easily seen that

$$\langle v^2 \rangle_{r,t} = \langle v_s^2 \rangle_{r,t} + \langle v_a^2 \rangle_{r,t} + \langle v_{sxa}^2 \rangle_{r,t} . \qquad \text{(A4.13)}$$

B. POWER INPUT

Recall from Appendix III that the forcing function is of the form

$$q(\alpha_1,\alpha_2,t) = \left[f_s\, e^{-j\phi_s}\, \delta(\alpha_1-c_1)\delta(\alpha_2-c_2) + f_a\, e^{-j\phi_a} \right] e^{j\omega t} \quad . \tag{A4.14}$$

The velocity produced by this input was given by

$$v(\alpha_1,\alpha_2,t) = \sum_{m=1}^{\infty} \sum_{n=1}^{\infty} \omega \left[s_{mn}\, e^{-j\phi_s} + a_{mn}\, e^{-j\phi_a} \right] \cdot U_{mn}\, e^{j(\omega t-\gamma_{mn}+\pi/2)} \quad . \tag{A4.15}$$

Now the total time averaged power input to the plate is given by

$$\langle \dot{W}(t) \rangle_t = \left\langle \int_0^{d_2} \int_0^{d_1} \vec{F}\cdot\vec{V}\, d\alpha_1 d\alpha_2 \right\rangle_t$$

$$= \lim_{T\to\infty} 1/T \int_0^T \left[\int_0^{d_2} \int_0^{d_1} \mathrm{Re}\{q(\vec{r},t)\}\mathrm{Re}\{v(\vec{r},t)\}\, d\alpha_1 d\alpha_2 \right] dt$$

$$= \int_0^{d_2} \int_0^{d_1} 1/2\ \mathrm{Re}\{q^*(\vec{r},t)v(\vec{r},t)\}\, d\alpha_1 d\alpha_2 \quad . \tag{A4.16}$$

Substituting the appropriate expressions

$$\langle \dot{W}(t) \rangle_t =$$

$$< \int_0^{d_2} \int_0^{d_1} 1/2 \; Re\{ \left[f_s \, e^{+j\phi_s} \, \delta(\alpha_1 - c_1)\delta(\alpha_2 - c_2) + f_a \, e^{+j\phi_a} \right]$$

$$\cdot e^{-j\omega t} \sum_{m=1}^{\infty} \sum_{n=1}^{\infty} \omega \left[s_{mn} \, e^{-j\phi_s} + a_{mn} \, e^{-j\phi_a} \right] U_{mn}$$

$$\cdot e^{j(\omega t - \gamma_{mn} + \pi/2)} \; \} \; d\alpha_1 d\alpha_2 \; >_t \; . \qquad \text{(A4.17)}$$

Multiplying this out

$$\langle \dot{W}(t) \rangle_t =$$

$$< \int_0^{d_2} \int_0^{d_1} 1/2 \; Re\{ \sum_{m=1}^{\infty} \sum_{n=1}^{\infty} f_s \, e^{+j\phi_s} \; \delta(\alpha_1 - c_1)\delta(\alpha_2 - c_2) \; \omega$$

$$\cdot \left[s_{mn} \, e^{-j\phi_s} + a_{mn} \, e^{-j\phi_a} \right] U_{mn} \, e^{j(\omega t - \gamma_{mn} + \pi/2)} \; \} d\alpha_1 d\alpha_2 \; >_t$$

$$+ < \int_0^{d_2} \int_0^{d_1} 1/2 \; Re\{ \sum_{m=1}^{\infty} \sum_{n=1}^{\infty} f_a \, e^{+j\phi_a} \; \omega \; \cdot \left[s_{mn} \, e^{-j\phi_s} \right.$$

$$\left. + a_{mn} \, e^{-j\phi_a} \right] U_{mn} \, e^{j(\omega t - \gamma_{mn} + \pi/2)} \; \} \; d\alpha_1 d\alpha_2 \; >_t \; . \qquad \text{(A4.18)}$$

Expanding terms and bringing the integration inside,

$$\langle \dot{W}(t) \rangle_t =$$

$$\langle 1/2 \ \mathrm{Re}\{ \sum_{m=1}^{\infty} \sum_{n=1}^{\infty} f_s \omega \left[s_{mn} + a_{mn} e^{-j(\phi_s - \phi_a)} \right] e^{-j(\gamma_{mn} - \pi/2)}$$

$$\cdot \int_0^{d_2} \int_0^{d_1} \delta(\alpha_1 - c_1)\delta(\alpha_2 - c_2) \ U_{mn} \ d\alpha_1 d\alpha_2 \ \}\rangle_t$$

$$+ \langle 1/2 \ \mathrm{Re}\{ \sum_{m=1}^{\infty} \sum_{n=1}^{\infty} f_a \omega \left[s_{mn} e^{-j(\phi_a - \phi_s)} + a_{mn} \right] e^{-j(\gamma_{mn} - \pi/2)}$$

$$\cdot \int_0^{d_2} \int_0^{d_1} U_{mn} \ d\alpha_1 d\alpha_2 \ \}\rangle_t \ . \qquad \text{(A4.19)}$$

Evaluating the integrals

$$\langle \dot{W}(t) \rangle_t =$$

$$\langle 1/2 \ \mathrm{Re}\{ \sum_{m=1}^{\infty} \sum_{n=1}^{\infty} f_s \omega \left[s_{mn} + a_{mn} e^{-j(\phi_s - \phi_a)} \right] e^{-j(\gamma_{mn} - \pi/2)}$$

$$\cdot \sin(m\pi c_1/d_1)\sin(n\pi c_2/d_2) \ \}\rangle_t + \langle 1/2 \ \mathrm{Re}\{ \sum_{m=1}^{\infty} \sum_{n=1}^{\infty} f_a \omega$$

$$\cdot \left[s_{mn} e^{-j(\phi_a - \phi_s)} + a_{mn} \right] e^{-j(\gamma_{mn} - \pi/2)} \left[(1-\cos(m\pi))/(m\pi/d_1) \right]$$

$$\cdot \left[(1-\cos(n\pi)/(n\pi/d_2) \right] \}\rangle_t \ . \qquad \text{(A4.20)}$$

Now taking the real part and noting that there is no longer any time dependent terms left in the equations,

$$\langle \dot{W}(t) \rangle_t =$$

$$f_s \omega/2 \sum_{m=1}^{\infty} \sum_{n=1}^{\infty} \left[s_{mn} \cos(\pi/2 - \gamma_{mn}) + a_{mn} \cos(\pi/2 - \gamma_{mn} + \phi_a - \phi_s) \right]$$

$$\cdot \sin(m\pi c_1/d_1) \sin(n\pi c_2/d_2)$$

$$+ f_a S\omega/2 \sum_{m=1}^{\infty} \sum_{n=1}^{\infty} \left[s_{mn} \cos(\pi/2 - \gamma_{mn} + \phi_s - \phi_a) + a_{mn} \cos(\pi/2 - \gamma_{mn}) \right]$$

$$\cdot (1-\cos(m\pi))(1-\cos(n\pi))/(mn\pi^2) \; . \qquad \text{(A4.21)}$$

Now note that in the special case of zero airborne input

$$\langle \dot{W}_s(t) \rangle_t = f_s \omega/2 \sum_{m=1}^{\infty} \sum_{n=1}^{\infty} s_{mn} \cos(\pi/2 - \gamma_{mn})$$

$$\cdot \sin(m\pi c_1/d_1) \sin(n\pi c_2/d_2) \; . \qquad \text{(A4.22)}$$

And in the special case of zero structureborne input

$$\langle \dot{W}_a(t) \rangle_t = f_a S\omega/2 \sum_{m=1}^{\infty} \sum_{n=1}^{\infty} a_{mn} \cos(\pi/2 - \gamma_{mn})$$

$$\cdot (1-\cos(m\pi))(1-\cos(n\pi))/(mn\pi^2) \; . \qquad \text{(A4.23)}$$

Note that the power input for the combined airborne and structureborne forcing function is not equal to the sum of the powers input for the airborne and structureborne cases acting alone. Or, in terms of the equations,

$$\langle \dot{W}(t) \rangle_t \neq \langle \dot{W}_s(t) \rangle_t + \langle \dot{W}_a(t) \rangle_t \ . \qquad \text{(A4.24)}$$

C. POWER DISSIPATED

For simple harmonic motion, the time averaged power dissipated is given by (reference 56, pg. 331)

$$\langle \dot{W}(t) \rangle_t = \left\langle \int_0^{d_2} \int_0^{d_1} \mathrm{Re}\{\vec{F}(\vec{r},t)\} \cdot \mathrm{Re}\{\vec{v}(\vec{r},t)\} \ d\alpha_1 d\alpha_2 \right\rangle_t$$

$$= \lim_{T\to\infty} 1/T \int_0^T \left[\int_0^{d_2} \int_0^{d_1} \mathrm{Re}\{F_v(\vec{r},t)\}\mathrm{Re}\{v(\vec{r},t)\} \ d\alpha_1 d\alpha_2 \right] dt$$

$$= \int_0^{d_2} \int_0^{d_1} 1/2 \ \mathrm{Re}\{F_v^*(\vec{r},t)v(\vec{r},t)\} \ d\alpha_1 d\alpha_2 \qquad \text{(A4.25)}$$

where $\vec{F}$ is the resistive force of dissipation per unit area due to structural and fluid damping effects, and F_v is the component of this force in the direction of the transverse plate velocity. From the partial differential equation governing the plate's dynamics, given in appendix III, the component of this dissipative force in the direction of the transverse velocity is given by

$$F_v(\vec{r},t) = \lambda\dot{u}(\vec{r},t) = \lambda v(\vec{r},t) \ . \qquad \text{(A4.26)}$$

Substituting, the result is

$$\langle\dot{W}(t)\rangle_t =$$

$$\int_0^{d_2}\int_0^{d_1} 1/2\ \mathrm{Re}\{\lambda v^*(\vec{r},t)v(\vec{r},t)\}\ d\alpha_1 d\alpha_2, \qquad \text{(A4.27)}$$

thus

$$\langle\dot{W}(t)\rangle_t =$$

$$\lambda \int_0^{d_2}\int_0^{d_1} 1/2\ \mathrm{Re}\{v^*(\vec{r},t)v(\vec{r},t)\}\ d\alpha_1 d\alpha_2$$

$$= \lambda \int_0^{d_2}\int_0^{d_1} \langle v^2(\vec{r},t)\rangle_t\ d\alpha_1 d\alpha_2 = \lambda S\langle v^2(\vec{r},t)\rangle_{r,t} \ . \qquad \text{(A4.28)}$$

Substituting from Appendix IV section A. for $\langle v^2\rangle_{r,t}$

$$\langle\dot{W}(t)\rangle_t = \omega^2/8 \ \cdot$$

$$\sum_{m=1}^{\infty}\sum_{n=1}^{\infty} \lambda S\left[\ s_{mn}^2 + a_{mn}^2 + 2s_{mn}a_{mn}\cos(\phi_s-\phi_a)\ \right]. \qquad \text{(A4.29)}$$

For the special case of zero airborne input

$$\langle \dot{W}_s(t) \rangle_t = \omega^2/8 \sum_{m=1}^{\infty} \sum_{n=1}^{\infty} \lambda S \, s_{mn}^2 \, . \qquad \text{(A4.30)}$$

And for the special case of zero structureborne input

$$\langle \dot{W}_a(t) \rangle_t = \omega^2/8 \sum_{m=1}^{\infty} \sum_{n=1}^{\infty} \lambda S \, a_{mn}^2 \, . \qquad \text{(A4.31)}$$

So it is again clear that the power dissipated for the case of the combined airborne and structureborne inputs is not equal to the sum of the powers dissipated for the cases of the structureborne and airborne inputs acting alone. Or, in terms of the equations,

$$\langle \dot{W}(t) \rangle_t \neq \langle \dot{W}_s(t) \rangle_t + \langle \dot{W}_a(t) \rangle_t \, . \qquad \text{(A4.32)}$$

Appendix V

SOUND RADIATION OF A POINT SOURCE

A. MONOPOLE SOUND RADIATION

The ideal fluid potential function, $\underline{\Phi}$, for a simple harmonic point vibrating source (monopole) is well known in acoustics theory (see reference 59, pp. 153-171, reference 60, pp. 153-183, or reference 61, pp. 111-118) and is given by the relation

$$\underline{\Phi} = Q/(4\pi r')\, e^{j(\omega t - kr')} \qquad \text{(A5.1)}$$

where

Q = the volumetric flowrate of the fluid,

r' = the distance to the point of observation,

ω = the radian driving frequency of the source,

c_o = the speed of sound in air,

k = ω/c_o is the wavenumber,

t = time.

This potential function satisfies the wave equation

$$\nabla^2\underline{\Phi} - 1/c_o^2\, \partial^2\underline{\Phi}/\partial t^2 = Q\, e^{j\omega t}\, \delta(\vec{r}') \,. \qquad \text{(A5.2)}$$

The corresponding pressure and particle velocity produced by this point source are found from the equations

$$p(\vec{r}',t) = \rho_o\, \partial\underline{\Phi}/\partial t = j\omega\rho_o\, \underline{\Phi} \,, \qquad \text{(A5.3)}$$

$$\vec{v}(\vec{r},t) = -\nabla\, \underline{\Phi} = -\partial\underline{\Phi}/\partial r'\, \vec{e}_{r'} = (jkr'+1)/r'\, \underline{\Phi}\, \vec{e}_{r'} \,. \qquad \text{(A5.4)}$$

B. MONOPOLE NEAR A REFLECTING SURFACE

Now if the point source is placed a small distance h away from a perfectly rigid planar surface which extends to infinity in all directions as shown below,

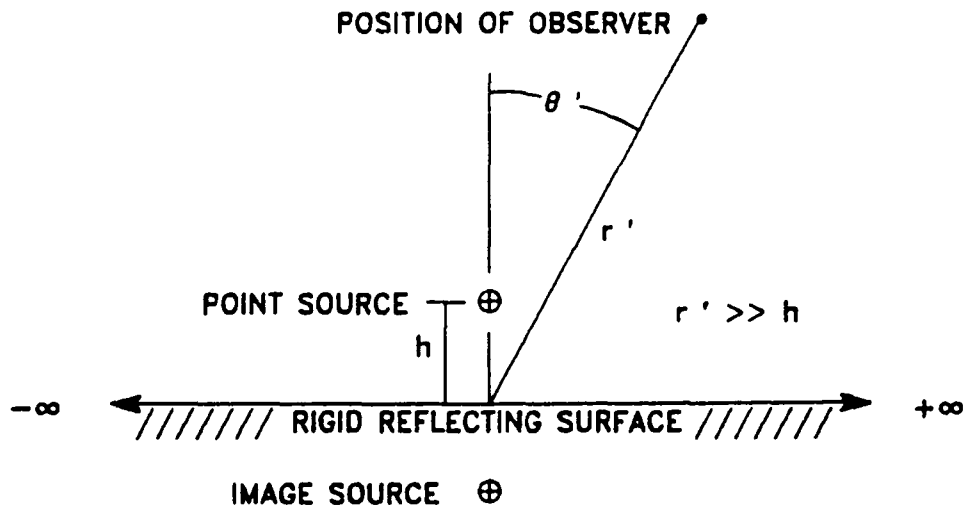

Figure (AV-1) -- Monopole near a reflecting surface.

and given that the distance to the point of observation r'>>h, so that the distance from the point of observation to the point source and its image are both approximately r', it can be shown that the potential function for this combination of monopole and image monopole is given by

$$\underline{\Phi} = Q/(2\pi r')\, e^{j(\omega t - kr')} \cos(kh\cos(\theta')) \; . \qquad (A5.5)$$

Now in the limit as h→0, this potential function becomes

$$\underline{\Phi} = Q/(2\pi r')\, e^{j(\omega t - kr')} . \qquad \text{(A5.6)}$$

And the corresponding expressions for the pressure and the particle velocity are given by

$$p(\vec{r}',t) = \rho_o\, \partial\underline{\Phi}/\partial t = j\rho_o\omega\, Q/(2\pi r')\, e^{j(\omega t - kr')}$$

$$= j\rho_o\omega\, \underline{\Phi} , \qquad \text{(A5.7)}$$

$$\vec{v}(\vec{r}',t) = -\nabla\, \underline{\Phi} = (jkr'+1)/r'\; Q/(2\pi r')\, e^{j(\omega t - kr')}\, \vec{e}_{r'},$$

$$= (jkr+1)/r'\; \underline{\Phi}\, \vec{e}_{r'} . \qquad \text{(A5.8)}$$

Since, in this case, the monopole is simple harmonic in character, the time averaged acoustic intensity of this source is given by

$$\langle \vec{I}(\vec{r}',t) \rangle_t = 1/2\ \mathrm{Re}\{\, p^*(\vec{r}',t)\, \vec{v}(\vec{r}',t)\, \} . \qquad \text{(A5.9)}$$

Now note that

$$\lim_{r'\to\infty} \vec{v}(\vec{r}',t)$$

$$= \lim_{r'\to\infty} (jkr'+1)/r'\; Q/(2\pi r')\, e^{j(\omega t - kr')}\, \vec{e}_{r'}$$

$$= jk\, Q/(2\pi r')\, e^{j(\omega t - kr')}\, \vec{e}_r = jk\, \underline{\Phi}\ \vec{e}_{r'} . \qquad \text{(A5.10)}$$

Multiplying by ρ_o/ρ_o

$$\lim_{r'\to\infty} \vec{v}(\vec{r}',t) = j\,(\rho_o\omega)/(\rho_o c_o)\,\underline{\underline{\Phi}}\,\vec{e}_{r'}$$

$$= p(\vec{r}',t)/(\rho_o c_o)\,\vec{e}_{r'}\ . \qquad \text{(A5.11)}$$

Thus, in the acoustic far field, as $r'\to\infty$

$$\vec{v}(\vec{r}',t) = p(\vec{r}',t)/(\rho_o c_o)\,\vec{e}_{r'}\ , \qquad \text{(A5.12)}$$

and substituting into the expression for intensity

$$\lim_{r'\to\infty} \langle\vec{I}(\vec{r}',t)\rangle_t$$

$$= 1/2\ \mathrm{Re}\{\ p^*(\vec{r}',t)\ p(\vec{r}',t)/(\rho_o c_o)\ \}\ \vec{e}_{r'}\ . \qquad \text{(A5.13)}$$

Thus, the magnitude of the far field time averaged acoustic intensity vector in the radially outward direction is given by

$$\langle I_{r'}(\vec{r}',t)\rangle_t = |p(\vec{r}',t)|^2/(2\rho_o c_o)\ . \qquad \text{(A5.14)}$$

Appendix VI

SOUND RADIATION FROM A SIMPLY SUPPORTED

RECTANGULAR FLAT ORTHOTROPIC PLATE

A. GEOMETRIC CONSIDERATIONS

Consider the following geometry:

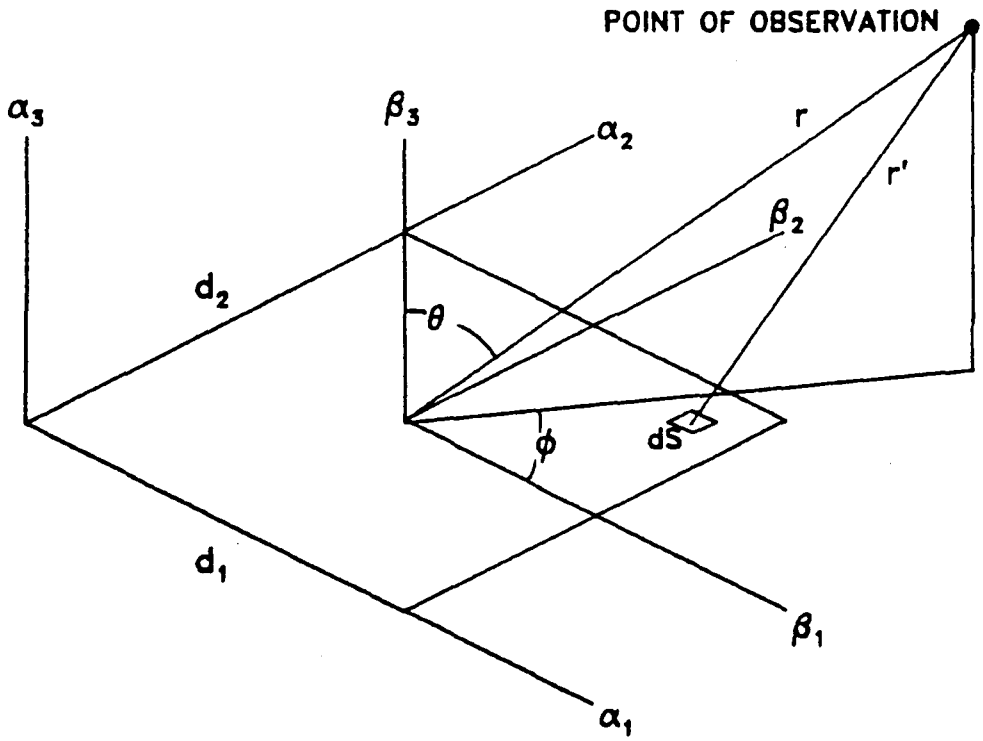

Figure (AVI-1) -- Geometry of the simply supported plate.

Note the α_i coordinate system has its origin at the corner of the plate. The β_i coordinate system has its origin at the center of the plate.

B. DERIVATION OF THE EQUATION FOR PRESSURE

Utilizing Huygens principle of superposition of simple sources along with the equations developed in Appendix V, the sound generation of each incremental area, dS, of the plate is modeled as a monopole lying on a rigid planar reflecting surface. Recall that the incremental pressure in this case was given by

$$dp(\vec{r}',t) = j\omega\rho_o Q/(2\pi r')\, e^{j(\omega t - kr')}$$

$$= j\omega\rho_o/(2\pi r')\, e^{-jkr'}\, Q\, e^{j\omega t} . \qquad \text{(A6.1)}$$

Recalling that Q represents the volumetric flowrate, it is seen that for simple harmonic vibration of the plate

$$Q\, e^{j\omega t} = v(\beta_1,\beta_2,t)\, d\beta_1 d\beta_2 \qquad \text{(A6.2)}$$

where $v(\beta_1,\beta_2,t)$ is the simple harmonic transverse plate velocity. Thus

$$dp(\vec{r}',t) =$$

$$j\omega\rho_o/(2\pi r')\, e^{-jkr'}\, v(\beta_1,\beta_2,t)\, d\beta_1 d\beta_2 . \qquad \text{(A6.3)}$$

In the β_i system, the coordinates of the point of observation are $(\beta_1,\beta_2,\beta_3) = (r_1,r_2,r_3)$, and the coordinates of the incremental plate area are $(\beta_1,\beta_2,\beta_3) = (\beta_1,\beta_2,0)$. Thus

$$r^2 = r_1^2 + r_2^2 + r_3^2, \tag{A6.4}$$

and

$$r'^2 = (r_1-\beta_1)^2 + (r_2-\beta_2)^2 + r_3^2$$

$$= r^2 - 2r_1\beta_1 - 2r_2\beta_2 + \beta_1^2 + \beta_2^2 \ . \tag{A6.5}$$

And from geometry

$$r_1 = r \sin(\theta)\cos(\phi), \tag{A6.6}$$

$$r_2 = r \sin(\theta)\sin(\phi) \ . \tag{A6.7}$$

Substituting this

$$r' = r \left[1 - 2 \sin(\theta)\cos(\phi)(\beta_1/r) - 2 \sin(\theta)\sin(\phi)(\beta_2/r) \right.$$

$$\left. + (\beta_1/r)^2 + (\beta_2/r)^2 \right]^{1/2} \ . \tag{A6.8}$$

Now if we use the far field approximations

$$1/r' \cong 1/r << 1 \ , \tag{A6.9}$$

so that

$$r >> d_1 \text{ and } r >> d_2 \tag{A6.10}$$

then

$$r' \cong$$

$$r \left[1 - \sin(\theta)\cos(\phi)(\beta_1/r) - \sin(\theta)\sin(\phi)(\beta_2/r) \right] \ . \tag{A6.11}$$

Substituting into the expression for the incremental pressure caused by the incremental plate area

$$dp(\vec{r},t) = j\omega\rho_o/(2\pi r)$$

$$\cdot\ e^{-jkr(1-\sin(\theta)\cos(\phi)(\beta_1/r)-\sin(\theta)\sin(\phi)(\beta_2/r))}$$

$$\cdot\ v(\beta_1,\beta_2,t)\ d\beta_1 d\beta_2\ . \qquad \text{(A6.12)}$$

Integrating over the entire area of the plate

$$p(\vec{r},t) =$$

$$\int_{-d_2/2}^{d_2/2}\int_{-d_1/2}^{d_1/2}\Big[\ j\omega\rho_o/(2\pi r)$$

$$\cdot\ e^{-jkr(1-\sin(\theta)\cos(\phi)(\beta_1/r)-\sin(\theta)\sin(\phi)(\beta_2/r))}$$

$$\cdot\ v(\beta_1,\beta_2,t)\ \Big]\ d\beta_1 d\beta_2\ .$$

$$= j\omega\rho_o/(2\pi r)\ e^{-jkr}$$

$$\cdot\ \int_{-d_2/2}^{d_2/2}\int_{-d_1/2}^{d_1/2}\Big[\ e^{jk\ \sin(\theta)(\beta_1\cos(\phi)+\beta_2\sin(\phi))}$$

$$\cdot\ v(\beta_1,\beta_1,t)\ \Big]\ d\beta_1 d\beta_1\ . \qquad \text{(A6.13)}$$

Now make the following change of variables:

$$\beta_1 = \alpha_1 - d_1/2, \qquad \beta_2 = \alpha_2 - d_2/2 \ . \tag{A6.14}$$

$$d\beta_1 = d\alpha_1, \qquad d\beta_2 = d\alpha_2 \ . \tag{A6.15}$$

Substituting this change of varibles

$$p(\vec{r},t) = j\omega\rho_o/(2\pi r)\ e^{-jkr}$$

$$\cdot \int_0^{d_2}\int_0^{d_1} \Big[e^{jk\ \sin(\theta)((\alpha_1 - d_1/2)\cos(\phi)+(\alpha_2-d_2/2)\sin(\phi))}$$

$$\cdot\ v(\alpha_1,\alpha_2,t) \Big]\ d\alpha_1 d\alpha_2 \ , \tag{A6.16}$$

thus

$$p(\vec{r},t) = j\omega\rho_o/(2\pi r)$$

$$\cdot\ e^{-jk(r\ +\ d_1/2\ \sin(\theta)\cos(\phi)\ +\ d_2/2\ \sin(\theta)\sin(\phi))}$$

$$\cdot \int_0^{d_2}\int_0^{d_1} \Big[e^{jk\ \sin(\theta)(\alpha_1\cos(\phi)+\alpha_2\sin(\phi))}$$

$$v(\alpha_1,\alpha_2,t) \Big]\ d\alpha_1 d\alpha_2 \ . \tag{A6.17}$$

Recall from Appendix III equation (A3.16)

$$v(\alpha_1,\alpha_2,t) = j\omega\ e^{j\omega t}$$

$$\cdot \sum_{m=1}^{\infty}\sum_{n=1}^{\infty} \eta_{mn}\ e^{-j\theta_{mn}}\ \sin(m\pi\alpha_1/d_1)\sin(n\pi\alpha_2/d_2) \ . \tag{A6.18}$$

Substituting this into our expression for pressure

$$p(\vec{r},t) = -\omega^2\rho_o/(2\pi r)$$

$$\cdot e^{j(\omega t-k(r + d_1/2\ \sin(\theta)\cos(\phi) + d_2/2\ \sin(\theta)\sin(\phi)))}$$

$$\cdot \int_0^{d_2}\int_0^{d_1}\left[e^{jk\ \sin(\theta)(\alpha_1\cos(\phi)+\alpha_2\sin(\phi))} \sum_{m=1}^{\infty}\sum_{n=1}^{\infty} \eta_{mn}\, e^{-j\theta_{mn}}\right.$$

$$\left.\cdot\sin(m\pi\alpha_1/d_1)\sin(n\pi\alpha_2/d_2)\right] d\alpha_1 d\alpha_2 \ . \qquad \text{(A6.19)}$$

Interchanging summation and integration

$$p(\vec{r},t) = -\omega^2\rho_o/(2\pi r)$$

$$\cdot e^{j(\omega t-k(r + d_1/2\ \sin(\theta)\cos(\phi) + d_2/2\ \sin(\theta)\sin(\phi)))}$$

$$\cdot \sum_{m=1}^{\infty}\sum_{n=1}^{\infty} \eta_{mn}\, e^{-j\theta_{mn}} \int_0^{d_2}\int_0^{d_1}\left[e^{jk\ \sin(\theta)(\alpha_1\cos(\phi)+\alpha_2\sin(\phi))}\right.$$

$$\left.\cdot \sin(m\pi\alpha_1/d_1)\sin(n\pi\alpha_2/d_2)\right] d\alpha_1 d\alpha_2 \ . \qquad \text{(A6.20)}$$

Separating integrals and rewriting

$$p(\vec{r},t) = -\omega^2\rho_o/(2\pi r)$$

$$\cdot\ e^{j(\omega t - k(r + d_1/2\ \sin(\theta)\cos(\phi) + d_2/2\ \sin(\theta)\sin(\phi)))}$$

$$\cdot \sum_{m=1}^{\infty} \sum_{n=1}^{\infty} \left[\eta_{mn}\ e^{-j\theta_{mn}} \right.$$

$$\cdot \int_0^{d_1} e^{jk\ \sin(\theta)\cos(\phi)\ \alpha_1}\ \sin(m\pi\alpha_1/d_1)\ d\alpha_1$$

$$\left. \cdot \int_0^{d_2} e^{jk\ \sin(\theta)\sin(\phi)\ \alpha_2}\ \sin(n\pi\alpha_2/d_2)\ d\alpha_2 \right] . \qquad \text{(A6.21)}$$

C. EVALUATION OF THE INTEGRALS

The resulting integrals found in the last section can be written as

$$Z_m = \int_0^{d_1} e^{jk\ \sin(\theta)\cos(\phi)\ \alpha_1}\ \sin(m\pi\alpha_1/d_1)\ d\alpha_1$$

$$= \int_0^{d_1} \cos(k\ \sin(\theta)\cos(\phi)\ \alpha_1)\ \sin(m\pi\alpha_1/d_1)\ d\alpha_1$$

$$+ j \int_0^{d_1} \sin(k\ \sin(\theta)\cos(\phi)\ \alpha_1)\ \sin(m\pi\alpha_1/d_1)\ d\alpha_1 . \qquad \text{(A6.22)}$$

and

$$Z_n = \int_0^{d_2} e^{jk \sin(\theta)\sin(\phi)\ \alpha_2} \sin(n\pi\alpha_2/d_2)\ d\alpha_2$$

$$= \int_0^{d_2} \cos(k \sin(\theta)\sin(\phi)\ \alpha_2)\ \sin(n\pi\alpha_2/d_2)\ d\alpha_2$$

$$+ j \int_0^{d_2} \sin(k \sin(\theta)\sin(\phi)\ \alpha_2)\ \sin(n\pi\alpha_2/d_2)\ d\alpha_2 \ . \qquad \text{(A6.23)}$$

With the integrals represented in this form, they can be evaluated by making a trigonometric substitution followed by straightforward integration, or more simply by looking them up in tables of integrals. (For example see reference 62.) From reference 62, pp. 435-437, formulae 296, 316, 318 and 319, the following formulae were obtained:

$$\int \sin(ax)\cos(bx)\ dx$$

$$= -(\cos((a-b)x)/(a-b) + \cos((a+b)x)/(a+b))/2 \quad \text{for } a^2 \neq b^2 \ ,$$

$$= (1/2a \sin^2(ax))\ \text{sgn}(a) \quad \text{for } a^2 = b^2 \ . \qquad \text{(A6.24)}$$

$$\int \sin(ax)\sin(bx)\,dx$$

$$= (\sin((a-b)x)/(a-b) - \sin((a+b)x)/(a+b))/2 \quad \text{for } a^2 \neq b^2 ,$$

$$= (x/2 - \sin(2ax)/(4a))\,\mathrm{sgn}(ab) \quad \text{for } a^2 = b^2 . \qquad \text{(A6.25)}$$

Evaluating the real part of Z_m:

If $(k \sin(\theta)\cos(\phi))^2 \neq (m\pi/d_1)^2$

$$\mathrm{Re}\{Z_m\} = \int_0^{d_1} \sin(m\pi\alpha_1/d_1)\cos(k \sin(\theta)\cos(\phi)\ \alpha_1)\,d\alpha_1$$

$$= (1-\cos(m\pi-k \sin(\theta)\cos(\phi)d_1))/(2m\pi/d_1-2k \sin(\theta)\cos(\phi))$$

$$+(1-\cos(m\pi+k \sin(\theta)\cos(\phi)d_1))/(2m\pi/d_1+2k \sin(\theta)\cos(\phi)) .$$

(A6.26)

And with several lines of algebra and trigonometric substitutions, the final result is

$$\mathrm{Re}\{Z_m\} = \left[\ 1 - \cos(m\pi)\cos(k \sin(\theta)\cos(\phi)d_1)\ \right]$$

$$\cdot(m\pi/d_1)/((m\pi/d_1)^2-(k \sin(\theta)\cos(\phi))^2) . \qquad \text{(A6.27)}$$

If $(k \sin(\theta)\cos(\phi))^2 = (m\pi/d_1)^2$

$$\mathrm{Re}\{Z_m\} = \int_0^{d_1} \sin(m\pi\alpha_1/d_1)\cos(k \sin(\theta)\cos(\phi)\ \alpha_1)\,d\alpha_1$$

$$= d_1/(2m\pi)\left[\sin^2(m\pi) - \sin^2(0)\right] = 0 \ . \qquad \text{(A6.28)}$$

Evaluating the imaginary part of Z_m:

If $(k \sin(\theta)\cos(\phi) \neq (m\pi/d_1)^2$

$$\mathrm{Im}\{Z_m\} = \int_0^{d_1} \sin(m\pi\alpha_1/d_1)\sin(k \sin(\theta)\cos(\phi)\alpha_1)\, d\alpha_1$$

$$= (\sin(m\pi - k \sin(\theta)\cos(\phi)d_1)/(2m\pi/d_1 - 2k \sin(\theta)\cos(\phi))$$

$$-\sin(m\pi + k \sin(\theta)\cos(\phi)d_1)/(2m\pi/d_1 - 2k \sin(\theta)\cos(\phi)) \ . \qquad \text{(A6.29)}$$

And with several lines of algebra and trigonometric substitutions, the final result is

$$\mathrm{Im}\{Z_m\} = -\cos(m\pi)\sin(k \sin(\theta)\cos(\phi)d_1)$$

$$\cdot(m\pi/d_1)/((m\pi/d_1)^2 - (k \sin(\theta)\cos(\phi))^2) \ . \qquad \text{(A6.30)}$$

If $(k \sin(\theta)\cos(\phi))^2 = (m\pi/d_1)^2$

$$\mathrm{Im}\{Z_m\} = \int_0^{d_1} \sin(m\pi\alpha_1/d_1)\sin(k \sin(\theta)\cos(\phi)\ \alpha_1)\, d\alpha_1$$

$$= \left[\, d_1/2 - d_1/(4m\pi)\, \sin(2m\pi) \,\right] \mathrm{sgn}(\sin(\theta)\cos(\phi))$$

$$= d_1/2\ \mathrm{sgn}(\sin(\theta)\cos(\phi)) \ . \qquad \text{(A6.31)}$$

Summarizing the evaluation of Z_m:

If $(k \sin(\theta)\cos(\phi))^2 \neq (m\pi/d_1)^2$ then

$$Z_m = \left[1 - \cos(m\pi)\, e^{jk \sin(\theta)\cos(\phi)d_1} \right] \cdot (m\pi/d_1)/((m\pi/d_1)^2-(k \sin(\theta)\cos(\phi))^2) \ . \qquad \text{(A6.32)}$$

If $(k \sin(\theta)\cos(\phi))^2 = (m\pi/d_1)^2$ then

$$Z_m = jd_1/2 \ \mathrm{sgn}(\sin(\theta)\cos(\phi)) \ . \qquad \text{(A6.33)}$$

An exactly analogous analysis can be performed on the integral Z_n. The results are given by:

If $(k \sin(\theta)\sin(\phi))^2 \neq (n\pi/d_2)^2$ then

$$Z_n = \left[1 - \cos(n\pi)\, e^{jk \sin(\theta)\sin(\phi)d_2} \right] \cdot (n\pi/d_2)/((n\pi/d_2)^2-(k \sin(\theta)\sin(\phi))^2) \ . \qquad \text{(A6.34)}$$

If $(k \sin(\theta)\sin(\phi))^2 = (n\pi/d_2)^2$ then

$$Z_n = jd_2/2 \ \mathrm{sgn}(\sin(\theta)\sin(\phi)) \ . \qquad \text{(A6.35)}$$

D. CALCULATION OF SOUND POWER RADIATED

Recalling the last equation in section B of this appendix, the equation for pressure is now given by

$$p(\vec{r},t) = -\omega^2\rho_o/(2\pi r)$$

$$\cdot\ e^{j(\omega t-k(r + d_1/2\ \sin(\theta)\cos(\phi) + d_2/2\ \sin(\theta)\sin(\phi)))}$$

$$\cdot \sum_{m=1}^{\infty} \sum_{n=1}^{\infty} \left[\eta_{mn}\ e^{-j\theta_{mn}}\ Z_m\ Z_n \right] \qquad \text{(A6.36)}$$

where the values of the complex numbers Z_m, and Z_n can be evaluated using the equations developed in section C of this appendix. From this last equation, the acoustic pressure at an arbitrary point in space can be calculated where it has been assumed that the point of observation is in the far acoustic field, i.e. $r >> d_1$ and $r >> d_2$. Now recall from Appendix V, section B, that in the far acoustic field, the time averaged magnitude of the acoustic intensity vector in the radially outward direction at a point in space for a simple harmonic, monopole source is given by

$$\langle I_r,(\vec{r}',t)\rangle_t = |p(\vec{r}',t)|^2/(2\rho_o c_o) \ . \qquad \text{(A6.37)}$$

Likewise, for simple harmonic motion of a simply supported rectangular plate, the far field time averaged magnitude of the acoustic intensity vector in the radially outward direction at a point in space is given by

$$\langle I_r(\vec{r},t)\rangle_t = |p(\vec{r},t)|^2/(2\rho_o c_o) \ , \qquad \text{(A6.38)}$$

where $r >> d_1$ and $r >> d_2$.

Making the appropriate substitutions, the far field time averaged magnitude of the acoustic intensity vector in the radially outward direction at a point in space for the plate vibrating in simple harmonic motion is given by

$$\langle I_r(\vec{r},t)\rangle_t = p^*(\vec{r},t)p(\vec{r},t)/(2\rho_o c_o)$$

$$= (\rho_o \omega^2/(2\pi r))^2/(2\rho_o c_o)$$

$$\cdot \left[\sum_{k=1}^{\infty} \sum_{l=1}^{\infty} \eta_{kl} \, e^{+j\theta_{kl}} \, z_k^* \, z_l^* \right]$$

$$\cdot \left[\sum_{m=1}^{\infty} \sum_{n=1}^{\infty} \eta_{mn} \, e^{-j\theta_{mn}} \, z_m \, z_n \right] . \qquad \text{(A6.39)}$$

Rearranging the order of summation

$$\langle I_r(\vec{r},t)\rangle_t = (\rho_o \omega^2/(2\pi r))^2/(2\rho_o c_o) \sum_{k=1}^{\infty} \sum_{l=1}^{\infty} \sum_{m=1}^{\infty} \sum_{n=1}^{\infty}$$

$$\left[\eta_{kl} \, e^{+j\theta_{kl}} \, \eta_{mn} \, e^{-j\theta_{mn}} \, z_k^* \, z_l^* \, z_m \, z_n \right] . \qquad \text{(A6.40)}$$

Now recall from Appendix I, section Q that the time averaged sound power is given by

$$\langle \Pi(t) \rangle_t = \int \int \langle \vec{I} \cdot \vec{n} \rangle_t \, dS \ . \qquad \text{(A6.41)}$$

In the present case under consideration, the control surface to be integrated over is a hemispherical surface in the far acoustic field, and the normal unit vector is in the radially outward direction. Thus

$$\langle \Pi(t) \rangle_t = \int_0^{2\pi} \int_0^{\pi/2} \langle I_r(t) \rangle_t \, r^2 \sin(\theta) \quad d\theta d\phi \ . \qquad \text{(A6.42)}$$

Substituting the expression for acoustic intensity, the time averaged sound power radiated by the plate is

$$\langle \Pi(t) \rangle_t =$$

$$\int_0^{2\pi} \int_0^{\pi/2} \left[(\rho_o \omega^2/(2\pi))^2 \sin(\theta)/(2\rho_o c_o) \quad \sum_{k=1}^{\infty} \sum_{l=1}^{\infty} \sum_{m=1}^{\infty} \sum_{n=1}^{\infty} \right.$$

$$\left. \left[\eta_{kl} \, e^{+j\theta_{kl}} \, \eta_{mn} \, e^{-j\theta_{mn}} \, Z_k^* \, Z_l^* \, Z_m \, Z_n \right] \right] d\theta d\phi \ . \qquad \text{(A6.43)}$$

E. SOUND POWER FOR THE SPECIAL CASE OF COMBINED INPUTS

Now recall from Appendix II, section C, that the equations for the influence coefficients are given by

$$\eta_{kl}\, e^{+j\theta_{kl}} = \left[s_{kl}\, e^{+j\phi_s} + a_{kl}\, e^{+j\phi_a} \right] e^{+j\gamma_{kl}} , \qquad \text{(A6.44)}$$

and

$$\eta_{mn}\, e^{-j\theta_{mn}} = \left[s_{mn}\, e^{-j\phi_s} + a_{mn}\, e^{-j\phi_a} \right] e^{-j\gamma_{mn}} . \qquad \text{(A6.45)}$$

Thus

$$\eta_{kl}\, e^{+j\theta_{kl}}\, \eta_{mn}\, e^{-j\theta_{mn}} = e^{j(\gamma_{kl}-\gamma_{mn})} \cdot \left[s_{kl}\, s_{mn} + a_{kl}\, a_{mn} + s_{kl}\, a_{mn}\, e^{j(\phi_s-\phi_a)} + a_{kl}\, s_{mn}\, e^{j(\phi_a-\phi_s)} \right]. \qquad \text{(A6.46)}$$

Substituting this equation for the product of the influence coefficients into the equation for the sound power

$$\langle \Pi(t) \rangle_t =$$

$$\int_0^{2\pi} \int_0^{\pi/2} \left[(\rho_o \omega^2/(2\pi))^2 \sin(\theta)/(2\rho_o c_o) \sum_{k=1}^{\infty} \sum_{l=1}^{\infty} \sum_{m=1}^{\infty} \sum_{n=1}^{\infty} \right.$$

$$\left[s_{kl}\, s_{mn} + a_{kl}\, a_{mn} + s_{kl}\, a_{mn}\, e^{j(\phi_s-\phi_a)} + a_{kl}\, s_{mn}\, e^{j(\phi_a-\phi_s)} \right]$$

$$\left. \cdot\, e^{j(\gamma_{kl}-\gamma_{mn})}\, Z_k^*\, Z_l^*\, Z_m\, Z_n \right] d\theta d\phi . \qquad \text{(A6.47)}$$

Now since the sound power is a real quantity (note that it is calculated from the conjugate product of the pressure times itself), it is known that the result of the series in the above equation is a real number. Using this knowledge, and some simple complex algebra, the equation for sound power can be written as:

$$\langle \Pi(t) \rangle_t =$$

$$\int_0^{2\pi} \int_0^{\pi/2} (\rho_o \omega^2/(2\pi))^2 \sin(\theta)/(2\rho_o c_o) \cdot \Bigg[$$

$$\sum_{k=1}^{\infty} \sum_{l=1}^{\infty} \Bigg[s_{kl}^2 \, |Z_k|^2 \, |Z_l|^2$$

$$+ \mathrm{Re}\Bigg\{ \sum_{m=1}^{\infty} \sum_{\substack{n=1 \\ (kl \neq mn)}}^{\infty} s_{kl} \, s_{mn} \, e^{j(\gamma_{kl} - \gamma_{mn})} \, Z_k^* \, Z_l^* \, Z_m \, Z_n \Bigg\} \Bigg]$$

$$+ \sum_{k=1}^{\infty} \sum_{l=1}^{\infty} \Bigg[a_{kl}^2 \, |Z_k|^2 \, |Z_l|^2$$

$$+ \mathrm{Re}\Bigg\{ \sum_{m=1}^{\infty} \sum_{\substack{n=1 \\ (kl \neq mn)}}^{\infty} a_{kl} \, a_{mn} \, e^{j(\gamma_{kl} - \gamma_{mn})} \, Z_k^* \, Z_l^* \, Z_m \, Z_n \Bigg\} \Bigg]$$

$$+ \sum_{k=1}^{\infty} \sum_{l=1}^{\infty} 2 \Bigg[s_{kl} \, a_{kl} \cos(\phi_s - \phi_a) \, |Z_k|^2 \, |Z_l|^2$$

$$+ \mathrm{Re}\Bigg\{ \sum_{m=1}^{\infty} \sum_{\substack{n=1 \\ (kl \neq mn)}}^{\infty} s_{kl} \, a_{mn} \, e^{j(\phi_s - \phi_a)} \, e^{j(\gamma_{kl} - \gamma_{mn})}$$

$$\cdot \, Z_k^* \, Z_l^* \, Z_m \, Z_n \Bigg\} \Bigg] \Bigg] \, d\theta d\phi \, . \qquad \text{(A6.48)}$$

Now define the terms in equation (A6.48) as follows:

$$\langle \Pi_s \rangle_t =$$

$$\int_0^{2\pi} \int_0^{\pi/2} (\rho_o \omega^2/(2\pi))^2 \sin(\theta)/(2\rho_o c_o) \cdot \Bigg[\sum_{k=1}^{\infty} \sum_{l=1}^{\infty} \Bigg[s_{kl}^2 |Z_k|^2 |Z_l|^2 + \mathrm{Re}\Big\{ \sum_{m=1}^{\infty} \sum_{n=1}^{\infty}{}_{(kl \neq mn)} s_{kl} s_{mn} e^{j(\gamma_{kl}-\gamma_{mn})} Z_k^* Z_l^* Z_m Z_n \Big\} \Bigg] \Bigg] d\theta d\phi \, . \qquad \text{(A6.49)}$$

$$\langle \Pi_a \rangle_t =$$

$$\int_0^{2\pi} \int_0^{\pi/2} (\rho_o \omega^2/(2\pi))^2 \sin(\theta)/(2\rho_o c_o) \cdot \Bigg[\sum_{k=1}^{\infty} \sum_{l=1}^{\infty} \Bigg[a_{kl}^2 |Z_k|^2 |Z_l|^2 + \mathrm{Re}\Big\{ \sum_{m=1}^{\infty} \sum_{n=1}^{\infty}{}_{(kl \neq mn)} a_{kl} a_{mn} e^{j(\gamma_{kl}-\gamma_{mn})} Z_k^* Z_l^* Z_m Z_n \Big\} \Bigg] \Bigg] d\theta d\phi \, . \qquad \text{(A6.50)}$$

$$\langle \Pi_{sxa} \rangle_t =$$

$$\int_0^{2\pi} \int_0^{\pi/2} (\rho_o \omega^2/(2\pi))^2 \sin(\theta)/(2\rho_o c_o) \cdot \Bigg[$$

$$+ \sum_{k=1}^{\infty} \sum_{l=1}^{\infty} 2 \Bigg[s_{kl}\, a_{kl} \cos(\phi_s - \phi_a)\, |z_k|^2\, |z_l|^2$$

$$+ \mathrm{Re}\Bigg\{ \sum_{m=1}^{\infty} \sum_{\substack{n=1 \\ (kl \neq mn)}}^{\infty} s_{kl}\, a_{mn}\, e^{j(\phi_s - \phi_a)}\, e^{j(\gamma_{kl} - \gamma_{mn})}$$

$$\cdot\, z_k^*\, z_l^*\, z_m\, z_n \Bigg\} \Bigg] \Bigg] \, d\theta d\phi \, . \qquad \text{(A6.51)}$$

Thus we see that the total sound power radiated can be written as

$$\langle \Pi \rangle_t = \langle \Pi_s \rangle_t + \langle \Pi_a \rangle_t + \langle \Pi_{sxa} \rangle_t \, . \qquad \text{(A6.52)}$$

Appendix VII

CALCULATION OF THE BENDING RIGIDITY CONSTANTS
FOR A SYMMETRIC LAMINATE
WITH MULTIPLE GENERALLY ORTHOTROPIC LAYERS

A. STRESS-STRAIN RELATIONS

The stress-strain relations for plane stress in a single orthotropic layer (from reference 42, pg.46) is given by

$$\begin{bmatrix} \sigma_1 \\ \sigma_2 \\ \tau_{12} \end{bmatrix} = \begin{bmatrix} Q_{11} & Q_{12} & 0 \\ Q_{12} & Q_{22} & 0 \\ 0 & 0 & Q_{66} \end{bmatrix} \begin{bmatrix} \varepsilon_1 \\ \varepsilon_2 \\ \gamma_{12} \end{bmatrix} \qquad \text{(A7.1)}$$

where the Q_{ij} are the reduced stiffnesses and are given in terms of the Young's moduli, the shear modulus, and the Poisson's ratios of the orthotropic layer by the relations

$$Q_{11} = E_1/(1-\mu_{12}\mu_{21}),$$

$$Q_{12} = \mu_{12}E_2/(1-\mu_{12}\mu_{21}) = \mu_{21}E_1/(1-\mu_{12}\mu_{21})$$

$$Q_{22} = E_2/(1-\mu_{12}\mu_{21}),$$

$$Q_{66} = G_{12}. \qquad \text{(A7.2)}$$

For an orthotropic layer of arbitrary orientation (angle) the stress-strain relations (from reference 42, pg. 51) are given by

$$\begin{bmatrix} \sigma_1 \\ \sigma_2 \\ \tau_{12} \end{bmatrix} = \begin{bmatrix} \bar{Q}_{11} & \bar{Q}_{12} & \bar{Q}_{16} \\ \bar{Q}_{12} & \bar{Q}_{22} & \bar{Q}_{26} \\ \bar{Q}_{16} & \bar{Q}_{26} & \bar{Q}_{66} \end{bmatrix} \begin{bmatrix} \varepsilon_1 \\ \varepsilon_2 \\ \gamma_{12} \end{bmatrix} \qquad \text{(A7.3)}$$

where the transformed reduced stiffnesses $\bar{Q}_{ij}$ are given by the relations

$$\begin{aligned}
\bar{Q}_{11} &= Q_{11}\cos^4\theta + 2(Q_{12}+2Q_{66})\sin^2\theta\cos^2\theta + Q_{22}\sin^4\theta, \\
\bar{Q}_{12} &= (Q_{11}+Q_{22}-4Q_{66})\sin^2\theta\cos^2\theta + Q_{12}(\sin^4\theta+\cos^4\theta), \\
\bar{Q}_{22} &= Q_{11}\sin^4\theta + 2(Q_{12}+2Q_{66})\sin^2\theta\cos^2\theta + Q_{22}\cos^4\theta, \\
\bar{Q}_{16} &= (Q_{11}-Q_{12}-2Q_{66})\sin\theta\cos^3\theta + (Q_{12}-Q_{22}+2Q_{66})\sin^3\theta\cos\theta, \\
\bar{Q}_{26} &= (Q_{11}-Q_{12}-2Q_{66})\sin^3\theta\cos\theta + (Q_{12}-Q_{22}+2Q_{66})\sin\theta\cos^3\theta, \\
\bar{Q}_{66} &= (Q_{11}+Q_{22}-2Q_{12}-2Q_{66})\sin^2\theta\cos^2\theta + Q_{66}(\sin^4\theta+\cos^4\theta).
\end{aligned} \qquad \text{(A7.4)}$$

B. CALCULATION OF THE BENDING RIGIDITIES

Once the transformed reduced stiffnesses $\bar{Q}_{ij}$ are known, the bending rigidities D_{ij} may be calculated (from reference 42, pp. 162-166) with the equation

$$D_{ij} = 1/3 \sum_{k=1}^{N} \left[(\bar{Q}_{ij})_k \left(h_k^3 - h_{k-1}^3 \right) \right] \qquad \text{(A7.5)}$$

where N is the total number of layers, h_k denotes the distance from the midsurface to the lower surface of the kth layer, and h_{k-1} denotes the distance from midsurface to the upper surface of the kth layer.

Appendix VIII

MEASUREMENT ERROR ANALYSIS

A. DESCRIPTION OF THE ANALYSIS

Recall from Chapter II equations (3.29) and (3.31):

$$\langle \tilde{\Pi}_a \rangle_t = \langle \Pi \rangle_t \, (\sigma_a/\sigma) \, (\sigma - \sigma_s)/(\sigma_a - \sigma_s) \, , \qquad (3.29)$$

$$\langle \tilde{\Pi}_s \rangle_t = \langle \Pi \rangle_t \, (\sigma_s/\sigma) \, (\sigma_a - \sigma)/(\sigma_a - \sigma_s) \, . \qquad (3.31)$$

These two equations represent the estimates of the airborne and structureborne sound power components of the measured combined sound power radiated by a structure. These estimates involve three independent measured quantities, viz. the airborne radiation efficiency, σ_a, the structureborne radiation efficiency, σ_s, and the radiation efficiency of the combined sound, σ. Measurement errors in any of these three quantities will cause errors in the estimates of the airborne and structureborne components. The results of an error analysis which investigates the sensitivity of the estimates to each type of possible measurement errors are presented here. In some cases, the severity of the error is seen to be heavily dependent on the difference in the actual airborne and structureborne radiation efficiencies or on the actual radiation efficiency of the combined noise. Therefore, the results are presented as

different plots for different values of $\sigma_a - \sigma_s$ with each plot showing a family of curves for different values of σ. In each figure it is assumed that the actual value of σ lies somewhere between the actual values of σ_s and σ_a. Thus, each figure has a family of curves with each curve representing a different value of the fractional combined efficiency, σ_f, defined by the equation:

$$\sigma_f = (\sigma - \sigma_s)/(\sigma_a - \sigma_s) \qquad \text{(A8.1)}$$

where σ_f takes on values between 0 and 1 exclusively. It should be noted that while under most circumstances σ has a value less that σ_a and greater than σ_s, this is not always the case. Furthermore, it can shown both analytically and experimentally that under relatively rare circumstances the value of σ_f can fall outside the range 0 to 1.

B. ERRORS IN THE STRUCTUREBORNE ESTIMATE

Figures (AVIII-1) through (AVIII-3) show the results of the error analysis on equation (3.31) for the errors expected in the structureborne sound power estimate, $\langle\tilde{\Pi}_s\rangle_t$, due to errors in the measurements.

Figures (AVIII-1a) through (AVIII-1c) show how errors in the measurement of σ_s effects the structureborne sound power estimate, $\langle\tilde{\Pi}_s\rangle_t$, for the cases of a 5

dB, 15 dB, and 25 dB difference in the airborne and structureborne radiation efficiencies ($\sigma_a - \sigma_s$), respectively. These three figures show that the relationship between measurement errors of σ_s and the estimate $\langle\tilde{\Pi}_s\rangle_t$ are essentially linear and independent of the radiation efficiency of the combined noise (since all six curves in each of these figures fall almost exactly on top of one another).

Figures (AVIII-2a) through (AVIII-2c) show how errors in the measurement of σ_a effects the structureborne sound power estimate, $\langle\tilde{\Pi}_s\rangle_t$, for the cases of a 5 dB, 15 dB, and 25 dB difference in the airborne and structureborne radiation efficiencies ($\sigma_a - \sigma_s$), respectively. These three figures show that the relationship between measurement errors of σ_a and the estimate $\langle\tilde{\Pi}_s\rangle_t$ is nearly independent of the value of ($\sigma_a - \sigma_s$), but is extremely sensitive to the value of the radiation efficiency of the combined noise σ. If the combined noise has a radiation efficiency nearly equal to that of the purely airborne input, then small errors in the measurement of σ_a can cause large errors in the estimate $\langle\tilde{\Pi}_s\rangle_t$.

Figures (AVIII-3a) through (AVIII-3c) show how errors in the measurement of the radiation efficiency of the combined noise, σ, effect the structureborne sound power

estimate, $\langle\tilde{\Pi}_s\rangle_t$, for the cases of a 5 dB, 15 dB, and 25 dB difference in the airborne and structureborne radiation efficiencies ($\sigma_a - \sigma_s$), respectively. These three figures show results that are similar to the results found in figures (AVIII-2a) through (AVIII-2c) in that measurement errors in σ produce errors in the estimate $\langle\tilde{\Pi}_s\rangle_t$ that are nearly independent of the value of ($\sigma_a - \sigma_s$), but are extremely sensitive to the actual value of the radiation efficiency of the combined noise. If the combined noise has a radiation efficiency nearly equal to that of the purely airborne input, small errors in the measurement of σ can produce large errors in the estimate $\langle\tilde{\Pi}_s\rangle_t$.

C. ERRORS IN THE AIRBORNE ESTIMATE

Figures (AVIII-4) through (AVIII-6) show the results of the error analysis on equation (3.29) for the errors expected in the airborne sound power estimate, $\langle\tilde{\Pi}_a\rangle_t$, due to errors in the measurements.

Figures (AVIII-4a) through (AVIII-4c) show how errors in the measurement of σ_s effects the airborne sound power estimate, $\langle\tilde{\Pi}_a\rangle_t$, for the cases of a 5 dB, 15 dB, and 25 dB difference in airborne and structureborne radiation efficiencies ($\sigma_a - \sigma_s$), respectively. These three figures indicate that measurement errors in σ_s cause sizable errors in the airborne estimate,

$\langle\tilde{\Pi}_a\rangle_t$, only if the difference in the airborne and structureborne radiation efficiencies ($\sigma_a - \sigma_s$) is small (5 dB or less) and if the radiation efficiency of the combined noise, σ is nearly equal to that of a purely structureborne input. (See figure (AVIII-4a)). As the difference in the airborne and structureborne radiation efficiencies ($\sigma_a - \sigma_s$) increases, the airborne estimate, $\langle\tilde{\Pi}_a\rangle_t$, becomes increasingly insensitive to the value of the combined radiation efficiency, σ, and eventually becomes completely independent of errors in the structureborne radiation efficiency σ_s altogether (as indicated in figures (AVIII-4b) and (AVIII-4c)).

Figures (AVIII-5a) through (AVIII-5c) show how errors in the measurement of σ_a effects the airborne estimate, $\langle\tilde{\Pi}_a\rangle_t$, for the cases of a 5 dB, 15 dB, and 25 dB difference in the airborne and structureborne radiation efficiencies ($\sigma_a - \sigma_s$), respectively. Figure (AVIII-5a) indicate that errors in the measurement of σ_a cause small errors in the estimate $\langle\tilde{\Pi}_a\rangle_t$ when the difference in the airborne and structureborne radiation efficiencies ($\sigma_a - \sigma_s$) is small (5 dB or less). The errors produced in the estimate $\langle\tilde{\Pi}_a\rangle_t$ become increasingly smaller as ($\sigma_a - \sigma_s$) becomes larger (as indicated by figures (AVIII-5b) and (AVIII-5c)). Furthermore, the errors

produced in the estimate are seen to be virtually independent of the value of the combined radiation efficiency σ.

Figures (AVIII-6a) through (AVIII-6c) show how errors in the measurement of σ effect the airborne sound power estimate, $\langle\tilde{\Pi}_a\rangle_t$, for the cases of a 5 dB, 15 dB, and 25 dB difference in the airborne and structureborne efficiencies ($\sigma_a - \sigma_s$), respectively. Figure (AVIII-6a) shows that the errors in the estimate can be quite large if the difference ($\sigma_a - \sigma_s$) in small (5 dB or less) and if the actual radiation efficiency of the combined noise, σ, is nearly equal to the structureborne radiation efficiency, σ_s. As the difference ($\sigma_a - \sigma_s$) becomes larger, however, the errors in the estimate become less severe and are almost independent of the actual value of σ (as indicated by figures (AVIII-6b) and (AVIII-6c)).

D. CONCLUSIONS

Based on the results of the error analysis, the most severe type of error possible occurs when the combined sound power is strongly dominated by the airborne component (σ is nearly equal to σ_a) and errors are made in the measurement of σ or in the measurement of σ_a. When this happens, the estimate $\langle\tilde{\Pi}_s\rangle_t$ will always be highly in error.

The second most severe type of error occurs when the combined sound power is strongly dominated by the

structureborne component (σ is nearly equal to σ_s) and errors are made in the measurement of σ or in the measurement of σ_s. When this happens, the estimate of the airborne sound power, $\langle\tilde{\Pi}_a\rangle_t$ will be largely in error only if the difference in the airborne and structureborne radiation efficiencies ($\sigma_a - \sigma_s$) is small (5 dB or less).

All other errors in the estimates due to measurement errors are insignificant in comparison with the aforementioned two most serious types. Furthermore, from these results, it can be seen that when applying these estimates to an arbitrary noise path identification problem, measurement errors are more likely to cause inaccuracies in the estimate of the structureborne sound power component than in the estimate of the airborne sound power component.

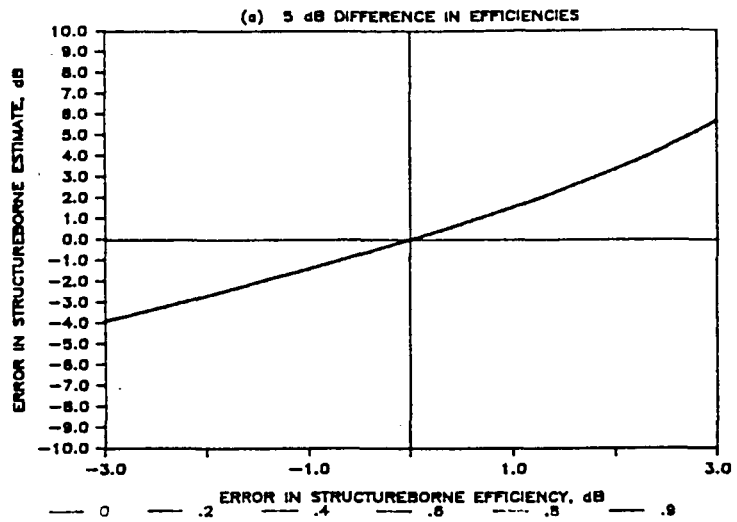

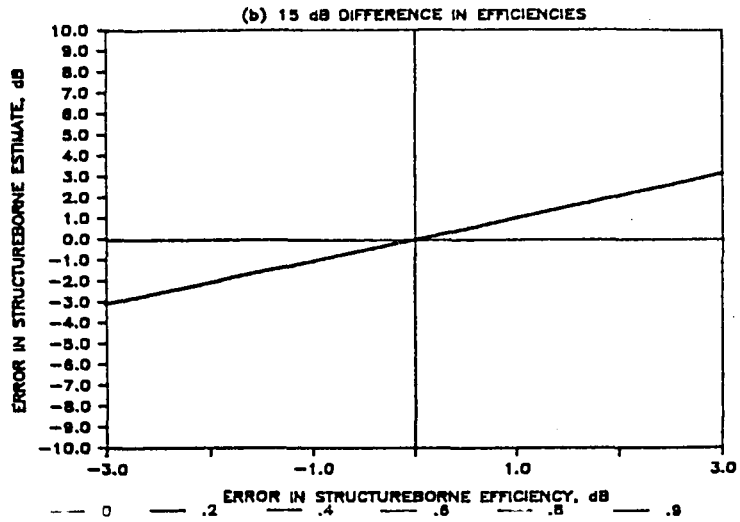

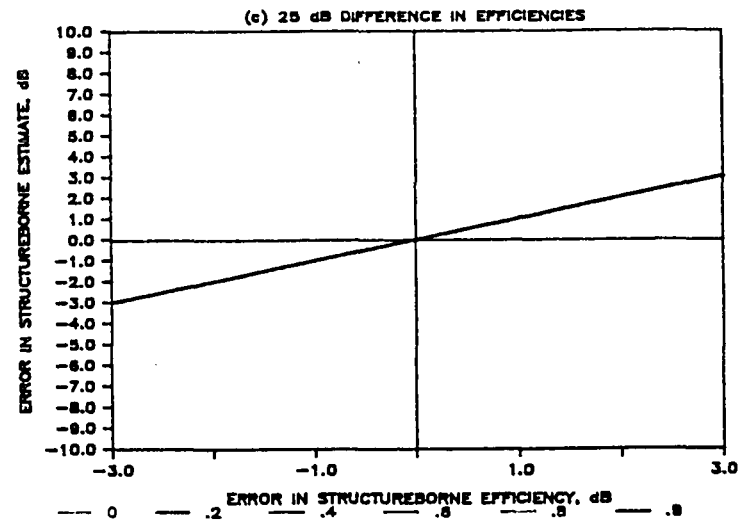

Figure (AVIII-1) -- Error in the structureborne sound power estimate due to measurement errors in σ_s.

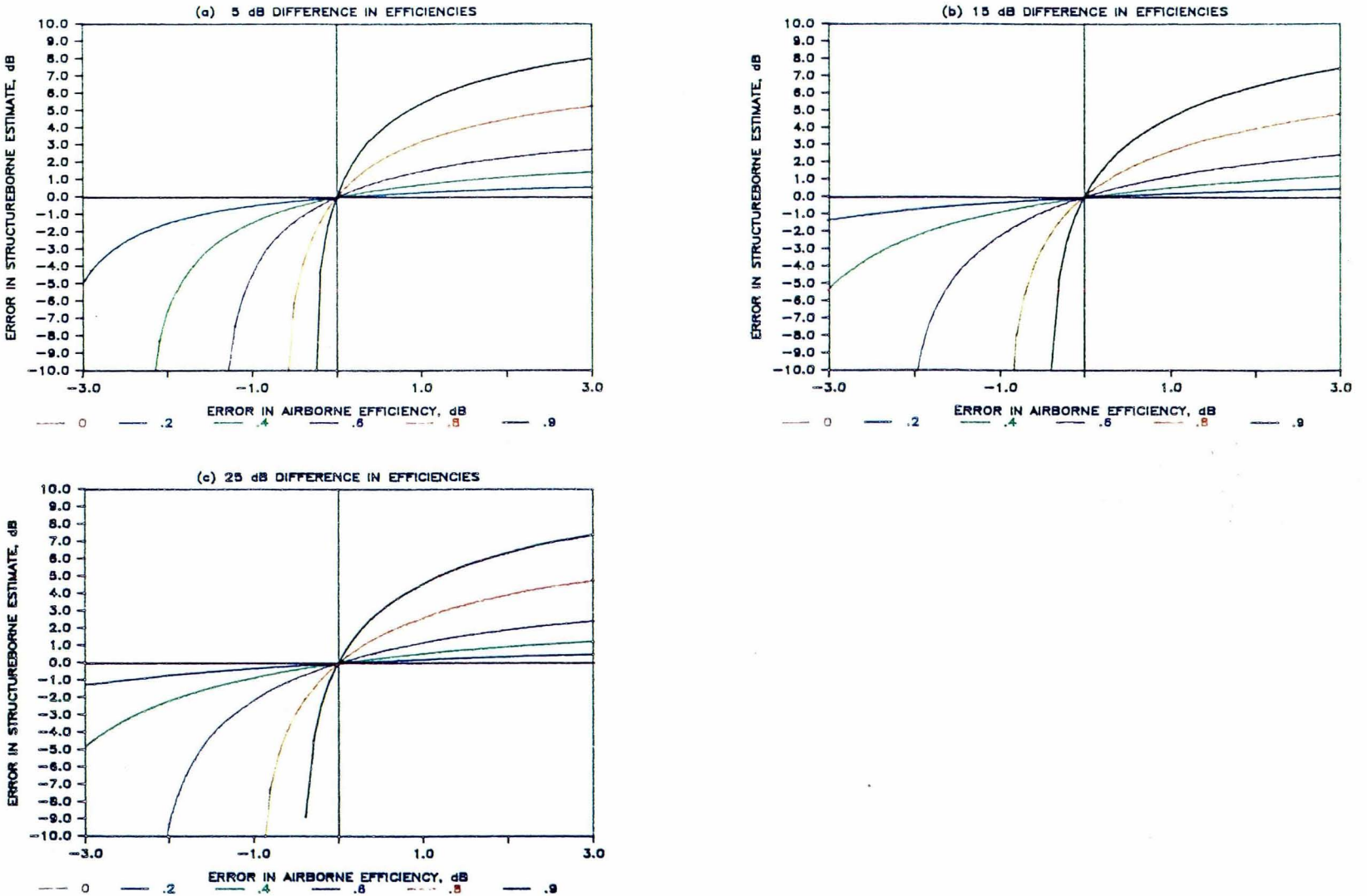

Figure (AVIII-2) -- Error in the structureborne sound power estimate due to measurement errors in σ_a.

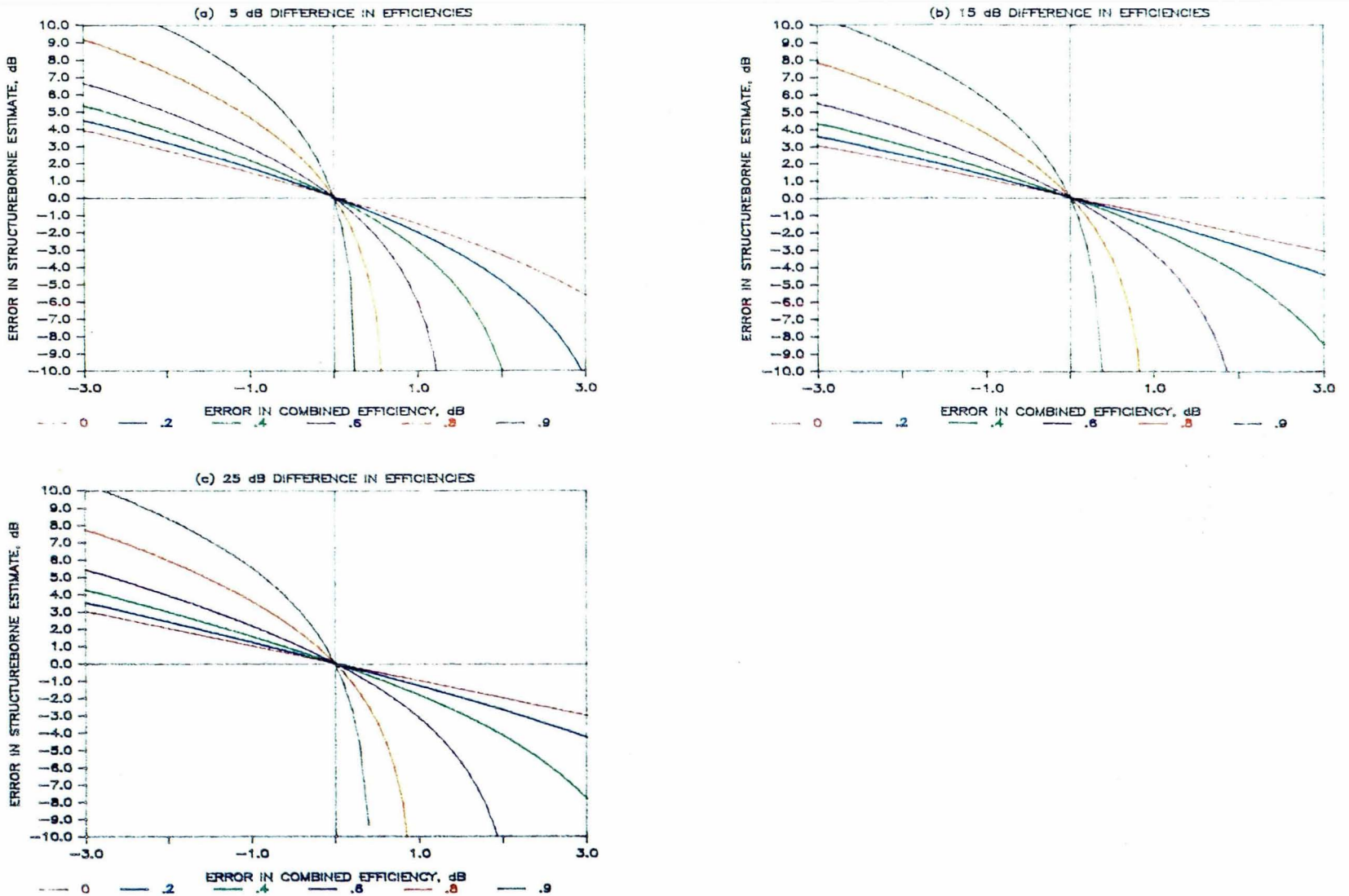

Figure (AVIII-3) -- Error in the structureborne sound power estimate due to measurement errors in σ.

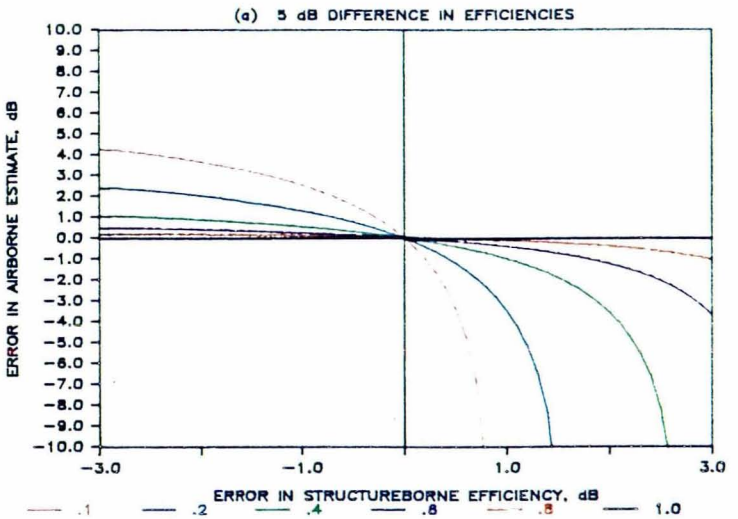

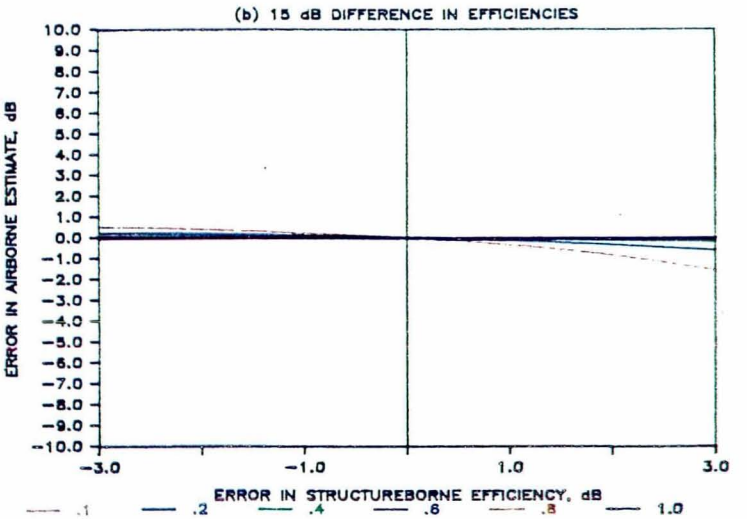

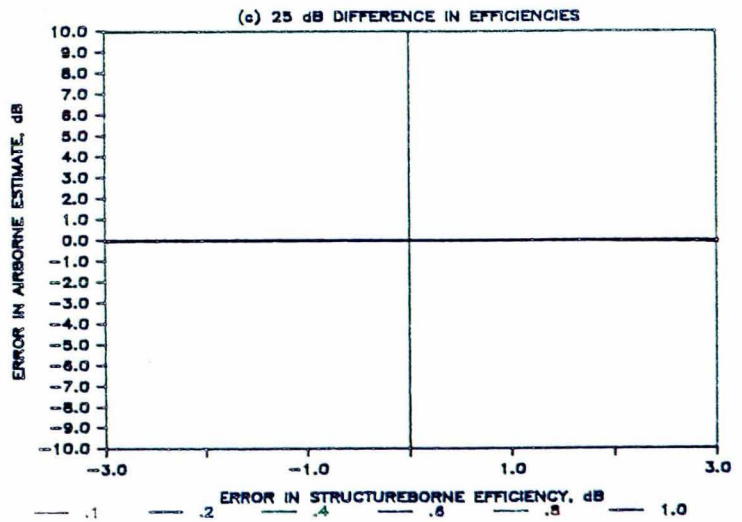

Figure (AVIII-4) -- Error in the airborne sound power estimate due to measurement errors in σ_s.

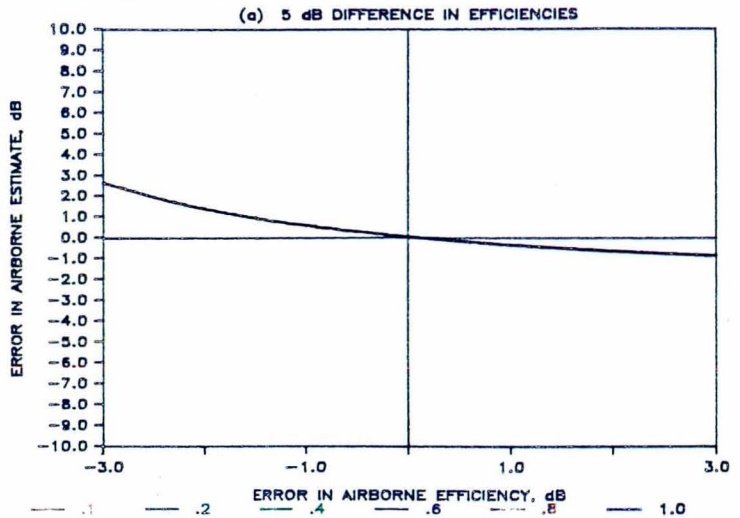

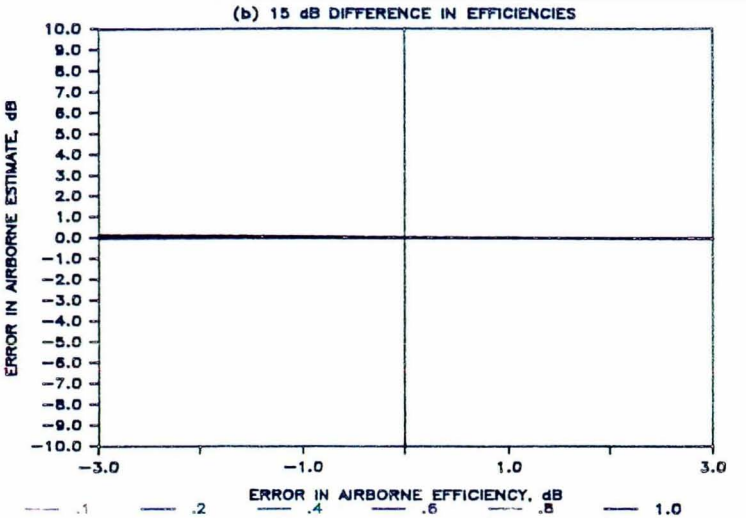

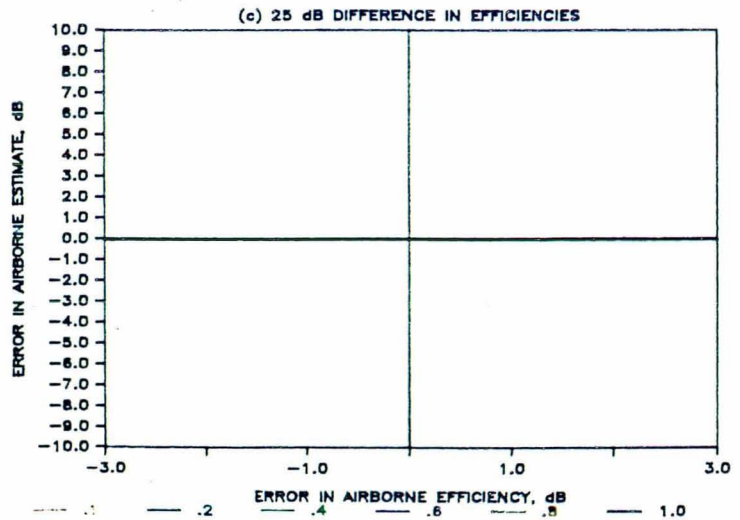

Figure (AVIII-5) -- Error in the airborne sound power estimate due to measurement errors in σ_a.

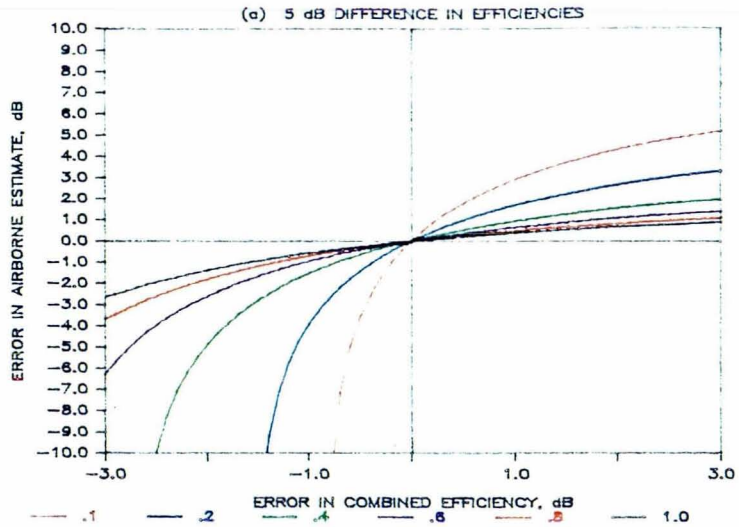

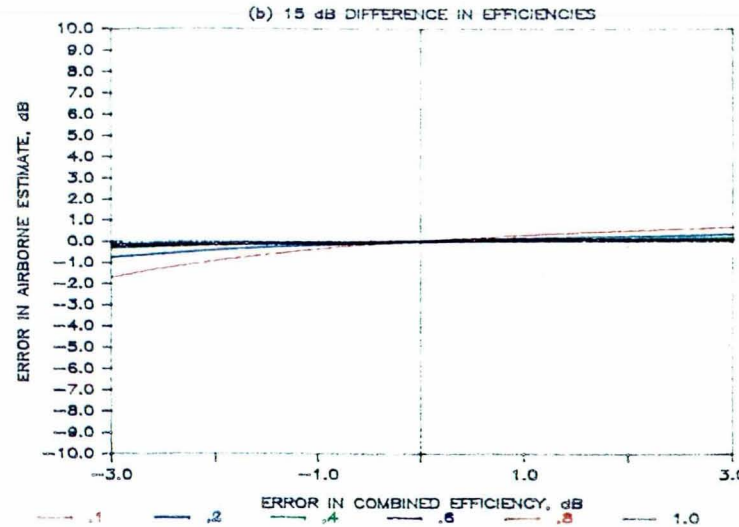

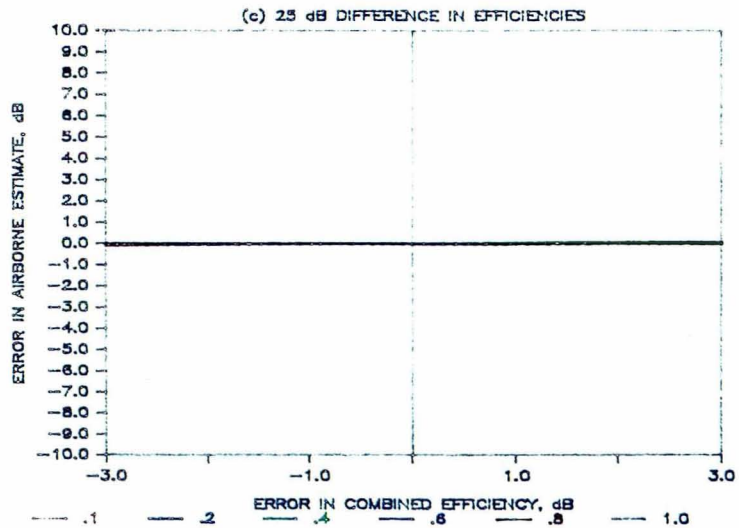

Figure (AVIII-6) -- Error in the airborne sound power estimate due to measurement errors in σ.

Appendix IX

COMPUTER PROGRAMS

A. PROGRAM MODAL

The purpose of program MODAL was to calculate the natural frequencies of a plate of either orthotropic or regular symmetric angle-ply laminate construction. Data files required as input to this program include file DATPCR which contains the physical characteristics of the plate, file DATPSP which contains the plate stiffness parameters, and file DATNFL which contains the uppermost frequency limit for the calculation of the natural frequencies. Information contained in file DATPCR includes the length, width, thickness, and density of the plate. Information in file DATPSP tells the program whether the plate is orthotropic or a laminate and includes information such as the Young's moduli, the modulus of rigidity, Poisson's ratios, and the number of plies and their orientation if the plate is a laminate. File DATNFL tells the program where it can stop calculating natural frequencies by specifying an uppermost frequency above which no natural frequencies shall be calculated.

The calculation scheme of this program is as follows: The main program calls subroutines RPCHR, RSPAR, and RFLIM which read and subroutines WPCHR, WSPAR, and WFLIM which write files DATPCR, DATPSP, and DATNFL respectively. If the

plate is orthotropic, subroutine RSPAR calculates the bending rigidity constants D_{ij} using equations (A2.4) through (A2.7). If the plate is a laminate, subroutine RSPAR calls subroutine CBC which calculates the bending constants using the equations outlined in Appendix VII. Subroutine CFREQ is then called to calculate the natural frequencies. The natural frequencies are calculated using equation (3.6). The algorithm begins by setting mode numbers m and n equal to 1. Natural frequencies are then calculated with mode number n being incremented by 1 each time through the loop until the natural frequency calculated exceeds the uppermost frequency limit set by file DATNFL. Mode number m is then incremented by 1 and the entire calculation procedure is then repeated. Calculations cease when for some value of m, n = 1 and the calculated natural frequency exceeds the uppermost frequency limit. With this calculation scheme, all flexural modeshapes which have natural frequencies less than or equal to the uppermost frequency limit are obtained. After the calulations are complete, program control is returned to the main program and subroutine SORT is called which sorts out the modes in their order of ascending natural frequency. Subroutine WFREQ is then called to write this sorted list of mode numbers versus natural frequency in file DATMNF which is used in subsequent calculations.

B. PROGRAM SOUND

The purpose of program SOUND was to calculate the sound power radiated by a plate and its radiation efficiency due to combined airborne and structureborne inputs. Data files required as input to this program include files DATPCR, DATPSP, DATNFL, and DATMNF (discussed in the previous section) and files DATFF and DATDMP which contain the forcing function and the damping model, respectively. Information contained in DATFF includes the magnitudes and relative phases of the airborne and structureborne inputs and the location of the point vibrational (structureborne) input. File DATDMP contains the two damping coefficients of equation (3.11) or (3.12).

The calculation scheme of this program is as follows: First, the program initializes the value of various constants such as the characteristic acoustic impedance of the fluid medium, and the number of lines of resolution desired in the frequency domain, etc... Second, the program calls several subroutines which both read and write the information contained in the input files. The program checks the forcing functions and if possible will take advantage of symmetry in the numerical integration which is to be performed later on. The program then begins its outermost loop which sets the forcing frequency. Subroutines SBIC and ABIC are called to calculate the modal influence coefficients for

the structureborne and airborne inputs at the specified forcing frequency using equations (3.16) and (3.17). (The natural frequency information contained in file DATMNF, the damping information in DATDMP, and the forcing function information in DATFF is used to perform these calculations.) Subroutine STAMSSV is then called to calculate the space-time averaged mean square surface velocity of the plate due to the combined inputs at the specified frequency using equation (3.19). Finally, subroutine CAREDB is called to perform the numerical integration and calculate the time averaged sound power radiated by the plate due to the combined inputs at the specified forcing frequency using equation (A6.43). At this point, control returns to the main program and the final results are calculated. The last step in the outer loop was to write the results including sound power level, radiation efficiency, mean-square surface velocity, and two error checks on the numerical integration to the output file named DATA. The entire outer loop is then repeated for different values of the forcing frequency. In addition to file DATA, the various input parameters used in the program were stored on a separate file named BANNER.

The numerical integration subroutine CAREDB utilizes an adaptive quadrature scheme to integrate over a two-dimensional hemispherical surface. This routine uses the trapezoidal approximation with interval halfing and utilizes

Richardson extrapolation to improve its estimates. To use subroutine CAREDB, the user must provide a function subroutine containing the integrand. Function subroutine FTAI was provided to calculate the value of the integrand at an arbitrary polar and azimuthal angle at a point on the hemispherical surface using equation (A6.43). Subroutine FTAI contains the innermost loop in the program and, according to equation (A6.43), must sum over all the modes of the plate to obtain the value of the integrand. Since modes whose natural frequencies are much, much greater than the forcing frequency are known to have a very small response, and since these modes are being driven in their stiffness controlled regions, their contribution to both the dynamic and acoustic responses of the plate are expected to be insignificant. Thus, when calculating the value of the integrand, function FTAI considers only those modes which have natural frequencies in the 0-1000 Hz frequency range plus any additional modes whose resonance frequencies are less than or equal to twice the forcing frequency. This method of calculating the integrand has virtually no effect on the accuracy of the calculations and reduces the necessary computation time significantly.

C. PROGRAM PREDICT

The purpose of program PREDICT was to implement equations (3.29) and (3.31) for the separation and prediction of the airborne and structureborne sound power components of some combined inputs case of interest. The code was written so that it could be used with the output data files (DATA) generated by the analytical computer model (program SOUND), and so that it could also be used with data files generated by the experimental study.

The calculation scheme of PREDICT is as follows: The user is prompted for the names of the three data files containing (1) the structureborne radiation efficiency, (2) the airborne radiation efficiency, and (3) the combined sound power and combined radiation efficiency. The program then uses equation (3.29) to predict the airborne component and equation (3.31) to predict the structureborne component of the combined sound power. No attempt at predicting the components is made if the difference in airborne and structureborne radiation efficiencies, $(\sigma_a-\sigma_s)$, is less than 2 dB, or if either of the predicted sound powers is negative. The indication that one of these two events has occured is signaled when the program returns a value of 0.0 for either or both of the airborne and structureborne sound power predictions. The requirement that the difference in efficiencies $(\sigma_a-\sigma_s)$ be greater that 2 dB was

selected on the basis that the experimental measurements of radiation efficiency are at best only accurate to plus or minus 1 dB. The requirement that the estimates be non-negative was dictated by the fact that one can not take the logrithm of a negative number (which is necessary on a dB scale), not because the estimates can not or should not ever be negative. In fact, both the analytical and experimental evidence suggests that the estimates will quite routinely have negative values.

The following pages are a listing of program MODAL:

```
      PROGRAM MODAL (INPUT,OUTPUT,TAPE5=INPUT,TAPE6=OUTPUT)
      DIMENSION OMEGA(1000),NMAX(50)
      DIMENSION MNSORT(1000,2),FREQ(1000)
      INTEGER IPTYPE,NPLYS,IPO(8)
      REAL NU1,NU2
      COMMON/LIMIT/FMAX
      COMMON/NF/MODES,MMAX,NMAX,OMEGA
      COMMON/PCHR/D1,D2,H,RHO
      COMMON/SPARA/D11,D22,D66,D12,D16,D26,DK,
     *E1,E2,G,NU1,NU2
      COMMON/SORT/MNSORT,NOM,FREQ
      COMMON/TYPE/IPTYPE,NPLYS,IPO
      OPEN(UNIT=1,FILE='DATPCR',STATUS='OLD')
      OPEN(UNIT=2,FILE='DATPSP',STATUS='OLD')
      OPEN(UNIT=3,FILE='DATNFL',STATUS='OLD')
      OPEN(UNIT=7,FILE='DATMNF',STATUS='NEW')
      CALL RPCHR
      CALL WPCHR
      CALL RSPAR
      CALL WSPAR
      IF(IPTYPE.NE.0.AND.IPTYPE.NE.1) THEN
      GOTO 10
      END IF
      CALL RFLIM
      CALL WFLIM
      CALL CFREQ
      CALL SORT
      CALL WFREQ
      CLOSE(1)
      CLOSE(2)
      CLOSE(3)
      CLOSE(7)
 10   STOP
      END
C
C
      SUBROUTINE RPCHR
      COMMON/PCHR/D1,D2,H,RHO
      READ(1,10)D1,D2
 10   FORMAT(//4X,E10.4/4X,E10.4)
      READ(1,20)H,RHO
 20   FORMAT(3X,E10.4/5X,E10.4)
      RETURN
      END
C
C
```

```
      SUBROUTINE WPCHR
      COMMON/PCHR/D1,D2,H,RHO
      WRITE(6,10)
 10   FORMAT(1X,14HPANEL GEOMETRY/)
      WRITE(6,20)D1,D2
 20   FORMAT(1X,3HD1=,E10.4/1X,3HD2=,E10.4)
      WRITE(6,30)H,RHO
 30   FORMAT(1X,2HH=,E10.4/1X,4HRHO=,E10.4//)
      RETURN
      END
C
C
      SUBROUTINE RSPAR
      INTEGER IPTYPE,NPLYS,IPO(8)
      REAL NU1,NU2
      COMMON/PCHR/D1,D2,H,RHO
      COMMON/SPARA/D11,D22,D66,D12,D16,D26,DK,
     *E1,E2,G,NU1,NU2
      COMMON/TYPE/IPTYPE,NPLYS,IPO
      READ(2,10)IPTYPE,NPLYS,IPO
 10   FORMAT(//7X,I1/8X,I2/13X,8I4)
      READ(2,20)E1,E2,G
 20   FORMAT(4X,E10.4/4X,E10.4/4X,E10.4)
      READ(2,30)NU1,NU2
 30   FORMAT(5X,F7.3/5X,F7.3)
      D11=0.0
      D22=0.0
      D66=0.0
      D12=0.0
      D16=0.0
      D26=0.0
      IF(IPTYPE.EQ.0) THEN
      CONST=H**3/12.0
      D11=CONST*E1/(1.0-NU1*NU2)
      D22=CONST*E2/(1.0-NU1*NU2)
      D66=CONST*G
      D12=CONST*E1*NU2/(1.0-NU1*NU2)
      DK=2.0*(D12+2.0*D66)
      END IF
      IF(IPTYPE.EQ.1) THEN
      CALL CBC
      END IF
      RETURN
      END
C
C
      SUBROUTINE CBC
      INTEGER IPTYPE,NPLYS,IPO(8)
      REAL NU1,NU2
      COMMON/PCHR/D1,D2,H,RHO
```

```
      COMMON/SPARA/D11,D22,D66,D12,D16,D26,DK,
     *E1,E2,G,NU1,NU2
      COMMON/TYPE/IPTYPE,NPLYS,IPO
      PARAMETER(PI=3.14159265359)
      Q11=E1/(1.0-NU1*NU2)
      Q22=E2/(1.0-NU1*NU2)
      Q12=NU1*E2/(1.0-NU1*NU2)
      Q66=G
      N2=NPLYS/2
      DZ=H/FLOAT(NPLYS)
      DO 10 K=1,N2
      ZK=H/2.0-FLOAT(K)*DZ
      ZKM1=ZK+DZ
      A=FLOAT(IPO(K))*PI/180.0
      DUM=2.0/3.0*(ZKM1**3-ZK**3)
      QB11=Q11*COS(A)**4+
     *2.0*(Q12+2.0*Q66)*SIN(A)**2*COS(A)**2+
     *Q22*SIN(A)**4
      QB12=(Q11+Q22-4.0*Q66)*SIN(A)**2*COS(A)**2+
     *Q12*(SIN(A)**4+COS(A)**4)
      QB22=Q11*SIN(A)**4+
     *2.0*(Q12+2.0*Q66)*SIN(A)**2*COS(A)**2+
     *Q22*COS(A)**4
      QB16=(Q11-Q12-2.0*Q66)*SIN(A)*COS(A)**3+
     *(Q12-Q22+2.0*Q66)*SIN(A)**3*COS(A)
      QB26=(Q11-Q12-2.0*Q66)*SIN(A)**3*COS(A)+
     *(Q12-Q22+2.0*Q66)*SIN(A)*COS(A)**3
      QB66=(Q11+Q22-2.0*(Q12+Q66))*SIN(A)**2*COS(A)**2+
     *Q66*(SIN(A)**4+COS(A)**4)
      D11=D11+QB11*DUM
      D22=D22+QB22*DUM
      D66=D66+QB66*DUM
      D12=D12+QB12*DUM
      D16=D16+QB16*DUM
      D26=D26+QB26*DUM
 10   CONTINUE
      DK=2.0*(D12+2.0*D66)
      RETURN
      END
C
C
      SUBROUTINE WSPAR
      INTEGER IPTYPE,NPLYS,IPO(8)
      REAL NU1,NU2
      COMMON/PCHR/D1,D2,H,RHO
      COMMON/SPARA/D11,D22,D66,D12,D16,D26,DK,
     *E1,E2,G,NU1,NU2
      COMMON/TYPE/IPTYPE,NPLYS,IPO
      WRITE(6,10)
 10   FORMAT(1X,9HSTIFFNESS/)
```

```
      WRITE(6,20)IPTYPE,NPLYS,IPO
 20   FORMAT(1X,5HTYPE=,1X,I1/1X,6HNPLYS=,1X,I2/1X,
     *12HORIENTATION=,8I4)
      WRITE(6,30)E1,E2,G
 30   FORMAT(1X,3HE1=,E10.4/1X,3HE2=,E10.4/1X,2HG=,E10.4)
      WRITE(6,40)NU1,NU2
 40   FORMAT(1X,4HNU1=,F6.3/1X,4HNU2=,F6.3)
      WRITE(6,50)D11,D22,D66,D12,D16,D26,DK
 50   FORMAT(/1X,4HD11=,E10.4/1X,4HD22=,E10.4/1X,4HD66=,
     *E10.4/1X,4HD12=,E10.4/1X,4HD16=,E10.4/1X,4HD26=,
     *E10.4/1X,4HDK= ,E10.4//)
      RETURN
      END
C
C
      SUBROUTINE RFLIM
      COMMON/LIMIT/FMAX
      READ(3,10)FMAX
 10   FORMAT(//6X,F7.0)
      RETURN
      END
C
C
      SUBROUTINE WFLIM
      COMMON/LIMIT/FMAX
      WRITE(6,10)
 10   FORMAT(1X,11HFREQ. LIMIT/)
      WRITE(6,20)FMAX
 20   FORMAT(1X,5HFMAX=,F7.0//)
      RETURN
      END
C
C
      SUBROUTINE CFREQ
      DIMENSION OMEGA(1000),NMAX(50)
      REAL NU1,NU2
      COMMON/LIMIT/FMAX
      COMMON/NF/MODES,MMAX,NMAX,OMEGA
      COMMON/PCHR/D1,D2,H,RHO
      COMMON/SPARA/D11,D22,D66,D12,D16,D26,DK,
     *E1,E2,G,NU1,NU2
      PARAMETER(PI=3.14159265359)
      MMAX=1000
      MODES=0
      DO 30 M=1,50
      NMAX(M)=0
      DO 10 N=1,50
      I=MODES+N
      RHOH=RHO*H
      CONST=PI**2/SQRT(RHOH)
```

```
      DUM=D11*(M/D1)**4+DK*(M/D1)**2*(N/D2)**2
     *+D22*(N/D2)**4-2.0*D16*(M/D1)**3*(N/D2)-
     *2.0*D26*(M/D1)*(N/D2)**3
      RNFREQ=CONST*SQRT(DUM)
      TEST=RNFREQ/(2.0*PI)
      IF(TEST.GT.FMAX) THEN
      GOTO 20
      ELSE
      NMAX(M)=N
      OMEGA(I)=RNFREQ
      END IF
      IF(I.EQ.1000) THEN
      MODES=1000
      MMAX=M
      GOTO 40
      END IF
 10   CONTINUE
 20   IF(N.EQ.1) THEN
      MMAX=M-1
      GOTO 40
      END IF
      MODES=MODES+NMAX(M)
 30   CONTINUE
 40   RETURN
      END
C
C
      SUBROUTINE SORT
      DIMENSION OMEGA(1000),NMAX(50),NMIN(50)
      DIMENSION MNSORT(1000,2),FREQ(1000)
      COMMON/NF/MODES,MMAX,NMAX,OMEGA
      COMMON/SORT/MNSORT,NOM,FREQ
      PARAMETER(PI=3.14159265359)
      NOM=MODES
      DO 10 M=1,MMAX
      NMIN(M)=1
 10   CONTINUE
      DO 30 I=1,MODES
      J=0
      FMIN=1.0E+10
      DO 20 M=1,MMAX
      K=J+NMIN(M)
      IF(NMIN(M).GT.NMAX(M)) THEN
      TEST=1.0E+10
      ELSE
      TEST=OMEGA(K)
      END IF
      IF(TEST.LT.FMIN) THEN
      FMIN=OMEGA(K)
      MNSORT(I,1)=M
```

```
      MNSORT(I,2)=NMIN(M)
      FREQ(I)=OMEGA(K)/(2.0*PI)
      END IF
      J=J+NMAX(M)
 20   CONTINUE
      M=MNSORT(I,1)
      N=MNSORT(I,2)
      NMIN(M)=N+1
 30   CONTINUE
      RETURN
      END
C
C
      SUBROUTINE WFREQ
      DIMENSION MNSORT(1000,2),FREQ(1000)
      COMMON/SORT/MNSORT,NOM,FREQ
      WRITE(7,10)
 10   FORMAT(1X,19HNATURAL FREQUENCIES/)
      WRITE(7,20)NOM
 20   FORMAT(1X,16HNUMBER OF MODES=,I4/)
      WRITE(7,30)
 30   FORMAT(4X,1HM,13X,1HN,10X,13HFREQUENCY, HZ/)
      DO 50 I=1,NOM
      M=MNSORT(I,1)
      N=MNSORT(I,2)
      WRITE(7,40)M,N,FREQ(I)
 40   FORMAT(1X,I4,10X,I4,12X,F9.4)
 50   CONTINUE
      RETURN
      END
```

The following pages are a listing of program SOUND:

```
      PROGRAM SOUND (INPUT,OUTPUT,TAPE5=INPUT,TAPE6=OUTPUT)
      DIMENSION MNSORT(300,2),FREQ(300)
      DIMENSION AMN(300),PSIMN(300)
      DIMENSION SMN(300),PHIMN(300)
      DIMENSION CLIM(5),EPS(3)
      INTEGER IPTYPE,NPLYS,IPO(8)
      REAL MU,NU,NU1,NU2
      EXTERNAL FTAI,DUMMY
      COMMON/AIC/AMN,PSIMN
      COMMON/DAMP/ZETA11,ZETA99
      COMMON/DIST/R
      COMMON/FFREQ/W
      COMMON/FFUNC/A1,A2,F0,MU,NU,P0
      COMMON/LIMIT/FLIM
      COMMON/MEDIUM/RHO0,C0
      COMMON/NI/NPOINTS
      COMMON/PCHR/D1,D2,H,RHO
      COMMON/SIC/SMN,PHIMN
      COMMON/SORT/MNSORT,NOM,FREQ
      COMMON/SPARA/D11,D22,D66,D12,D16,D26,DK,
     *E1,E2,G,NU1,NU2
      COMMON/TYPE/IPTYPE,NPLYS,IPO
      PARAMETER(PI=3.14159265359)
      OPEN(UNIT=1,FILE='DATPCR',STATUS='OLD')
      OPEN(UNIT=2,FILE='DATPSP',STATUS='OLD')
      OPEN(UNIT=3,FILE='DATNFL',STATUS='OLD')
      OPEN(UNIT=4,FILE='DATDMP',STATUS='OLD')
      OPEN(UNIT=7,FILE='DATMNF',STATUS='OLD')
      OPEN(UNIT=8,FILE='DATFF',STATUS='OLD')
      OPEN(UNIT=9,FILE='DATDIR',STATUS='NEW')
      OPEN(UNIT=10,FILE='DATA',STATUS='NEW')
      R=20.0
      RHO0=1.21
      C0=343.0
      LINES=500
      FMAX=1000.0
      DF=FMAX/LINES
      CLIM(1)=0.0
      CLIM(2)=0.0
      CLIM(3)=PI/2.0
      CLIM(4)=0.0
      EPS(1)=0.1
      EPS(2)=0.0
      EPS(3)=0.0
      ITEXT=0
      CALL RPCHR
```

```
      CALL RSPAR
      CALL RFLIM
      CALL RDAMP
      CALL RFREQ
      CALL RFFUNC
      CALL WPCHR
      CALL WSPAR
      CALL WFLIM
      CALL WDAMP
      CALL WFFUNC
      TEST1=A1/D1
      TEST2=A2/D2
      IF (TEST1.EQ..5.AND.TEST2.EQ..5) THEN
      SYM=4.0
      CLIM(5)=PI/2.0
      ELSE
      SYM=1.0
      CLIM(5)=PI*2.0
      END IF
      WRITE(6,10)
10    FORMAT(1X,10HRESOLUTION)
      WRITE(6,20) LINES,FMAX,DF
20    FORMAT(/1X,6HLINES=,I4/1X,5HFMAX=,
     *F6.0/1X,3HDF=,F10.4)
      WRITE(10,30)
30    FORMAT(//1X,6H"FREQ",4X,5H"PWL",3X,
     *10H"SIGMA,DB",4X,6H"<V2>",
     *6X,5H"PWR",6X,8H"EPS(3)",2X,6H"IERR",1X,6H"PNTS"/)
      DO 50 I=1,LINES
      FF=I*DF
      W=2.0*PI*FF
      V2=0.0
      PWR=0.0
      IERR=0
      PWL=0.0
      SIGLGT=0.0
      NPOINTS=0
      CALL SBIC
      CALL ABIC
      CALL STAMSSV(NOM,MU,NU,V2)
      CALL CAREDB(CLIM,DUMMY,FTAI,EPS,ITEXT,PWR,IERR)
      PWR=SYM*PWR
      SIGMA=PWR/(RHO0*C0*V2*D1*D2)
      PWL=10.0*ALOG10(PWR)+120.0
      SIGLGT=10.0*ALOG10(SIGMA)
      WRITE(10,40)FF,PWL,SIGLGT,V2,PWR,EPS(3),IERR,NPOINTS
40    FORMAT(1X,F8.3,3X,F5.1,3X,F6.1,3X,E10.4,3X,E10.4,3X,
     *E10.4,4X,I1,3X,I5)
50    CONTINUE
      CLOSE(1)
```

```
      CLOSE(2)
      CLOSE(3)
      CLOSE(4)
      CLOSE(7)
      CLOSE(8)
      CLOSE(9)
      CLOSE(10)
      STOP
      END
C
C
      SUBROUTINE RPCHR
      COMMON/PCHR/D1,D2,H,RHO
      READ(1,10)D1,D2
 10   FORMAT(//4X,E10.4/4X,E10.4)
      READ(1,20)H,RHO
 20   FORMAT(3X,E10.4/5X,E10.4)
      RETURN
      END
C
C
      SUBROUTINE RSPAR
      INTEGER IPTYPE,NPLYS,IPO(8)
      REAL NU1,NU2
      COMMON/PCHR/D1,D2,H,RHO
      COMMON/SPARA/D11,D22,D66,D12,D16,D26,DK,
     *E1,E2,G,NU1,NU2
      COMMON/TYPE/IPTYPE,NPLYS,IPO
      READ(2,10)IPTYPE,NPLYS,IPO
 10   FORMAT(//7X,I1/8X,I2/13X,8I4)
      READ(2,20)E1,E2,G
 20   FORMAT(4X,E10.4/4X,E10.4/4X,E10.4)
      READ(2,30)NU1,NU2
 30   FORMAT(5X,F7.3/5X,F7.3)
      D11=0.0
      D22=0.0
      D66=0.0
      D12=0.0
      D16=0.0
      D26=0.0
      IF(IPTYPE.EQ.0) THEN
      CONST=H**3/12.0
      D11=CONST*E1/(1.0-NU1*NU2)
      D22=CONST*E2/(1.0-NU1*NU2)
      D66=CONST*G
      D12=CONST*E1*NU2/(1.0-NU1*NU2)
      DK=2.0*(D12+2.0*D66)
      END IF
      IF(IPTYPE.EQ.1) THEN
      CALL CBC
```

```
      END IF
      RETURN
      END
C
C
      SUBROUTINE CBC
      INTEGER IPTYPE,NPLYS,IPO(8)
      REAL NU1,NU2
      COMMON/PCHR/D1,D2,H,RHO
      COMMON/SPARA/D11,D22,D66,D12,D16,D26,DK,
     *E1,E2,G,NU1,NU2
      COMMON/TYPE/IPTYPE,NPLYS,IPO
      PARAMETER(PI=3.141592653 59)
      Q11=E1/(1.0-NU1*NU2)
      Q22=E2/(1.0-NU1*NU2)
      Q12=NU1*E2/(1.0-NU1*NU2)
      Q66=G
      N2=NPLYS/2
      DZ=H/FLOAT(NPLYS)
      DO 10 K=1,N2
      ZK=H/2.0-FLOAT(K)*DZ
      ZKM1=ZK+DZ
      A=FLOAT(IPO(K))*PI/180.0
      DUM=2.0/3.0*(ZKM1**3-ZK**3)
      QB11=Q11*COS(A)**4+
     *2.0*(Q12+2.0*Q66)*SIN(A)**2*COS(A)**2+
     *Q22*SIN(A)**4
      QB12=(Q11+Q22-4.0*Q66)*SIN(A)**2*COS(A)**2+
     *Q12*(SIN(A)**4+COS(A)**4)
      QB22=Q11*SIN(A)**4+
     *2.0*(Q12+2.0*Q66)*SIN(A)**2*COS(A)**2+
     *Q22*COS(A)**4
      QB16=(Q11-Q12-2.0*Q66)*SIN(A)*COS(A)**3+
     *(Q12-Q22+2.0*Q66)*SIN(A)**3*COS(A)
      QB26=(Q11-Q12-2.0*Q66)*SIN(A)**3*COS(A)+
     *(Q12-Q22+2.0*Q66)*SIN(A)*COS(A)**3
      QB66=(Q11+Q22-2.0*(Q12+Q66))*SIN(A)**2*COS(A)**2+
     *Q66*(SIN(A)**4+COS(A)**4)
      D11=D11+QB11*DUM
      D22=D22+QB22*DUM
      D66=D66+QB66*DUM
      D12=D12+QB12*DUM
      D16=D16+QB16*DUM
      D26=D26+QB26*DUM
 10   CONTINUE
      DK=2.0*(D12+2.0*D66)
      RETURN
      END
C
C
```

```
      SUBROUTINE RFLIM
      COMMON/LIMIT/FLIM
      READ(3,10)FLIM
 10   FORMAT(//6X,F7.0)
      RETURN
      END
C
C
      SUBROUTINE RDAMP
      COMMON/DAMP/ZETA11,ZETA99
      READ(4,10)ZETA11
 10   FORMAT(//8X,E10.4)
      READ(4,20)ZETA99
 20   FORMAT(8X,E10.4)
      RETURN
      END
C
C
      SUBROUTINE RFREQ
      DIMENSION MNSORT(300,2),FREQ(300)
      COMMON/SORT/MNSORT,NOM,FREQ
      READ(7,10)NOM
 10   FORMAT(//17X,I4///)
      DO 30 I=1,NOM
      READ(7,20)MNSORT(I,1),MNSORT(I,2),FREQ(I)
 20   FORMAT(1X,I4,10X,I4,12X,F9.4)
 30   CONTINUE
      RETURN
      END
C
C
      SUBROUTINE RFFUNC
      REAL MU,NU
      COMMON/FFUNC/A1,A2,F0,MU,NU,P0
      READ(8,10) F0,P0
 10   FORMAT(//4X,E10.4/4X,E10.4)
      READ(8,20) MU,NU
 20   FORMAT(////4X,E10.4/4X,E10.4)
      READ(8,30) A1,A2
 30   FORMAT(////4X,E11.5/4X,E11.5)
      RETURN
      END
C
C
      SUBROUTINE WPCHR
      COMMON/PCHR/D1,D2,H,RHO
      WRITE(6,10)
 10   FORMAT(1X,14HPANEL GEOMETRY/)
      WRITE(6,20)D1,D2
 20   FORMAT(1X,3HD1=,E10.4/1X,3HD2=,E10.4)
```

```
      WRITE(6,30)H,RHO
 30   FORMAT(1X,2HH=,E10.4/1X,4HRHO=,E10.4//)
      RETURN
      END
C
C
      SUBROUTINE WSPAR
      INTEGER IPTYPE,NPLYS,IPO(8)
      REAL NU1,NU2
      COMMON/PCHR/D1,D2,H,RHO
      COMMON/SPARA/D11,D22,D66,D12,D16,D26,DK,
     *E1,E2,G,NU1,NU2
      COMMON/TYPE/IPTYPE,NPLYS,IPO
      WRITE(6,10)
 10   FORMAT(1X,9HSTIFFNESS/)
      WRITE(6,20)IPTYPE,NPLYS,IPO
 20   FORMAT(1X,5HTYPE=,1X,I1/1X,6HNPLYS=,
     *1X,I2/1X,12HORIENTATION=,8I4)
      WRITE(6,30)E1,E2,G
 30   FORMAT(1X,3HE1=,E10.4/1X,3HE2=,E10.4/1X,2HG=,E10.4)
      WRITE(6,40)NU1,NU2
 40   FORMAT(1X,4HNU1=,F6.3/1X,4HNU2=,F6.3)
      WRITE(6,50)D11,D22,D66,D12,D16,D26,DK
 50   FORMAT(/1X,4HD11=,E10.4/1X,4HD22=,
     *E10.4/1X,4HD66=,E10.4/1X,4HD12=,E10.4/1X,4HD16=,
     *E10.4/1X,4HD26=,E10.4/1X,4HDK= ,E10.4//)
      RETURN
      END
C
C
      SUBROUTINE WFLIM
      COMMON/LIMIT/FLIM
      WRITE(6,10)
 10   FORMAT(1X,11HFREQ. LIMIT/)
      WRITE(6,20)FLIM
 20   FORMAT(1X,5HFLIM=,F7.0//)
      RETURN
      END
C
C
      SUBROUTINE WDAMP
      COMMON/DAMP/ZETA11,ZETA99
      WRITE(6,10)
 10   FORMAT(1X,7HDAMPING/)
      WRITE(6,20)ZETA11
 20   FORMAT(1X,7HZETA11=,E10.4)
      WRITE(6,30)ZETA99
 30   FORMAT(1X,7HZETA99=,E10.4//)
      RETURN
      END
```

```
C
C
      SUBROUTINE WFFUNC
      REAL MU,NU
      COMMON/FFUNC/A1,A2,F0,MU,NU,P0
      WRITE(6,10)
 10   FORMAT(1X,9HMAGNITUDE/)
      WRITE(6,20) F0,P0
 20   FORMAT(1X,3HF0=,E10.4/1X,3HP0=,E10.4)
      WRITE(6,30)
 30   FORMAT(//1X,5HPHASE/)
      WRITE(6,40) MU,NU
 40   FORMAT(1X,3HMU=,E10.4/1X,3HNU=,E10.4)
      WRITE(6,50)
 50   FORMAT(//1X,15HSHAKER LOCATION/)
      WRITE(6,60) A1,A2
 60   FORMAT(1X,3HA1=,E11.5/1X,3HA2=,E11.5//)
      RETURN
      END
C
C
      SUBROUTINE SBIC
      DIMENSION MNSORT(300,2),FREQ(300)
      DIMENSION PHIMN(300),SMN(300)
      REAL MU,NU,NUM
      COMMON/DAMP/ZETA11,ZETA99
      COMMON/FFREQ/W
      COMMON/FFUNC/A1,A2,F0,MU,NU,P0
      COMMON/PCHR/D1,D2,H,RHO
      COMMON/SIC/SMN,PHIMN
      COMMON/SORT/MNSORT,NOM,FREQ
      PARAMETER(PI=3.14159265359)
      DO 10 I=1,NOM
      M=MNSORT(I,1)
      N=MNSORT(I,2)
      WMN=2.0*PI*FREQ(I)
      ZMN=ZETA11*FREQ(1)/FREQ(I)+ZETA99
      DEN=SQRT((1.0-W**2/WMN**2)**2+(2.0*ZMN*W/WMN)**2)
      NUM=SIN(M*PI*A1/D1)*SIN(N*PI*A2/D2)
      DUM=NUM/DEN
      SMN(I)=4.0*F0/(D1*D2*RHO*H*WMN**2)*DUM
      NUM=2.0*ZMN*W/WMN
      DEN=1.0-W**2/WMN**2
      PHIMN(I)=ATAN2(NUM,DEN)+MU*PI/180.0
 10   CONTINUE
      RETURN
      END
C
C
      SUBROUTINE ABIC
```

```
      DIMENSION MNSORT(300,2),FREQ(300)
      DIMENSION AMN(300),PSIMN(300)
      REAL MU,NU,NUM
      COMMON/AIC/AMN,PSIMN
      COMMON/DAMP/ZETA11,ZETA99
      COMMON/FFREQ/W
      COMMON/FFUNC/A1,A2,F0,MU,NU,P0
      COMMON/PCHR/D1,D2,H,RHO
      COMMON/SORT/MNSORT,NOM,FREQ
      PARAMETER(PI=3.14159265359)
      DO 10 I=1,NOM
      M=MNSORT(I,1)
      N=MNSORT(I,2)
      WMN=2.0*PI*FREQ(I)
      ZMN=ZETA11*FREQ(1)/FREQ(I)+ZETA99
      DEN=SQRT((1.0-W**2/WMN**2)**2+(2.0*ZMN*W/WMN)**2)
      NUM=(1.0-COS(M*PI))*(1.0-COS(N*PI))
      DUM=NUM/DEN
      AMN(I)=4.0*P0/(M*N*PI**2*RHO*H*WMN**2)*DUM
      NUM=2.0*ZMN*W/WMN
      DEN=1.0-W**2/WMN**2
      PSIMN(I)=ATAN2(NUM,DEN)+NU*PI/180.0
 10   CONTINUE
      RETURN
      END
C
C
      SUBROUTINE STAMSSV(NOM,MU,NU,V2)
      DIMENSION SMN(300),AMN(300)
      REAL MU,NU
      COMMON/AIC/AMN
      COMMON/FFREQ/W
      COMMON/SIC/SMN
      PARAMETER( PI=3.14159265359)
      PCOEFF=COS((MU-NU)*PI/180.0)
      DO 10 I=1,NOM
      V2INC=SMN(I)**2+AMN(I)**2+2.0*SMN(I)*AMN(I)*
     *PCOEFF
      V2=V2+V2INC
 10   CONTINUE
      V2=V2*W**2/8.0
      RETURN
      END
C
C
      FUNCTION FTAI(THETA,PHI)
      DIMENSION AMN(300),PSIMN(300)
      DIMENSION SMN(300),PHIMN(300)
      DIMENSION MNSORT(300,2),FREQ(300)
      REAL K
```

```
COMPLEX PCMPLX,PSUM,P2,JM,JN
COMMON/AIC/AMN,PSIMN
COMMON/DIST/R
COMMON/FFREQ/W
COMMON/MEDIUM/RHO0,C0
COMMON/NI/NPOINTS
COMMON/PCHR/D1,D2
COMMON/SIC/SMN,PHIMN
COMMON/SORT/MNSORT,NOM,FREQ
PARAMETER(PI=3.14159265359)
K=W/C0
FF=W/(2.0*PI)
TEST=2.0*FF
CONST=-RHO0*W**2/(2.0*PI*R)
PSUM=(0.0,0.0)
TAI=0.0
NPOINTS=NPOINTS+1
DO 10 I=1,NOM
IF((I.GT.30).AND.(FREQ(I).GT.TEST)) GOTO 20
IF(SMN(I).NE.0.0.OR.AMN(I).NE.0.0) THEN
M=MNSORT(I,1)
N=MNSORT(I,2)
ARG1=K*SIN(THETA)*COS(PHI)
ARG2=ARG1**2
ARG3=M*PI/D1
ARG4=ARG3**2
IF(ARG2.EQ.ARG4) THEN
VR=0.0
VI=D1/2.0*SIGN(1.0,ARG1)
ELSE
DUM=ARG3/(ARG4-ARG2)
ARG=ARG1*D1
VR=DUM*(1.0-COS(M*PI)*COS(ARG))
VI=DUM*(-COS(M*PI)*SIN(ARG))
END IF
JM=CMPLX(VR,VI)
ARG1=K*SIN(THETA)*SIN(PHI)
ARG2=ARG1**2
ARG3=N*PI/D2
ARG4=ARG3**2
IF(ARG2.EQ.ARG4) THEN
VR=0.0
VI=D2/2*SIGN(1.0,ARG1)
ELSE
DUM=ARG3/(ARG4-ARG2)
ARG=ARG1*D2
VR=DUM*(1.0-COS(N*PI)*COS(ARG))
VI=DUM*(-COS(N*PI)*SIN(ARG))
END IF
JN=CMPLX(VR,VI)
```

```
      VR=SMN(I)*COS(PHIMN(I))+AMN(I)*COS(PSIMN(I))
      VI=-SMN(I)*SIN(PHIMN(I))-AMN(I)*SIN(PSIMN(I))
      PSUM=PSUM+CMPLX(VR,VI)*JM*JN
      END IF
 10   CONTINUE
 20   PCMPLX=CONST*PSUM
      P2=PCMPLX*CONJG(PCMPLX)
      TAI=REAL(P2)/(2.0*RHO0*C0)
      FTAI=TAI*R**2*SIN(THETA)
      RETURN
      END
C
C
      SUBROUTINE CAREDB(CLIM,FLIM,FX,EPS,ITEXT,SUM,IERR)
C*************************************************************
C*                                                           *
C* PURPOSE:                                                  *
C*  TO EVALUATE THE DOUBLE INTEGRAL OF F(X,Y)DYDX USING      *
C*  CAUTIOUS ROMBERG INTEGRATION. (THE INTEGRAL IS COM-       *
C*  PUTED BY CALCULATING THE INTEGRAL OVER SUITABLY           *
C*  SMALL SUBINTERVALS OF THE INTERVALS OF INTEGRATION,       *
C*  SIMULTANEOUSLY ALONG THE INNER INTEGRAL AT GIVEN          *
C*  OUTER LIMIT VALUES AND ALONG THE ENTIRE OUTER INTE-       *
C*  GRAL, AND SUMMING THE RESULTS.  THE INTEGRAL OVER         *
C*  EACH SUBINTERVAL IS COMPUTED THROUGH ROMBERG              *
C*  EXTRAPOLATION WHERE THE VALUE OF THE INTEGRAL IS          *
C*  ACCEPTED WHEN THE COMPUTED ERROR IS LESS THAN:            *
C*  MAXIMUM (ABSOLUTE ERROR, RELATIVE ERROR * CURRENT         *
C*           ESTIMATE OF THE INTEGRAL).  )                    *
C*                                                           *
C*                                                           *
C* USE:                                                      *
C*  CALL CAREDB(CLIM,FLIM,FX,EPS,ITEXT,SUM,IERR)             *
C*                                                           *
C*                                                           *
C* PARAMETERS:                                               *
C*                                                           *
C*  CLIM      AN INPUT ONE-DIMENSIONAL ARRAY DIMENSIONED     *
C*  FIVE.  SPECIFIES THE INTEGRATION LIMITS.                 *
C*                                                           *
C*  CLIM(1)  INTEGRATION LIMIT INDICATOR.                    *
C*           =0.  F1(X) AND F2(X) ARE CONSTANT               *
C*                FUNCTIONS.                                 *
C*           =1.  F1(X) AND F2(X) ARE NON-CONSTANT           *
C*                FUNCTIONS.                                 *
C*                                                           *
C*  CLIM(2)  LOWER LIMIT OF INTEGRATION FOR X, A.            *
C*                                                           *
C*  CLIM(3)  UPPER LIMIT OF INTEGRATION FOR X, B.            *
C*                                                           *
```

```
C*  CLIM(4)  LOWER LIMIT OF INTEGRATION FOR Y, F1(X),    *
C*           WHEN CLIM(1)=0.                            *
C*                                                      *
C*  CLIM(5)  UPPER LIMIT OF INTEGRATION FOR Y, F2(X),    *
C*           WHEN CLIM(1)=0.                            *
C*                                                      *
C*  IF CLIM(1)=1., THE PARAMETERS CLIM(4) AND CLIM(5)   *
C*  ARE NOT USED BY SUBROUTINE CAREDB.                  *
C*                                                      *
C*  FLIM      AN INPUT PARAMETER SPECIFYING THE NAME OF *
C*  A USER-PROVIDED SUBROUTINE WITH ARGUMENTS X, P, AND *
C*  Q USED TO EVALUATE THE INNER LIMITS OF INTEGRATION  *
C*  WHEN CLIM(1)=1.  THE ARGUMENTS P AND Q ARE RESPECT- *
C*  IVELY THE LOWER AND UPPER LIMITS F1(X) AND F2(X),   *
C*  EVALUATED AT X.  THE NAME OF THE SUBROUTINE MUST    *
C*  BE DECLARED IN AN EXTERNAL STATEMENT IN THE CALLING *
C*  PROGRAM WHEN CLIM(1)=1.                             *
C*                                                      *
C*  IF CLIM(1)=0., FLIM IS A DUMMY ARGUMENT.  THE USER  *
C*  NEED NOT PROVIDE A SUBROUTINE AND THE EXTERNAL      *
C*  STATEMENT IS NOT NEEDED.                            *
C*                                                      *
C*  FX        AN INPUT PARAMETER SPECIFYING THE NAME OF *
C*  A USER-PROVIDED FUNCTION SUBPROGRAM WITH ARGUMENTS X*
C*  AND Y USED TO EVALUATE F(X,Y).  THE NAME OF THE SUB-*
C*  PROGRAM MUST BE DECLARED IN AN EXTERNAL STATEMENT   *
C*  IN THE CALLING PROGRAM.                             *
C*                                                      *
C*   EPS      AN INPUT/OUTPUT ONE-DIMENSIONAL ARRAY     *
C*   DIMENSIONED THREE SPECIFYING MAXIMUM ALLOWABLE     *
C*   ERROR CRITERIA.                                    *
C*                                                      *
C*  EPS(1)  INPUT VARIABLE CONTAINING THE MAXIMUM       *
C*          ALLOWABLE RELATIVE ERROR.                   *
C*                                                      *
C*  EPS(2)  INPUT VARIABLE CONTAINING THE MAXIMUM       *
C*          ALLOWABLE ABSOLUTE ERROR.                   *
C*                                                      *
C*  EPS(3)  OUTPUT VARIABLE CONTAINING AN ESTIMATE OF   *
C*          THE ERROR IN COMPUTING THE INTEGRAL OVER    *
C*          THE ENTIRE DOUBLE INTERVAL OF INTEGRATION.  *
C*                                                      *
C*  ITEXT      AN INPUT INTEGER CODE PROVIDING THE USER *
C*  WITH THE OPTION OF HAVING CAREDB PRINT OUT IRREGULAR*
C*  FUNCTION BEHAVIOR (INCLUDING END POINT SINGULARI-   *
C*  TIES, JUMP DISCONTINUITIES AND REGIONS INDICATING   *
C*  FUNCTIONAL NOISE), AND INTERVALS OF UNSUCCESSFUL    *
C*  INTEGRATIONS WITH CORRESPONDING ESTIMATES.  THIS    *
C*  PRINTOUT SHOULD ONLY BE REQUESTED FOR PROBLEMS      *
C*  WHICH MUST BE RERUN DUE TO UNSATISFACTORY RESULTS   *
```

```
C*  THE FIRST TIME.                                                  *
C*                                                                   *
C*        ITEXT = 0  NO PRINTOUT REQUESTED.                          *
C*        ITEXT  =  1  PRINTOUT REQUESTED WITH RESPECT
C*                     TO INNER INTEGRAL ONLY.                       *
C*        ITEXT = 2  PRINTOUT REQUESTED WITH RESPECT                 *
C*                     TO OUTER INTEGRAL ONLY.                       *
C*        ITEXT = 3  PRINTOUT ON BOTH INTEGRALS                      *
C*                     REQUESTED                                     *
C*                                                                   *
C*  SUM       AN OUTPUT VARIABLE CONTAINING THE COMPUTED            *
C*  VALUE OF THE DOUBLE INTEGRAL.  (THE VALUES OF SUM                *
C*  AND EPS(3) SHOULD BE CONSIDERED FOR ALL POSSIBLE                 *
C*  RETURNS - SEE IERR.)                                             *
C*                                                                   *
C*  IERR       AN OUTPUT ERROR PARAMETER                             *
C*  =0  INTEGRATION SUCCESSFUL - NORMAL RETURN                       *
C*       (RELATIVELY SMOOTH INTEGRAND)                               *
C*  =1  INTEGRATION SUCCESSFUL  (WITH RESPECT TO AT                  *
C*        LEAST ONE VALUE OF X, FUNCTION SINGULARITIES               *
C*        WITHIN THE INNER INTEGRAL WERE SUCCESSFULLY                *
C*        HANDLED DURING THE INTEGRATION PROCESS.)                   *
C*  =2  INTEGRATION SUCCESSFUL  (IN ONE OR MORE SUB-                 *
C*        INTERVALS OF THE INTERVALS OF INTEGRATION,                 *
C*        FUNCTION SINGULARITIES IN X, OR BOTH X AND Y,              *
C*        WERE SUCCESSFULLY HANDLED DURING THE INTE-                 *
C*        GRATION PROCESS.)                                          *
C*  =3  INTEGRATION SUCCESSFUL  (WITH RESPECT TO AT                  *
C*        LEAST ONE VALUE OF X, NO REGULAR FUNCTION                  *
C*        BEHAVIOR WAS DETECTED WITHIN THE INNER INTE-               *
C*        GRAL BUT THE CONVERGENCE CRITERION WAS SATIS-              *
C*        FIED.)  (THE INTEGRAL VALUE SHOULD BE ACCEPTED*
C*        WITH CAUTION.)                                             *
C*  =4  INTEGRATION SUCCESSFUL  (IN ONE OR MORE SUB-                 *
C*        INTERVALS OF BOTH INTERVALS OF INTEGRATION NO              *
C*        REGULAR FUNCTION BEHAVIOR WAS DETECTED IN X,               *
C*        OR BOTH X AND Y, BUT THE CONVERGENCE CRI-                  *
C*        TERION WAS SATISFIED.)  (THE INTEGRAL VALUE                *
C*        SHOULD BE ACCEPTED WITH CAUTION.)                          *
C*  =5  UNSUCCESSFUL INTEGRATION  (IN SUBROUTINE                     *
C*        QXZ056,*QXZNA508                                           *
C*        THE STORAGE ARRAY, *TS*, CONTAINING THE FUNC-              *
C*        TION VALUES STILL TO BE USED DURING THE INTE-              *
C*        GRATION PROCESS ALONG Y AND AT SOME VALUE OF               *
C*        X IS EXHAUSTED RELATIVE TO SUPPLIED ERROR                  *
C*        CRITERION.)                                                *
C*  =6  UNSUCCESSFUL INTEGRATION  (WHILE EVALUATING THE              *
C*        FUNCTION ALONG Y AT A GIVEN VALUE OF X, A                  *
C*        SUBINTERVAL SMALLER THAN THE MINIMUM ALLOW-                *
C*        ABLE STEP IS REQUESTED, OR THE MAXIMUM NUMBER              *
```

```
C*         OF SUBINTERVALS STILL TO BE CONSIDERED EX-    *
C*         CEEDS THE ALLOWABLE MAXIMUM SIZE OF THE SUB-  *
C*         INTERVAL STACK.)                              *
C*   =7  UNSUCCESSFUL INTEGRATION  (THE STORAGE ARRAY,   *
C*         *TS*, IS EXHAUSTED RELATIVE TO SUPPLIED ERROR *
C*         CRITERION.)                                   *
C*   =8  UNSUCCESSFUL INTEGRATION  (A SUBINTERVAL SMALL- *
C*         ER THAN THE MINIMUM ALLOWABLE STEP IS REQUES- *
C*         TED, OR THE MAXIMUM NUMBER OF SUBINTERVALS    *
C*         STILL TO BE CONSIDERED EXCEEDS THE ALLOWABLE  *
C*         MAXIMUM SIZE OF THE SUBINTERVAL STACK.)       *
C*   =9  INTEGRATION SUCCESSFUL (THE INNER INTEGRAL LIMIT*
C*         SMALLER THAN MINIMUN ALLOWABLE STEP ONE OR    *
C*         MORE TIMES DURING THE INTEGRATION PROCESS. A  *
C*         SINGLE TRAPEZOIDAL SUM IS USED TO ESTIMATE THE*
C*         INTEGRAL AND INTEGRATION CONTINUES. )         *
C*                                                       *
C*   UPON RETURN FROM HIS PARAMETER SHOULD BE            *
C*   TESTED IN THE CALLING PROGRAM.                      *
C*                                                       *
C*     REQUIRED ROUTINES     QXZ056      QXZNA509        *
C*                                                       *
C*     LANGUAGE                          FORTRAN         *
C*                                                       *
C*     AUTHOR         /   IMPLEMENTER                    *
C*     COMPUTER SCIENCES / ACD PROGRAMMER SUPPORT        *
C*   CORPORATION         GROUP, EXT. 3548                *
C*                                                       *
C*     DATE RELEASED                    JUNE 1975        *
C*                                                       *
C*     LATEST REVISION                  APRIL 1983       *
C*                                                       *
C*******************************************************
```

The following pages are a listing of program PREDICT:

```
      PROGRAM PREDICT
      REAL PWL(500),SIGMA(500),V2(500),PWR(500)
      REAL SDATA(500,2),ADATA(500,2),PRED(500,2)
      REAL FF,DEN,DNUM,DUM,DIFF,TEST
      COMMON/INPUT/PWL,SIGMA,V2,PWR
      CONST=40.695
      WRITE(*,10)
10    FORMAT(/1X,' PLACE THE INPUT DATA DISK IN SLOT B:'/)
      WRITE(*,20)
20    FORMAT(/1X,' PLACE THE OUTPUT DATA DISK IN SLOT A:'/)
      PAUSE
      WRITE(*,30)
30    FORMAT(/1X,' ENTER THE NAME OF THE STRUCTUREBORNE DATA
     *FILE'/)
      OPEN(1,FILE=' ',STATUS='OLD')
      WRITE(*,40)
40    FORMAT(/1X,' ENTER THE NAME OF THE AIRBORNE DATA
     *FILE'/)
      OPEN(2,FILE=' ',STATUS='OLD')
      WRITE(*,50)
50    FORMAT(/1X,' ENTER THE NAME OF THE COMBINED INPUTS DATA
     *FILE'/)
      OPEN(3,FILE=' ',STATUS='OLD')
60    OPEN(4,FILE='PREDICT.PRN',STATUS='NEW')
      WRITE(*,70)
70    FORMAT(/1X,' TANDY 2000 READING THE STRUCTUREBORNE DATA
     *FILE'/)
      CALL RFILE(1)
      CLOSE(1)
      DO 80 J=1,500
      SDATA(J,1)=PWL(J)
      SDATA(J,2)=10.0**(SIGMA(J)/10.0)
80    CONTINUE
      WRITE(*,90)
90    FORMAT(/1X,' TANDY 2000 READING THE AIRBORNE DATA
     *FILE'/)
      CALL RFILE(2)
      CLOSE(2)
      DO 100 J=1,500
      ADATA(J,1)=PWL(J)
      ADATA(J,2)=10.0**(SIGMA(J)/10.0)
100   CONTINUE
      WRITE(*,110)
110   FORMAT(/1X,' TANDY 2000 READING THE COMBINED INPUTS
     *DATA FILE'/)
      CALL RFILE(3)
```

```
      CLOSE(3)
      WRITE(*,120)
  120 FORMAT(/1X,' TANDY 2000 NOW BUSY COMPUTING THE
     *RESULTS'/)
      DO 130 J=1,500
      DNUM=SDATA(J,2)*(PWR(J)-ADATA(J,2)*CONST*V2(J))
      DEN=SDATA(J,2)-ADATA(J,2)
      DIFF=10.0*ALOG10(ADATA(J,2)/SDATA(J,2))
      TEST=ABS(DIFF)
      IF(TEST.LT.2.0) THEN
      PRED(J,1)=0.0
      ELSE
      DUM=DNUM/DEN
      IF(DUM.LE.0.0) THEN
      PRED(J,1)=0.0
      ELSE
      PRED(J,1)=10.0*ALOG10(DUM)+120.0
      END IF
      END IF
  130 CONTINUE
      DO 140 J=1,500
      DNUM=ADATA(J,2)*(PWR(J)-SDATA(J,2)*CONST*V2(J))
      DEN=ADATA(J,2)-SDATA(J,2)
      DIFF=10.0*ALOG10(ADATA(J,2)/SDATA(J,2))
      TEST=ABS(DIFF)
      IF(TEST.LT.2.0) THEN
      PRED(J,2)=0.0
      ELSE
      DUM=DNUM/DEN
      IF(DUM.LE.0.0) THEN
      PRED(J,2)=0.0
      ELSE
      PRED(J,2)=10.0*ALOG10(DUM)+120.0
      END IF
      END IF
  140 CONTINUE
      WRITE(*,150)
  150 FORMAT(/1X,' TANDY 2000 NOW WRITING THE RESULTS TO
     *DISK'/)
      DO 170 J=1,500
      FF=2.0*FLOAT(J)
      WRITE(4,160)FF,PWL(J),SDATA(J,1),PRED(J,1),ADATA(J,1),
     *PRED(J,2)
  160 FORMAT(1X,F8.3,1X,F6.1,1X,F6.1,1X,F6.1,1X,F6.1,1X,F6.1)
  170 CONTINUE
      CLOSE(4)
      WRITE(*,180)
  180 FORMAT(/1X,' PROGRAM COMPLETE'/)
      STOP
      END
```

```
C
C
      SUBROUTINE RFILE(IUNIT)
      REAL PWL(500),SIGMA(500),V2(500),PWR(500)
      INTEGER IUNIT
      COMMON/INPUT/PWL,SIGMA,V2,PWR
      READ(IUNIT,10)
 10   FORMAT(////)
      DO 30 J=1,500
      READ(IUNIT,20)PWL(J),SIGMA(J),V2(J),PWR(J)
 20   FORMAT(13X,F5.1,3X,F6.1,3X,E10.4,3X,E10.4)
 30   CONTINUE
      RETURN
      END
```

Appendix X

VALIDATION OF THE COMPUTER PROGRAMS

A. GRAPHICAL APPROACH

It was decided that several simple tests of programs MODAL and SOUND should be performed to insure that the these programs were operating correctly (free of bugs). The tests were designed so that the results produced by the programs were expected to exhibit simple physical principles known in advance. The tests were also designed so that the results could be presented in simple graphical form. This graphical approach provided a reliable method for debugging the programs almost at a glance.

B. VALIDATION OF PROGRAM MODAL

It was decided that an acceptable test of program MODAL (the program which performs the eigenvalue analysis) would be to plot the natural frequencies computed by the program versus mode numbers m and n. This should be a good test of the program since an important characteristic of this type of plot (for plates and shells) is known in advance. In reference 56, it is shown that one of the characteristics of the flexural modes of all plates and shells is that as mode numbers m and n increase without bound, the various curves of natural frequency versus mode number m, obtained for different values of mode number n, tend to collapse on top

of one another. (For example, see reference 56, figure 5.5.2.)

A small computer program was written so that the natural frequencies computed by program MODAL and stored in file DATMNF could be called up and plotted versus mode numbers m and n. An example of the output produced by this program is given in figure (AX-1). The data shown in figure (AX-1) are for the AA 2024 aluminum plate (plate no. 1). From the data in this figure, it is seen that the natural frequencies computed by program MODAL exhibit the expected physical characteristic. Similar results were obtained for plates 2 through 6.

C. VALIDATION OF PROGRAM SOUND

Since program SOUND was the workhorse of the analytical study, the tests of this program were more extensive. The tests hinged on checks of two simple quantities, however. First, directivity of the sound radiation was checked by plotting acoustic intensity versus azimuthal angle (for different values of the polar angle), and secondly, the input parameters to program SOUND were adjusted so that the coincidence phenomenon could be observed and verified in terms of the radiation efficiency of the structure.

Checking Sound Field Directivity

Plots of sound field directivity provided a graphical means for checking at least three different physical principles. The directivity plots also give the programmer an idea of what the numerical integration routine is using to compute the overall sound power radiated. (It should be noted that the numerical integration routine, CAREDB, is by far the largest and most complicated portion of program SOUND.)

First of all, directivity plots provide a means of checking symmetry. For example, the sound field produced by two of the three forcing functions used in this study, viz. the normally incident acoustic input and the point vibrational input located at the center of the plate, should be symmetric about the β_1 ($\phi = 0$) and the β_2 ($\phi = 90$) axes. Conversely, the sound field produced by the third forcing function, viz. the point vibrational input located near the corner of the plate, should have no axis of symmetry.

Secondly, directivity plots give an indication of the degree of evanescence in the sound field. Since structure-borne noise tends to be an inefficient form of noise radiation, the sound field produced by a point vibrational input to a plate should be very reactive and highly directional in character. In contrast, a normally incident, spatially

uniform acoustic input produces a vibrational response that generates noise much more efficiently. Therefore, the sound field associated with the airborne noise is expected to be much less directional in character by comparison (more like the sound field of a plane wave or a simple monopole).

Thirdly, directivity plots permit examination of the frequency dependent characteristics of the sound field. For example, as the forcing frequency becomes larger, more and more higher order vibrational modes participate in the noise generation. As long as the forcing frequency is below coincidence, the higher order modes will be inefficient, highly directional noise radiators. This means that as the forcing frequency is increased, the sound field (and therefore the directivity plots) should become more directional.

As part of the validation procedure, program SOUND was modified so that these properties of frequency dependence, evanescence, and symmetry (or asymmetry) could be observed and verified. The program was altered so that each time the numerical integration routine calls function FTAI (the routine which calculates the intensity at a point in space), the azimuthal angle ϕ, the polar angle θ, and the outward normal component of the acoustic intensity I_n are recorded in the data file DATDIR. (The portions of the program which take advantage of symmetry were removed. Also note that the original listing of program SOUND in Appendix

IX defines and opens file DATDIR but does not use it.) Since the storage of ϕ, Θ, and I_n for each call of function FTAI for a 500 line spectra would produce an excessively large data base, program SOUND was further modified so that data was computed for only one forcing frequency at a time (instead of 500).

For the purposes of validating program SOUND, results are presented here for the cases of the forcing frequency equal to 500 Hz and the forcing frequency equal to 1000 Hz. From the discussion of the calculation scheme given in Appendix IX, it can be seen that if the forcing frequency is 500 Hz, all of the modes with natural frequencies between 0 and 1000 Hz participate in the analysis. Similarly, if the forcing frequency is 1000 Hz, all of the modes with natural frequencies between 0 and 2000 Hz participate in the analysis.

In addition to the restrictions on the forcing frequency, the results given here are limited to the cases of polar angle Θ equal to 22.5, 45, 67.5 and 90 degrees. Although program SOUND generates data for many, many other values of the angle Θ (in fact, it must do so to perform the numerical integration), it was decided that the data from the four angles stated were fairly representative of the entire sound field and certainly adequate for validation of the program.

The results of test runs of the modified program SOUND for the case of the AA 2024 aluminum plate (plate no. 1) subjected to a 1 Pa peak, normally incident, spatially uniform acoustic load at forcing frequencies of 500 and 1000 Hz are presented in figures (AX-2) and (AX-3), respectively. Note that for the case of the forcing frequency equal to 500 Hz that the sound field is nearly uniform with only small variations in I_n (versus ϕ) even for large values of θ (e.g. $\theta = 90$). In contrast, the plots of I_n versus ϕ in figure (AX-3) (forcing frequency equal to 1000 Hz) show more directional preference for the noise radiation with the larger and more rapid variations occuring at the larger values of θ (e.g. $\theta = 67.5, 90$). Thus, the two figures verify that the sound field becomes more directional as the forcing frequency is increased. Also note that the directivity plots in the two figures are symmetric about the β_1 ($\phi = 0$) and the β_2 ($\phi = 90$) axes as expected.

The results of test runs of program SOUND for the case of the AA 2024 aluminum plate subjected to a .01 N peak, point vibrational load located at the center of the plate at forcing frequencies of 500 and 1000 Hz are presented in figures (AX-4) and (AX-5), respectively. Note that in figure (AX-4), the sound field possesses much larger variations in the intensity level I_n versus ϕ for all values of θ when compared to the corresponding cases of the acoustic

input (figure (AX-2)). Figures (AX-4) and (AX-5) also corroborate the earlier findings for the acoustic input by once again indicating that the sound field becomes more directional as the forcing frequency is increased. Again note that the directivity plots in figures (AX-4) and (AX-5) are symmetric about the β_1 (ϕ = 0) and the β_2 (ϕ = 90) axes as expected.

Finally, the results of test runs of program SOUND for the case of the AA 2024 aluminum plate subjected to .01 N peak, point vibrational load located near the corner of the plate (α_1 = .06033 m and α_2 = .13547 m) at forcing frequencies of 500 and 1000 Hz are presented in figures (AX-6) and (AX-7), respectively. The first and most obvious characteristic of the plots in these two figures is that the intensity level I_n is no longer symmetric (as expected) about any axis in ϕ or Θ. Also, recall that the plots in figures (AX-2) through (AX-5) were, for the most part, limited to roughly a 15 dB variation in the intensity level over the hemispherical surface. (Only one case in figure (AX-4) shows substantially more than a 15 dB variation.) Figures (AX-6) and (AX-7), however, tend to exhibit larger variations than 15 dB in the intensity level. Figure (AX-7) also exhibits larger differences in the shape of the curves (as the angle Θ is varied) than was observed in the previous cases.

All of these observations tend to confirm that program SOUND is free of errors and producing the correct (and expected) results.

Checking for the Coincidence Effect

Thus far, no specific evidence has been offered to show that the absolute values of the sound power radiated by the plates or the vibrational response of the plates predicted by program SOUND are correct. Since the radiation efficiency calculations involve both the acoustic and dynamic portions of the analysis, the calculations of σ are the best candidate for checking to be sure that no shift (up or down) has occured in the predicted values of either the sound power or the space-time averaged mean-square surface velocity.

It might be argued that the fact that σ never exceeded the value 1 (0 on the dB scale) in any of the more than 10000 separate calculations of radiation efficiency presented in this paper is very strong evidence in itself that the absolute values predicted by program SOUND are correct. The close agreement in the radiation efficiency levels predicted analytically and those measured for plates 1 through 6 is offered as further evidence that the predicted levels are correct. In order to further establish the credibility of the absolute levels predicted by program SOUND, it was

decided that a case should be run in which the radiation efficiency is expected to exceed the value 1.

From the discussions contained in reference 48, it is clear that the only frequency region in which the radiation efficiency σ is expected to exceed the value 1 for a simply supported flat plate is near the critical frequency. Plates 1 through 6 all have critical frequencies which are much greater than 1000 Hz (outside the range of analysis). Therefore, in order to observe the coincidence phenomenon, it was necessary to find (or invent) a plate which has its critical frequency in the 0 to 1000 Hz frequency range. Since the author was unaware of any material which (when made into a plate of comparable size and without the aid of stiffeners) would meet this requirement, it was decided to invent an imaginary plate with the desired qualities. Therefore, program SOUND was run for the case of a plate that is the same size as plate no. 1 (.79 mm thick AA 2024 aluminum) except that it is 5 times thicker and is constructed of an imaginary material. The imaginary material has a density that is exactly the same as the aluminum (2.22 kg/m^2) but has moduli of elasticity and rigidity (E and G) that are exactly 10 times greater. Simple calculations using equation (A2.20) show that this plate has only two modes with natural frequencies in the 0 - 2000 Hz range and only one of these two occurs within the 0 - 1000 Hz range.

Thus, the fundamental frequency of this plate is found to be roughly 717 Hz. Using equation (A1.57), the calculated critical frequency of this plate is found to be roughly 954 Hz. Since, in this case, the response of the plate is controlled almost exclusively by the fundamental mode, there is expected to be little or no difference in the airborne and structureborne radiation efficiencies of the plate.

Figures (AX-8) and (AX-9) show the results of the computations for a 1 Pa peak, normally incident, spatially uniform acoustic load, and a .01 N peak, point vibrational load located near the corner of the plate (α_1 = .06033 m and α_2 = .13547 m). Figure (AX-8) shows that, as expected, there is virtually no difference in the radiation efficiencies resulting from the two forcing functions. Futhermore, the radiation efficiency σ exceeds the value 1 (0 dB) slightly in advance of the critical frequency of 954 Hz as predicted by the theory (see reference 48). Figure (AX-9) shows that the peak noise radiation occurs near the fundamental mode at 717 Hz. This result was expected since the plate's level of vibration should peak in this range. Figure (AX-9) also shows that the acoustic input produces more noise radiation than the vibrational input. This result was also anticipated since the net force input to the plate by the airborne forcing function is roughly ten times

the net force that is input by the structureborne forcing function.

The author contends that these results, taken together with the results of the directivity studies, and the results presented for plates 1 through 6 serve as adequate proof that program SOUND is free of bugs.

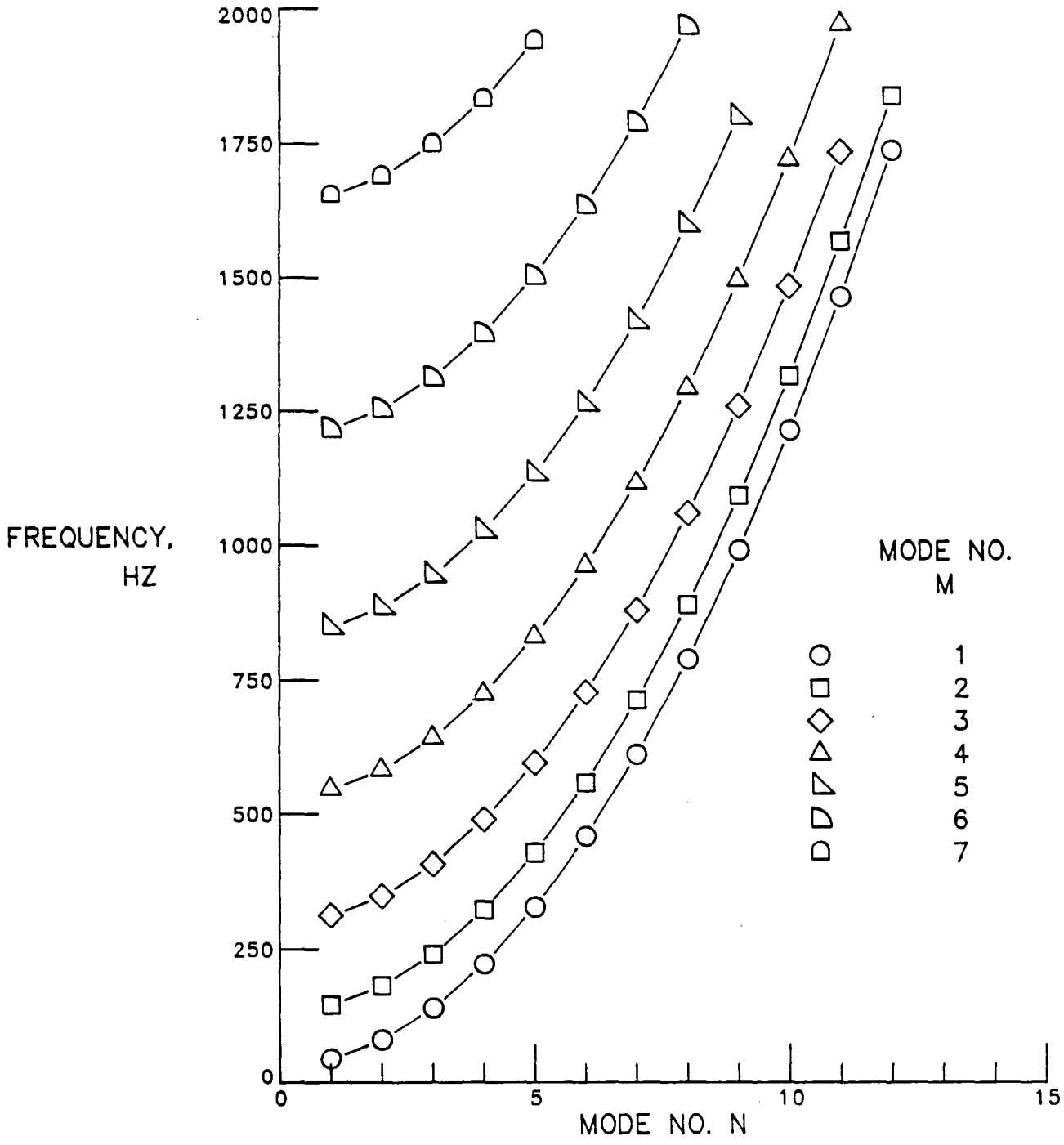

Figure (AX-1) -- Natural frequencies versus mode number m for different values of mode number n for plate no. 1.

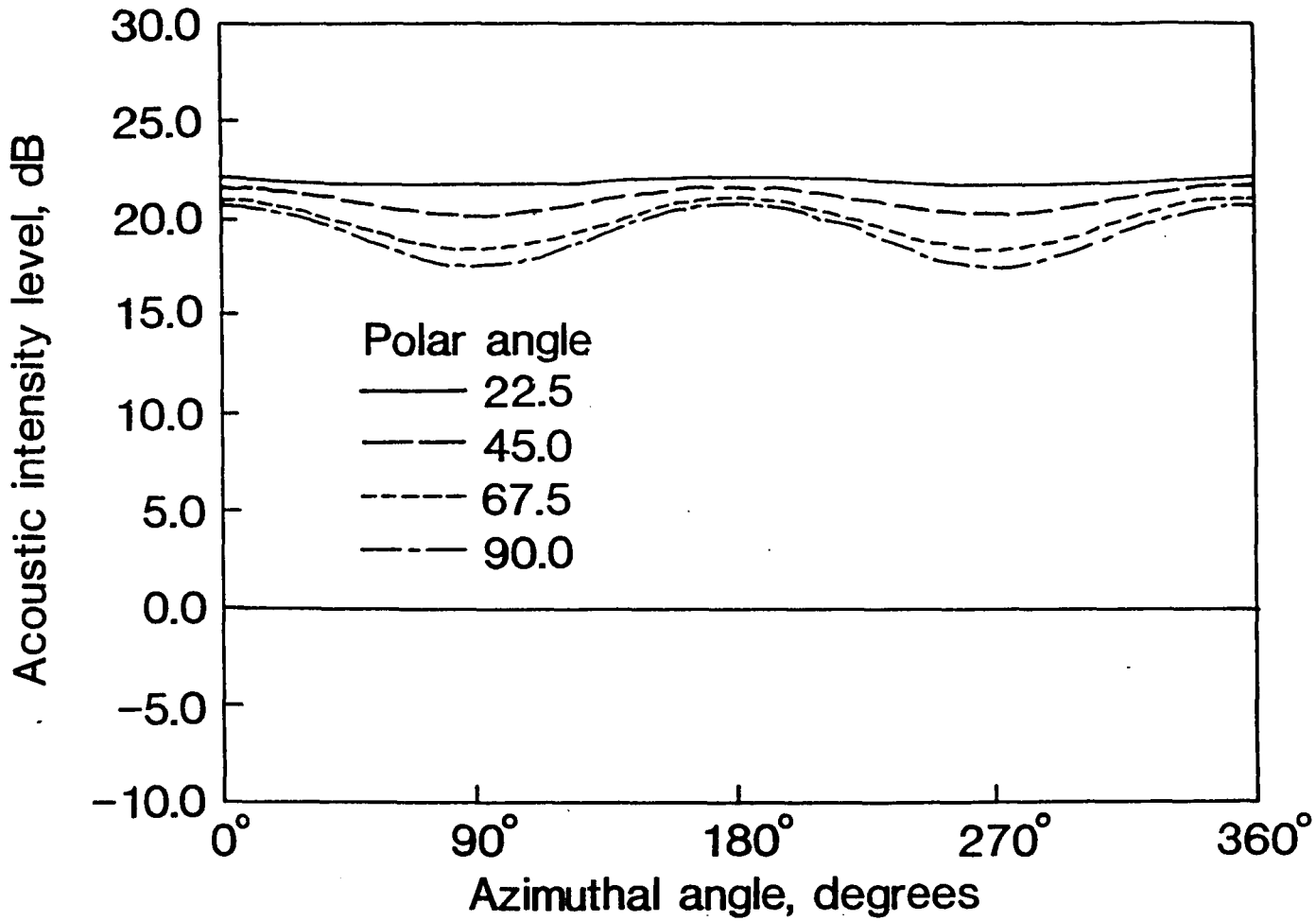

Figure (AX-2) -- Plate no. 1 directivity plots at 20 m distance for a 1 Pa peak, normally incident, spatially uniform acoustic input with a forcing frequency of 500 Hz.

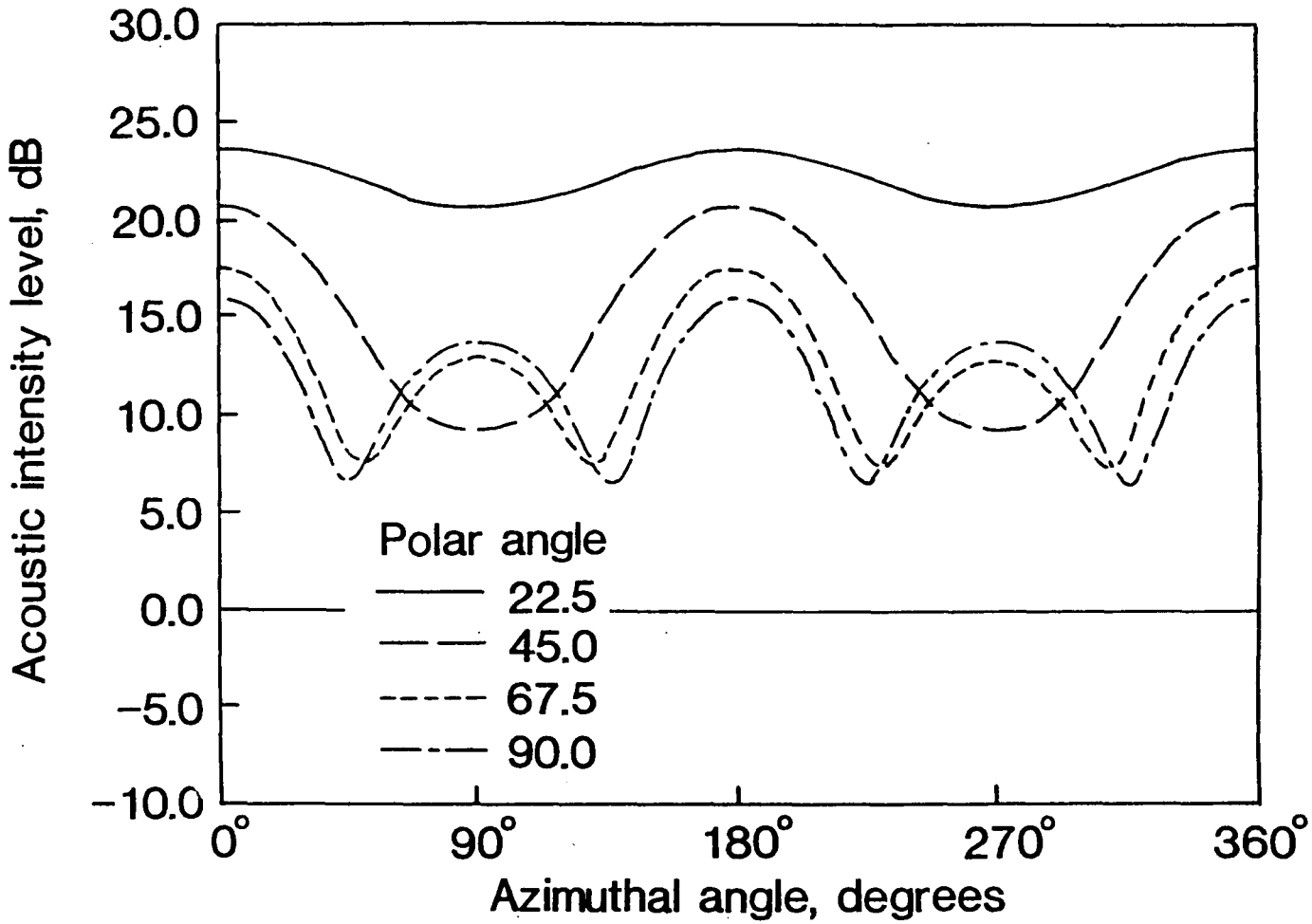

Figure (AX-3) -- Plate no. 1 directivity plots at 20 m distance for a 1 Pa peak, normally incident, spatially uniform acoustic input with a forcing frequency of 1000 Hz.

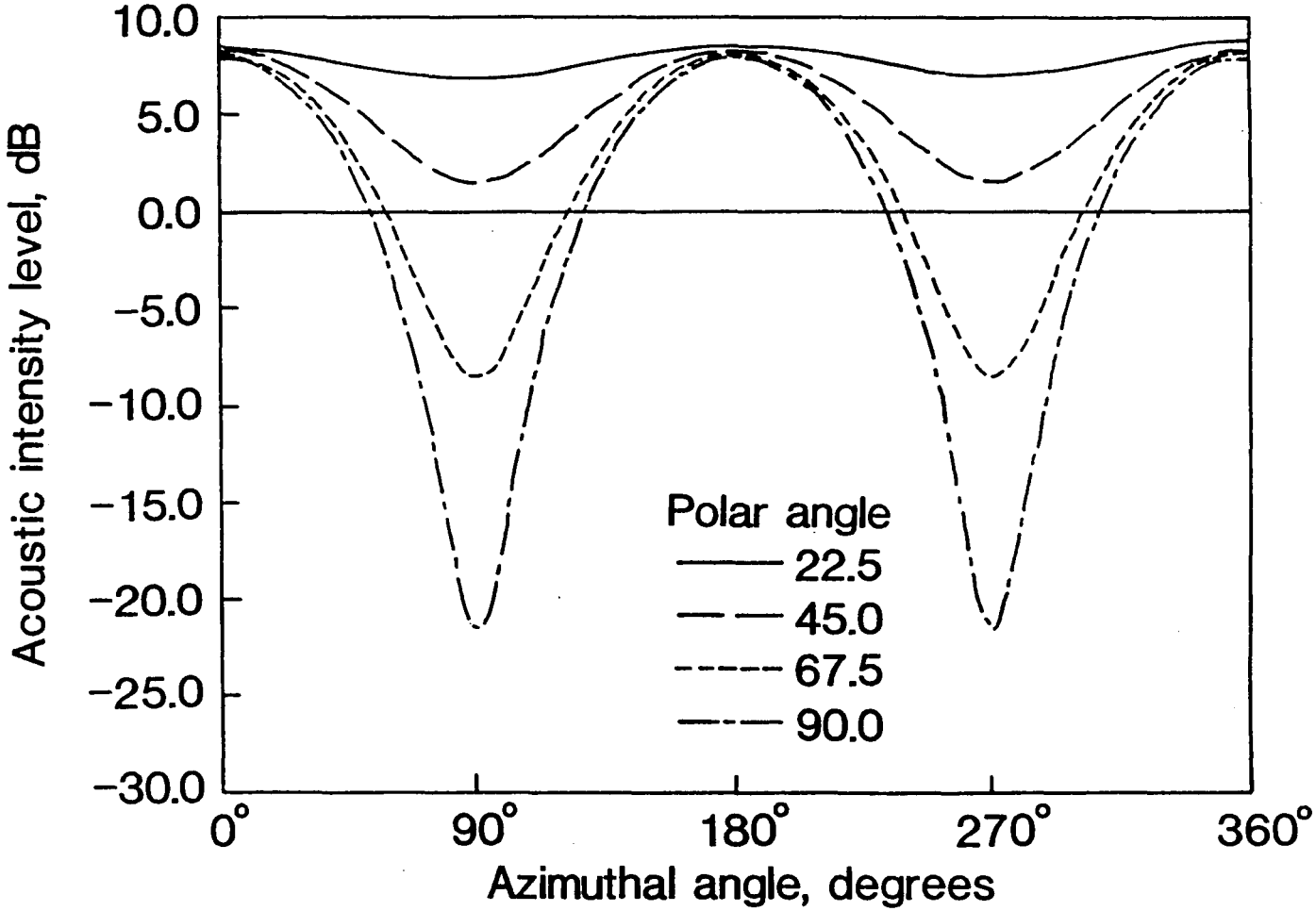

Figure (AX-4) -- Plate no. 1 directivity plots at 20 m distance for a .01 N peak, point vibrational input at the center of the plate with a forcing frequency of 500 Hz.

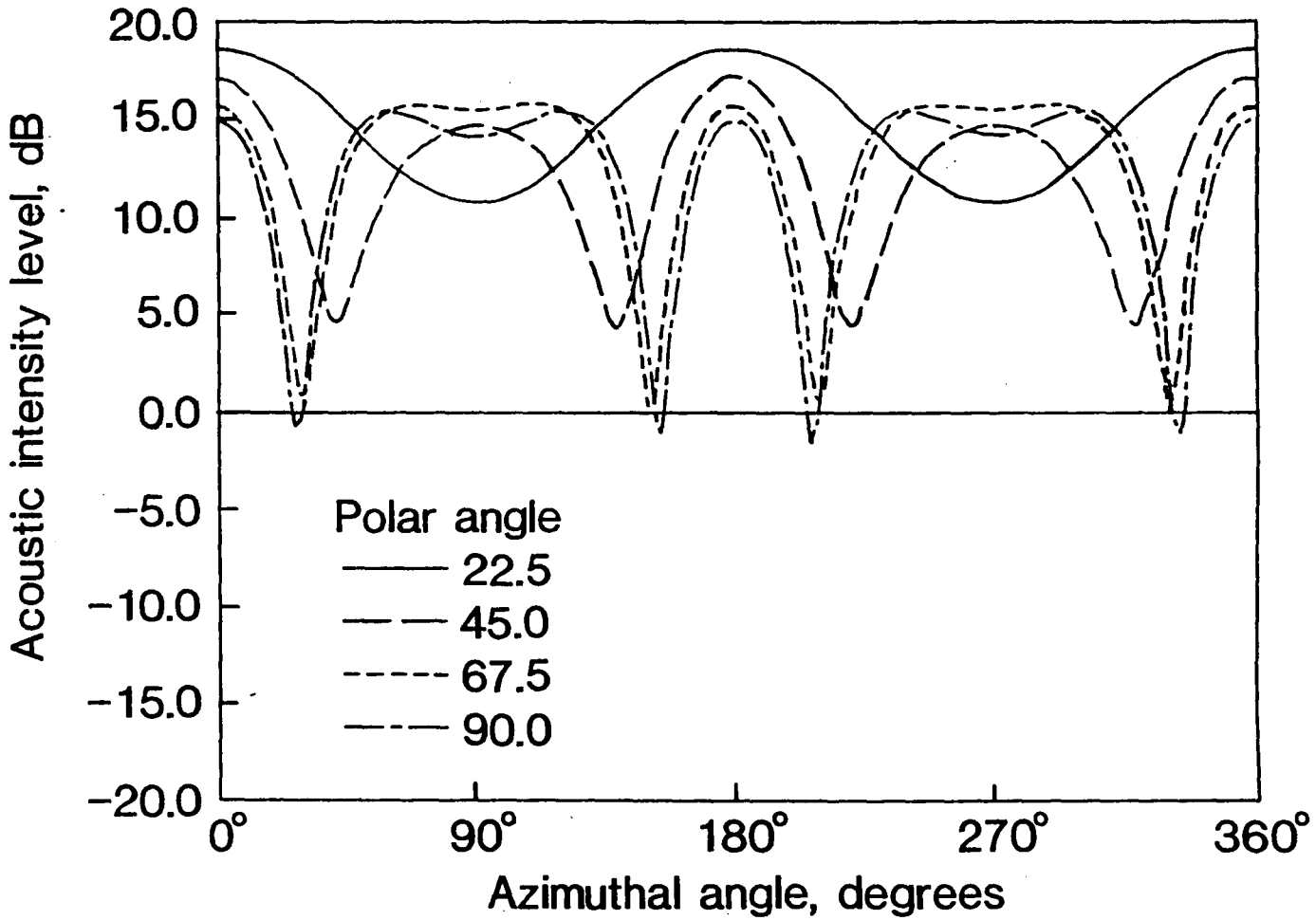

Figure (AX-5) -- Plate no. 1 directivity plots at 20 m distance for a .01 N peak, point vibrational input at the center of the plate with a forcing frequency of 1000 Hz.

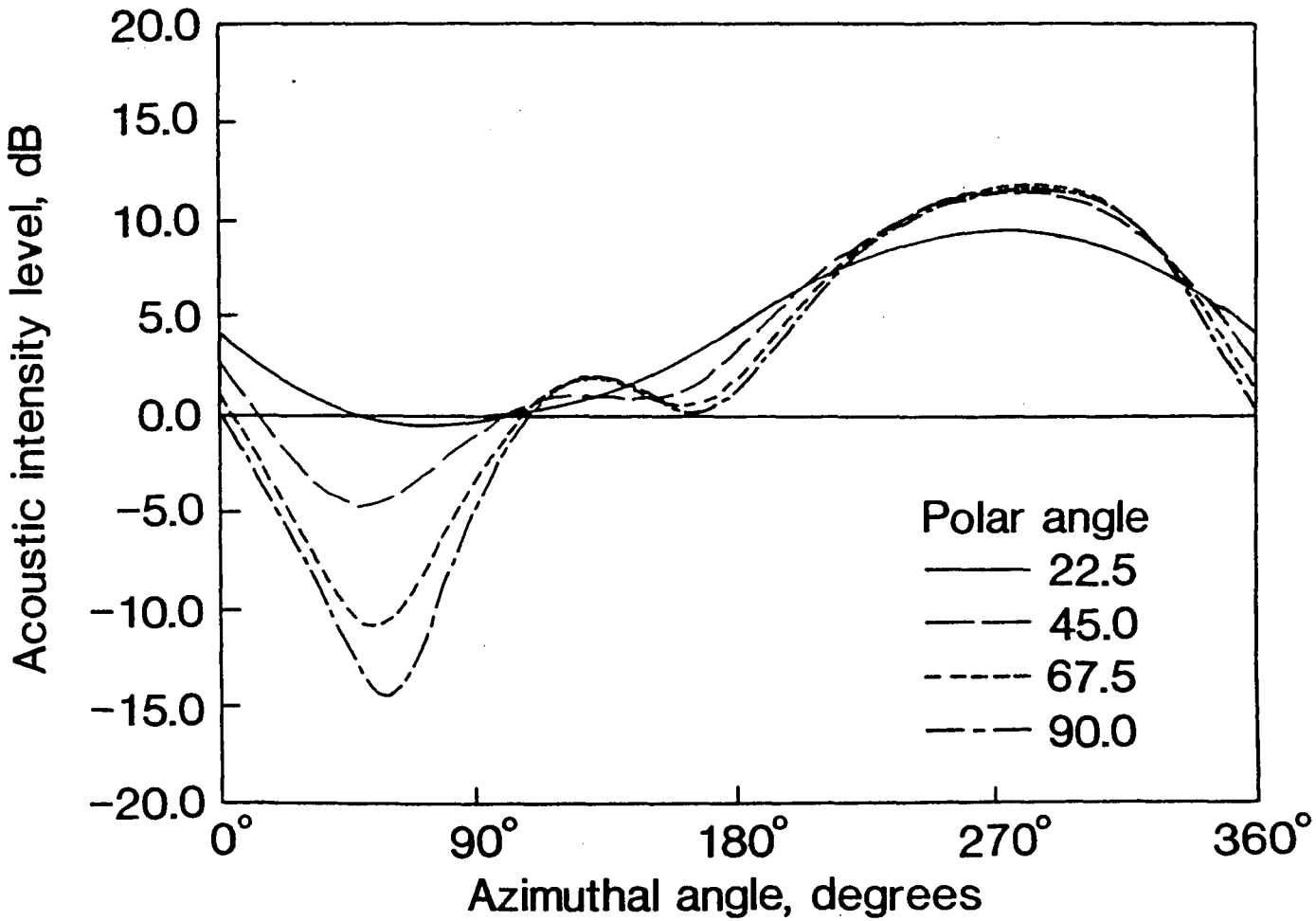

Figure (AX-6) -- Plate no. 1 directivity plots at 20 m distance for a .01 N peak, point vibrational input near the corner of the plate with a forcing frequency of 500 Hz.

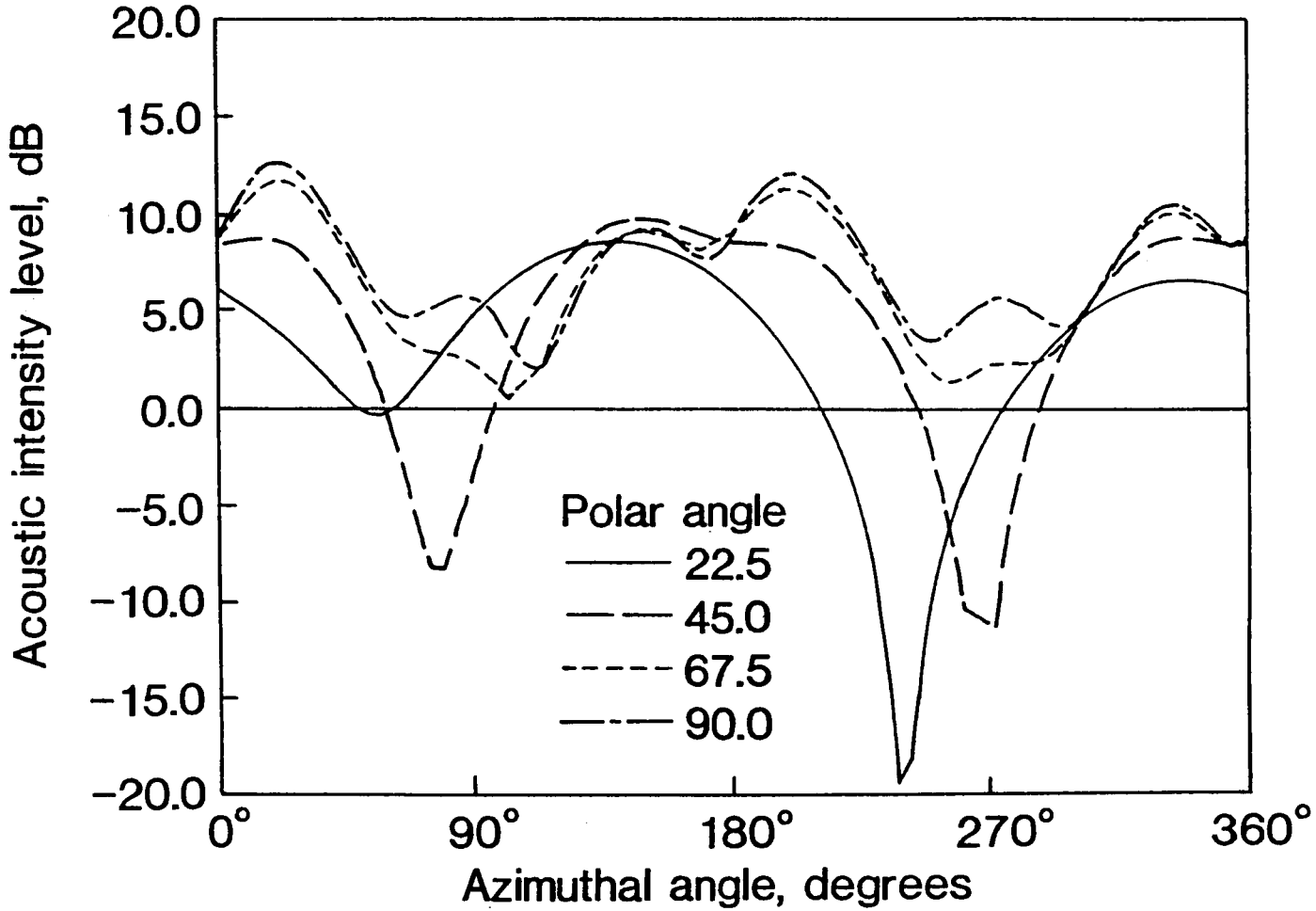

Figure (AX-7) -- Plate no. 1 directivity plots at 20 m distance for a .01 N peak, point vibrational input near the corner of the plate with a forcing frequency of 1000 Hz.

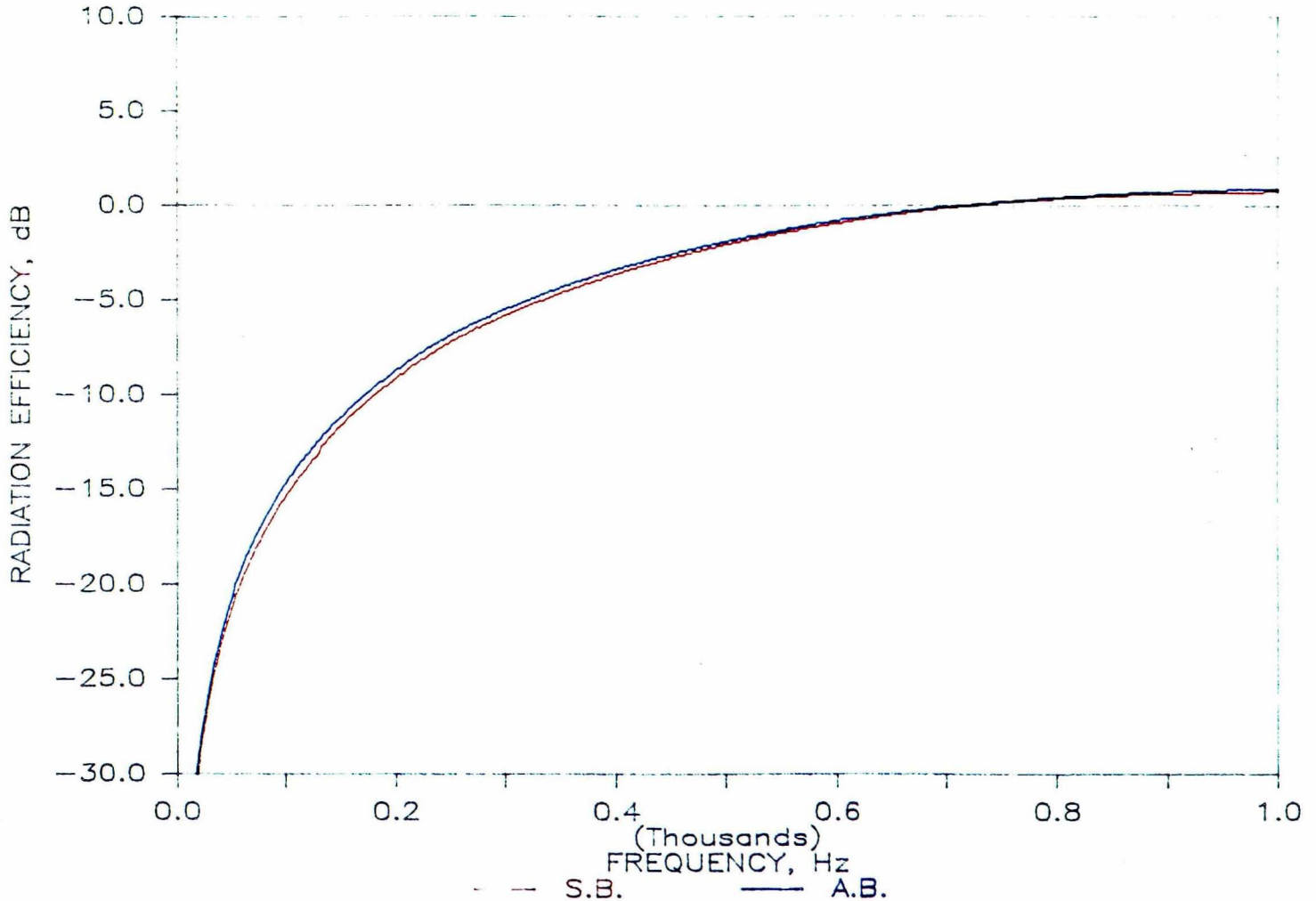

Figure (AX-8) -- Airborne and structureborne radiation efficiencies of an extremely stiff plate constructed of an imaginary material.

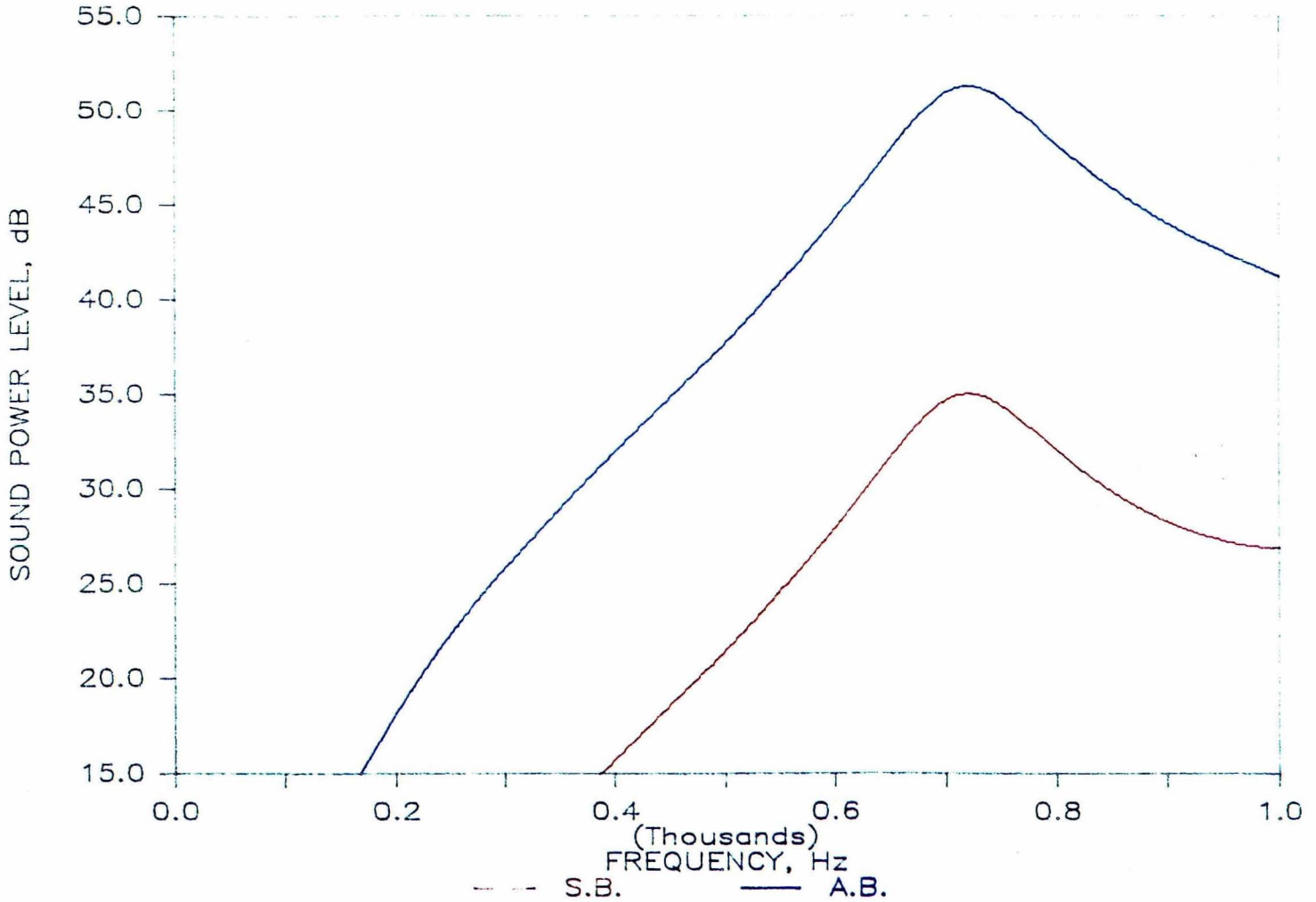

Figure (AX-9) -- Airborne and structureborne sound powers radiated by an extremely stiff plate constructed of an imaginary material.

Appendix XI

TWO MICROPHONE ACOUSTIC INTENSITY MEASUREMENT METHOD

A. DERIVATION OF THE FUNDAMENTAL EQUATION FOR INTENSITY

Recall from Appendix I, equation (A1.47) that the acoustic intensity is given by

$$\langle I \rangle_t = R_{pv}(0) = \int_0^\infty C_{pv}(f)\, df = Re\{ \int_0^\infty G_{pv}(f) \quad df\} , \qquad (A11.1)$$

and recall that an estimate of $G_{pv}(f)$ can be obtained from equation (A1.39) as

$$\tilde{G}_{pv}(f) = 2/T \left[P^*(f)V(f) \right] . \qquad (A11.2)$$

Substituting the estimate given by (A11.2) into (A11.1)

$$\langle I \rangle_t = Re\{ \int_0^\infty 2/T \left[P^*(f)V(f) \right] df\} . \qquad (A11.3)$$

Thus, the acoustic intensity as a function of frequency is given by

$$\langle I(f) \rangle_t = Re\{2\Delta f/T \left[P^*(f)V(f) \right] \} . \qquad (A11.4)$$

And from the theory of Finite Fourier transforms, it is known that $\Delta f = 1/T$, thus the equation for intensity as function of frequency is given by

$$\langle I(f)\rangle_t = 2/T^2 \; Re\{P^*(f)V(f)\} \; , \qquad (A1.5)$$

where the Finite Fourier transforms are defined by the equations (A1.4) and (A1.5) given in Appendix I, viz.

$$P(\vec{r},f) = F\{p(\vec{r},t)\} = \int_0^T p(\vec{r},t)\, e^{-j2\pi ft}\, dt \; , \qquad (A1.6)$$

$$V(\vec{r},f) = F\{v(\vec{r},t)\} = \int_0^T v(\vec{r},t)\, e^{-j2\pi ft}\, dt \; . \qquad (A1.7)$$

Now recall that the Navier-Stokes equation of momentum conservation for a compressible flow is given by

$$\rho_o D\vec{v}/Dt = \rho_o \vec{g} - \nabla p + \nabla\cdot\vec{\vec{\tau}}, \qquad (A1.8)$$

where ρ_o is the density of the fluid medium, $\vec{v}$ is the particle velocity, $\vec{g}$ is the acceleration due to gravity, p is the acoustic pressure, $\vec{\vec{\tau}}$ is the stress tensor due to viscous effects, ∇ is the gradient operator, and D/Dt is the substantial or total derivative given by

$$D/Dt = \partial/\partial t + v_1\partial/\partial x_1 + v_2\partial/\partial x_2 + v_3\partial/\partial x_3 \; . \qquad (A1.9)$$

It is well known in acoustic theory that the effects of the viscous stress tensor on acoustic wave propagation is that of a damping factor which is proportional to the acoustic driving frequency squared (see reference 59, pg. 518). Thus, the damping effects are known to be insignificant at

low frequency. Neglecting the effects of viscosity, the momentum equation simplifies to the familiar Euler's equation, viz.

$$\rho_o D\vec{v}/Dt = \rho_o \vec{g} - \nabla p \ . \qquad \text{(A11.10)}$$

Furthermore, gravity has a negligible influence on acoustic disturbances except at extremely low driving frequencies (see reference 59, pg. 9). Making a small perturbation assumption and neglecting the effects of gravity, the momentum equation becomes

$$\partial\vec{v}/\partial t = -1/\rho_o \nabla p \ . \qquad \text{(A11.11)}$$

If the analysis is confined to a single dimension, the momentum equation becomes

$$\partial v_x/\partial t = -1/\rho_o \ \partial p/\partial x_1 \ . \qquad \text{(A11.12)}$$

Making a finite difference approximation for the pressure gradient yields

$$\partial v_x/\partial t = -1/(\rho_o \Delta x) \ (p_1 - p_2) \qquad \text{(A11.13)}$$

where Δx is the spacing between the two microphones. Applying the Fourier transform as defined in Appendix I, equation (A1.3), the momentum equation becomes

$$\int_{-\infty}^{\infty} \partial v_x(\omega)/\partial t \ e^{-j\omega t} \ dt = -1/(\rho_o \Delta x) \left[P_1(\omega) - P_2(\omega) \right] . \qquad \text{(A11.14)}$$

Integrating the left side of equation (A11.14) by parts,

$$j\omega \int_{-\infty}^{\infty} v_x(\omega)\, e^{-j\omega t}\, dt = -1/(\rho_o \Delta x) \left[P_1(\omega) - P_2(\omega) \right] . \quad (A11.15)$$

Rearranging equation (A11.15) algebraically

$$\int_{-\infty}^{\infty} v_x(\omega)\, e^{-j\omega t}\, dt = j/(\rho_o \omega \Delta x) \left[P_1(\omega) - P_2(\omega) \right] . \quad (A11.16)$$

The term on the left side of equation (A11.16) is the Fourier transform of the particle velocity. Therefore,

$$V(\omega) = j/(\rho_o \omega \Delta x) \left[P_1(\omega) - P_2(\omega) \right] . \quad (A11.17)$$

Equation (A11.17) is an approximation of the particle velocity at a point midway between two microphones. The pressure midway between two microphones can be estimated by

$$P(\omega) = \left[P_1(\omega) + P_2(\omega) \right] /2 . \quad (A11.18)$$

Substituting equations (A11.17) and (A11.18) into equation (A11.5), and letting the frequency dependence be implicit

$$\langle I \rangle_t = 2/T^2 \, \mathrm{Re}\{P^* V\}$$

$$= 2/T^2 \, \mathrm{Re}\{ j/(2\rho_o \omega \Delta x) \left[P_1^* P_1 - P_2^* P_2 + P_2^* P_1 - P_1^* P_2 \right] \} . \quad (A11.19)$$

Recalling the equations for the estimation of auto and cross spectral density functions (A1.38) and (A1.39) and substituting into equation (A11.19), the result is

$$\langle I \rangle_t =$$

$$2/T^2 \; \mathrm{Re}\{ \; (j/2\rho_o\omega\Delta x)\cdot(T/2) \left[\; G_{11} - G_{22} + G_{12}^{*} - G_{12} \; \right] \}$$

$$= 1/T \; \mathrm{Re}\{ \; (j/2\rho_o\omega\Delta x) \left[\; G_{11} - G_{22} + 2jQ_{12} \; \right] \} \; . \qquad \text{(A11.20)}$$

Taking the real part of the right side of equation (A11.20) as indicated, the result is

$$\langle I \rangle_t = -1/T \; Q_{12}/(\rho_o\omega\Delta x) = -Q_{12}\Delta f/(\rho_o\omega\Delta x)$$

$$= \mathrm{Im}\{G_{12}\}\Delta f/(\rho_o\omega\Delta x) \qquad \text{(A11.21)}$$

where $-Q_{12}$ is the imaginary part of the one sided cross spectral density between microphones 1 and 2 (quad-spectral density).

B. ERRORS ASSOCIATED WITH ACOUSTIC INTENSITY MEASUREMENTS

There are five principle sources of error associated with the two microphone cross spectral method of intensity measurement in the 0-1000 Hz range. They are as follows:

1. Instrumentation phase mismatch.
2. Finite difference error.
3. Directional effects and errors of interpretation.
4. Near field effects.
5. Random errors.

For the convenience of the reader, a brief discussion of each type of error is presented here. More detailed discussions are contained in references 30, and 63-65.

Recall equation (A11.21) which states

$$\langle I \rangle_t = \mathrm{Im}\{G_{12}\}\Delta f/(\rho_o \omega \Delta x) \ . \qquad \text{(A11.21)}$$

Utilizing equation (A1.39) from Appendix I, the equation for time averaged intensity can be written as

$$\langle I \rangle_t = \mathrm{Im}\{\ 2/T\ P_1^* P_2\ \}\ \Delta f/(\rho_o \omega \Delta x) \ . \qquad \text{(A11.22)}$$

The complex Fourier transforms in equation (A11.22) can be represented in complex polar form and the equation can be rewritten as

$$\langle I \rangle_t = \mathrm{Im}\{\ 2/T\ |P_1|\ |P_2|\ e^{j(\theta_1-\theta_2)}\ \}\ \Delta f/(\rho_o \omega \Delta x)$$

$$= 2/T^2 \; |P_1| \; |P_2| \; \sin(\theta_1-\theta_2) \; /(\rho_o \omega \Delta x) \; . \qquad \text{(A11.23)}$$

Thus, it is obvious from equation (A11.23) that the magnitude of the intensity vector is proportional to the sine of the relative phase difference between the two microphones. This measured relative phase difference ($\theta_1-\theta_2$ or $\Delta\theta$) has a component due to instrumentation phase mismatch. The instrumentation phase mismatch causes the largest errors when it is of the same order of magnitude or larger than the physical phase difference. (The physical phase difference is the actual phase difference between the microphone signals that one hopes to measure.) This leads to the conclusion that the instrumentation phase mismatch causes its most serious errors at low frequencies where the wavelengths are long and the intensity probe is measuring a very small phase difference. Hence, this type of error is largest primarily in the low frequency regime. Elimination of the instrumentation phase mismatch may be approached in one of two ways. One method proposed by Chung et. al. (see reference 30) uses a microphone interchange technique to eliminate this type of error. The more common method is to carefully measure the instrumentation phase mismatch and compensate for it in subsequent computer calculations. The microphone interchange technique was used for the measurements in this study. This method utilizes two measurements

of the cross spectra and uses the following equation to calculate the acoustic intensity:

$$\langle I \rangle_t = \mathrm{Im}\{ \left[G_{12} \cdot G_{21} \right]^{1/2} \} \Delta f / (\rho_o \omega \Delta x) \ . \qquad \text{(A11.24)}$$

The use of this equation for the intensity measurments cancels all instrumentation phase mismatch exactly.

The second type of error introduced by the two microphone method is the error associated with the finite difference approximation of equation (A11.13). This error occurs primarily in the high frequency regime. To assure that this error is small, it should be required that

$$k\Delta x = \omega / c_o \ \Delta x = 2\pi \ \Delta x / \lambda << \pi / 2 \ , \qquad \text{(A11.25)}$$

so that $\Delta x / \lambda << 1/4$, where Δx is the spacing between microphones and λ is the wavelength of interest.

The third type of measurement error stems from misinterpretation of the results. Directional effects and flanking from multiple sources can result in the measurement of components of intensity vectors unintended by the measurer. Careful planning and execution of the measurements can help to prevent the acquisition of data contaminated with acoustic intensity vector components from unwanted sound sources.

The fourth type of error is near field measurement error. In theory, the large pressure gradients in the near field of higher order acoustic sources such as dipoles and

quadrapoles can cause considerable error in the measurement accuracy of the two microphone method. For a detailed discussion of this type of error see reference 63.

The final category of errors is random or statistical errors. Errors in the space averaging and time averaging are included in the random error. An extensive analysis of the statistical errors encountered in the time averaging of acoustic intensity measurements is contained in reference 64. Random errors due to the selected method of space averaging are not as well understood. Recent studies (see reference 65) indicate that, for the same number of measurements, the continuous sweep method of space averaging is more accurate than the fixed point method of averaging even under conditions where the sweep rate is non-constant.

Appendix XII

INSTRUMENT SPECIFICATIONS

Altec 405-8H Loudspeakers

Power	-	10 Watts music power
Frequency response	-	60-15000 Hz
Sensitivity	-	92 dB SPL at 4 ft. from 1 Watt
Impedance	-	8 Ohms
Size	-	4 3/8 in. X 4 3/8 in. X 2 1/8 in.

BBN 501 Piezoelectric Accelerometers

Sensitivity	-	10 mV/g
Amplitude linearity	-	Within 1% up to 212 g
Noise floor (1 Hz to 25 kHz)	-	.000020 V
Frequency response	-	Flat from 7 to 20000 Hz
Temp. range	-	-54 to 121 degrees Celsius
Peak operating g's	-	212
Weight	-	1.8 grams
Size	-	0.31 in. Dia. X 0.42 in. H

Bruel & Kjaer 2610 Measuring Amplifiers

Measuring range	-	.00001 V to 30 V FSD
Frequency range	-	Flat response 2 Hz to 200 kHz (within 0.5 dB)
Phase deviation	-	Within 5 degrees between any two instruments from 20 Hz to 20kHz
Overall gain	-	From -30 to +100 dB selectable in accurate 10 dB steps plus extra 0 to 10 dB gain for continuous adjustment between steps
Preamp input	-	Standard B & K 7 pin microphone socket with +200 V polarization
Filter mode	-	22.4 Hz high pass filter with 18 dB/octave fall off
Power required	-	115 V at 60 Hz
Temp. range	-	+5 to +40 degrees Celsius
Humidity	-	0 to 90 % relative humidity

Bruel & Kjaer 2706 Power Amplifier

Power output cap.	-	75 VA into 3 Ohm resistor load
Limiting	-	5 A for Vibration Exciter Type 4809
Frequency range	-	10 Hz to 20 kHz within 0.5 dB
Noise and Hum	-	At least 70 dB below full output
Attenuator	-	0 to 40 dB in 10 dB steps
Gain control	-	0 to minus infinity logrithmic
Power required	-	115 V at 60 Hz approx. 140 Watts
Temp. range	-	5 to 40 degrees Celsius

Bruel & Kjaer 4809 Vibration Exciter

Rated force	-	44.5 Newton, 10 lbf sine peak
Frequency range	-	10 Hz to 20 kHz bare table
Axial resonance	-	20 kHz bare table
Max. acceleration	-	736 m/s2 (75 g)
Max. displacement	-	8 mm (0.315 in) peak-to-peak
Maximum velocity	-	1.65 m/s (65 in/s) peak
Max. input current	-	5 A rms

Bruel & Kjaer 4166 Condenser Microphone with 2619 preamp.

Measuring range	-	25 to 145 dB SPL (lin. noise level 20 Hz to 20 kHz)
Frequency range	-	Flat response 20 to 20 kHz
Size	-	1/2 in. diameter

Fluke 2205A Switch Controller (scanner)

Channel capacity	-	10 channels used in this study (expandable to 100 channels)
Isolation	-	Signal lines to power ground greater than 10 billion Ohms
Cross talk	-	Less than 30 dB below applied signal from DC to 1 MHz when terminated with 1 MegaOhm
Temp. range	-	0 to 50 degrees Celsius
Humidity	-	0% to 80% relative humidity
Power required	-	120 V at 60 Hz, 15 VA maximum

Genrad 1382 Random Noise Generator

Spectrum	-	White noise from 20 Hz to 20 kHz within 1 dB with 1/2 power points at 10 Hz and at 50 kHz
Output voltage	-	Maximum open circuit output voltage is at least 3 V rms for any bandwidth
Amplitude control	-	Output amplitude is continuously adjustable from full output to approx. 60 dB below that level
Power required	-	6W at 100 to 125 V at 60 Hz

Genrad 2515 Computer-Aided Test System

Number of channels	-	8 (expandable to 16)
Frequency range	-	DC to 25.6 kHz with alias protection on all channels (DC to 1024 Hz used in this study)
Dynamic range	-	> 70 dB with 12 bit A/D conversion
Amplitude flatness	-	Within 0.25 dB over entire range
Channel deviation	-	Within 0.2 dB amplitude < 2.0 degrees phase up to 10 kHz
Sensitivity	-	8 ranges (0.0625 V full scale lowest range) (8.0 V full scale highest range)
Max. Voltage	-	Protected to 25 V
Bandwidths	-	15 selectable ranges from 1.28 Hz to 20.5 kHz plus 25.6 kHz
Storage	-	10 Mbytes on Winchester drive and 0.5 Mbytes on mini-floppy
Averaging	-	Summation averaging with Hanning and 50% redundancy used in this study

Genrad 2515 Computer-Aided Test System (cont'd)

Processing	-	Measurement and calculation of transfer functions and auto power spectra were used in this study
Power required	-	120 V at 60 Hz 500 Watts
Temp. range	-	10 to 45 degrees Celsius
Humidity	-	20% to 80% relative humidity

Hewlett Packard 350D Attenuator Set

Attenuation	-	110 dB in 10 dB and 1 dB steps
Accuracy	-	For the 10 dB section from 0 to 100 kHz error is less than 0.125 dB For the 100 dB section from 0 to 100 kHz error is less than 0.25 dB at any step up to 70 dB and less than 0.5 dB for steps above 70 dB
Power capacity	-	In 600 Ohms; 5 Watts (55 V rms)

Hewlett Packard 3403C True RMS Voltmeter

Ranges	-	.01 V .1 V 1.0 V 10.0 V 100.0 V 1000.0 V
Voltage measurement accuracy	-	Error within 0.2% of full scale plus 0.2% of reading for the 25 Hz to 100 kHz range for the 1 V, 10 V, and 100 V settings
Response time	-	Fast: 1 second Slow: 10 seconds

Kenwood KA-52 Stereo Integrated Amplifier

Power output	-	55 Watts when both channels driven at 8 Ohms 1 kHz
Total Harmonic Distortion (20 Hz to 20 kHz)	-	.09% at rated power into 8 Ohms
Frequency response	-	Flat 10 Hz to 100 kHz
SNR	-	101 dB for 150 mV input
Power required	-	120 V at 60 Hz 185 Watts

PCB 221 Force Transducer

Dynamic range	-	.004 to 100 lbs.
Sensitivity	-	50 mV/lb
Resonant frequency	-	70,000 Hz
Full scale ouput	-	5 volts
Temp. range	-	-73 to 121 degrees Celsius
Max. vibration	-	2000 g

Rockland 1022F Analog Filter

Filter type	-	2 analog filters which can be selected as either high pass or low pass
Frequency range	-	10 Hz to 111 kHz
Roll-off	-	24 db/octave/section
Responses	-	Butterworth, RC
Passband gains	-	Selectable 0, 20, 40 dB

Tektronix T922R Oscilloscope

Type	-	Dual channel
Frequency range	-	DC to 5 MHz
Max. input voltage	-	30 V
Power required	-	120 V at 60 Hz
Temp. range	-	0 to 45 degrees Celsius

End of Document